TECHNISCHE UNIVERSITÄT MÜNCHEN

Lehrstuhl für Biologische Bildgebung

Multi-Spectral Optoacoustic Tomography: Methods and Applications

Andreas B. Bühler

Vollständiger Abdruck der von der Fakultät für Elektrotechnik und Informationstechnik der Technischen Universität München zur Erlangung des akademischen Grades eines

Doktors der Naturwissenschaften (Dr. rer. nat.)

genehmigten Dissertation.

Vorsitzender: Univ.-Prof. Dr. Samarjit Chakraborty

Prüfer der Dissertation:

1. Univ.- Prof. Vasilis Ntziachristos, Ph. D.
2. Univ.- Prof. Dr. Axel Haase

Die Dissertation wurde am 26.07.2013 bei der Technischen Universität München eingereicht und durch die Fakultät für Elektrotechnik und Informationstechnik am 09.06.2014 angenommen.

Abstract

Macroscopic optical small animal imaging plays an increasingly important role in biomedical research, as it can noninvasively examine structural, physiological, and molecular tissue features *in vivo*. A novel modality that emerged in the last decade is optoacoustic (photoacoustic) imaging, which combines versatile optical absorption contrast with high ultrasonic resolution and real-time imaging capabilities by capitalizing on the optoacoustic (photoacoustic) effect. Using illumination with multiple wavelengths and spectral unmixing methods, multispectral optoacoustic tomography (MSOT) has the potential to specifically resolve tissue chromophores or administered extrinsic molecular agents non-invasively in deep tissue with unprecedented resolution performance and in real-time.

The presented work explores MSOT in the context of small animal imaging. Different instrumentation and detection geometry related effects are analyzed regarding their influence on the imaging performance. Based on the findings, two dedicated MSOT imaging platforms for 2D and 3D real-time imaging of small animals and tissue samples are conceived, implemented and imaging performance is characterized by simulation, on phantoms and *ex vivo* in mice.

Beside instrumentation, the utilized signal processing, image reconstruction and spectral unmixing strategy is of great importance for achieving best imaging results. The research presented shows how reconstruction artifacts can be reduced by compensating for the electrical impulse response of the system and that the calculation of intermediate projections can alleviate artifacts due to sparse angular sampling. Moreover, two regularization approaches for 2D limited view reconstructions are presented and a 3D model-based inversion scheme for improving 3D reconstructions in the developed systems by modeling the shape of the detection elements. Finally, the challenges of multispectral unmixing in deep tissue are discussed; two unmixing schemes for detection of molecular agents are presented and a method to partially compensate for the effect of light attenuation is proposed.

Using the unique imaging performance of the developed methods, it is further established that MSOT can actually resolve anatomical, dynamic and molecular information in mice and that it can be used for assessing biodistribution and pharmacokinetic parameters of molecular probes and contrast agents in tissue. A complete whole-body mouse scan is shown, resolving anatomical hemoglobin-based contrast. Functional imaging is presented by tracking contrast enhancement in the kidneys due to perfusion of systemically administered Indocyanine green (ICG). Also the clearance rate of ICG and liposomal ICG from the blood pool is determined by means of MSOT. Molecular imaging performance is shown by detecting optical reporter agents (here a phosphatidylserine targeting fluorescent dye) within mouse xenograft tumors.

List of abbreviations

AF750	AlexaFluo750
GN	Gold nanoparticles
BP	Backprojection algorithm
CT	Computed tomography
DOT	Diffuse optical tomography
EFR	Electrical frequency response
EIR	Electrical impulse response
FMT	Fluorescent molecular tomography
FWHM	Full width at half maximum
GSVD	Generalized singular value decomposition
Hb	Oxygenated hemoglobin
HbO_2	Deoxygenated hemoglobin
ICA	Independent component analysis
ICG	Indocyanine green
IMMI	Interpolated matrix model-based inversion
LSQR	Algorithm for solving sparse linear equations
MB	Model-based algorithm
3D MB+SIR	3D model-based algorithm with incorporated spatial impulse response
3D MB1SP+SIR	3D MB+SIR reconstructions using data from only one scanning position
MPE	Maximal permissible skin exposure
MIP	Maximum intensity projection
MRI	Magnetic resonance imaging
MSE	Mean square error
MSOT	Multispectral optoacoustic tomography
NIR	Near-infrared
OPO	Optical parametric oscillator
PCA	Principal component analysis
PET	Positron emission tomography
PLSQR	Preconditioned LSQR
PSF	Point spread function
PSS-794	Phosphatidylserine targeting fluorescent probe
ROI	Region of interest
RMSD	Root mean square deviation
SIR	Spatial impulse response
SNR	Signal-to-noise ratio
SPECT	Single photon emission computed tomography
SVD	Singular value decomposition
TGSVD	Truncated generalized singular value decomposition
TIR	Total impulse response
TSVD	Truncated singular value decomposition
XCT	X-ray computed tomography

Contents

1 Introduction

1.1 Motivation

Small animals, especially mice, are widely used in biomedical research and drug discovery as mammalian models to study biological interactions, systemic responses and human diseases. Imaging provides a means to probe structural, physiological and molecular information noninvasively and *in vivo*. By enabling extended longitudinal studies of the same animal, imaging minimizes the amount of animals needed in a particular study. This reduces costs and finally accelerates biomedical research [1]. As a consequence, a lot of research is ongoing to develop new small animal imaging methodologies that can provide versatile contrast at high resolution [1-3].

In 2007, a novel and promising concept called multispectral optoacoustic tomography (MSOT) has emerged [4, 5]. Capitalizing on the optoacoustic phenomenon, *i.e.* the generation of acoustic waves due to thermoelastic expansion caused by absorption of nanosecond short optical pulses, it combines optical absorption contrast with the high resolution of ultrasound and the potential for real-time operation. First experiences with MSOT showed that this method is able to resolve fluorescent dyes injected in an excised mouse leg [6] and fluorescent proteins in zebra-fish [7]. The ability to resolve chromophoric probes or reporter agents that are frequently used in biomedical research through several millimeters to centimeters of tissue with high resolution, makes MSOT an interesting tool for biomedical imaging applications [4].

Yet, in order to fully exploit the potential benefits that the MSOT technology offers, especially for preclinical small animal imaging, dedicated small animal imaging systems and improved image reconstruction algorithms are necessary. Existing implementations presented in the literature until 2009 when this work was started, were generally inappropriate for this task and thus *in vivo* multispectral optoacoustic mouse imaging not shown yet. First, because these systems frequently used detection arrangements and detector characteristics which yield long acquisition times (minutes to hours). Control of animal physiological parameters, motion and anesthesia during such extended measurement periods can present a significant challenge for obtaining high quality images. Furthermore, interesting *in vivo* imaging studies such as dynamic monitoring the biodistribution of targeted contrast agents or functional responses to physiological stimuli require acquisition times in the order of seconds to milliseconds and are therefore not possible in such systems [8]. Second, because in these systems the mouse was generally completely immersed into water, which is used as a coupling medium to propagate the ultrasound waves from the sample to the detector. Whereas this is not problematic for *ex vivo* or partial body imaging, this poses severe difficulties considering *in vivo* whole body imaging.

The goal of this work is therefore to develop a dedicated small animal optoacoustic imaging system and image reconstruction algorithms for convenient and fast *in vivo* imaging of mice and to use the system to examine the potential the MSOT technology offers with respect to small animal imaging, with a specific focus on visualizing anatomical, functional and molecular information in small animals *in vivo*.

1.2 Preclinical imaging today

Various small animal imaging methodologies are currently available. With respect to the information an imaging modality can assess, one distinguishes between anatomical, functional and molecular imaging. Anatomical imaging relates to the extraction of structural information. It is used to study morphological changes. Typically, these images are high resolution images based on endogenous contrast. Functional imaging relates to imaging of organ function and movement after physiological or pharmacological stimulations. It requires fast image acquisition in order to be able to sense temporal changes. Molecular imaging refers to the visualization of biological processes at a cellular and molecular level. It generally includes the use of molecular probes to target specific classes of cells, receptors and other cellular and subcellular constituents [9]. Preferentially, modern small animal imaging systems provide all these three types of information.

To develop small animal imaging technologies, two approaches have been followed. On the one hand, established radiological modalities, like X-ray computed tomography (CT), magnetic resonance imaging (MRI), positron emission tomography (PET), single photon emission computed tomography (SPECT) or ultrasonography, have been downscaled and adapted to small animal dimensions. On the other hand, new imaging modalities have been developed, mostly in the field of macroscopic optical imaging. Due to a smaller field of view and modified operation characteristics (*e.g.* higher field strength in MRI, or higher frequencies in ultrasound), these downsized radiological systems attain higher resolution and higher detection sensitivity than their clinical counterparts [2, 10-12]. For anatomical imaging the methods of choice are CT and MRI. Both modalities provide submillimeter resolution and excellent deep tissue imaging capabilities. The advantage of CT is imaging speed and excellent bone tissue contrast. Soft tissue contrast however is relatively poor. It can be improved by using X-ray attenuating contrast agents (*e.g.* iodinated agents), as is done for angiographic imaging. CT is generally not used for molecular imaging. A further drawback is the use of ionization radiation. MRI on the contrary is insensitive to bones but provides excellent soft tissue contrast. In addition, it allows assessment of the blood oxygenation status *via* the blood oxygenation level dependent (BOLD) effect [13], thus can be used for functional imaging. For molecular imaging applications, probes labeled with paramagnetic particles (*e.g.* gadolinium) are available. Thus MRI is a methodology which allows anatomical, functional and molecular imaging. Drawbacks of MRI are costs and sensitivity, the latter being several orders of magnitudes less than for nuclear imaging techniques. PET and SPECT are typical molecular imaging modalities. In order to probe molecular targets, radionuclides emitting gamma rays are frequently used. By these means, PET and SPECT achieve high sensitivity. Drawbacks are low resolution and the use of

ionizing radiation. Ultrasonography is the most widespread clinical imaging modality, because of its low cost, safe use and real-time image formation but it does not allow molecular imaging [11].

Optical imaging is a powerful modality with several advantages over the existing radiological techniques. First, optical photons are non-ionizing, therefore non-hazardous and safe to use for *in vivo* imaging. Second, optical imaging provides versatile contrast. Optical absorption and scattering for instance allows differentiation between tissues types and constituents indistinguishable with other modalities. Moreover, optical absorption allows assessing the oxygenation status of blood, thus can be used, analogous to MRI, to extract functional information [14]. Third, many optical reporter agents that probe tissue constituents and their function by labeling certain classes of cells, receptors and other entities of cellular activity have already been developed for *in vitro* applications [4]. Utilizing these concepts that are well established *in vitro* for macroscopic *in vivo* imaging, offers new possibilities to extract biological relevant information from living subjects [11].

Among the optical imaging technologies, microscopy is the most common one. It provides sub-micrometer resolution and is well established in biochemical research as a tool to visualize cellular and subcellular structures and processes *in vitro* and *in vivo* [9]. The resolution however, relies on the ability to focus light into tissue which degrades with depth due to photon scattering in tissue. Microscopic technologies are therefore limited to the ballistic regime, which is in the order of 100 µm [15]. To image deeper in tissue, confocal microscopy [16] and multiphoton microscopy [17] have been developed. These technologies can account for light scattering in tissue and allow imaging in depths between 100 - 200 µm and 300 - 500 µm, respectively. For whole body small animal imaging, these technologies are generally not suited due to the limited imaging depth and the limited field of view. In response, macroscopic optical imaging technologies have been developed. Beside photon scattering in tissue, which reduces the resolution both in microscopic and macroscopic imaging modalities, light attenuation becomes an additional limiting factor for macroscopic optical imaging [15]. Therefore macroscopic optical imaging modalities generally work in the near-infrared region (NIR) between 650 and 950 nm, where biological tissue possesses a "spectral window" with reduced light attenuation. Imaging depths beyond 5-6 cm in biological tissues are not realistic, but they are also not needed for small animal imaging, because the diameter of mice is in the order of 2 cm. Early implementations of macroscopic optical imaging systems are 2D photographic methods based on epi- or transillumination techniques [2, 18]. Target localization and quantification in such planar implementations is however complicated due to the loss of depth information, light attenuation and scattering, which also reduces the resolution [4]. In response to this, with progress in the mathematical description of photon transport in tissue, diffuse optical tomography (DOT) methods have been developed. These methods use information from different illumination and detection paths and combine them mathematically to reconstruct the 3D distribution of the optical contrast inside the imaged object. In this way, diffuse DOT yields significantly improved resolution and quantification over its 2D photographic counterparts [4]. For detection of fluorescent probes, fluorescent molecular tomography (FMT) has been developed [19]. Similar to DOT,

FMT uses tomographic illumination and detection patterns combined with mathematical models of photon transport to yield quantitative 3D images of fluorescence distribution. More recently, new hybrid approaches have been developed, such as the combination of FMT with computed X-ray tomography (XCT) [20]. In this approach, the anatomical information obtained from the XCT scanner is used to assign appropriate optical properties to a priori segmented organs such as lung, heart, and bones, leading to improved imaging performance compared to stand-alone approaches [21], however with the drawback of using ionizing X-ray radiation.

A different and very promising approach is optoacoustic tomography, also termed photoacoustic or thermoacoustic tomography [2, 22-24]. This method provides high resolution maps of optical absorption by measuring ultrasound waves resulting from thermal expansion following the deposition of short light pulses in the imaged tissue. Since the method relies on acoustic waves for detection, which are scattered 2 to 3 orders of magnitude less in tissue than optical photons, optoacoustic tomography achieves high resolution while preserving optical absorption contrast [23, 25, 26]. In the last decade, optoacoustic imaging has mainly been used to visualize hemoglobin-based contrast, owing to the fact that hemoglobin besides melanin is one of the strongest absorbers in biological tissue and therefore gives the strongest optoacoustic signal. Examples are imaging of superficial vasculature [27], tumor angiogenesis [28, 29], breast tumor detection [30] or functional brain imaging by monitoring the blood-oxygenation status [23]. Extrinsic contrast agent based approaches using dyes [6], carbon [31] and gold nanoparticles [32] or quantum dots [33] have also been developed. However, detection of extrinsic probes in presence of the strong endogenous background absorbers by using single wavelength illumination is challenging. A typical approach to distinguish the probe from the background absorbers is the subtraction of background measurements made before probe administration. This requires the exact same animal positioning which is difficult to realize, especially in longitudinal studies. To overcome this problem, the concept of multispectral optoacoustic tomography (MSOT) has been proposed by Razansky *et al.* [6]. To increase the detection sensitivity, MSOT uses multi-wavelength illumination to take into account the spectral profile of the absorber of interest. In initial experiments, MSOT was shown to resolve a fluorescent dye injected in an excised mouse leg [6] and fluorescent proteins in zebra-fish [7]. By being able to resolve such biologically relevant reporter agents in tissue, MSOT has the potential to become an important tool for biomedical research.

1.3 MSOT – Principle of operation

The MSOT principle of operation is illustrated in Fig. 1.1. The underlying physical principle is the photoacoustic effect, which refers to the generation of acoustic waves resulting from the absorption of electromagnetic energy [34]. In the imaging process, the object to be imaged is illuminated by short laser pulses in the range of 1 - 100 ns. Some of the electromagnetic energy is absorbed within the object and partially converted into heat. A temperature rise leads to thermo-elastic expansion, which, in turn, is followed by a pressure rise. As a results of the initial pressure rise,

a broadband ultrasound wave propagates through the tissue and can be detected outside the object. Typically, this is done with ultrasound transducers. The amplitude of this pressure wave reflects the local energy absorption. It is possible to calculate the distance between the optoacoustic source (*i.e.* the optical absorber) and the detector, from the time of arrival of the pressure wave, *i.e.* the time elapsed between the laser pulse and the detection of the optoacoustic signal (assuming the speed of sound in the object is known). By tomographic detection and inversion, the spatial distribution of the absorbers in the object can be calculated [26, 35]. In order to take the spectral signature of the absorbers into account, MSOT utilizes pulses at different wavelengths. This is done in a time-shared fashion. The wavelengths are selected according to the absorption profile of the absorbers of interest. Best performance can be achieved when the spectral profile of the absorbers differs significantly from the background absorbers. To separate the multi-wavelength images and resolve the absorber with the spectral profile of interest, multi-spectral unmixing algorithms are employed [4].

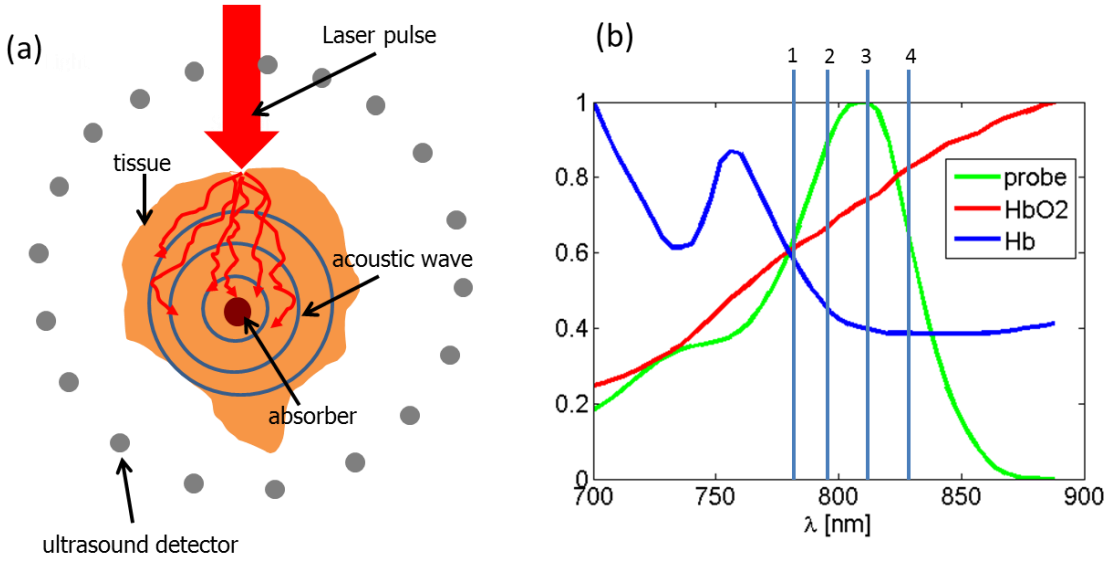

Fig. 1.1: Principle of MSOT operation. (a) Pulsed laser light illuminates the tissue of interest: Electromagnetic energy is absorbed and partially converted into heat. This creates a pressure wave *via* a thermo-elastic expansion. The pressure wave is detected with ultrasound sensors. Using tomographic inversion methods, an image of the initial pressure distribution can be calculated. (b) Multi-wavelength illumination can be used to take the spectral characteristics of the tissue absorbers into account, thus yielding an increased detection sensitivity compared to single wavelength methods.

1.4 Questions addressed in this work

This work focuses on methods for multispectral optoacoustic imaging, including system development, the algorithms necessary for image reconstruction and the application of both to small animal imaging.

Specific questions addressed in this work are:

1. Regarding instrumentation:
   - Which are the technology and instrumentation related requirements for successful MSOT imaging? How does the chosen instrumentation and detection geometry affect the imaging outcome?
   - What is an appropriate system design to enable practical *in vivo* whole body MSOT imaging of mice?

2. Regarding signal processing, image reconstruction and multispectral unmixing:
   - What are the optimal signal processing and image reconstruction approaches for imaging in the developed system? How to alleviate artifacts due to sparse angular sampling? Does the reconstruction accuracy improve when we model experimental factors such as the electrical impulse response of the system or the shape of the transducer elements? How do these methods perform in limited view situations?
   - How to detect specific absorbers in a set of multi-wavelength images? What are the challenges in deep tissue with respect to probe detection and quantification? Is there a benefit of using blind unmixing techniques? Is there a practical approach to achieve correction of light fluence attenuation?

3. With respect to applications:
   - Is it possible to image a whole mouse *in vivo*? Which structures and organs of clinical relevance are visible?
   - Is it possible to monitor dynamic events such as motion or perfusion? Can this be done in 2D and 3D? What is the benefit of this capability?
   - Can we specifically detect contrast agents or molecular probes in deep tissue? Is it possible to visualize their biodistribution and extract pharmacokinetic properties from this? Is there any benefit over other macroscopic optical small animal modalities?

1.5 Outline of this work

The presented work is organized as follows:

Chapter 2 provides the theoretical and technical background for optoacoustic imaging. It reviews the physics behind and approaches for optoacoustic image formation. It also briefly discusses general aspects of instrumentation and effects related to hardware deviating from ideal imaging conditions, including bandwidth limited detection, finite size detectors, limited view detection and sparse angular sampling. The goal of the chapter is to establish the framework necessary to appreciate the subsequent chapters, which describe original research on the topic of optoacoustic imaging.

Chapter 3 describes the development and characterization of a 2D real-time small animal MSOT imaging system. The motivation for assembling such a system is given along with a short overview about existing state-of-art small animal imaging systems. Design aspects and its technical implementation are discussed, followed by

an in-depth characterization of the component performance. It is shown that such considerations are important, because some of these parameters (*e.g.* the electrical impulse response), improve accuracy, if they are taken into account during the imaging reconstruction process.

Chapter 4 delineates signal processing and image reconstruction for 2D imaging. In this case, 2D is defined by the reconstruction of cross-sectional images that are reconstructed from tomographic data acquired at a single scanning position using a cylindrically focused 1D detector array. Chapter 4 outlines the steps needed for generating images of the best quality. Specifically, the following points are discussed: (1) correction for the electrical impulse response of the ultrasound detectors; (2) reduction of aliasing artifacts and (3) regularization of model-based image reconstructions in limited view scenarios.

Chapter 5 deals with the 3D image reconstruction capacity of the system. Since the system uses focused detectors to enable cross-sectional real-time imaging, conventional 3D image reconstruction approaches assuming unfocused point-detectors are inappropriate for this task. Simple stacking of cross-sectional slices also does not yield satisfying results due to a frequency dependent elevational resolution. Therefore an advanced 3D model-based reconstruction algorithm was developed accounting for the shape of the detection elements. It was found that the algorithm can improve both the 2D and 3D image reconstruction accuracy of the system.

Chapter 6 deals with multispectral imaging. Starting with the formulation of the multispectral unmixing problem and the particular challenges in deep tissue, namely spectral coloring due to wavelength dependent light attenuation, two multispectral unmixing algorithms for detection of molecular agents and a method for partial compensation of light attenuation effects are presented and tested in simulation and on experimental data.

Chapter 7 presents *in vivo* imaging results that are achieved with the developed system. Specifically, whole body anatomical imaging based on intrinsic hemoglobin-based contrast is shown, as well as 2D functional imaging by tracking perfusion after injection of extrinsic contrast agents and 2D molecular imaging by detecting systemically administered tumor targeting agents.

Optoacoustic imaging is a 3D problem and has the intrinsic potential for 3D real-time imaging. Chapter 8 presents a 3D real-time optoacoustic imaging prototype conceived as an attempt improve on the limitations of the 2D real-time system, namely the need to scan to acquire a 3D dataset and the strong frequency dependent elevational resolution. It will be used to showcase for the first time high resolution optoacoustic real-time imaging of small volumes (*e.g.* excised organs) and 3D perfusion of fluorescent contrast agents in deep tissue structures.

Finally, at the end of this thesis a conclusion about the work accomplished and an outlook about future developments is given.

2 Theoretical and technical background

2.1 Introduction

The goal of this chapter is to establish the theoretical and technical background for successful optoacoustic imaging[1]. The chapter is divided into three parts:

Section 2.2 presents the physics for optoacoustic imaging. Starting with light and sound behavior in tissue, it also discusses optoacoustic signal generation and related effects such as the directivity of signals.

Section 2.3 presents technological requirements and general instrumentation for optoacoustic imaging as well as detection system related parameters such as the electrical and spatial impulse response. An understanding of these parameters is important since they influence reconstruction accuracy and thus should be considered in the acoustic inversion process, as will be shown in chapters 4 and 5.

Section 2.4 reviews concepts of optoacoustic image formation, including focused detector techniques and computed reconstructions available. It also discusses spatial resolution and effects related to hardware deviating from ideal imaging conditions, including bandwidth limited detection, finite size detection elements, limited view detection and sparse angular sampling. Understanding of these factors is important for designing an optoacoustic imaging system. It also lays the ground-work for chapter 4.3, which presents approaches to alleviate these effects.

2.2 The physics of optoacoustic imaging

2.2.1 Light in tissue

All matter is composed of charged particles, like protons, electrons and ions. Electro-magnetic waves, such as light, interact with these charged particles [35]. When light propagates through biological tissue it might therefore be scattered and/or absorbed. Scattering refers to the redirection of light and is the strongest in structures whose size match the optical wavelength. In the visible and near infrared range (400 - 1000 nm), these structures are supporting tissue like elastin or collagen, blood cells and cell organelles, such as nucleus, mitochondria or endoplasmic reticulum [9]. Absorption means uptake of electromagnetic energy by the electronic and vibrational structures of the tissue constituents and is intrinsically sensitive to chemical composition [35]. Absorbed light can be converted into heat, consumed in a chemical reaction or re-emitted, for example as fluorescence. Important intrinsic absorbers in biological tissue are oxygenated (HbO_2) and deoxygenated (Hb) hemo-

[1] The chapter is based on several books [35, 25, 49], review papers [9, 14, 46, 26, 58] and theses [37, 41] with both overlapping and complementary content and is complemented by own considerations and simulations.

globin, tissue pigments like melanin, water and lipids [14]. Fig. 2.1 shows their absorption spectra. Absorption in tissue is strongly sensitive to the wavelength. There is an optical window between 650 - 900 nm in which the optical absorption of tissue drops two orders of magnitude, which allows penetration of light relatively deeply (up to several centimeters into biological tissue). Below 650 nm, light penetration is hindered by hemoglobin absorption, above 900 nm by water absorption. To describe the scattering, one uses the bulk scattering coefficient μ_s which gives the probability of a scattering event per unit path length. In biological tissue, μ_s has an approximate value of 100 cm^{-1} [35]. To describe the optical absorption an analogue expression termed the optical absorption coefficient is used with a representative value in biological tissue between 0.15 - 0.5 cm^{-1} at 750 nm [9]. Optical absorption in tissue is weak compared to the scattering. The mean free path between two scattering events is only about 0.1 mm, whereas the optical absorption length can extend to 10 - 100 mm. As a consequence, light is scattered multiple times before being absorbed and progressively loses its directivity shortly after entering the tissue. With respect to light propagation in tissue, one therefore distinguishes between two regimes: the ballistic regime (under 1 mm), in which light is not (or hardly) scattered and therefore still preserves its original directivity, and the diffusive regime where light propagates omnidirectionally due to multiple scattering events. In the ballistic regime, light transport can still be described by the laws of geometrical optics and in the diffuse regime one generally uses the diffusion equation [14]:

$$\frac{1}{c}\frac{\partial \emptyset(\boldsymbol{r},t)}{\partial t} - \vec{\nabla}D(\boldsymbol{r})\vec{\nabla}\emptyset(\boldsymbol{r},t) + \mu_a(\boldsymbol{r})\emptyset(\boldsymbol{r},t) = S(\boldsymbol{r},t), \tag{2.1}$$

where $S(\boldsymbol{r},t)$ is the source term, $\emptyset(\boldsymbol{r},t)$ the fluence rate in $J(m^3s)^{-1}$, c in ms^{-1} the speed of light and $D(\boldsymbol{r}) = 1/3(\mu'_s + \mu_a)$ is the diffusion coefficient. $\mu'_s = (1-g)\mu_s$ is the reduced scattering coefficient established to describe the light scattering as an isotropic phenomenon, although each individual scattering event is anisotropic. In other words, it is a measure to describe directive scattering in

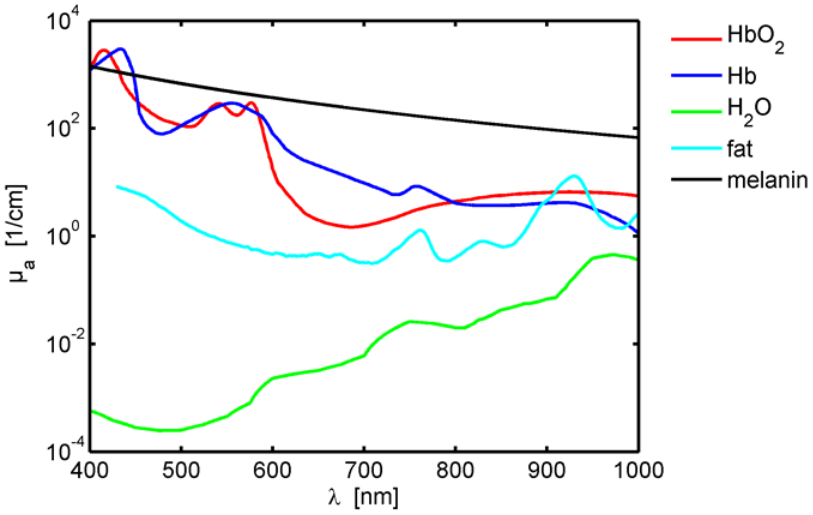

Fig. 2.1: Absorption spectra of common tissue absorbers. A hemoglobin concentration of 150 $mg(ml)^{-1}$ is assumed. Data compiled by Scott Prahl, Oregon Medical Laser Center (http://www.omlc.ogi.edu/spectra).

an isotropic scattering environment. g is the anisotropy factor which takes into account this loss of directivity and has a value between 0.8 and 0.99 in biological tissue [9].

In optoacoustics, light fluence inside tissue is often estimated under continuous wave illumination. This is possible because photon propagation through the region of interest is significantly shorter than the duration of the laser pulse used for excitation [36]. In this case, the diffusion equation (2.1) simplifies to

$$\nabla^2 \emptyset(\boldsymbol{r}) + \frac{\mu_a}{D(\boldsymbol{r})} \emptyset(\boldsymbol{r}) = \frac{S(\boldsymbol{r})}{D(\boldsymbol{r})}. \tag{2.2}$$

For uniform broad beam illumination, the light fluence within the object can be approximated by the 1D solution of the diffusion equation. It follows the Beer's law and is given by [14]:

$$\phi(r) = \phi_0 exp(-\sqrt{\frac{\mu_a}{D}} r) \tag{2.3}$$

where r represents the distance from the surface. To get a realistic idea about the effect of the light attenuation in tissue, one has to consider tissue-realistic values ($\mu'_s = 10$ cm^{-1} and $\mu_a = 0.3$ cm^{-1}). Using these values in Eq. (2.3), we see that 1 cm below the surface, the light fluence has already dropped to about 5% of its initial value. As will be shown in section 2.2.3.1, the optoacoustic signal strength is proportional to the light fluence. Signals from deep inside the mouse are therefore weaker than signals from the directly illuminated surface. In this respect, light attenuation is a major challenge in optoacoustic tomography which, from an instrumentation point of view, has as consequence that the detection system has to be very sensitive with a large dynamic range to detect both the weak signals from deep inside the mouse and the strong signals from superficial structures [37]. Moreover, special attention should be paid to optimizing the light delivery, for instance by illumination from several directions, in order to maximize the light deposition in deep tissue structures.

2.2.2 **Sound in tissue**

Acoustic waves at frequencies higher than 20 kHz are referred to as ultrasound. Ultrasound travels through tissue in form of a longitudinal compression wave. The propagation speed v_s [ms^{-1}] of acoustic waves in tissue depends on the density ρ [gcm^{-3}] and compressibility κ [Pa^{-1}] of the material:

$$v_s = \sqrt{\frac{1}{\rho\kappa}} \tag{2.4}$$

i.e. the denser or more rigid the material, the higher the propagation speed. In soft tissue or water, the velocity is about 1500 ms^{-1}. Variations are typically in the order of 5%. The sound speed for bones is approximately 3500 ms^{-1} and in air around

330 ms^{-1} [9]. The product of sound speed and material density is called acoustic impedance:

$$Z = v_s \rho. \tag{2.5}$$

The unit of the acoustic impedance is the Rayl, corresponding to $kgm^{-2}s^{-1}$. The pressure generated by these acoustic waves depends on the displacement velocity of the particles v_d:

$$P = Z v_d. \tag{2.6}$$

If a sound wave hits an interface between areas with different acoustic impedances at normal incidence, a fraction of the intensity of the incident wave will be reflected back into the first medium according to

$$R = \left(\frac{Z_2 - Z_1}{Z_2 + Z_1}\right)^2 \text{ and } T = \frac{4Z_1 Z_2}{(Z_1 + Z_2)^2} \tag{2.7}$$

where R is the reflection and T the transmission coefficient describing the percentage of the reflected and transmitted energy, respectively [38]. Reflection of ultrasonic waves by tissue structures is the basis of ultrasound imaging, where these reflected waves are detected and used to form an image. Since the difference in acoustic impedance in soft tissue is rather small (between 1.38 and 1.63 MRayl), ultrasound imaging only provides limited soft tissue contrast but a good penetration depth [9]. On the other hand, the acoustic mismatch between tissue and air (Z = 416 Rayl) is quite high. Therefore, whenever acoustic waves are to be detected outside the tissue (*e.g.* in optoacoustic imaging), a matched coupling medium (*e.g.* water) has to be used to enable propagation of the acoustic waves to the detector; otherwise they would remain confined in the tissue. If the ultrasound wave arrives upon a boundary at an angle θ_i, it is refracted. The change of the angular direction of the transmitted wave depends on the speed of sound of the two materials according to Snell's law:

$$n = \frac{sin\theta_i}{sin\theta_t} = \frac{v_{s1}}{v_{s2}} \tag{2.8}$$

where n represents the index of refraction. In soft tissue $n \approx 1$, thus ultrasound is little refracted and generally preserves its direction of propagation. When an ultrasound wave encounters a surface roughness or particles much smaller or approximately equal to the acoustic wavelength, it is scattered. However, the scattering coefficient for ultrasound in tissue is 2-3 orders of magnitudes less than for light and can be ignored in optoacoustic imaging [35]. Due to the reduced scattering and little refraction of the acoustic waves in soft tissue, ultrasound imaging can achieve much higher resolution in deep tissue than optical imaging methods.

When propagating through tissue, acoustic waves are also attenuated. This is mainly due to friction losses when tissue particles are displaced and can be described phenomenologically by [39]

$$p(r) = p_0 e^{-\alpha(f)r}, \tag{2.9}$$

where p_0 is the initial amplitude, r the propagated distance [cm] and $\alpha(f) = Af^m$ the attenuation coefficient [dBcm^{-1}] in which $1 \leq m \leq 2$. A is a tissue-dependent constant with a typical value of 0.5 dBMHz^{-1}cm^{-1} and f the frequency of the wave [MHz] [9]. Hence, biological tissue acts as a low pass filter, attenuating high frequencies more than low frequencies. Since resolution depends on the availability of high frequencies (cf. section 2.4.3), imaging depth scales with resolution loss. Nevertheless in all that follows, acoustic attenuation is neglected because we are dealing with macroscopic imaging in the frequency range up to 7 MHz and depths up to 2.5 cm. For these frequencies, signal attenuation and distortion due to acoustic attenuation is small compared to the signal distortion and filtering due to the transducer properties (cf. section 2.3.3) and light attenuation [39].

2.2.3 Combining light with sound – the optoacoustic effect

Optoacoustic imaging is based on a phenomenon called the photoacoustic (or optoacoustic) effect. It was discovered more than a century ago by Alexander Bell [34] and describes the conversion of electromagnetic radiation into acoustic waves *via* a thermoelastic expansion.

2.2.3.1 Optoacoustic signal generation and wave propagation

The process of the optoacoustic signal generation can be understood as follows: when an object is irradiated with a short laser pulse, and the light is then absorbed by the object, some of the absorbed energy is converted into heat. This induces a temperature rise (in the order of millikelvins) and pressure builds up. The tissue then relaxes by heat diffusion and emission of the optoacoustic waves.

Two important timescales exist for optoacoustic signal generation:

- The thermal relaxation time τ_{th}, defined as the time it takes for the heat to dissipate into neighboring volume elements

$$\tau_{th} = \frac{d_c^2}{D_T}, \tag{2.10}$$

  where d_c is the size of this elementary volume (resolution-limited voxel) and $D_T \sim 1.4 \text{ x } 10^{-3}$ cm^{2}s^{-1} (in soft tissue) the thermal diffusivity. If the exciting laser pulse is shorter than the thermal relaxation time, the heating, and also the generation of the optoacoustic signal, is localized. This is known as the condition of thermal confinement [14].

- The stress relaxation time defined as the time the pressure takes to propagate through a resolution-limited voxel d_c:

$$\tau_s = \frac{d_c}{v_s}, \tag{2.11}$$

where v_s is the speed of sound. If the laser pulse is shorter than the stress relaxation time then pressure relaxation during the initial pressure rise is avoided and the optoacoustic signal generation is optimized. This condition is known as stress confinement [14].

Generation and propagation of the optoacoustic signals is described by the optoacoustic equation. Under thermal and stress confinement it is [14]:

$$\frac{\partial^2 p(\boldsymbol{r},t)}{\partial t^2} - {v_s}^2 \nabla^2 p(\boldsymbol{r},t) = \Gamma \frac{\partial H(\boldsymbol{r},t)}{\partial t}, \tag{2.12}$$

where $p(\boldsymbol{r},t)$ denotes the photoacoustic pressure [Pa] at location $\boldsymbol{r}$ and time t. $H(\boldsymbol{r},t)$ in J(m³s)$^{-1}$ is the heating function defined as the energy per unit volume and unit time deposited by the electromagnetic radiation and converted into heat. $\Gamma = \beta {v_s}^2 / C_p$ is the dimensionless and temperature dependent Grüneisen parameter which describes the conversion properties of the medium, in which C_p is the isobaric heat capacity in J(kgK)$^{-1}$ and β the isobaric volume expansion coefficient [K^{-1}]. The heating function is proportional to the fluence rate $\emptyset(\boldsymbol{r},t)$ of the excitation radiation, as well as the optical absorption $\mu_a(\boldsymbol{r})$ of the medium. Thus,

$$H(\boldsymbol{r},t) = \mu_a(\boldsymbol{r})\emptyset(\boldsymbol{r},t). \tag{2.13}$$

Since propagation of light can be considered instantaneous, the heating function is generally separable, *i.e.* it can be decomposed as $H(\boldsymbol{r},t) = H_r(\boldsymbol{r})H_t(t)$. In most biological tissues, except from bones, lungs and other air-containing body cavities, Γ as well as v_s vary only slightly and can therefore be considered as being spatially independent [40]. The left hand side of Eq. (2.12) describes the wave propagation, whereas the right hand side gives the source of the optoacoustic signal generation. The first time derivative in the source term shows that the heating has to be time variant, otherwise it is not possible to generate a photoacoustic signal.

For impulse heating, *i.e.* $H_t(t) = \delta(t)$, the temperature rise within the sample is given by

$$T(\boldsymbol{r}) = \frac{H_r(\boldsymbol{r})}{\rho C_V}. \tag{2.14}$$

The corresponding initial pressure at a point $\boldsymbol{r}$ can be expressed as:

$$p_0(\boldsymbol{r}) = \Gamma H_r(\boldsymbol{r}) = \Gamma \mu_a(\boldsymbol{r})\emptyset(\boldsymbol{r}) \tag{2.15}$$

where C_V in J(kgK)$^{-1}$ is the specific heat capacity at constant volume [14].

2.2.3.2 The forward solution

The optoacoustic equation (2.12) can be solved with the Green function approach [14]. Under stress confinement and for delta heating $H_t(t) = \delta(t)$ the expression for the acoustic field writes [35]

$$p_\delta(\boldsymbol{r}, t) = \frac{\Gamma}{4\pi v_s^2} \frac{\partial}{\partial t} \left[\frac{1}{v_s t} \int_{\mathrm{V}} H_r(\boldsymbol{r}') \delta(t - \frac{|\boldsymbol{r} - \boldsymbol{r}'|}{v_s}) d\boldsymbol{r}' \right], \tag{2.16}$$

where the integration is done over the whole illuminated object V and $\boldsymbol{r}'$ is a point within this object. From the expression we see that a detector at the location $\boldsymbol{r}$ and at the time t will sense the integrated pressure, originating from optoacoustic point sources on a spherical shell with the radius $v_s t$ and centered at $\boldsymbol{r}$ as shown in Fig. 2.2 (a). For a homogenous spherical absorber with radius a positioned at $\boldsymbol{r}_s$, it is possible to derive an analytical solution to Eq. (2.16). It writes [14]

$$p_\delta(\boldsymbol{r}, t) = p_0 U(a - |R - v_s t|) \frac{(R - v_s t)}{2R} \tag{2.17}$$

where U is the Heavyside function, $R = |\boldsymbol{r} - \boldsymbol{r}_s|$ the distance of the source from the detection point and p_0 the amplitude of the initial pressure. Fig. 2.2 (b) displays the time resolved photoacoustic signal from three spheres with the radius a = 500 µm, 1 and 1.5 mm, positioned at 36, 38 and 40 mm, respectively, in front of the detection device. We see the optoacoustic signal has a characteristic bipolar shape. The duration of the optoacoustic pulse represents the time the sound needs to propagate along the sphere diameter, thus scales with the size of the sphere. The positive peak indicates a pressure rise due to compression followed by a pressure drop due to rarefaction. The pressure amplitude is proportional to the size of the sphere and inversely proportional to the propagated distance. Fig. 2.2 (c) displays the frequency spectrum of the signals obtained by a fast Fourier transformation of the optoacoustic signals. The spectra are very broad, ranging from low ultrasonic frequencies which correspond to the dimensions of the acoustic source, to high frequencies from the object boundaries. The maximal amplitude of the spectra defines the central frequency f_c of the source, which is approximately $f_c \sim 0.8\, v_s/2a$ for a sound speed within the object of v_s [41]. The full width at half maximum of the lobe defines the bandwidth B_w of the signal for which the ratio $B_w/f_c = const$. We see that frequency and bandwidth scale with the size of the optoacoustic source. The smaller the object, the higher is the central frequency and the broader the frequency spectrum. Anatomical structures within tissue span from centimeter-sized objects (*e.g.* organs), to several micrometers (*e.g.* microvasculature), thus emit optoacoustic waves ranging from frequencies of several kilohertz to tens of megahertz. With respect to instrumentation this means that broadband detection devices are required to accurately detect these signals.

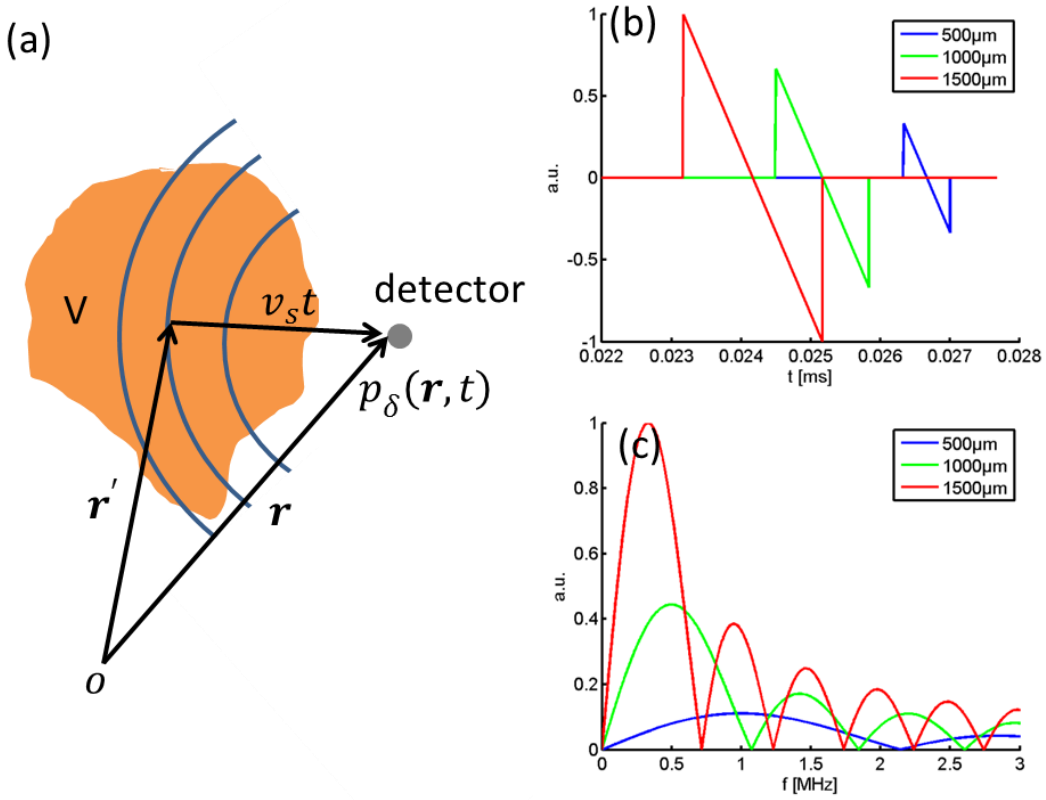

Fig. 2.2: (a) The optoacoustic signal, detected at a certain time *t*, by a point detector at *r*, comes from optoacoustic sources located on a spherical shell centered at the detector position with the radius $v_s t$. (b) Optoacoustic signal from spherical sources with a diameter of 1, 2 and 3 mm displays the characteristic bipolar shape. (c) Corresponding frequency spectra.

In experimental conditions the optoacoustic signals are broadened due to the finite temporal width of the laser pulse. The broadening is described by a temporal convolution between the solution for impulse heating $p_\delta(\boldsymbol{r}, t)$ and shape of the laser pulse $H_t(t)$:

$$p(\boldsymbol{r}, t) = p_\delta(\boldsymbol{r}, t) * H_t(t) = \int_{-\infty}^{\infty} p_\delta(\boldsymbol{r}, t - \tau) H_t(\tau) d\tau \qquad (2.18)$$

where $*$ denotes the temporal convolution operator [42].

2.2.3.3 Signal strength in an small animal experiment

Next, an estimate of the optoacoustic signal strength expected in a small animal imaging experiment is derived. A spherically shaped absorber, located within the cylinder, is considered as the source of the optoacoustic signal. Furthermore, constant and uniform illumination onto the surface of the cylinder is assumed. A diagram explaining this geometry is shown in Fig. 2.3 (a). The optoacoustic signal from a spherical absorber is given by Eq. (2.17). It depends on the initial pressure p_0, which is proportional to the light fluence and local absorption coefficient (cf. 2.2.3.2). An estimate of the light fluence $\emptyset$ can be derived from the homogenous form of the light diffusion equation (2.2). In cylindrical coordinates and taking into account the symmetry of the problem ($\partial\emptyset/\partial z = 0$ and $\partial\emptyset/\partial\varphi = 0$), it writes [43]

$$\mathrm{r}^2 \frac{\partial^2 \emptyset(r)}{\partial r^2} + \mathrm{r} \frac{\partial \emptyset(r)}{\partial r} - \frac{\mu_a}{D} \mathrm{r}^2 \emptyset(\boldsymbol{r}) = 0. \tag{2.19}$$

This is a modified Bessel equation of the type one zero order and has a solution of the type

$$\phi(r) = A I_0 \left(\sqrt{\frac{\mu_a}{D}} r \right), \tag{2.20}$$

where A is a constant and I_0 the modified Bessel function of the first kind order zero. Setting (2.20) into (2.19) for the initial condition $\phi(R) = \phi_0$ yields

$$A = \frac{\phi_0}{I_0 \left(\sqrt{\frac{\mu_a}{D}} R \right)} \tag{2.21}$$

Under assumption that the observation point lies outside the spherical absorber and the acoustic attenuation is negligible, it is possible to derive an expression for the optoacoustic pressure amplitude at position $\boldsymbol{r}$ generated by a spherical absorber with the radius a positioned at $\boldsymbol{r_s}$ within a tissue mimicking cylinder with the radius d, so that:

$$p(\boldsymbol{r}, t) = \Gamma \mu_a^s \frac{\phi_0}{I_0 \left(\sqrt{\frac{\mu_a}{D}} d \right)} I_0 \left(\sqrt{\frac{\mu_a}{D}} r_s \right) \frac{(R - v_s t)}{2R} \tag{2.22}$$

where Γ is the Grüneisen coefficient, μ_a^s the absorption coefficient of the spherical optoacoustic source, $\emptyset_0$ [Jm^{-2}] the initial light fluence on the surface of the object, I_0 the modified Bessel function of the first kind and order zero, $D(\boldsymbol{r}) = 1/3(\mu'_s + \mu_a)$ the diffusion constant, μ'_s and μ_a the optical absorption and reduced scattering coefficient of the background, respectively, d the radius of the cylinder, v_s the sound velocity and $R = |\boldsymbol{r} - \boldsymbol{r}_s|$ the distance between source position and detection point. We see that the magnitude of the detected optoacoustic signal is directly related to its absorption coefficient, the thermo-acoustic efficiency given by the Grüneisen coefficient, its size and the initial light fluence, but inversely related to the distance from the transducer and attenuated with respect to the depth. Numerical estimations have been performed for realistic experimental values: $\Gamma = 0.25$, $\mu'_s = 10$ cm^{-1}, $\mu_a = 0.3$ cm^{-1}, $\mu_a^s = 0.5$ cm^{-1}, $\emptyset_0 = 20$ mJcm^{-2}, $r = 4$ cm, $0.2 < a < 2$ mm and $d = 1$ cm. Fig. 2.3 (b) displays the optoacoustic signal strength as a function of the distance between source and center of the phantom for different source sizes. Fig. 2.3 (c) displays the optoacoustic pressure amplitude for the microsphere with a diameter of 500 µm and for different detector distances. Since the optoacoustic signals are relatively weak, only a few to a few tens of Pascals are available for detection, depending on the exact location within the phantom. Signals from deep inside the phantom are approximately 8 times smaller than close to the surface. With respect to instrumentation this means that it is important to have a sensitive detection device with a sufficiently large dynamic range to be able to detect both, the signals from the surface of the animal as well as the weak signal

from the inside. We also see that it is important to do multisided illumination, since this increases the signal strength from structures deep inside the object (about 16%) compared to single side illumination (around 4%, cf. section 2.2.1).

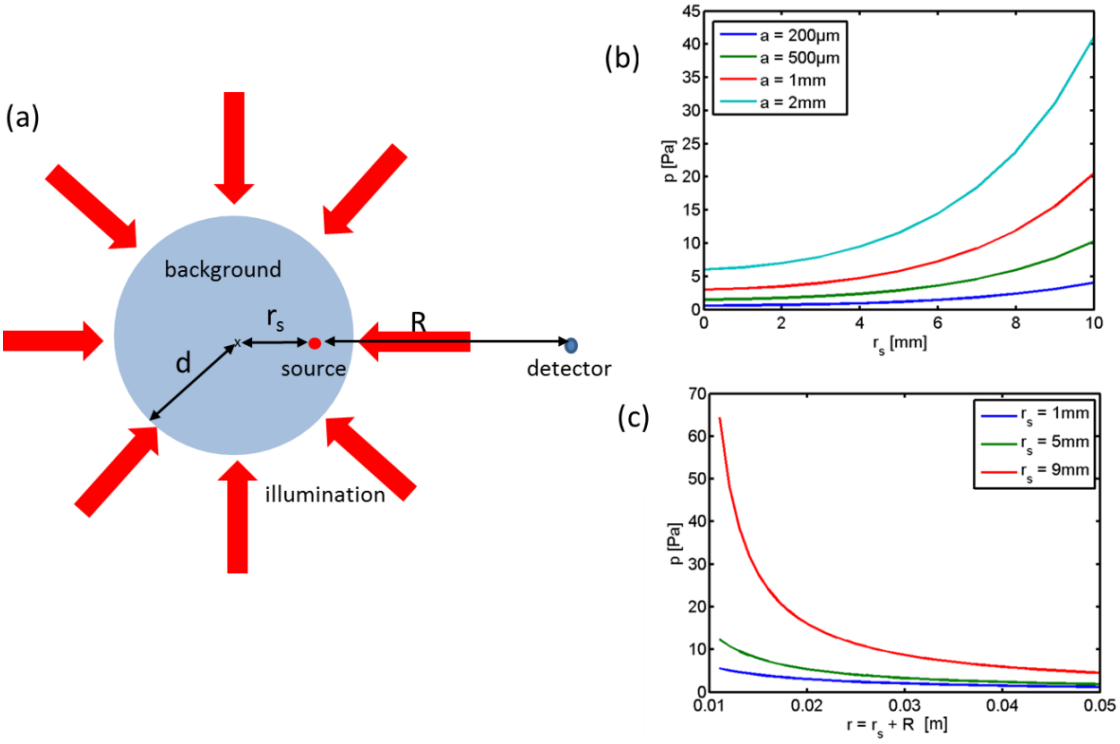

Fig. 2.3: Estimation of optoacoustic signal strength. (a) Diagram explaining the geometry of the model: An infinite cylinder (top view) with tissue mimicking properties is uniformly illuminated from the side. Signals are generated by a spherical absorber in the phantom. (b) Optoacoustic pressure amplitude from the spherical optoacoustic source, detected 4 cm away of the center from the cylinder as a function of target size and distance from the center of the phantom. (c) Optoacoustic pressure amplitude for the microsphere (500 µm), for three different target position as a function of the detector location.

2.2.3.4 Directivity of optoacoustic signals

Due to the high velocity of light, all of the optical absorbers in the tissue are excited simultaneously, thus produce coherent pressure waves. Since ultrasound scattering in tissue is low, the coherence is preserved over long distances, causing diffraction phenomena due to the interference of the wavefronts originating at neighboring points of the source. Objects with a high aspect ratio, like blood vessels for example, emit directive radiation. To show this behavior, the directivity pattern for optoacoustic sources with the aspect ratios of 1, 2, and 10, respectively, was calculated. The resulting wave forms were obtained by the superposition of the bipolar signals from optoacoustic point sources, see Eq. (2.17). The results are displayed in Fig. 2.4. The optoacoustic source is located in the image center at the coordinate (0,0). It has to be considered rotationally symmetric around its longitudinal axis. Each point in the image of the first row represents the energy of the emitted acoustic wave. The second row depicts the polar plots of the energy emitted for a distance of 2, 20 and 40 mm. The graph was normalized to the 0° direction. Obviously, optoacoustic sources with an aspect ratio greater one emit directive pressure waves. The directivity increases with increasing aspect ratio. In small animals anatomical structures (*e.g.* blood vessels) are arbitrarily shaped and

oriented. Therefore, depending on the shape, aspect ratio and orientation of the structure, the optoacoustic signals are emitted in a different direction. In order to be able to capture the optoacoustic signals from all the absorbers, a closed detection surface is required. With respect to designing an imaging system, this means that if the object is not completely surrounded with detection elements, structures may be invisible, because their emitted signal is not captured by any detection elements. This is known as the limited view problem and will be discussed in more detail in section 2.4.6.

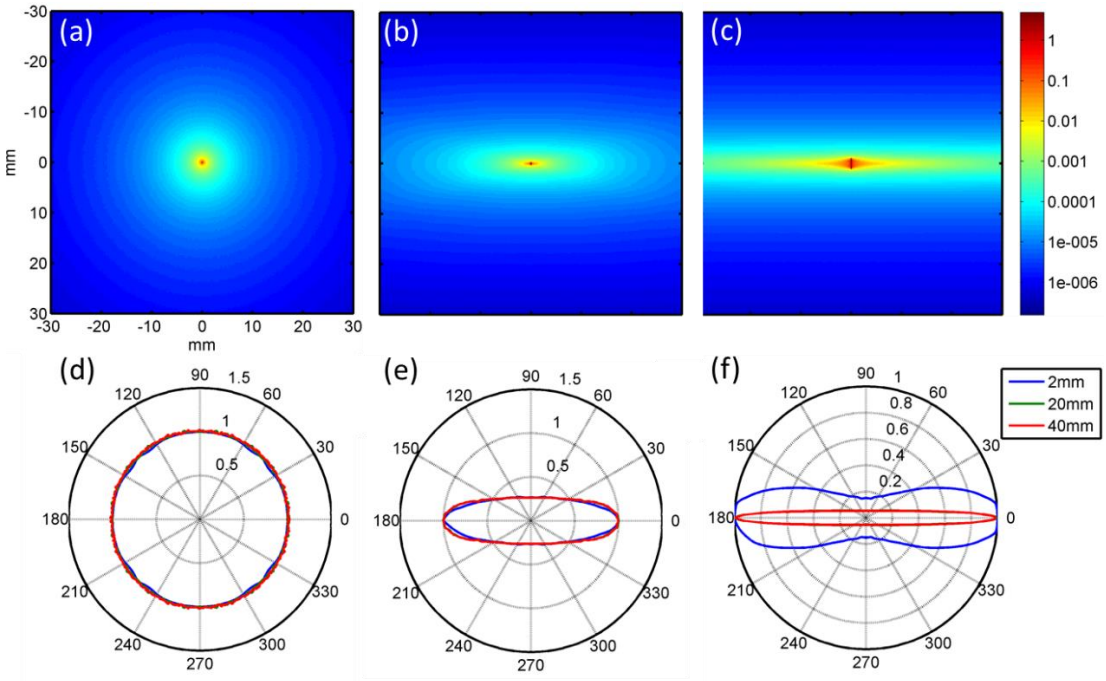

Fig. 2.4: Directivity of optoacoustic signals: Directivity maps for an optoacoustic source with an aspect ratio of 1 (a), 2 (b) and 10 (c). Each point represents the emitted energy detectable at this position. The corresponding polar plots, normalized to the value at the 0° position, are shown in the second row for distances of 2, 20 and 40 mm, respectively.

2.3 Technological aspects of multispectral optoacoustic tomography

2.3.1 Illumination

2.3.1.1 Pulse duration

The description of the optoacoustic phenomena, presented in section 2.2.3.1, has been derived under the assumption that heat and stress propagation during the excitation pulse is negligible. To ensure that these equations are valid and that the optoacoustic signals are generated efficiently, the pulse duration of the laser employed in the imaging system has to be shorter than the thermal and stress relaxation time of the sample. Expressions to estimate these thresholds have been presented in section 2.2.3.1, see Eqs. (2.10) and (2.11). They depend on the targeted resolution of the system and the thermal diffusivity of the tissue. To give a numerical

example we calculate the thermal and stress relaxation time for the system developed herein. It aims for a maximal resolution of $d_c = 150\ \mu\text{m}$. A typical value for the thermal diffusivity in soft tissue is $D_T = 1.3\ \text{x}\ 10^{-3}\ \text{cm}^2\text{s}^{-1}$ [14]. The corresponding values for the thermal and stress relaxation time are then $\tau_{th} \approx 170\ \text{ms}$ and $\tau_s \approx 100\ \text{ns}$, respectively. Such time-scale values can easily be achieved with modern nanosecond laser technologies. Pulse durations exceeding these thresholds would compromise the spatial solution of the system by broadening the photoacoustic signal.

2.3.1.2 Laser technologies

Various nanosecond pulsed laser technologies are available. Herein, we aim for deep tissue imaging. Since light attenuation in tissue severely hinders the penetration of light, high pulse energies are preferential. Q-switched solid state lasers based on neodymium-doped laser crystals (e.g. Nd:YAG) can deliver 10 ns pulses with pulse energies of multiple joules in the 1 µm spectral region at a repetition rate of several hertz [44] and are therefore very attractive for deep tissue optoacoustic imaging [45]. Since MSOT technology uses multi-wavelength illumination, the output wavelength of the laser has to be tunable. For deep tissue imaging, the tuning range should be in the near-infrared region to benefit from the spectral window in tissue. Conversion stages, such as optical parametric oscillators (OPOs), can be employed for this purpose. The OPO technology is particularly attractive for MSOT because wavelength tuning can be done fast. It depends only on the speed with which the orientation of the parametric oscillator crystal can be changed and it allows wide tuning ranges. For the imaging of superficial structures, lower pulse energies are sufficient and additional technologies like diode-pumped dye lasers, laser diodes or fiber lasers become suitable. With pulse repetitions rates in the order of several kilohertz, these lasers provide the potential to design fast scanning-based imaging systems [45].

2.3.1.3 Maximum permissible exposure

The key parameter for yielding good signal-to-noise ratio (SNR) is the per-pulse energy. For *in vivo* applications, however, laser safety standards have to be respected. The American National Standards Institute (ANSI) defines the maximal permissible skin exposure (MPE) for nanosecond laser up to a repetition rate of 10 Hz as 20 mJcm^{-2} per pulse for wavelengths in the visible range (400 - 700 nm), which gradually increases through the near-infrared region (NIR) according to the formula [35]

$$\text{MPE} = 20\ \text{mJcm}^{-2}\ \text{x}\ 10^{2\ (\lambda\ -\ 700\ \text{nm})/\ 1000\ \text{nm}} \tag{2.23}$$

to 100 mJcm^{-2} at 1050 nm. For repetitive laser pulses onto the same area the exposure limits for the average power deposition have to be met. They are 200 mWcm^{-2} in the visible and gradual increase to 1 Wcm^{-2} in the NIR.

2.3.2 Detection of optoacoustic signals

Detection of the optoacoustic signals is the critical component in optoacoustic imaging. For accurate detection, the detection device requires a high sensitivity; a broad detection bandwidth and a large dynamic range (cf. section 2.2.3.3.) Various approaches to detect the optoacoustic signals have been explored in the literature. They can be divided into two categories: piezoelectric detection and optical [46].

2.3.2.1 Piezoelectric detection

Piezoelectric detection is adopted from the field of ultrasound imaging. It is based on the piezoelectric effect, *i.e.* the property of certain materials to generate a voltage difference at its surface due to a reorientation of its electrical dipoles after mechanical deformation. The voltage difference is proportional to the deformation, which enables to detect pressure variations and thus measure an acoustic field. On the other hand, since the piezoelectric effect is a reversible process it can also be used to generate pressure waves by applying a voltage to the material [41, 47]. In ultrasound imaging this is used to send an acoustic pulse. The efficiency of the material to convert one form of energy to the other is defined by the electromechanical coupling coefficient k_t defined as the ratio of stored mechanical energy in thickness resonance mode and the total stored energy [48]. The advantage of piezoelectric detection is the high sensitivity, the flexibility to manufacture arbitrary shapes and the possibility of parallelization [49].

2.3.2.2 Piezoelectric materials

Piezoelectric materials used for optoacoustic imaging should have a high electromechanical coupling coefficient k_t (*i.e.* sensitivity) and acoustical impedance matched to soft tissue. Three major types of piezocomposites are generally available: ceramics, polymers and composites [41].

Ceramics, with lead-zirconate-titanate (PZT) as the most prominent representative, have a good electromechanical coupling (k_t = 0.55) but an acoustical impedance ($Z \sim$ 34 MRayl) badly matched to soft tissue ($Z \sim$ 1.6 MRayl) [48]. As a consequence, when applied for tissue imaging, there is little energy transfer between tissue and piezoelectric material.

Therefore, for tissue imaging, piezoceramics are usually used in form of a composite, *i.e.* piezocomposite rods embedded in a polymer matrix to adjust the acoustic impedance to the one of tissue. By varying the ratio between the ceramic and polymer content, piezo-composites can be designed flexibly attaining high coupling efficiencies. Drawbacks are the higher production costs due to the complicated fabrication process [48].

Piezoelectric polymers such as polyvinylidene fluoride (PVDF) have also been found to be useful for biomedical applications. They have the advantage of being better matched ($Z \sim$ 3.6 MRayl) to tissue and can easily be produced in thin layers necessary for high frequency applications. However, the electromechanical coupling is low (k_t = 0.11) [48] which limits the transducers' sensitivity [41].

2.3.2.3 Ultrasound transducer

Ultrasound transducers are highly sophisticated and complex electronic instruments. The basic components of a simple single element ultrasound transducer are depicted in Fig. 2.5.

The most important component is the piezoelectric element. It is a resonating device which converts the pressure wave into an electrical signal. The resonance frequency is determined by the thickness material [48]

$$f_R = \frac{n\, v_T}{2L} \tag{2.24}$$

where v_T is the acoustic wave velocity in the piezoelectric material, L its thickness and n an odd integer. The thinner the piezoelectric material, the higher is the resonance frequency. The two surfaces of the piezoelectric material are connected to electrodes to measure the generated voltage difference. The matching layer in front of the piezoelectric material has intermediate acoustic impedance between the one of the piezoelectric crystal and the one of tissue. Its purpose is to reduce the impedance mismatch between tissue and piezoelectric material in order to improve the transfer of acoustic energy into the transducer. The backing material serves to damp the reverberations of the piezoelectric material after excitation and therefore determines the bandwidth of the transducer. The better it is matched to the impedance of the piezoelectric material, the better is the absorption of acoustic energy and thus the better the damping of the oscillations and wider the bandwidth of the transducer. Conversely, with a mismatched backing, acoustic energy is be reflected back into the piezoelectric material, thus little acoustic energy is lost yielding ringing and a narrow bandwidth of the transducer. To increase the bandwidth of the transducer it is therefore necessary to match the backing material to the acoustic impedance of the piezoelectric material. The trade-off of increasing the bandwidth is however a loss of sensitivity because most of the acoustic energy is absorbed in the backing [47, 48]. With respect to designing an optoacoustic imaging system, the technical challenge consists of finding the right balance between sensitivity and bandwidth of the transducer, in order to be able to detect the weak optoacoustic signals without much signal distortion.

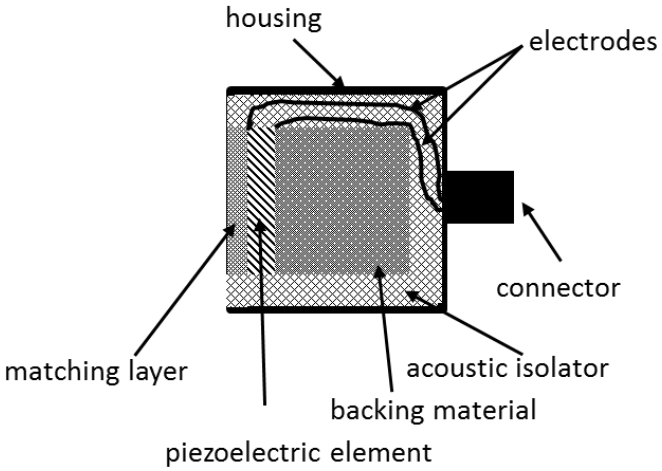

Fig. 2.5: Components of an ultrasound transducer.

The frequency characteristics of an ultrasound transducer are described in terms of central frequency [MHz] and fractional bandwidth of the central frequency [%]. A transducer with a central frequency of 5 MHz and a bandwidth of 60% has its main sensitivity between 3.5 and 6.5 MHz. Outside this spectral region the frequency amplitude is lower than -6 dB of its maximal sensitivity.

2.3.2.4 Optical detection

Optical detection, based on optical interferometry to probe the ultrasonic displacement [50, 51], provides wide and uniform detection bandwidth and small size, which is highly interesting for optoacoustic imaging since signals distortions due to the element size and bandwidth of the detection element is significantly reduced. However, they also have a low sensitivity level, which is two orders of magnitudes less compared to piezoelectrical detection devices [52]. For that reason, optical approaches are currently only applied for imaging superficial structures [46]. Additional drawbacks are difficulties in parallelisation which is desirable in order to increase the imaging speed. Optical detection devices might however be very useful for minimal-invasive imaging devices, such as intravascular imaging, where size plays an important role.

2.3.3 Electrical impulse response

Optoacoustic signals are broadband (cf. section 2.2.3.2). Ultrasound detection devices on the other hand generally have a relatively limited spectral bandwidth and non-uniform frequency characteristics, resulting from the resonance properties of piezoelement, backing and the electronics utilized [41]. They act as a band-pass filter and thus distort the optoacoustic signals. The distortion of the optoacoustic signals is a linear process and can be modeled with the electrical impulse response (EIR) of the system according to [53]

$$p_d(\boldsymbol{r}, t) = p(\boldsymbol{r}, t) * \mathrm{EIR}(t) \tag{2.25}$$

where $*$ stands for a temporal convolution, $p_d(\boldsymbol{r}, t)$ the distorted and $p(\boldsymbol{r}, t)$ the undistorted optoacoustic signal, respectively. $\mathrm{EIR}(t)$ represents the electrical impulse response of the detection system [54]. It describes how the detection system reacts to an impulse excitation, *i.e.* a source with constant frequency spectrum and infinite bandwidth. It is spatially invariant, thus the same for each optoacoustic signal and independent of the location of the source.

The distortion of optoacoustic signals due to the electrical impulse response is shown in Fig. 2.6 for a spherical absorber with diameter 200 µm and 2 mm. The electrical frequency response is assumed to have a Gaussian shape, characteristic for piezoelectric detection elements [39], with a central frequency of 3 MHz and a fractional bandwidth of 90%. The distortion effect of the optoacoustic signals due to the influence of the electrical impulse response is clearly visible. Obviously, the detection bandwidth is insufficient to detect the sharp edges of the N shape of the optoacoustic signal resulting in a broadening of the signals. The part of the optoacoustic signal that decreases linearly, is associated with low-frequencies. For a small object the detection bandwidth is suited to accurately detect this part

(Fig. 2.6. c), which is however not the case for a big object (Fig. 2.6 d), where a lack of low frequencies leads to a completely erroneous representation of this part of the signal. A deconvolution approach to correct for the distortion of the optoacoustic signals due to the electrical impulse response is presented in section 4.2.

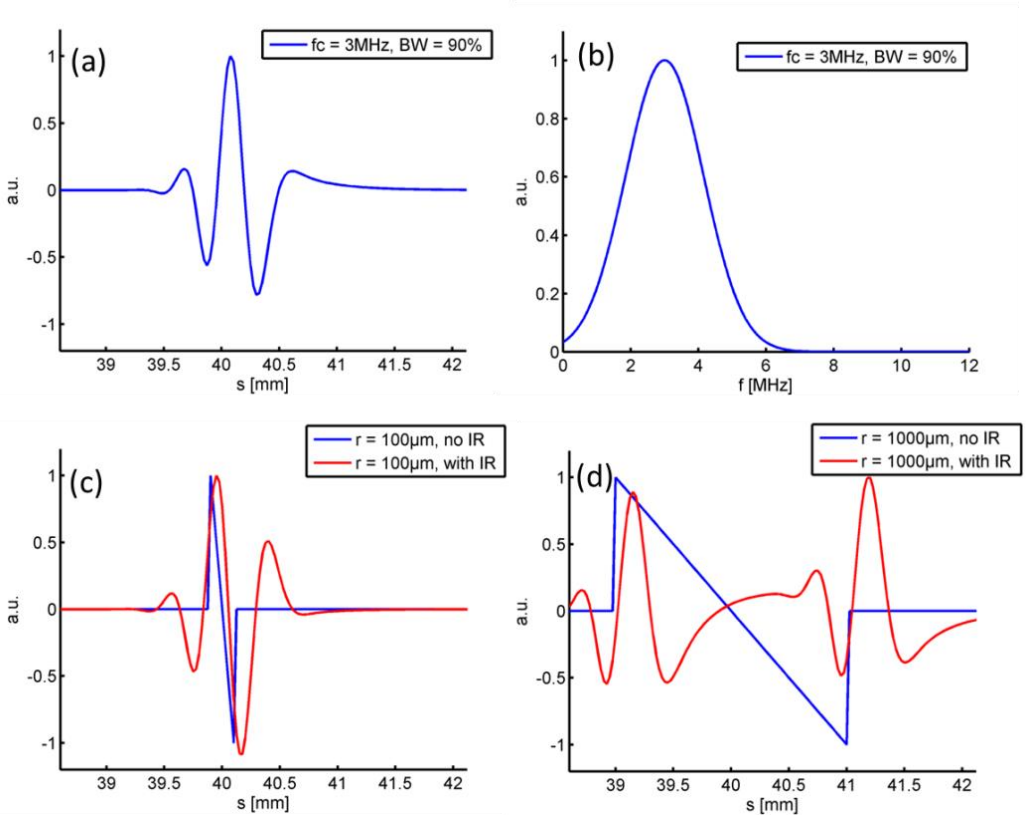

Fig. 2.6: Distortion of the optoacoustic signal due to the electrical impulse response of the detection system. (a) Electrical impulse response utilized in this simulation study. (b) Depicts the Fourier transform of the electrical impulse response, which is the electrical frequency response, having a Gaussian shape with a central frequency of 3 MHz and a fractional bandwidth of over 90%. (c) Effect of the electrical impulse response on the optoacoustic signal from a spherical source with a 200 µm diameter. (d) The same on a spherical source with a 2 mm diameter.

2.3.4 Spatial impulse response

Detection of optoacoustic signals with detectors having a finite size leads to a spatial averaging and a distortion of the optoacoustic signals because different points $\boldsymbol{r_d}$ of the surface S of the transducer detect the optoacoustic signal $p(\boldsymbol{r_d}, t)$ at different time points [55], according to

$$p_d(t) = \int_S p(\boldsymbol{r_d}', t) dS(\boldsymbol{r_d}'). \tag{2.26}$$

It was shown in [56] for an optoacoustic point source $p_{ps}(\boldsymbol{r_d}, \boldsymbol{r}, t)$ located at $\boldsymbol{r}$ and detected with a detector located at $\boldsymbol{r_d}$, the surface integral in Eq. (2.26) can be expressed in form of a 1D convolution

$$\int_S p_{ps}(\boldsymbol{r_d}', \boldsymbol{r}, t) dS(\boldsymbol{r_d}') = \mathrm{SIR}(\boldsymbol{r_d}, \boldsymbol{r}, t) * p_{ps}(\boldsymbol{r_d}, \boldsymbol{r}, t) \tag{2.27}$$

where

$$\mathrm{SIR}(\boldsymbol{r_d}, \boldsymbol{r}, t) = \frac{1}{2\pi} \int_S \frac{\delta(t - \frac{|\boldsymbol{r_d}' - \boldsymbol{r}|}{v_s})}{|\boldsymbol{r_d}' - \boldsymbol{r}|} dS(\boldsymbol{r_d}') \tag{2.28}$$

is the spatial impulse response (SIR) of the transducer element located at $\boldsymbol{r_d}$ [41]. The SIR characterizes the distortion of the pressure profile from an optoacoustic point source induced by the detector aperture. Convolved with the electrical impulse response (EIR), the spatial impulse response is termed total impulse response (TIR).

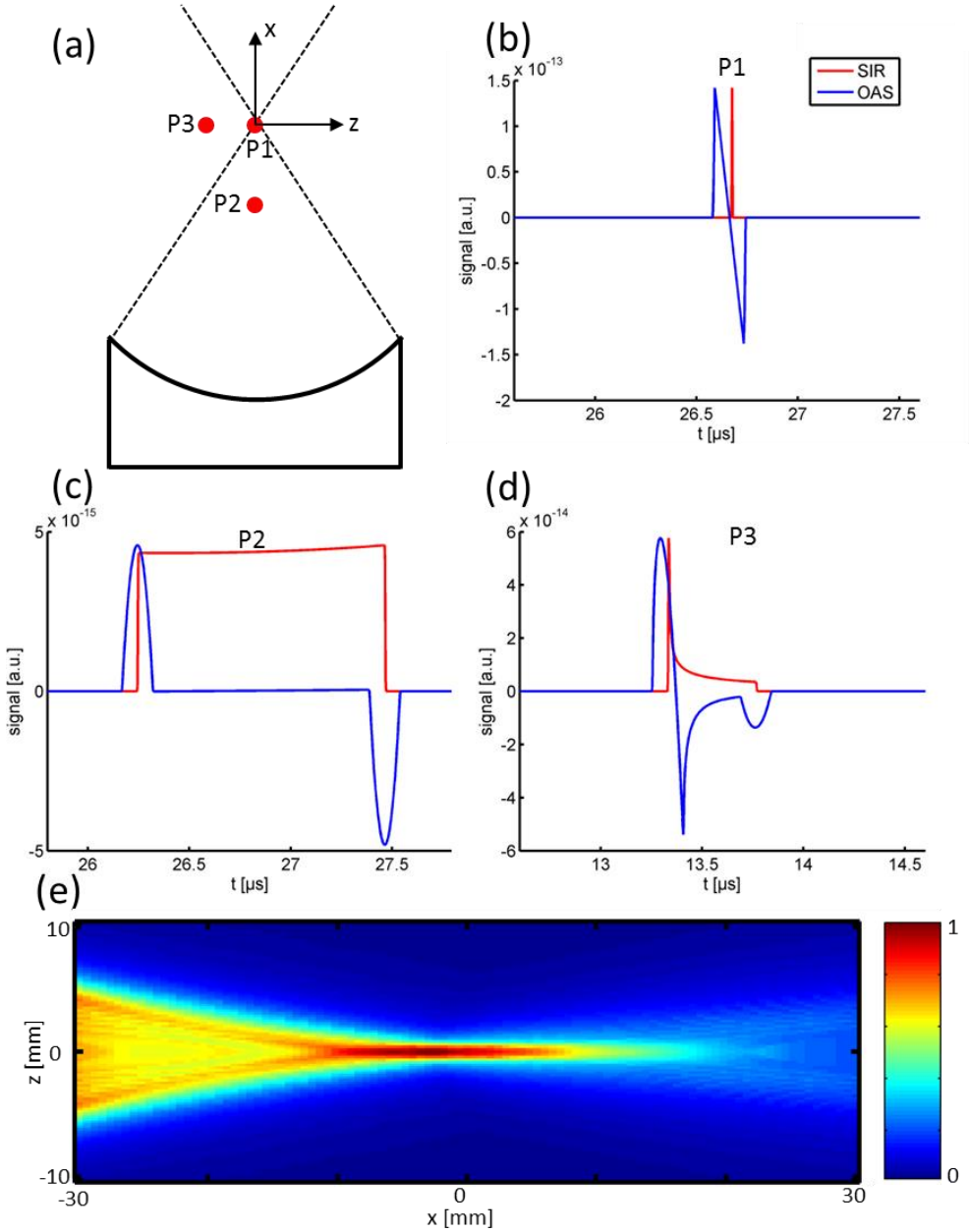

Fig. 2.7: Optoacoustic signals measured with a focused detector for different source positions. (a) Source positions for which the signal was calculated. (b) Optoacoustic signal (blue line) and spatial impulse response (red line) for the source position "P1". (c) Source position "P2" and (d) source position "P3": The influence of the spatial impulse response distorts the optoacoustic signal outside the focal point. (e) Depicts the sensitivity field of the transducer.

TIR can be used to visualize the anisotropic detection sensitivity of the transducer (*i.e.* its sensitivity field), arising from its finite detection surface and finite detection bandwidth. Generally this is accomplished by plotting the amplitude of the total impulse response as a function of the geometrical coordinates [41].

Fig. 2.7 displays the optoacoustic signals from three spherical absorbers measured with a focused transducer as well as the corresponding spatial impulse response. The relative location of the sources is shown in Fig. 2.7 (a). The size and curvature radius of the focused transducer was 15 mm x 1 mm and 40 mm, respectively. The position of the point sources are the following, in each case with coordinates given in mm: P1 (0,0,0), P2 (0,0,-20) and P3 (0,-5,0). The mechanical focal point of the transduce is located at (0,0,0). If the source is located in the focal point (*i.e.* P1) then the acoustic wave arrives at each surface point of the transducer at the same time. Thus, the measured signal is not distorted and duration of the measured signal the shortest. The spatial impulse response in that case is a delta function, like shown in Fig. 2.7 (b). For source positions outside the focus, the detected signals are stretched in time and distorted, which is due to the asynchronous arrival of the pressure wave at the individual points of the transducer surface, see Fig. 2.7 (c) and (d). The sensitivity field of the transducer is depicted in (e). It was obtained by plotting the amplitude of the TIR versus its geometrical coordinates. The EIR assumed had a Gaussian shape with a central frequency of 3 MHz and a bandwidth of 90%, as depicted in Fig. 2.6 (b). In chapter 5 it will be shown how to consider the spatial impulse response in the image reconstruction in thus improve the reconstruction results.

2.3.5 **Sensitivity**

When designing an optoacoustic imaging system, it is important to achieve high signal-to-noise ratio (SNR), since it determines the system sensitivity and thus the detectability of an optoacoustic absorber. The SNR depends on various parameters. An expression to estimate the SNR in an optoacoustic image as a function of the individual parameters can be found in [57]. It writes:

$$\mathrm{SNR} \sim S\gamma A\sqrt{PM}/N \tag{2.29}$$

where S is the magnitude of the optoacoustic signal arriving at the detector, γ the ultrasonic detector sensitivity, A the detection aperture of the detector, P the number of tomographic projections used in the reconstruction, M the number of signal averages and N the noise floor of the system. To achieve high SNR, it is therefore important to increase the magnitude of the optoacoustic signal arriving at the detector. On the one hand, this can be achieved by optimizing the light delivery, since the generated optoacoustic signal is proportional the light fluence (cf. section 2.2.3.1). On the other hand, by minimizing the source detector distance, the optoacoustic signals are attenuated as a function of the distance propagated. Another way to improve SNR is increasing the detector sensitivity, enlarging the detection element and decreasing the noise floor of the system. Further improvements can be achieved by signal averaging and increasing the number of tomographic projections used in the reconstruction. However, this increases the SNR

only as a function of their square root. It has to be noted that some of these measures have a negative effect on the imaging performance and are therefore less desired. For instance, signal averaging prolongs the imaging time and hinders real-time applications. Big detectors compromise the lateral resolution when standard reconstruction methods that do not take the shape of the detector into account are used (*e.g.* the backprojection algorithm), cf. section 2.4.3.1. Hence, from a practical imaging perspective, it is more desirable to maximize the optoacoustic signal arriving at the transducer, to reduce the noise floor of the system and/or to increase the detection sensitivity, than it is to average signals or use big detectors.

2.4 Optoacoustic image formation

2.4.1 Focused transducer-based techniques

The goal of optoacoustic imaging is to reconstruct the absorbed energy distribution based on a set of measured optoacoustic signals.

The easiest way to achieve this is using a spherical focused detection element. It has a narrow acceptance angle and can in first approximation be considered as being only sensitive to signals originating within a 1D line along its acoustic axis. Fig. 2.8 (a) depicts the sensitivity field of such a spherical transducer. Since the detected signals are time resolved, they can be regarded as 1D depth images (A-scan). Thus, the 3D reconstruction problem is reduced to 1D. The location of the optoacoustic source along the acoustic axis of the detector can be identified exactly from the time of arrival of the optoacoustic signals, if the sound speed in the propagation medium is known. To form an optoacoustic image, the transducer is scanned over the sample to acquire a set of 1D depth images which are then combined to obtain a 2D or 3D image. This image formation technique is frequently used in the field of photoacoustic microscopy. Implementation where this technique is applied can be found in [27, 58, 59]. It has the advantage that the detected pressure signals can be directly mapped onto the image space without computational reconstructions.

Similarly, the reconstruction problem can be reduced in first approximation to 2D by using cylindrically focused transducers. These kinds of transducers have a wide reception angle in one direction and a narrow one perpendicular to it, along the focused direction. In first approximation, they can be considered as only being sensitive to signals originating from a 2D plane. Although the detected signals are time resolved, it is not possible to identify the exact location of the optoacoustic source. It can be located everywhere on the arc with the radius $r = ct$, surrounding the detector position. To form an image, multiple projections need to be acquired on a circle around the object and inverted using 2D reconstruction algorithms, one of which is presented in the next section. Different slices can be reconstructed individually. A 3D image is then obtained by stacking these 2D slices. An example of such an implementations can be found in reference [57]. The real-time optoacoustic imaging system developed in this work and presented in chapter 3 also uses this image formation technique. The advantage of this quasi 2D approach is that for a

small amount of detectors it can achieve high in-plane resolution, good sensitivity due the large area of focused detectors and thus, real-time imaging performance.

Finally, unfocused transducer elements with a large angle of acceptance generally have a small element size. They detect acoustic signals originating from a large volume in the tissue. As a result, 3D computed reconstruction algorithms are needed to obtain an image. The tomographic dataset is either acquired along a cylindrical or spherical surface surrounding the sample, or along an infinitely long 2D plane (cf. Fig. 2.9). An implementation of such a system can be found in [60, 61].

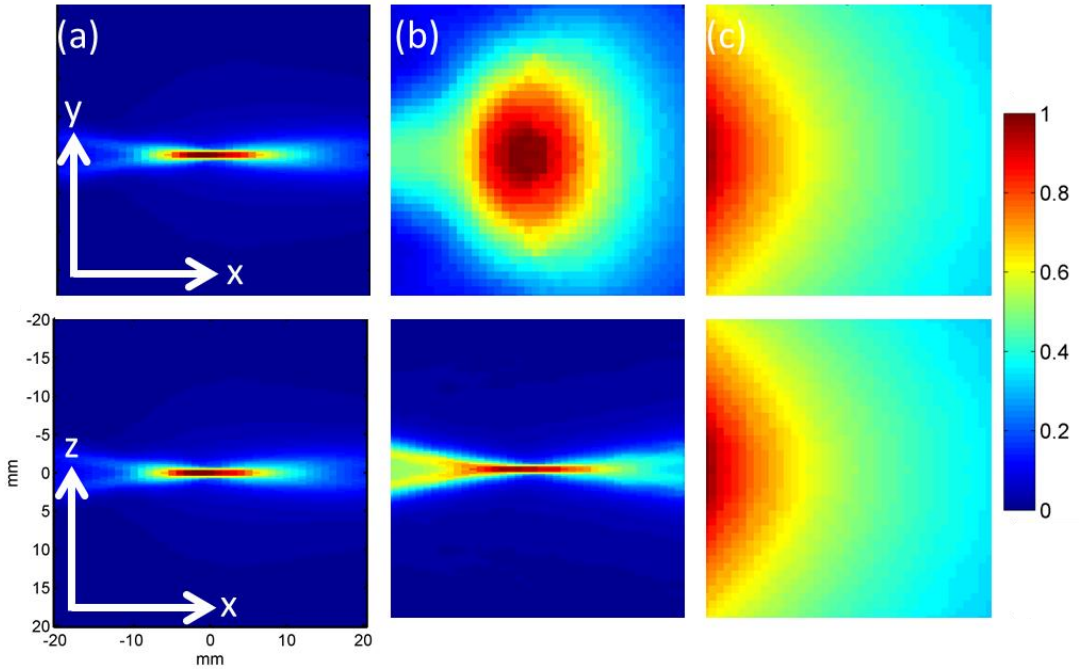

Fig. 2.8: Sensitivity fields for different focus types: (a) a spherically focused transducer with an element size of 15 mm x 15 mm, (b) a cylindrically focused transducer with an element size of 0.5 mm x 15 mm and (c) an unfocused transducer with an element size of 0.5 mm x 0.5 mm. The transducer is located at position (-40,0,0) in mm; The radius of the element curvature is 40 mm.

2.4.2 Computed reconstruction techniques

Computed reconstruction techniques use mathematical techniques to reconstruct an image from the set of measured optoacoustic signals. They are typically based on simple delay-and-sum beamforming techniques [26], also known as synthetic aperture techniques [14], or on more rigorously derived analytical formulas related to the spherical Radon transform. They can be implemented in spatiotemporal domain or Fourier domain [62, 63] and exist for several detection geometries (planar, cylindrical or spherical), as depicted in Fig. 2.9. They are typically referred to as the backprojection formula, because they are based on backprojecting the time-resolved optoacoustic signals onto spherical shells and summing them up in order to form an image. These formulas are exact under ideal conditions, *i.e.* when the wavefront is detected by an infinite number of omnidirectional infinitely broadband point detectors distributed on an infinite planar, closed spherical, or infinitely long cylindrical detection surface [63].

In addition, algebraic or model-based inversion schemes [64-66] have been suggested as more accurate alternatives to backprojection algorithms in non-ideal detection scenarios. These methods are based on numerically modeling the optoacoustic forward problem and using that model in an inversion algorithm to reconstruct the image. In contrast to backprojection algorithms, model-based schemes can explicitly take into account experimental characteristics which deviate from ideal propagation and detection conditions and can also be applied to arbitrary detection geometries.

In this work two already existing reconstruction schemes are essentially used, a modified version of the universal backprojection algorithm [63] and the 2D interpolated matrix model inversion method [66]. Later in chapter 5, a new approach is presented, which was conceived during this thesis to improve the reconstruction accuracy in the optoacoustic imaging system developed.

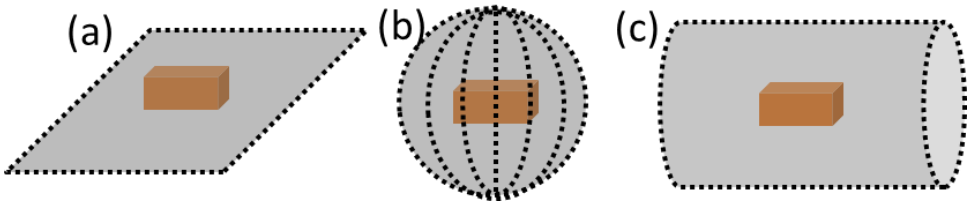

Fig. 2.9: Three ideal detection geometries for optoacoustic tomography showing (a) a planar detection geometry in which the optoacoustic signals are detected along an infinitely long planar detection surface, (b) a spherical detection geometry in which the optoacoustic signals are detected on a spherical surface completely enclosing the sample and (c) a cylindrical detection geometry in which the optoacoustic signals are detected along an infinitely long cylindrical surface enclosing the sample. Image inspired by [58]

2.4.2.1 The backprojection algorithm

The backprojection algorithm [63] is a closed form time domain solution to the optoacoustic equation (2.12) under assumption of thermal and stress confinement and delta heating. For a spherical or cylindrical detection geometry, it writes

$$H_r(\boldsymbol{r}) = \frac{1}{\Gamma \Omega_0} \int_{\Omega_0} b(\boldsymbol{r_0}, \bar{t} = |\boldsymbol{r} - \boldsymbol{r_0}|) d\Omega_0 \tag{2.30}$$

where

$$b(\boldsymbol{r_0}, \bar{t}) = 2p(\boldsymbol{r_0}, \bar{t}) - 2\bar{t}\frac{\partial p(\boldsymbol{r_0}, \bar{t})}{\partial \bar{t}} \tag{2.31}$$

is the backprojection term for detection position $\boldsymbol{r_0}$ which is backprojected onto spherical shells centered at $\boldsymbol{r_0}$ and

$$d\Omega_0 = \frac{dS_0}{|\boldsymbol{r} - \boldsymbol{r_0}|^2} \frac{n_0^s \cdot (\boldsymbol{r} - \boldsymbol{r_0})}{|\boldsymbol{r} - \boldsymbol{r_0}|} \tag{2.32}$$

the solid angle element subtended by the detection element dS_0 with respect to the reconstruction point P at position $\boldsymbol{r}$. $H_r(\boldsymbol{r})$ is the deposited energy, n_0^s a vector

pointing outwards perpendicular to the detection surface S_0. Ω_0 is a the solid angle of the whole measurement surface and for spherical and cylindrical geometries $\Omega_0 = 4\pi$.

The system, presented in chapter 3, uses a 2D circular detection geometry where the detectors are cylindrically focused and lie in the imaging plane. To reconstruct in this scenario, a modified two-dimensional backprojection formula is used [24] which is defined as

$$H_r(\boldsymbol{r}) = \frac{{\boldsymbol{r_0}}^2}{2\pi\Gamma {v_s}^2} \int_{\theta_0} d\theta_0 \frac{1}{t^2} \left[p(\boldsymbol{r_0}, t) - t \frac{\partial p(\boldsymbol{r_0}, t)}{\partial t} \right]_{t=|\boldsymbol{r}-\boldsymbol{r_0}|/v_s} . \tag{2.33}$$

The t^{-2} weightening comes from the solid angle term which is proportional to the square of the distance between the receiving element dS_0 and the point P, thus leads to a compensation factor of t^{-2}. The solid angle weightening is neglected because it had no visible effect on the reconstruction and only increased the reconstruction time.

The backprojection formulas are very convenient for optoacoustic image reconstruction. Due to their simplicity they are easy to implement, memory efficient and fast. In the real-time MSOT system, these formulas are used for real-time reconstructions. Although not being exact in the presented conditions, they are very useful for detecting the shape and position of the absorbers and for assessing parameters such as speed of sound and radius of rotation. On the downside, for 2D geometries, *i.e.* where all detectors and optoacoustic sources are located in one plane, they suppress slowly varying image components associated with the light fluence or big objects and accentuate fast changes in the image, *i.e.* object boundaries. In addition, backprojection reconstructions in non-ideal detection geometries often show negative optical absorption values which have no physical meaning [66]. To overcome these drawbacks, Rosenthal *et al.* developed a 2D model-based reconstruction algorithm.

2.4.2.2 The interpolated matrix model-based inversion (IMMI)

This inversion method [66] is a model-based reconstruction technique for optoacoustic image reconstruction in a 2D geometry, *i.e.* where all the optoacoustic sources and detectors are located in one plane. It employs a discretized semi-analytical time domain solution of the optoacoustic wave equation (2.12) and can be written in form of a matrix relation

$$\mathbf{p} = \mathbf{M}\mathbf{z}\,, \tag{2.34}$$

where $\mathbf{p}$ represents the optoacoutic signals measured at different positions (projections) and instants arranged as a column vector. The column vector $\mathbf{z}$ contains the originating optoacoustic image on the defined grid, *i.e.* values of the heat deposition. $\mathbf{M}$ is the acoustic forward-model matrix, it is sparse and does not depend on the imaged object, but only on the experimental acquisition geometry. $\mathbf{M}$ is calculated by interpolating for coordinates in-between the grid points in order to be able to integrate over arcs, according to formula (2.16). For a fixed acquisition

geometry, $\mathbf{M}$ has to be calculated only once and can be reused for consecutive reconstructions.

The optoacoustic image is obtained by inverting the matrix relation (2.34). A common method of doing this is the minimization of the mean square error (MSE):

$$\mathbf{z} = \arg\min \left\| \mathbf{p} - \mathbf{M}\mathbf{z} \right\|_2^2 \tag{2.35}$$

where $\| \ \|_2^2$ is an l_2 norm. In Ref. [66] two methods are suggested to solve Eq. (2.34): the Moore-Penrose pseudoinverse [67] and the LSQR algorithm [68].

The pseudoinverse of the matrix **M** is given by

$$\mathbf{M}^{\dagger} = (\mathbf{M}^{\mathrm{T}}\mathbf{M})^{-1}\mathbf{M}^{\mathrm{T}} \tag{2.36}$$

where $^{\mathrm{T}}$ denotes the transpose operator. To reconstruct the image, the measured optoacoustic signal is then multiplied with the pseudoinverse matrix, *i.e.*

$$\mathbf{z}_{\mathbf{sol}} = \mathbf{M}^{\dagger}\mathbf{p}^{\mathrm{T}} \tag{2.37}$$

The advantage of using the pseudoinverse approach is that it does not depend on the measured data but is determined only by parameters of the experimental setup, *e.g.* the position of the sensors employed with respect to center of rotation, the sampling resolution, etc. Therefore, given a rigid measurement configuration, the pseudoinverse $\mathbf{M}^{\dagger}$ may be pre-calculated, thus leading to a real time inversion procedure which involves only the product operation of Eq. (2.37). The disadvantage of this approach is that in order to perform the inversion, the entire matrix $\mathbf{M}$ needs to be stored in the computer's memory, which could lead to challenging memory utilization, especially for high resolution reconstructions.

The computational requirements for image inversion can be mitigated by the LSQR algorithm [68], which capitalizes on the sparse nature of $\mathbf{M}$. This algorithm avoids matrix-matrix operations but instead multiplies vectors by the matrix and operates on the resulting vectors. In this way, a sequence of approximate solutions $\mathbf{z}_1$, $\mathbf{z}_2$, …, $\mathbf{z}_n$ to the problem is attained which minimize the residual error

$$R = \left\| \mathbf{M}\mathbf{z} - \mathbf{p} \right\|. \tag{2.38}$$

As the number of iterations increases, the algorithm converges to a solution which is expected to be close to the original image.

The high accuracy achieved by the forward model allows data inversion without regularization when 360° tomographic views are available. More importantly the model eliminates a variety of image artifacts associated with conventional back-projection algorithms, such as negative image values and other quantification artifacts, and overall offer superior accuracy and image fidelity in a 2D reconstruction scheme [66].

2.4.3 Spatial resolution

The width of optoacoustic signals in the time domain scales with the size of the optoacoustic source. Ultimately, the limiting factor for the achievable resolution is the maximally detectable frequency. But it also depends on other factors such as duration of the laser pulse, detection geometry, size, shape and number of the transducer elements and image formation technique [26].

The small animal imaging system presented in the next chapter uses a cylindrically focused transducer array for 2D cross-sectional imaging. Volumetric images are obtained by stacking the individual 2D slices. The in-plane resolution therefore depends on computed reconstruction techniques whereas in elevation the resolution depends on acoustic focusing.

2.4.3.1 Spatial resolution achieved by computed reconstructions

The resolution of an imaging system can be assessed by the point spread function (PSF) which describes how the system represents an elementary volume. Xu *et al.* [69] derived an expression to estimate the bandwidth limited resolution of an imaging system in an idealized detection scenario (*i.e.* full view detection, point detectors, continuous spatial sampling and constant sound speed), based on the full width half maximum (FWHM) of such a point spread function (PSF)

$$R_{bw} \approx 0.8\, v_s / f_{co} \tag{2.39}$$

where R_{bw} is the bandwidth limited resolution, v_s the sound speed an f_{co} the cut-off frequency of the transducer. This resolution is spatially invariant.

Real ultrasound transducers however have a finite size detection aperture rather than a point. Like shown in section 2.3.4 this adds an extra spatially variant broadening of the optoacoustic signals, which is generally not taken into account in standard optoacoustic reconstruction algorithms, like the backprojection algorithm (c.f. section 2.4.2.1). Hence, the spatial resolution of the optoacoustic imaging system gets additionally degraded perpendicular to the acoustic axis of the transducer, which is herein referred to as the lateral direction. Xu *et al.* also derived an expression to estimate this degradation by the lateral extension of the PSF. The axial extension of the PSF is negligible compared to the lateral blurring. In a spherical or circular scanning geometry for an unlimited detection bandwidth and a detector with the same curvature properties as the detection surface, it is given by

$$R_{ap}(r) \approx \frac{r}{r_0} D \tag{2.40}$$

where R_{ap} is the aperture limited resolution, r the distance between the point source and the center of the scan circle, r_0 the radius of the scan circle and D the dimension of the detector.

To characterize the spatial resolution in a tomographic system, one distinguishes therefore between the axial and the lateral resolution. The axial resolution is the

resolution along the acoustic axis of each transducer intersecting the center of rotation of the detection surface (or arc in 2D). It depends principally on the detection bandwidth of the transducer, *i.e.*

$$R_{ax} = R_{bw}\,. \tag{2.41}$$

The lateral resolution is the resolution perpendicular to the acoustic axis of the transducer. It is spatial variant and depends both on the bandwidth and the aperture of the transducer element

$$R_{lat}(r) = \sqrt{{R_{bw}}^2 + {R_{ap}(r)}^2}. \tag{2.42}$$

The more the source approaches the center of rotation of the transducer array the more the lateral resolution improves until it is only bandwidth limited. An example of the spatially variant PSFs is shown in Fig. 2.10.

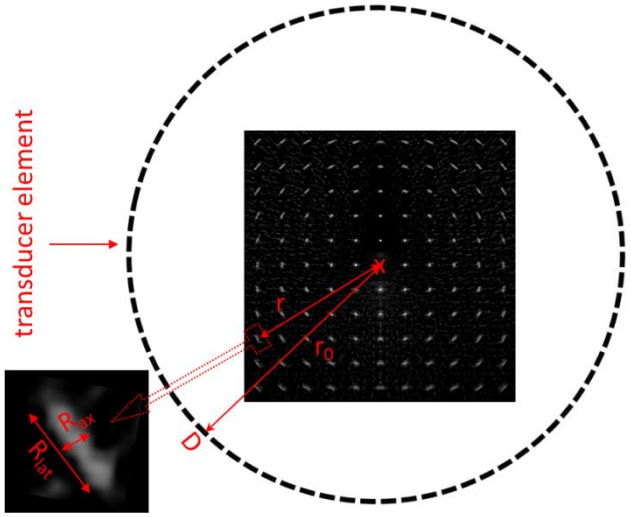

Fig. 2.10: Point spread functions (PSFs) in an optoacoustic tomography system. The dimension of the PSF in axial direction, *i.e.* along a radial line through the center of the detection arc, is constant for each position. Perpendicular to it, the PSFs elongates the farther it is located from the center of the detection arc.

2.4.3.2 Spatial resolution achieved by acoustic focusing[2]

The spatial resolution in a focused detector-based setup is determined by the focusing capacities of the detector which, beside the shape of the detection aperture, depends on the frequency of the detected signal. Fig. 2.11 depicts the sensitivity field of a cylindrically focused transducer for three different frequencies (1, 3 and 5 MHz). The point with the coordinates (0, 0) mm corresponds to the geo-

[2] The sensitivity fields of the transducer were obtained by calculating the spatial impulse response (SIR) with the ultrasound simulation package Field II [94], filtering it to the desired frequency range and plotting the amplitude as a function of its spatial coordinates.

metrical focus of the transducer. Focusing restricts the sensitivity of the transducer to a smaller area. The area of maximized sensitivity is stretched along the acoustic axis of the transducer. To characterize the sensitivity field one refers to the -6 dB focal zone, *i.e.* the area within which the pressure amplitude drops to half its value. This defines the area of effective imaging. The width of the focal area determines the slice thickness which can be achieved; the length determines the monitoring depth. We see the strong frequency dependence of the focusing ability of the transducer. The higher the frequency of the signal, the better is the focusing and therefore the achievable resolution.

A formula to estimate the width W and length L of the sensitivity field for cylindrically focused transducers as a function of the characteristic frequency f_c, defined as the 1/e level in the spectrum of the detected signals and the aperture angle θ, was derived by Khockova *et al.* [70]. The equations are

$$L = \frac{1.1 v_s}{f_c(1 - \cos(\theta/2))} \tag{2.43}$$

and

$$W = \frac{0.5 v_s}{f_c \sin(\theta/2)} \tag{2.44}$$

where v_s is the sound velocity in the medium. We see from the formulas that width and length of the focal area decrease with an increasing aperture angle and increasing characteristic frequency. This trade-off between resolution and monitoring depth is a major challenge in designing a focused detector-based imaging system.

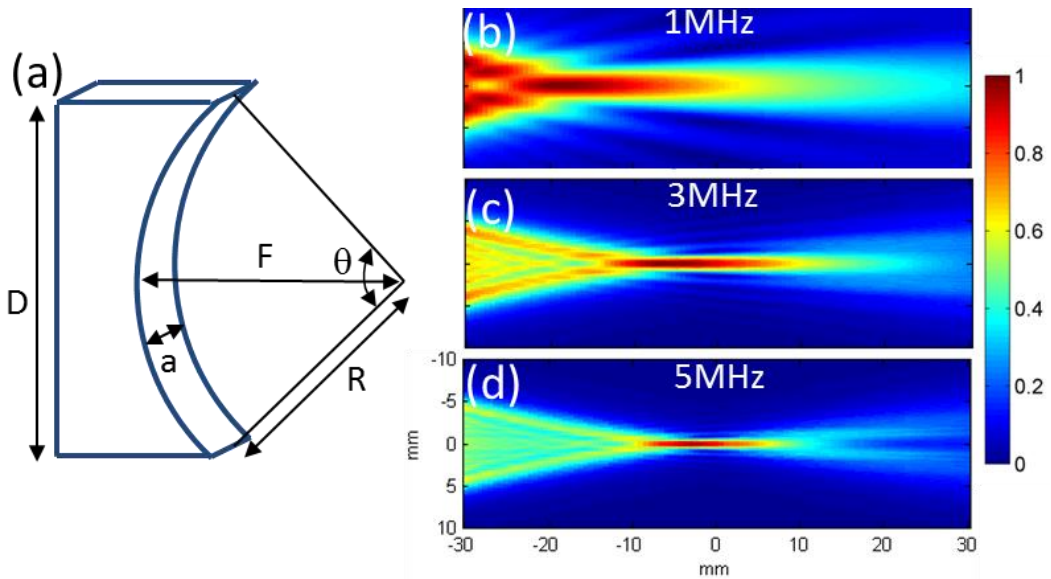

Fig. 2.11: Sensitivity fields for cylindrically focused detection elements. (a) Illustration of the geometry. (b) Sensitivity field for a frequency f = 1 MHz, a focal length F = 40 mm and an aperture size of D = 15 mm and a = 1 mm. Sensitivity field of the same detector geometry at (c) a frequency of 3 MHz and (d) at 5 MHz. The focal point is located at (0,0) mm.

2.4.4 Effects of a limited detection bandwidth on images[3]

For exact reconstructions, it is necessary to detect the whole bandwidth of the optoacoustic signals. The effects of a limited detection bandwidth are shown in Fig. 2.13. It depicts optoacoustic reconstructions of a complex phantom in a 2D full view ($\Delta\alpha = 360°$) circular detection geometry for different detection bandwidths. The detection geometry is presented in Fig. 2.12. Fig. 2.13 (a) depicts the reconstruction with an unconstrained and uniform detection bandwidth. It can be considered as exact. Fig. 2.13 (b) depicts the reconstruction with a detection bandwidth from 0 to 2 MHz. It is blurred and cannot resolve small absorbers like the two indicated by the arrow. Fig. 2.13 (c) shows the reconstruction with a detection bandwidth between 1 and 7.5 MHz. Small absorbers are resolved clearly but from the big absorbers only the boundaries are visible. The three examples clearly show the importance of having an adapted and sufficient large detection bandwidth. High frequencies are necessary for resolution and thus the ability to resolve small objects (*e.g* vessels).

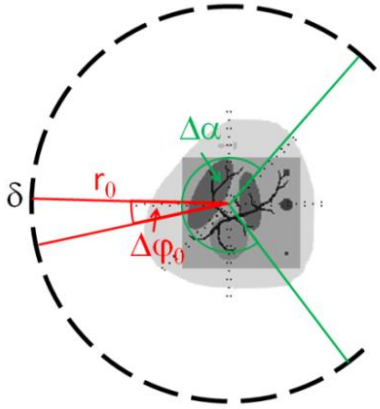

Fig. 2.12: 2D detection geometry. r_0 represents the radius of the detection arc, δ the width of the detection element, $\Delta\varphi_0$ the angular sampling period and $\Delta\alpha$ the angular coverage of the detection aperture.

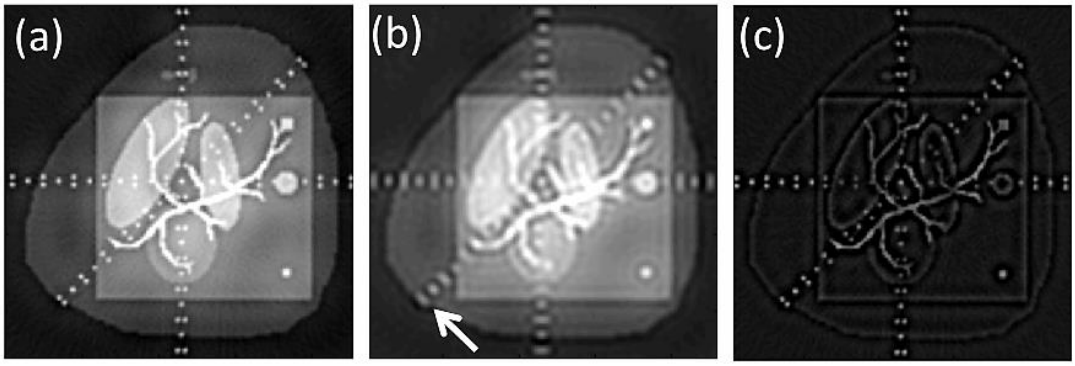

Fig. 2.13: Effects of limited detection bandwidth. (a) Reconstruction with full detection bandwidth (up to 7.5 MHz), (b) detection bandwidth only up to 2 MHz and (c) detection bandwidth between 1 and 7.5 MHz. Accurate reconstructions require a full detection bandwidth. High frequencies are needed for resolution. Low frequencies are required for visualizing big objects.

[3] Optoacoustic signals were simulated using the k-wave optoacoustic simulation toolbox [98]. The simulation grid had a size of 802 x 802 x 5 voxels and each voxel a size of 100 x 100 x 100 µm³ thus supporting frequencies up to 7.5 MHz. Images were reconstructed with the 2D IMMI algorithm (cf. section 2.4.2.2) using 720 tomographic projections uniformly distributed on the 360° detection arc. A limited detection bandwidth was simulated by filtering the signals appropriately.

Low frequencies are necessary for visualizing low spatial frequencies originating from big objects, such as organs, but also slowly varying phenomena like the attenuation of light in tissue. Failing in detecting the necessary frequencies leads to inaccurate reconstructions. With respect to designing an imaging system this means that the detection bandwidth has to be chosen, according to the required imaging performance. The system, presented in chapter 3 is for macroscopic small animal imaging with a targeted resolution of about 150 µm. In this case the maximal required frequency is about 8 MHz according to Eq. (2.39). Preferentially the ultrasound detection device has a uniform sensitivity in this spectral range. Since this is not the case in experimental imaging systems, present a deconvolution approach to correct for a non-uniform detection bandwidth is presented in section 4.2.

2.4.5 Effects of a finite detector size[4]

In order to achieve the maximal signal-to-noise ratio, detectors should have a large element size (cf. section 2.3.5). Yet, the spatial impulse response of large elements leads to a distortion of the optoacoustic signals (cf. section 2.3.4). If this effect is not considered in the reconstruction, this results in a resolution loss in lateral direction, *i.e.* perpendicular to the acoustic axis of the transducer (cf. 2.4.3.1). This is shown in Fig. 2.14: (a) depicts the reconstructions assuming detection with a point detector, (b) the reconstructions assuming a 2 mm large and (c) assuming a 6 mm large detection element. Comparing the individual reconstructions, we see a loss of resolution in lateral direction when using finite size detection elements. Small objects, *i.e.* the two spots indicated by the white arrow, cannot be resolved anymore. The loss of resolution is worse for bigger elements and for longer distances between the source and center of detection. The resolution along the axis of the transducer elements, *i.e.* along radial lines through the center of rotation

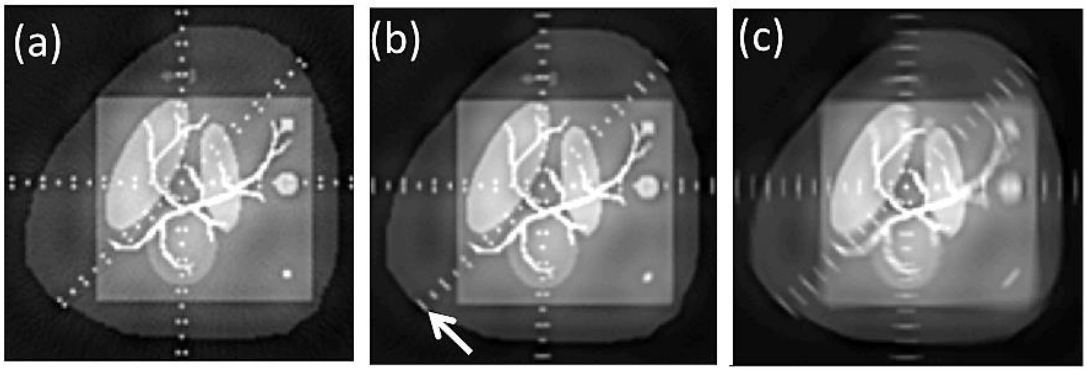

Fig. 2.14: Effects of a finite detector size. (a) Reconstruction using signals detected with a point detector and (b) a detector having a 2 mm or (c) a 6 mm large detection surface. Detection with finite size detectors leads to a lateral resolution loss, which becomes worse the bigger the detector and farther the source from the center of the detection circle.

[4] Signals have been simulated as mentioned in section 2.4.4. A finite size detector was simulated by a set of point detectors and summing up the individual signals. For image reconstruction, the 2D IMMI method was used assuming point detectors but the effects are the same for the backprojection algorithm.

of the detection arc, remains constant. When designing an imaging system it is therefore important to reduce the lateral dimension of the detection element in order to achieve homogenous resolution. Since this reduces sensitivity, 2D imaging approaches using cylindrically focused detectors with a small azimuthal, but large elevational dimensions, are a good compromise.

2.4.6 Effects of a limited view detection

Exact optoacoustic reconstructions require detection of the photoacoustic signals on a closed detection surface around the object [26]. In many imaging implementations, such as the system described in the next chapter, this cannot be achieved due to constraints like limited access or cost. Optoacoustic imaging systems, for instance, generally employ water as matching medium between the surface of the imaged object and the acoustic detector. In order to be able to acquire a complete data set, the object has to be entirely immersed in water. *In vivo* imaging applications however, especially whole body small animal imaging, only allow partial immersion of the animal into water resulting into a restricted detection surface. This combined with the directivity of optoacoustic signals (cf. section 2.2.3.4) might render some structures within the object undetectable (invisible), while other structures are highly defined. This is known as the limited view problem. The condition, under which an object is visible in a given detection geometry, has been given by Xu *et al.* in reference [71]. Accurate boundary detection requires that, for each boundary point, the normal line to the boundary's defining curve intersects the detection curve (or line for scanning geometries) in at least one point. Points without such a normal line intersecting the detection curve are invisible because the wavefront is not detected and therefore will be blurred away in the reconstruction. The blurring effect is illustrated in Fig. 2.15 (a) for a 2D circular detection geometry, in which a round phantom with rectangular insertion is imaged. The findings are however also valid in 3D. The detection arc, denoted by the blue solid curve, defines a "visibility zone", shown in gray, in which the boundary of the imaged object always fulfills the detection criterion, and thus can be accurately reconstructed [71]. Sections of the boundary lying outside the detection region, *i.e.* in the "invisibility zone", may be still reconstructed subject to fulfilling the detection criterion. The boundary sections which can be accurately reconstructed are marked with a solid red line. Fig. 2.15 (b) to (f) show the IMMI reconstruction obtained for the phantom, using the detection geometry depicted in Fig. 2.12 for different detection arcs ($\Delta\alpha = 360°$, 240°, 180°, 140°, 90°, respectively). The reconstructions clearly show the blurring effect of the object's boundary segments which do not fulfill the detection criterion. The blurring is worse for smaller detection arcs and model-based reconstructions require specific regularization techniques. This topic is discussed in section 4.4. With respect to designing an imaging system, the limited view problem implies that the detection arc should be as long as possible and the sample should be positioned in the "visibility zone" to maximize the accuracy of the reconstruction.

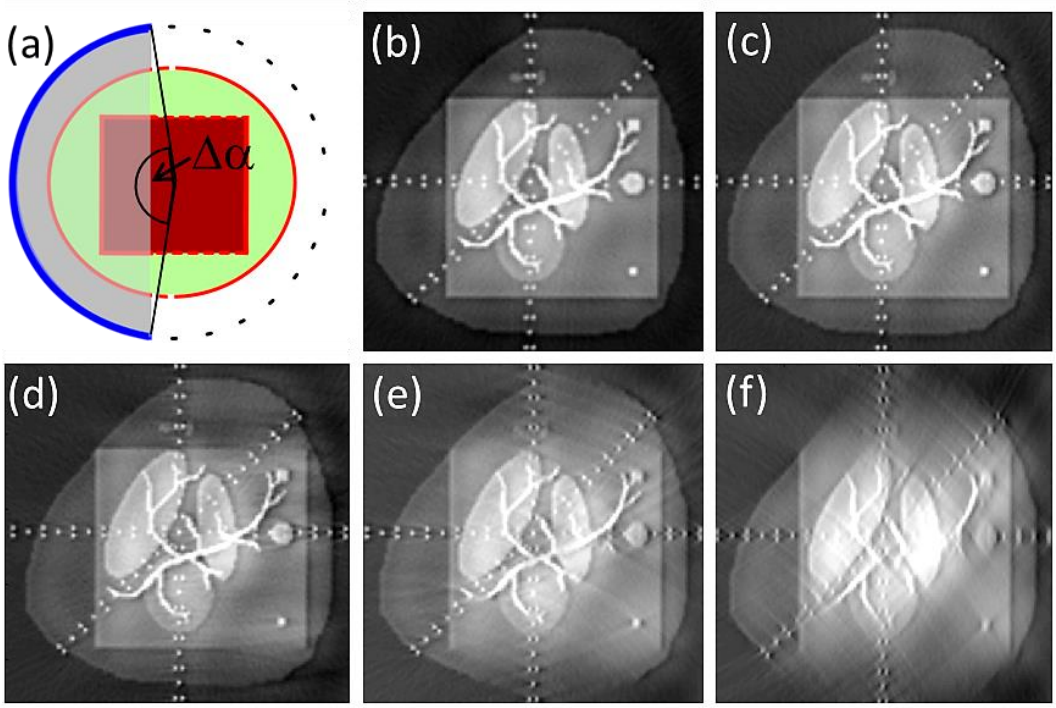

Fig. 2.15: The limited view problem. (a) Reconstructable (red solid line) and "invisible" (red dashed line) boundaries of a round object with a square insertion partially lying in the "visibility region" (shaded area) and the "invisibility domain" for a detector moving along the blue solid arc. Dashed boundaries blur away since they do not fulfill detection criterion, *i.e.* they do not have a normal passing at least through one detector position. (b) IMMI reconstruction of the numerical phantom using full view ($\Delta\alpha$ = 360°) data and partial view data with (c) $\Delta\alpha$ = 240°, (d) $\Delta\alpha$ = 180°, (e) $\Delta\alpha$ = 140° and (f) $\Delta\alpha$ = 90°, showing that boundaries do not fulfill the detection criterion blur away.

2.4.7 Effects of insufficient spatial sampling

In optoacoustic tomography, the acoustic field emitted from the object under investigation is measured in form of temporal signals along a two-dimensional detection surface. In order to be able to reconstruct the object accurately, the acoustic field has to be sampled according to the Nyquist criterion, *i.e.* with a temporal and spatial sampling frequency (which is the inverse of the sampling period) at least twice the maximum frequency of the detected optoacoustic signal. Otherwise, aliasing occurs causing significant reconstruction errors by disguising high frequency components above the sampling frequency as low frequency components [26]. Anti-aliasing due to the temporal sampling is straightforward by using anti-aliasing filters prior to the analog to digital (A/D) converter to filter out frequencies higher than twice the sampling frequency. Aliasing due to the spatial sampling can be avoided by sampling the detection surface with a sampling period smaller than half the size of the detection element δ. The reason is that the finite size of the detection element acts like a spatial frequency filter and thus limits the maximal available frequency. For detection scan along a circle, like in a spherical or cylindrical scan this is $r_0\Delta\varphi_0 < \delta/2$, where $\Delta\varphi_0$is the angular sampling period and r_0 the radius of the detection surface. For a detection scan along a line like in a planar scan, this is $\Delta x_0 < \delta/2$ where Δx_0 are the spatial sampling periods [72]. In practical terms, this can be achieved by scanning a single detection element (or an array) around (or along) the sample, yet at expense of imaging speed. Herein we aim for cross-sectional real-time imaging, thus have to acquire the whole dataset for a 2D

tomographic reconstruction in parallel. A multi-element transducer array is employed for this purpose. Due to SNR, manufacture and cost reasons, it might however not be possible to equip the transducer with enough densely spaced elements to achieve a fine enough angular sampling and aliasing artifacts are expected. The effects of an insufficient angular sampling are showcased in Fig. 2.16. It depicts optoacoustic reconstructions of the phantom using sparse angular sampling. The detection geometry is depicted in Fig. 2.12 assuming full view detection ($\Delta\alpha = 360°$) and a detector size of $\delta = 0.7$ mm. Fig. 2.16 (a) to (c) show the reconstruction with an angular sampling period of $\Delta\varphi_0 = 0.5°$, $\Delta\varphi_0 = 1°$ and $\Delta\varphi_0 = 2°$, respectively. In the first case, the spatial Nyquist theorem is fulfilled, in the other both cases not. We can see that insufficient angular sampling causes aliasing artifacts which manifest themselves as streak artifacts and image roughness. The sparser the angular sampling, the stronger are the artifacts. Streak artifacts are generally only seen to radiate from sharp edges because for smoothly varying objects high frequencies are absent. The origin of these artifacts can be understood intuitively considering backprojection reconstructions where images are formed by backprojecting the optoacoustic signals, measured at various tomographic detection positions onto spherical shells (or circles in 2D) and summing up the individual contributions. If the detection arc is closed and detection positions are densely spaced, the arcs originating from the individual backprojected signals will compensate each other due to the complementary information from different detection position, yielding an image of the actual source distribution. If the spatial sampling of the acoustic field is sparse, this compensating effect is missing and partial streaks remain. Whereas it is straightforward to fulfill the spatial Nyquist theorem in scanning-based setups, this is not possible in some fixed array configurations used for real-time image reconstruction. Section 4.3, presents a practical approach to alleviate the aliasing effects in such fixed geometry systems not fulfilling the spatial Nyquist criterion.

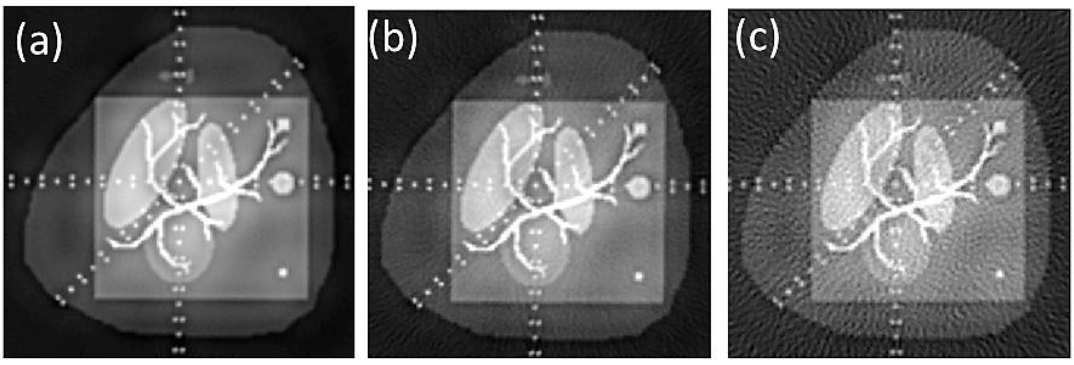

Fig. 2.16: Effects of insufficient angular sampling. Reconstructions using an angular sampling period of (a) $\Delta\varphi_0 = 0.5°$, (b) $\Delta\varphi_0 = 1°$ and (c) $\Delta\varphi_0 = 2°$. Sparse angular sampling leads to aliasing artifacts manifested as streaks.

2.4.8 Thin slice illumination vs. broad beam illumination

The imaging system developed is conceived for cross-sectional real-time imaging of mice. To examine, whether it is beneficial to do thin slice illumination or to distribute the laser energy over a larger area, the 3D light fluence pattern was simulated for a cylindrical phantom with mouse mimicking properties (*i.e.* 2 cm in diameter, μ_a = 0.3 cm^{-1}, μ_s' = 10 cm^{-1}) and illumination rings with different widths (1, 8 and 16 mm) using a FEM based package for modeling light transport in tissue [73]. Fig. 2.17 illustrates the light fluence distribution within the phantom. Cross-sectional slices through the light fluence distribution are shown in the first row and sagittal slices in the second. The profiles along the dashed lines are shown in (g) and (h). The ratio between out-of-plane and in-plane energy deposition as a function of depth and width of the illumination ring is depicted in (i). Due to strong light scattering in tissue, focusing of light to the imaging plane is severely impeded, especially for deep tissue structures and optoacoustic signals are also generated outside the imaging plane. Thin slice illumination produces less out-of-plane signals than illumination of a larger area. On the other hand for the same surface exposure, being limited by the MPE, more light reaches deep tissue structures when a larger area is illuminated (18 % vs. 4 %). Hence, it is beneficial to use a broad illumination beam from a signal to noise ratio point of view. Conversely, from an image reconstruction and quantification point of view, it is better to do thin slice illumination because less out-of-plane absorbers contribute to the photoacoustic signal.

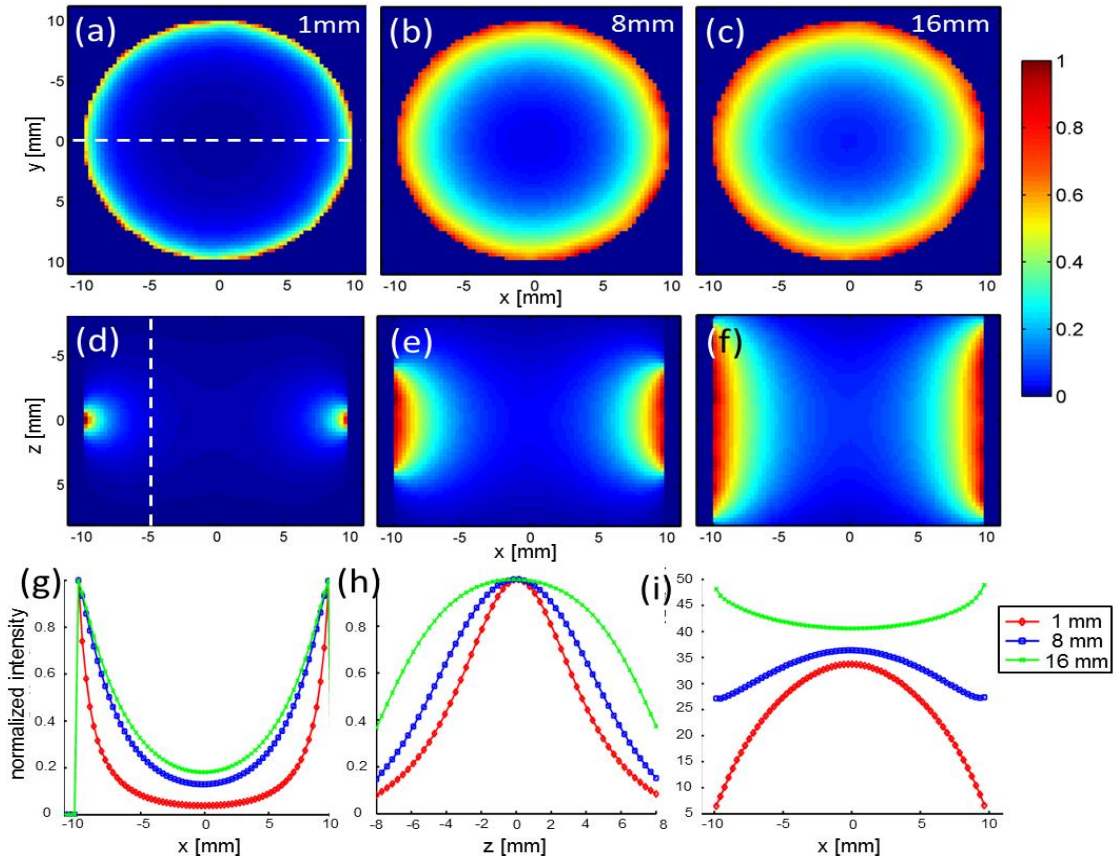

Fig. 2.17: Simulated illumination pattern in a cylindrical tissue mimicking phantom. Cross-section through the phantom for different widths of the Illumination ring (1 mm, 8 mm, 16 mm) are shown in (a) - (c), the corresponding sagittal slices through the phantom in (d) - (f) and the profiles along the dashed lines in (g) and (h). The ratio between out-of-plane energy deposition and in-plane energy deposition as a function of the position and width of the illumination ring is given in (i).

2.5 Summary and Conclusion

In this chapter the theoretical and technological background for optoacoustic imaging was presented.

Starting with a discussion of light and ultrasound behavior in biological tissue, it was further explained how optoacoustic signals are generated as well as properties of optoacoustic signals and directivity effects due to diffraction. It was also specified that in optoacoustic imaging contrast is based on optical absorption, whereas resolution stems from the emitted ultrasound waves and thus is independent of light scattering. Moreover, an analytical estimate for optoacoustic signal strength expected in a small animal imaging scenario was given, being in the range of several tens of Pascals depending on their locations, size and absorption coefficient.

In the second part of the chapter, general aspects of optoacoustic instrumentation were discussed. Since optoacoustic signals are weak, signal-to-noise ratio is a crucial factor. For whole body mouse imaging, it is therefore important to maximize light delivery to deep tissue structures, which can be achieved by an optimized illumination scheme, high pulse energies (within the laser safety standards), and wavelengths in the NIR. Nanosecond pulsed lasers with OPO based wavelength tuning are particularly suited for that, since they provide high pulse energies and fast wavelength change. With respect to signal detection, piezocomposite transducer arrays have the advantage that they can be produced in arbitrary shapes adapted to the specific imaging task and parallelized for high frame-rate imaging. It was also shown that the detection system distorts the shape of the detected optoacoustic signal by its electrical (EIR) and spatial impulse response (SIR). Thus it is important that the detection device is sufficiently broadband to avoid signal distortion, sensitive and with a sufficiently large dynamic range to capture both the weak optoacoustic signals from deep inside tissue and the stronger signals close to the illuminated surface.

In the third part of this chapter, optoacoustic image formation was discussed. Optoacoustic images can be obtained by using focused transducers or by tomographic reconstruction methods. Focusing can reduce the reconstruction problem to one respectively two dimensions, thus can facilitate the reconstruction problem for potential real-time imaging. For optoacoustic image reconstruction, the back-projection algorithm and the 2D model-based inversion scheme were presented, followed by a discussion of the spatial resolution and the artifacts due to bandwidth limited detection, finite size detection elements, limited views and sparse angular sampling with the goal of providing an understanding of the effects associated with the different detection parameters. In that sense, when designing an imaging system it is necessary to match the bandwidth of the detection system to the targeted resolution and the dimensions of the features to be imaged. Moreover, detection elements should have a small lateral dimension to fit more elements on the array, thus reduce aliasing artifacts and improve lateral resolution. It is also important to increase the length of the detection arc as much as possible and position the sample within the visibility zone to avoid limited view artifacts such as blurring of boundaries. Moreover it was shown that for 2D imaging it is best to do thin slice

illumination. This reduces the amount of out-of-plane signals, in particular close to the surface of the subject. This is important with respect to quantification. In deep tissue (> 1 cm) on the other hand, illuminating a big area enables delivering of more light energy to deep tissue structures, which is beneficial with respect to SNR.

3 An innovative preclinical MSOT system

3.1 Introduction

This chapter presents the development of a 2D real-time MSOT system for *in vivo* imaging of small animals that was designed to fulfil the need of biomedical research for high frame-rate and practical *in vivo* whole body imaging capabilities. Previously developed optoacoustic imaging systems, were not suitable for this task, because they either utilized single element scanning arrangements yielding long acquisition times [5, 6, 23, 24, 57, 74] or because they used clinical transducer arrays with frequency characteristics and geometries not adapted for small animal dimensions [75, 76]. In addition, in these systems the sample was to be completely submersed in water. Whereas this is not problematic for *ex vivo* or partial body imaging, this poses severe difficulties with respect to *in vivo* whole body imaging, because a diving bell arrangement is required for delivering anesthesia and respiratory gases, making animal position delicate and time consuming. Also, there are hygienic reasons for avoiding direct immersion of the animal in water, because animals are frequently used as a model system for studying disease and thus might be a carrier of various pathological agents. To overcome these limitations, a new concept for whole body MSOT small animal imaging was developed. Light energy delivery was optimized using cylindrical ring illumination, allowing optimal concentration of light energy around the mouse body. Correspondingly, a highly sensitive concave ultrasound detector array was used to effectively collect optoacoustic responses from the illuminated area. To enable the detection of multiple biomarker spectra, the system uses multiple wavelengths illumination. The system design further incorporates an acoustically and optically matched membrane, which allows placement of small animal in the centre of the imaging system while prohibiting direct contact of tissue with the surrounding matching medium, utilized for optimally coupling acoustic response from tissue to the detector. I presented this system 2010 in OPTICS LETTERS in an article with the title "*Video rate optoacoustic tomography of mouse kidney perfusion*" [77] and successfully showcased on various occasions its ability to visualize anatomical, dynamic and molecular information in mice. This chapter starts with a short overview about the state of art optoacoustic small animal imaging systems published in the literature. It serves as a motivation to see the need for a new innovative design of an optoacoustic small animal imaging system. Then, technological and design aspects of the individual components in the developed system are discussed and it is shown how they are implemented, followed by an in-depth characterization of the overall system's performance. This chapter describes the iterative process of going from a conceptual small animal imaging system based on the optoacoustic effect to a fully functional device that can be utilized in biomedical research. To further illustrate this point, the described prototype imaging device was successfully commercialized and next-generation MSOT scanners are now commercially available from iThera Medical GmbH.

3.2 State of the art preclinical optoacoustic imaging systems

Optoacoustic imaging has gained enormous interest in the last years. As a consequence, various imaging devices have been developed recently and new developments focused on improving imaging performance are emerging continuously. Implementations range from optoacoustic microscopes [27, 58, 59, 78], to devices for macroscopic small animal imaging, clinical handheld scanners [79-82], mammoscopes [83-85] and endoscopic and intravascular imaging systems [86-88]. Next, a short overview over optoacoustic small animal imaging systems available is given.

3.2.1 Single transducer scanning-based systems

Frequently, optoacoustic systems used for small animal imaging are based on a single transducer element which is mechanically scanned around the sample in order to capture the dataset for a tomographic reconstruction [5, 6, 23, 24, 57, 74]. Fig. 3.1 depicts the implementation of Ma *et al.* [57], which is a representative example of such a single element-based imaging system. In the system, the animal is directly immersed in water for acoustic coupling. Illumination is achieved by a nanosecond pulsed laser. For signal detection a cylindrically focused transducer element is utilized. The light beam is focused on a thin plane in order to excite photoacoustic signals in semi-transparent samples, only within a narrow volume confocal to the focal plane of the detection element. The animal can be rotated around its longitudinal axis in order to acquire a 360° tomographic dataset for a 2D reconstruction. An additional linear stage allows moving the transducer along the longitudinal axis of the animal for acquisition of a volumetric dataset.

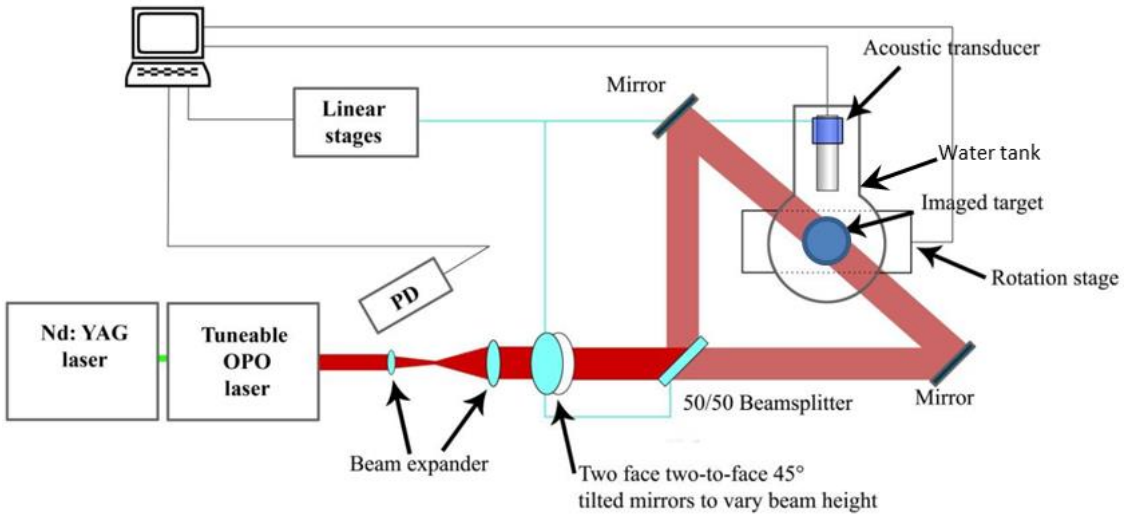

Fig. 3.1: Single element MSOT system. Illumination is achieved by a pulsed laser. The beam is expanded, focused into a sheet of light and split into two beams confocal with the focal zone of the transducer element. The sample is immersed in water and can be rotated for acquisition of a tomographic dataset for a cross-sectional reconstruction. A linear stage allows translation of the transducer and light sheet along the vertical axis of the sample allows for volumetric measurements. (Reprinted with permission from [57], Copyright 2009, Optical Society of America).

The system was showcased to be able to image zebra-fish [7] as well as the brain area of a 10 days old mouse post-mortem [89]. First images of the mouse neck area have also been shown. Yet, for large scale *in vivo* multispectral imaging of mice, the system is not suited. A major issue is the long acquisition times (minutes to hours for a single cross-sectional image and wavelength). Control of animal physiological parameters, motion and anesthesia during these extended measurement periods can present a significant challenge for obtaining high quality images. Further-more interesting *in vivo* imaging studies, such as dynamic monitoring, biodistribution of targeted contrast agents or functional responses to physiological stimuli all require acquisition times in the order of seconds to milliseconds [8] and are not possible with the described set-up. Due to the long acquisition time, *in vivo* multispectral imaging applications also become unrealistic. In addition, the animal is immersed in water, which complicates *in vivo* imaging since the animals head has to be kept above the water level. Studies of the animal brain *in vivo* are therefore not possible. Dedicated imaging systems for imaging the brain vasculature have been shown by Wang *et al.* in [23], however due to their geometrical arrangement, these systems are only suitable for imaging the brain area. Additional limitations arise from the projection-dependent and therefore varying illumination. We have shown in [90] that projection-dependent illumination may induce erroneous reconstructions. Fig. 3.2 presents results from a simulation study showing this effect. It shows a tissue mimicking phantom with two insertions reconstructed in a rotational system like the one developed by Ma [57] with uniform illumination onto the surface and projection dependent illumination. In case of the varying illumination, the reconstruction is blurred and represents erroneous intensity values. The reason for this can be understood easily. Tomographic reconstructions assume that the global pressure field is the same for each projection; however, the acoustic field is different for each sample orientation because the illumination changes during acquisitions with projection-dependent illuminations. As we have further shown in [90], there are approaches to compensate this projection-dependent illumination by model-based reconstruction however, for the sake of accuracy, projection-dependent illumination should be avoided whenever possible.

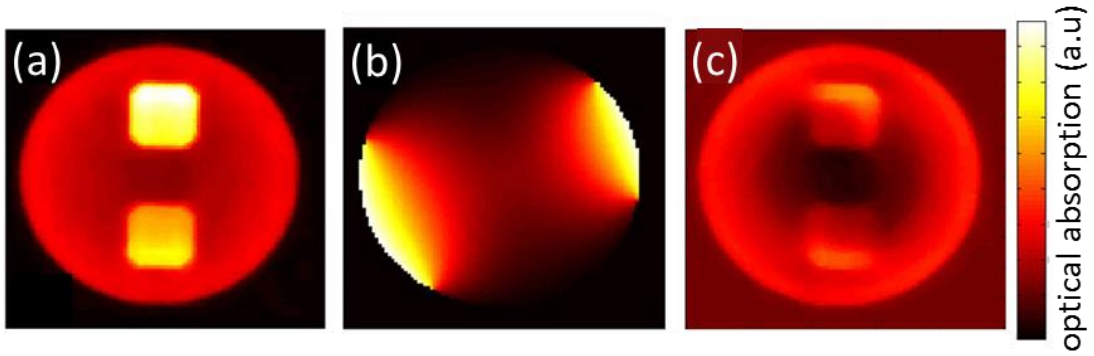

Fig. 3.2: Constant vs. projection-dependent illumination. (a) Simulation of an absorbing phantom with two rectangular insertions and uniform illumination from all directions. (b) Projection-dependent illumination pattern comparable to the illumination in the system presented by Ma *et al.* [90]. (c) Reconstruction with projection-dependent illumination. (Figure published in [90], Copyright 2010, Optical Society of America).

3.2.2 **Array-based systems**

In order to increase temporal resolution, the use of ultrasound transducer arrays from clinical ultrasound systems has been considered. However, clinical transducer arrays generally do not have the optical geometrical arrangement, sensitivity and broadband frequency characteristics for generating high quality optoacoustic images from small animals in real-time. To achieve this, ultrasound detectors that are adjusted to the need for optoacoustic imaging are required. During the development period of the system presented in the next section, two dedicated small animal imaging systems have been presented in the literature. Firstly, a 3D small animal optoacoustic scanner, utilizing an unfocused multi-element detector array scanned on a spherical surface around the animal, generated 3D anatomical images [60]. The mouse was completely immersed in water and for *in vivo* imaging a complicated diving bell arrangement was required for delivery of anesthetic and respiratory gases, thus considerably complicating animal positioning. Furthermore, the illumination was not kept stationary and since the elements were unfocused and small, it was only possible to reconstruct an image after signal averaging. This caused a complete three-dimensional scan to take about 8 minutes. Moreover, the detection system was designed with an US array with a central frequency of 3 MHz, diminishing resolution. Thus, high resolution imaging, visualization of dynamic processes, or multispectral imaging, all of which require the minimal animal motion at each wavelength, was impossible. A different system designed for brain imaging based on an 512 element ring-shaped focused ultrasound transducer array was presented late 2009 and applied for anatomical imaging of cerebral blood vessels as well as for imaging of cortical hemodynamics [8, 91]. Due to its mouse positioning and illumination from the top, it was however not suited for whole body imaging and since multiplexing was required, also not real-time. Neither did it incorporate the MSOT technology.

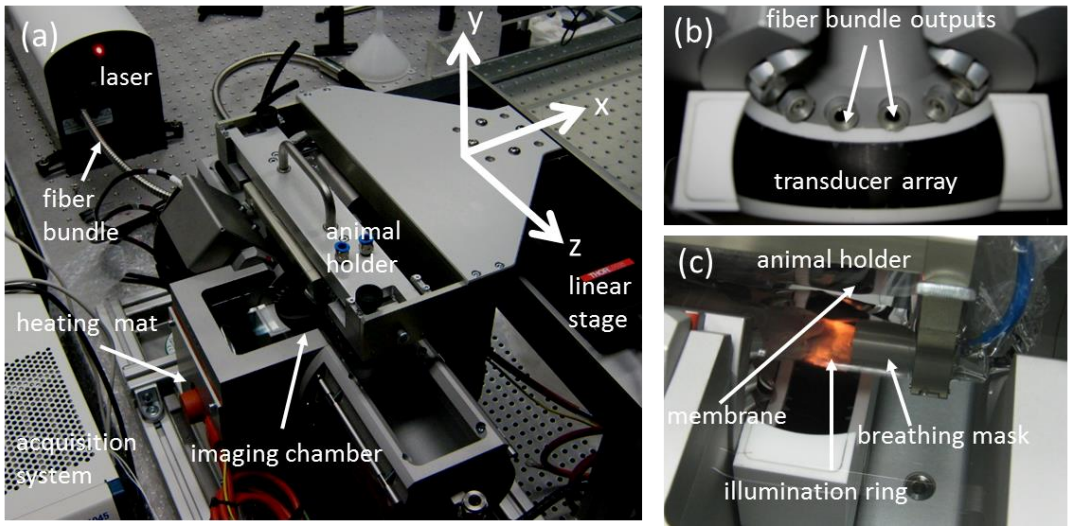

Fig. 3.3: MSOT system and its key components. (a) The MSOT system with its key components labeled. (b) The transducer array and illumination arrangement. (c) The imaging chamber during an *in vivo* measurement. (Panels (a) and (c) published in [92], Copyright 2011, Nature publishing group)

3.3 System implementation

The MSOT scanner developed for whole body mouse imaging comprises four major hard-ware components: (i) the illumination system, including a tunable pulsed laser; (ii) the imaging chamber; (iii) the ultrasound detection array and (iv) the parallel data acquisition and computing system responsible for system operation and image reconstruction. Photographs of the system are shown in Fig. 3.3 and a block diagram, describing the system and the interaction of its major components, is shown in Fig. 3.4. In the following subsections detailed explanations of the different subsystems are given.

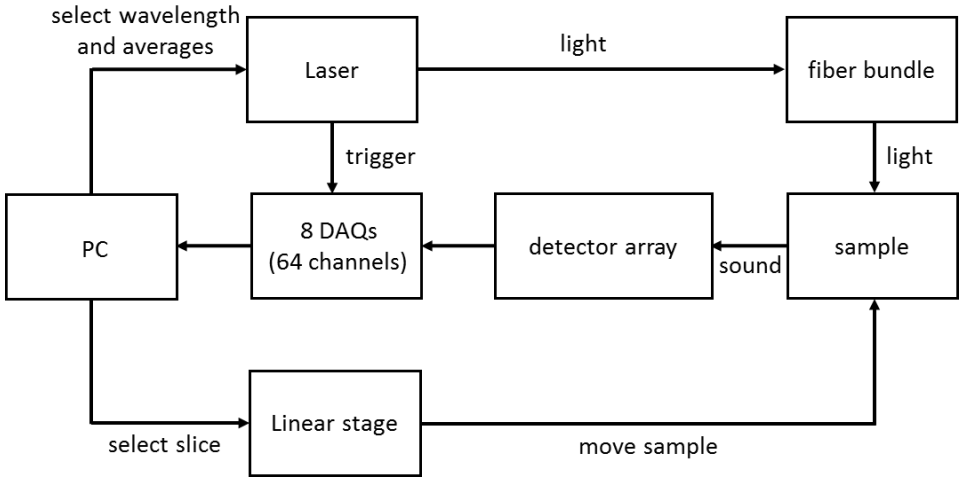

Fig. 3.4: Block diagram describing the interaction between the key components of the small animal scanner.

3.3.1 Illumination unit

Illumination comes from a Q-switched Nd:YAG laser, producing 8 ns pulses at a wavelength of 1064 nm with a repetition rate of 10 Hz for fast data acquisition. The beam is frequency doubled to 532 nm with a second harmonics generator and coupled into an optical parametric oscillator (Phocus, Opotek) to obtain a tunable wavelength range in the near-infrared (NIR) regime between 700 and 900 nm. The tuning curve of the OPO is depicted in Fig. 3.5. Per pulse variations yield a root mean square variation of 4%. The maximal pulse energy of this laser system is 115 mJ at 750 nm. The pulse duration was chosen to fulfill the condition of thermal and stress confinement. The wavelength range of the laser is chosen in the near-infrared regime to exploit the spectral window for deep tissue imaging. For doing MSOT, it is necessary to be able to change the wavelength fast. In the current implementation, a wavelength change takes about 2 seconds achieved by turning the OPO crystal. To maximize the signal-to-noise ratio, the beam is directed onto the animal's surface to create a ring-shaped illumination pattern of about 8 mm width, coinciding with the detection plane of the ultrasound transducer array. A scheme of the illumination arrangement with respect to the transducer and animal position is shown in Fig. 3.6 (a). Technically, this is realized by using a silica fused-end fiber bundle (Model PowerLightGuide, CeramOptec), consisting of 630 fibers (179 µm core diameter and a numerical aperture of 0.37) partitioned into ten arms. The input end

of the fiber bundle has an active diameter of 5 mm, whereas, at the output end, each arm has a diameter of 1.74 mm. The beam is coupled into a fiber bundle using a spherical lens (f = 5 mm). The fiber repartition in the bundle is pseudo-randomized to make the illumination on the mouse surface less sensitive to fluctuations of the beam shape. Due to mechanically constraints (width of the transducer), the illumination angle was oblique at an angle of 33° to the normal of the animal's surface. The coupling efficiency of the bundle is about 80%. The distance that light propagates through water is only 3 cm to minimize absorption losses. In the current configuration the animal is exposed to a maximal fluence of 20 $mJcm^{-2}$ and average intensity of 200 $mWcm^{-2}$ on its surface (at 750 nm), fulfilling the laser safety recommendations (cf. section 2.3.1.3).

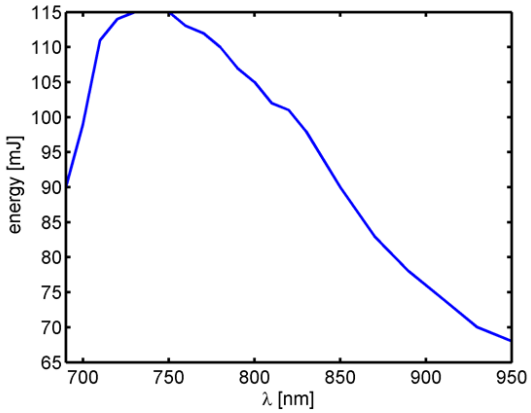

Fig. 3.5: Pulse energy as a function of the wavelength. In the following used for energy normalization in multispectral applications.

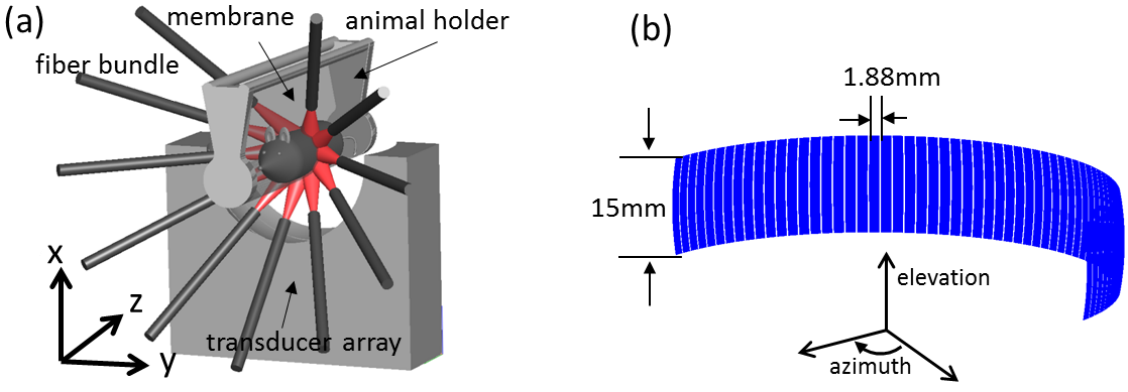

Fig. 3.6: (a) Schematic drawing of the animal holder, illumination device and transducer array. A curved array of wide-band and cylindrically focused ultrasound transducers enables parallel data acquisition. Optical fibers are used to homogeneously illuminate the object. (b) Arrangement of the individual elements in the detection array. (Panel (a) published in [92], Copyright 2011, Nature publishing group).

3.3.2 Ultrasound detection

The mouse-body can be approximated as a cylindrical imaging object and it is addressed herein by collecting optoacoustic responses using a multi-element ultrasound transducer array with elements cylindrically focused onto a common plane and arranged on an arc surrounding the animal for cross-sectional imaging. By being mostly sensitive to signals originating from a thin slice, the dimensionality of the reconstruction problem is reduced to quasi 2D and thus the number of projections (*i.e.* tomographic views) required for a tomographic reconstruction. Therefore, from a technological and financial point of view, it becomes possible to acquire the complete dataset for a cross-sectional reconstruction in parallel and process it fast enough for real-time imaging. In addition, this 2D imaging configuration has the advantage of attaining high sensitivity, because the size of the detector in elevation can be large and light energy is concentrated on a small volume, thus yielding high signals.

In the current implementation, a custom-made cylindrically focused 64 element-curved transducer array (Imasonic SAS, France) is used, covering a solid angle of 172° around the imaged object. According to the detection criterion presented in section 2.4.6, this arc length allows cross-sectional reconstructions only slightly affected by blurring of boundaries due to the limited view problem. The individual transducer elements are manufactured using piezocomposite technology with central frequency of 4.7 MHz and a reception bandwidth (-6 dB) greater than 90%. To maximize the sensitivity, the individual elements are directly shaped out of the piezocomposite to create a mechanical focus 40 mm in front of the surface of the transducer. The flat dimensions of the individual transducer elements are 15 mm × 1.88 mm (lying on a 40 mm radius spherical surface). The kerf is 0.1 mm. The housing of the transducer is metalized to minimize sensitivity to parasitic electromagnetic radiation. The sensitivity of the transducer was determined to be 9 μVPa^{-1} ± 5% over a 1 – 9 MHz bandwidth. Having a noise level of 33 µV, this translates to a noise equivalent pressure of about 4 Pa. It has to be noted that the current array design is a compromise between imaging performance and cost effectiveness. Image quality can be improved by increasing the detection arc and/or the number of elements, whereas reducing the length of the total detection aperture or number of elements will increase imaging artifacts due to less tomographic views. Within these constraints, the transducer parameters and their geo-metrical arrangement are optimized to achieve the best possibly fit with the dimensions required for mouse imaging.

3.3.3 Imaging chamber and animal positioning

The imaging chamber, of which a photograph is shown in Fig. 3.3, accommodates the fiber bundle arrangement for illumination, the transducer array for signal detection and an animal holder designed for *in vivo* imaging. The chamber is filled with water for optimal signal coupling. A temperature controlled heating unit stabilizes the temperature at 34°C to maintain a constant speed of sound and prevent hypothermia of the animal during anesthesia. The animal holder is a novel design concept that allows placing the animal either in prone or supine position horizontally in the center of the transducer array. A schematic representation of the

animal holder is depicted in Fig. 3.7 (a). It comprises a water-impermeable, optically and acoustically transparent polyethylene membrane that averts animal contact with water while providing a wide tomographic view of approximately 270° for multidirectional illumination and tomographic data detection. The shape of the front and back plate of the holder allows for immersion of the animal deeply in water while keeping a cylindrical shape matching the animal's body contour. With a thickness of about 15 µm, it is thin enough to not interfere with the acoustic waves ($\lambda_{min} \approx 150$ µm) and shows sufficient flexibility to tightly wrap around the mouse under water due to the water pressure. This can be seen in Fig. 3.7 (b) representing a photograph of a mouse, being positioned in the animal holder in supine position and submersed in water. The holder also features a gas anesthesia supply through a port mounted on the side of the holder where the mouse snout latches on. A linear stage (NRT150, Thorlabs) allows linear translation of the animal holder along its long axis (z-axis) over a 150 mm range with a minimal step size of 2 µm for acquisition of whole body data sets.

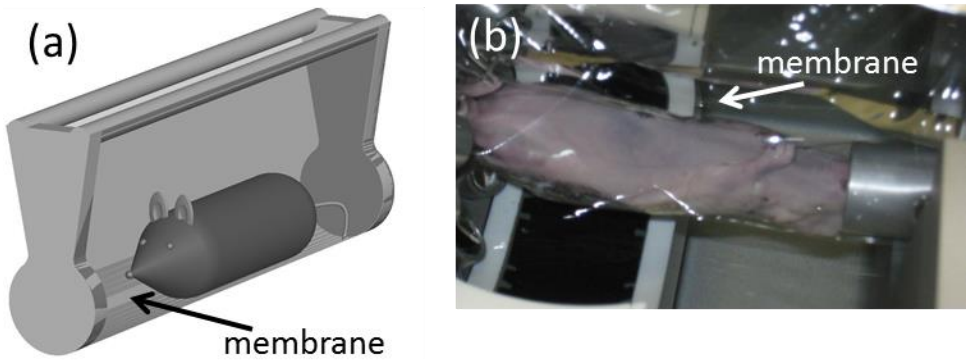

Fig. 3.7: (a) Schematic representation of the animal holder in which a water proof and optically and acoustically transparent membrane is used to avoid direct contact of the animal with water. (b) Photograph of the mouse in the animal holder.

3.3.4 Data acquisition and control unit

Due to the relatively weak photoacoustic signals (cf. section 2.3.3), the parallel data acquisition system should have a low noise floor. The sampling frequency has to be chosen to satisfy the Nyquist sampling theorem. The dynamic range of the system should be set in order to obtain best signal coverage. In the described implement-tation, the signals are digitized at a frequency of 60 megasamples per second, by eight 12 bit multichannel analog-to-digital converters (Model PXI-5105, National Instruments) with an inbuilt anti-aliasing filter, rejecting frequencies above 24 MHz. The number of samples to be recorded for each pulse depends on the desired field of view. For the current 60 megasamples per second acquisition speed, samples are acquired approximately every 16.667 ns, corresponding to ultrasound travel distance of 25 µm in water. In that case, 3000 samples will, for instance, cover a field of view of 7.5 cm, sufficient to see the entire area covered by the ultrasound array. The dynamic range of the acquisition board is set to ± 25 mV, with input impedance set to 1 MΩ to maximize voltage transfer. The acquisition process is synchronized by the Q-switch trigger of the laser, which drives an embedded controller (NI PXI-8106, National Instruments), interfacing to LabVIEW (National Instruments). As a whole,

the acquisition system is capable of acquiring 2D cross-sectional images in less than 1 ms and at a rate of 10 frames per second. Repetition rate is limited by the laser. By translating the mouse through the detector, 3D scans can also be obtained, with each imaging slice acquired in less than 1 ms. The system can offer multi-wavelength scans and if needed, signals can be averaged in order to increase the SNR. The multispectral image acquisition sequence, shown in Fig. 3.8, consists of six steps. First, the animal is translated along the z-axis in order to center the region of interest in the center of the detector. Then, the illumination wavelength and the number of averages are selected and the tissue is illuminated correspondingly. In the next step, the optoacoustic signals are acquired in a time-resolved manner using the 64 different detector channels. This process is triggered by the Q-switch of the laser. The collected data are then stored in the PC memory, reconstructed by the backprojection algorithm for online visualization and displayed as cross-sectional 2D images. After the sequence is completed, the system can be programmed to either select another wavelength or to change z-position, after which the sequence starts again. For multispectral data sets, the animal typically remains in the same imaging plane during acquisition of the selected wavelengths, before moving to the next position. In the single wavelength imaging mode, the animal holder can also be translated with constant speed without stopping while continuously illuminating and acquiring data. Using this method, data from large volumes can be acquired fast.

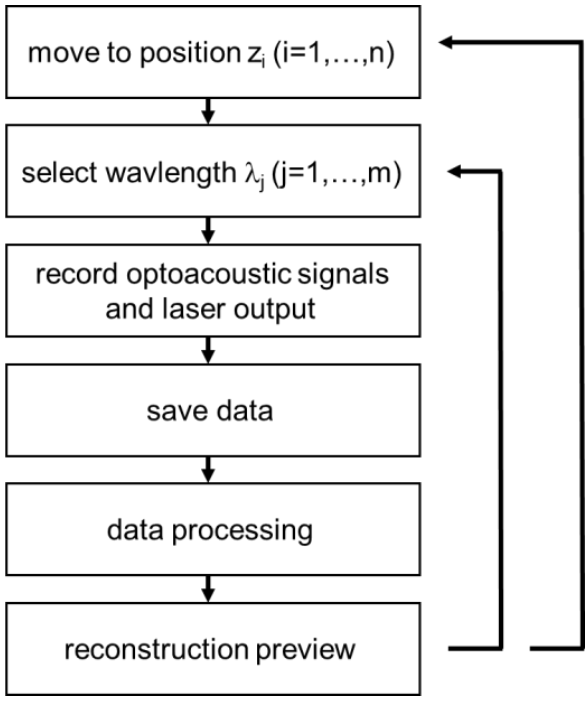

Fig. 3.8: Flow chart of the multispectral imaging loop. For each position of the translation stage, cross-sectional optoacoustic data is acquired at several wavelengths. Afterwards, the stage moves to the next position. (Figure published in [92], Copyright 2011, Nature publishing group).

3.4 Performance characterization

A combination of experimental measurements has been performed to systematically characterize the performance of the components. Parameters of interest include homogeneity of the illumination plane, electrical frequency response of the detection system, directivity and sensitivity of the transducers and the signal-to-noise characteristic of the system.

3.4.1 Tissue mimicking phantoms

In this work, tissue-mimicking agar phantoms are used to test the performance of the system or developed algorithms with defined datasets. Agar phantoms can be produced in various shapes. Their production is straightforward and fast and they are stable for several weeks if stored at 4°C. They are made of a 1.5% (w/v) agar (Sigma-Aldrich, St. Louis, MO) solution which heated up to the boiling point solidifies after cooling down. The acoustic properties of the solidified agar are comparable to these of water [93]. Scattering properties (μ_s' = 10 cm^{-1}) are achieved my adding 6% (v/v) of Intralipid-20% (Sigma-Aldrich, St. Louis, MO) to the agar solution before it solidifies [57]. Additional dyes like black India ink (Higgins, Sanford Bellwood, IL) can be added to the solution to attain defined optical absorption properties. Fig. 3.9 shows a photograph of a representative tissue mimicking agar phantom with two cylindrical insertions.

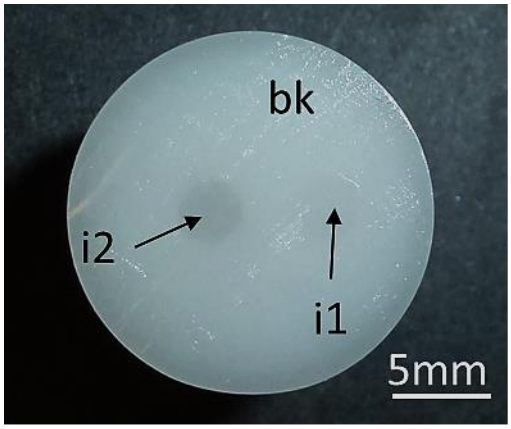

Fig. 3.9: Photography of a tissue mimicking phantom with two cylindrical insertions. The absorption coefficient for the background and the two insertions is μ_a = 0.2, 0.4 and 0.6 cm^{-1}, respectively. Scattering is μ_s' = 10 cm^{-1} everywhere.

3.4.2 Illumination homogeneity

The system uses a fiber bundle partitioned into 10 arms to create a ring shape illumination pattern of 8 mm width at the surface of the sample. To experimentally validate the achieved illumination homogeneity inside an object, a tissue-mimicking cylindrical agar phantom with a reduced scattering coefficient of μ_s' = 10 cm^{-1}, an absorption coefficient of μ_a = 0.6 cm^{-1} and a diameter of 1.9 cm was imaged at a wavelength of 740 nm. Image reconstruction was done with the 2D IMMI method using the PLSQR algorithm (cf. section 4.4.2). From the experimental measurements shown in Fig. 3.10 (a), we see minimal illumination inhomogeneities at the surface of

the sample which homogenize inside the object due to optical scattering. The slight illumination inhomogeneities are due to the quality of the laser beam, which makes a uniform coupling of light into the ten arms of the fiber bundle difficult. To reduce the sensitivity to coupling, we used a fiber bundle has a pseudo-randomized structure shown in Fig. 3.10 (b). A completely randomized fiber distribution in the bundle would further reduce illumination inhomogeneities. In section 2.4.8 it was discussed that from an image reconstruction and quantification point of view, it is better to do thin slice illumination because less out-of-plane absorbers contribute to the photoacoustic signal. Herein, the width of the illumination ring was chosen to be 8 mm, for the reason that the width of the transducer required illuminating at an angle (see Fig. 3.6). This is problematic when the diameter of the mouse changes because then the illumination ring will shift with respect to the detection plane of the transducer array. A wider illumination ring reduces the sensitivity to this effect. Future system implementation should therefore focus on reducing the width of the transducer array to achieve a possible steep illumination angle and thus enable a thinner illumination ring.

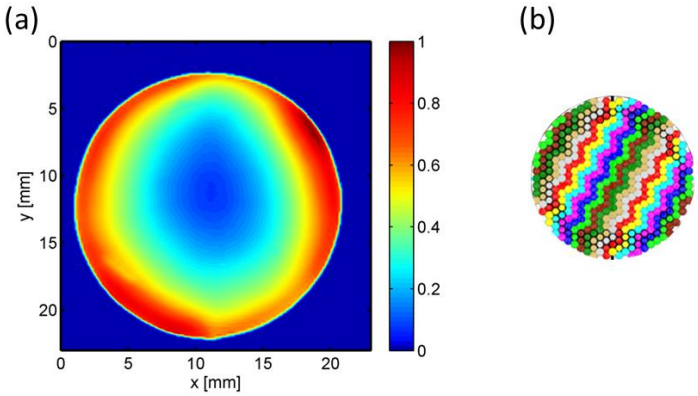

Fig. 3.10: (a) Illumination homogeneity visualized by imaging an absorbing and scattering agar phantom with a 1.9 cm diameter. (b) Pseudo-randomized fiber bundle. Each color represents a different arm.

3.4.3 Electrical impulse response

In section 2.3.3 we have seen that the electrical impulse response (EIR) of the detection system influences the shape of the optoacoustic signals and therefore may lead to artifacts in the reconstructions. The EIR was characterized in order to be able to compensate for the influence it has on image quality.

Method

To measure the EIR of the system we followed the approach presented by Rosenthal *et al.* [53]. It consists of generating an wideband optoacoustic signal in the focal point of the transducer, which can be achieved either by illuminating a point-like absorber with dimensions much smaller than the achievable resolution of the optoacoustic system or by focusing the laser beam to a small spot on a highly absorbing black agar slap. The pressure wave $p_d(\boldsymbol{r_d}, \boldsymbol{r}, t)$ from a point source located at $\boldsymbol{r}$ and detected with a transducer at position $\boldsymbol{r_d}$ is given by

$$p_d(\boldsymbol{r_d}, \boldsymbol{r}, t) = p(\boldsymbol{r_d}, \boldsymbol{r}, t) * \mathrm{TIR}(\boldsymbol{r_d}, \boldsymbol{r}, t) = p(\boldsymbol{r_d}, \boldsymbol{r}, t) * \mathrm{EIR}(t) * \mathrm{SIR}(\boldsymbol{r_d}, \boldsymbol{r}, t) \quad (3.1)$$

where $*$ denotes the temporal convolution operator, $\mathrm{TIR}(\boldsymbol{r_d}, \boldsymbol{r}, t)$ the total impulse response, $\mathrm{SIR}(\boldsymbol{r_d}, \boldsymbol{r}, t)$ the spatial impulse response and $\mathrm{EIR}(t)$ the electrical impulse response of the system. If the source is located at the focal point, each point of the detector surface is excited simultaneously, *i.e.* $\mathrm{SIR}(\boldsymbol{r_d}, \boldsymbol{r}, t) = \delta(t)$. Moreover, the optoacoustic signal from a point source is proportional to the derivative of a delta function $p(\boldsymbol{r_0}, t) \sim \partial\delta(t)/\partial t$ as seen by substituting $H_r(\boldsymbol{r}) = \delta(\boldsymbol{r})$ in the optoacoustic forward solution Eq. (2.16). It then directly follows from Eq. (3.1) that

$$p_d(\boldsymbol{r_0}, t) = \frac{\partial\delta(t)}{\partial t} * \mathrm{EIR}(t) = \delta(t) * \frac{\partial \mathrm{EIR}(t)}{\partial t} = \frac{\partial \mathrm{EIR}(t)}{\partial t}. \tag{3.2}$$

Hence, the measured photoacoustic signal from an optoacoustic point-source corresponds to the derivative of the electrical impulse response of the measurement system. To retrieve the electrical impulse response, the measured optoacoustic signal has to be integrated over time so that:

$$\mathrm{EIR}(t) = \int_0^t p_d(\boldsymbol{r_0}, t')dt'. \tag{3.3}$$

A 50 µm black polyethylene microsphere (Cospheric LLC, Santa Barbara, California) embedded in a scattering agar phantom was used as a source to generate the optoacoustic signals. The microsphere was black, which ensures high absorption and thus a strong optoacoustic signal. In order to avoid reflections, due to strong impedance mismatches, the phantom was made of agar with matching acoustic properties to water and had scattering properties to achieve homogeneous the illumination. The microsphere was positioned in the center of rotation of the transducer array so that it had the same distance from each transducer element. This enabled the simultaneous measurement of the electrical impulse response of all elements. The signals were averaged over 1000 laser pulses to increase the SNR.

Results

Fig. 3.11 (a) depicts the simulated signal of a 50 µm microsphere and (b) its frequency spectrum obtained from the fast Fourier transform. Panel (c) depicts the signal after integration and (d) the corresponding frequency spectrum being constant within a standard deviation of 3% for frequencies up to 10 MHz. Hence for determining the EIR the microsphere is considered small enough. Panel (e) shows the mean electrical impulse response (EIR) of the system obtained by averaging the impulse responses from the 64 different transducer elements and (f) the corresponding amplitude spectrum of the electrical frequency response (EFR). The error bars describe the standard deviation between the 64 channels. The array has a central frequency of 4.7 MHz and a -6 dB reception bandwidth between 2.1 and 6.9 MHz, which translates into a fractional bandwidth of 97%. The -3 dB cutoff frequency is at 7.8 MHz. The variation of frequency response between the individual elements is about 3% increasing to 6% towards the low frequencies.

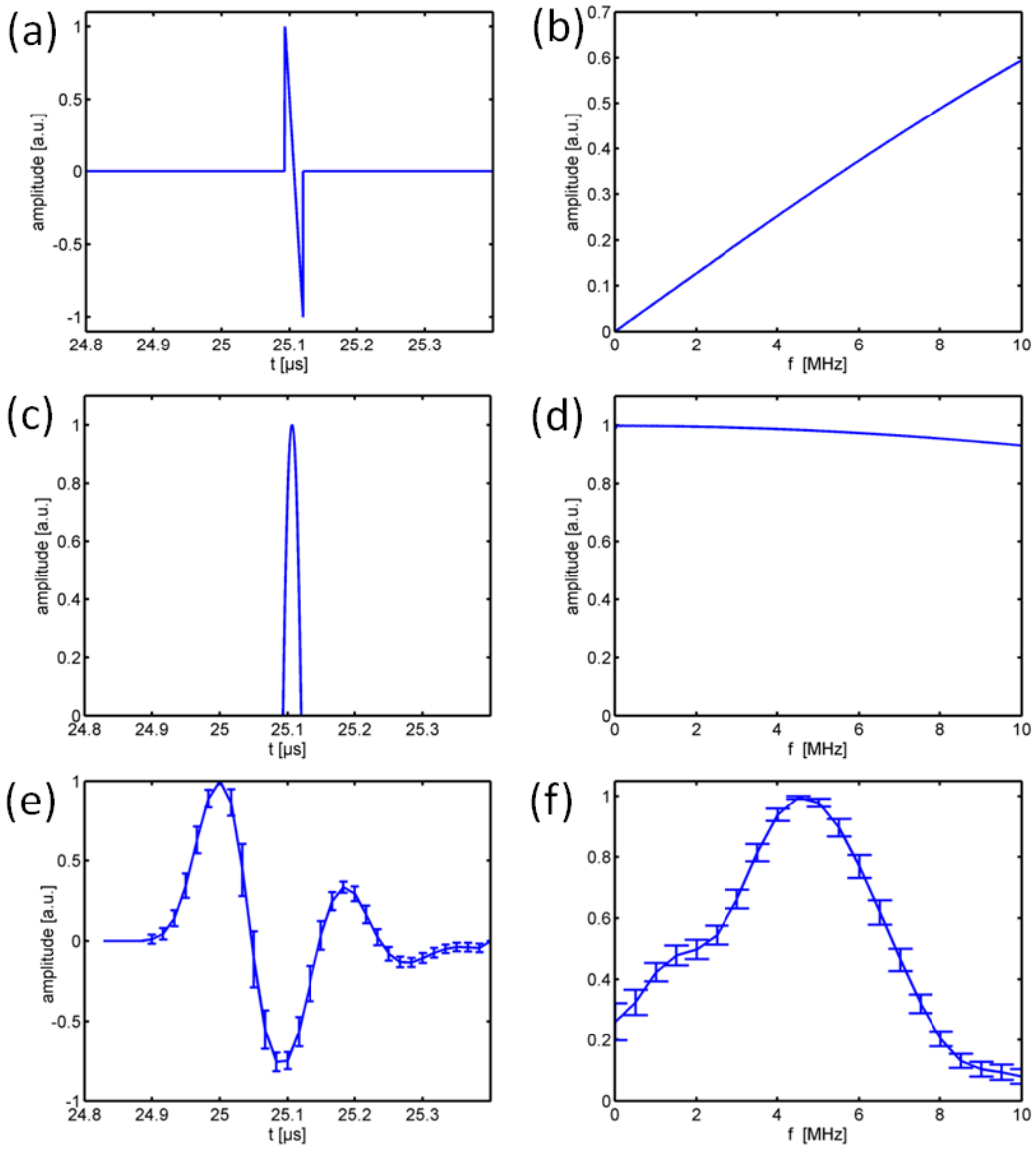

Fig. 3.11: (a) Simulated signal of a 50 µm big spherical absorber and (b) its amplitude spectrum. (c) Simulated signal after integration and (d) corresponding amplitude spectrum. (e) Experimentally determined electrical impulse response of the detection system and (f) corresponding amplitude spectrum of the electrical frequency response.

Discussion

The retrieved values are in good correspondence with the specifications of the manufacturer (f_c = 5 MHz, B_W = 55%). Differences between the individual elements are due to fabrication inaccuracies as characterized by the manufacturer. The inter-element differences are higher in the low frequency range because low frequency noise is amplified by the integration. Low frequency components in the signal are actually more prone to errors because they are weaker for small sources as seen in Fig. 3.11 (b). The difference in bandwidth stems from the pulse-echo method utilized by the manufacturer. As explained by Araque Caballero in [41], the spectral bandwidth determined by the pulse-echo method is the convolution of the send and receive spectra, which are the same, *i.e.* $\mathrm{EIR}_{p-e} = \mathrm{EIR} * \mathrm{EIR} = \mathrm{EFR}^2$. The convolution of EIR with itself, effectively squares the frequency of the transducer. On the other hand, the method employed herein considers only the receive spectrum, thus the difference in the measured optoacoustic bandwidth and the one determined by

the manufacturer. This also shows the importance of determining the EIR in receive mode when it is to be used to correct signal distortions in optoacoustic imaging scenarios. A method to accomplish this is presented in section 4.2. From the measured electrical frequency response it is possible to determine the maximal achievable resolution of the system. Solving equation (2.36) for the -3 dB cutoff frequency yields for the bandwidth limited resolution $R_{bw} \approx 0.8\, v_s/f_{co}$ = 154 µm.

3.4.4 Sensitivity distribution of the system[5]

Having characterized the electrical properties of the transducer array, we also determined its spatial properties, *i.e.* its sensitivity distribution, which is necessary to understand what area the transducer actually covers.

Method

The total impulse response (TIR) was measured by scanning the imaging area of the transducer with a sub-resolution point absorber (cf. section 2.3.4). According to Eq. (3.1), this yields signals in the form $\mathrm{TIR}(\boldsymbol{r}, t)/\partial t$, from which the TIR can be obtained by integration over time.

To allow for scanning of the transducer, the measurement was done outside the imaging chamber; all other components were in place as described above. A black polyethylene microsphere (Cospheric LLC, Santa Barbara, California) with a diameter of 50 µm was used as the optoacoustic source. In order to achieve uniform illumination, the microsphere was embedded in a light-scattering cylindrical agar phantom, 5 mm in diameter. The phantom was illuminated with a laser beam of about 3 mm in diameter, perpendicular to the scanning direction. The source can be thus considered a point-like emitter of isotropic, broadband optoacoustic signals. First, the transducer array was scanned in the xy-plane within a region of 40 mm by 40 mm, centered in its mechanical center of rotation. The step size was 800 µm in both directions, resulting in a square grid of 51 pixels on each side. Then, the transducer was scanned within its yz-plane in a 10 mm by 40 mm region, with a step size of 100 µm in z-direction and 800 µm in y-direction. In both cases, the microsphere and its illumination were left static and at each scanning position the signals were averaged for 50 laser pulses. After integration of the measured signals over time, the signals were bandpass-filtered between 500 kHz and 8 MHz in order to reduce low frequency noise introduced by the integration. The sensitivity field was calculated by plotting the amplitude of the measured signals versus its spatial coordinates. Furthermore, the amplitude map was smoothed with a 5 x 5 median filter to reduce intensity variations between neighboring pixels due to slight fluctuations of the laser energy during the measurement.

For comparison, the amplitude maps were also numerically simulated. This was done with the software package Field II [56, 94]. The program calculates the spatial impulse response (SIR) of an arbitrary shaped transducer by dividing the surface of the transducer into small sub-apertures and solving Eq. (2.28). In order to yield the

[5] The measurement was done in cooperation with Miguel Angel Araque Caballero who reused the data for his work on optoacoustic imaging with full knowledge of sensor properties [41] .

TIR, each calculated spatial impulse response was convolved with the electrical impulse response (EIR) of the system, determined as described before. Then, the simulated TIR was processed in analogy to the experimental one and used to plot an amplitude map.

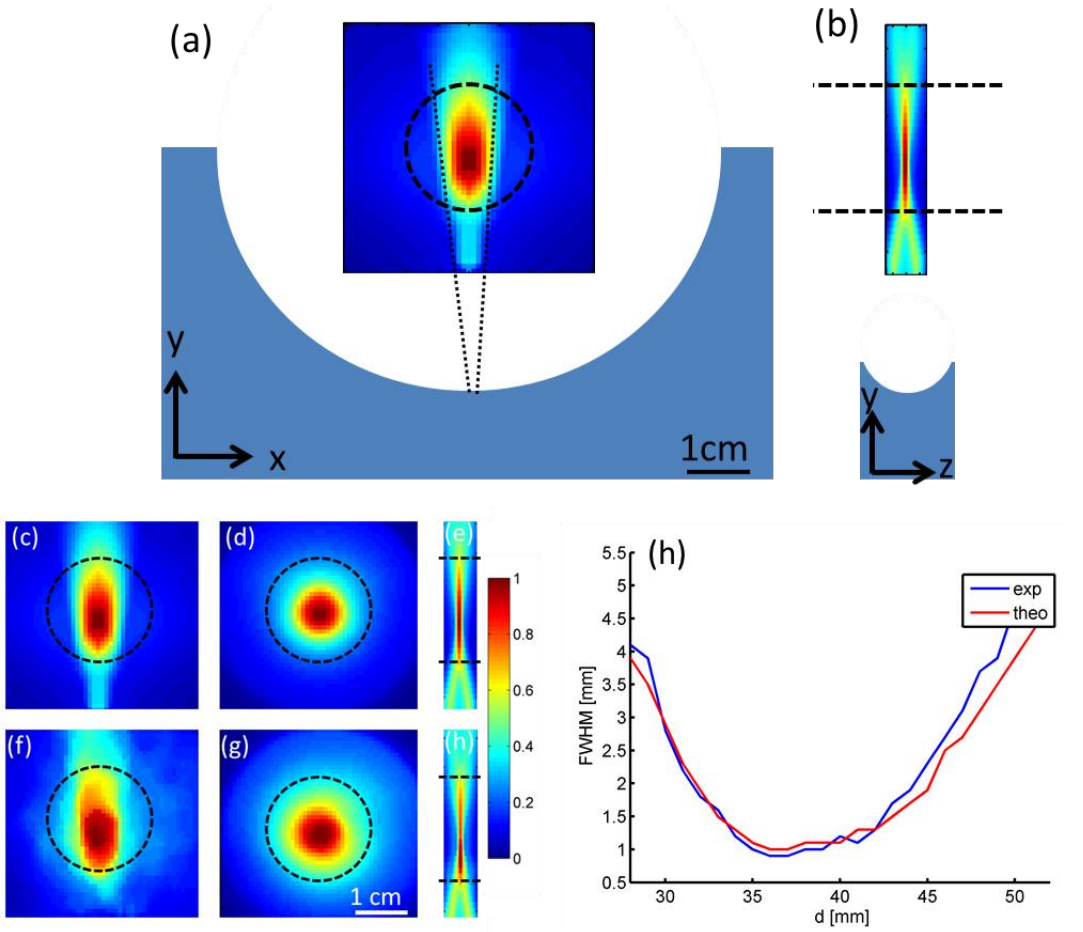

Fig. 3.12: Sensitivity distribution of the system. (a) Section through the sensitivity field of the 32nd transducer element within the imaging plane (xy-plane), with the transducer array as reference. (b) Section through the same sensitivity field along the xz-plane with the element as reference. (c) Simulated sensitivity field of a single element within the imaging plane. (d) Combined sensitivity distribution of all elements within the imaging plane. (e) Sagittal section (yz-plane) through the sensitivity field. (f) to (h) Corresponding sections through the measured sensitivity fields. (h) FWHM of the sagittal section as a function of the distance from the transducer. The dashed line depicts the position of the mouse with an assumed diameter of 2 cm.

Results

Fig. 3.12 shows a section of the amplitude map of the 32nd element within the imaging plane (xy-plane) and (b) the corresponding section through the yz-plane. The transducer array is also depicted for reference. Panel (c) depicts the simulated single element sensitivity field and (d) the combined sensitivity field of all elements within the xy-plane. Panel (e) depicts the section through the simulated sensitivity field within the yz-plane. The experimentally measured sensitivity fields are depicted in corresponding order in panels (f) to (j). Panel (h) displays the FWHM of the sagittal section as a function of the distance from the transducer. The position of the mouse (2 cm in diameter) is represented with dashed lines. Simulated and experimental sensitivity fields show high congruence. The focal zone of each transducer element,

characterized by the -6 dB zone (*i.e.* the area in which the sensitivity drops to half its maximum value), is approximately 1.6 cm long along the acoustic axis of the transducer and 1 cm broad perpendicular to it. The first is referred to as the depth of the sensitivity field and the latter as the width. Its thickness, *i.e.* dimension along the z-axis, is approximately 1 mm. All transducers together form a circular shaped imaging window with a diameter of about 1.6 cm. The total sensitivity of the system increases towards the center of the transducer array.

Discussion

Slight discrepancies between the simulations and experimental measurements presented herein are due to illumination fluctuations as well as the sensitivity of the integration of the experimental signals to low frequency noise.

The -6 dB sensitivity field of single transducer element spans an area of 1.6 cm x 1 cm x 0.1 cm, thus does not cover the whole cross section of the mouse. As a result some voxels are seen with a high sensitivity from fewer angles than others resulting in limited views on the borders of the sample. This is due to the shape of the detection elements. The width of the sensitivity field is determined by the width of the transducer element (here 1.88 mm) and it can be increased by reducing the width of the element. As determined in an additional simulation study following the numerical approach presented herein, the width of the detection element has to be reduced to at least 0.85 mm to fully cover the 2 cm big area for a frequency range up to 8 MHz Actually, reducing the width of the element has an additional benefit; by using smaller elements it is possible to fit more elements within the array. This improves the angular sampling of the acoustic field and finally the lateral resolution (cf. section 2.4.7).

Depth and thickness of the sensitivity field depend on the focusing properties of the transducer. As mentioned in section 2.4.1, they are inversely related, *i.e.* reducing the thickness of the sensitivity field to improve the elevation resolution (in z-direction), results in a shorter depth of field and vice versa. In that sense, we are limited to a compromise between elevational resolution and depth of field, especially in limited view detection geometries like the one presented here. The situation changes for full view (360°) detection. Due to the redundancy of information, it is sufficient that each transducer covers only the proximal half of the mouse's cross section. Thus, shorter depths of fields are possible and focusing is increased. Yet, when such an toroid focusing approach is applied, half-time image reconstruction [95] is necessary. In this case, only the part of the signal which corresponds to the area of high focusing is used.

3.4.5 Signal-to-noise ratio characteristics

Optoacoustic signals are weak and generally affected by noise, which can be due to several instrumentation related factors such as system's thermal noise, insufficient electrical and acoustical shielding or electrical and acoustical impedance mismatches. The ability to improve SNR in the system by means of signal averaging and per pulse laser energy was analyzed. For that a 300 µm in diameter big

transparent plastic tube was filled with rabbit blood, embedded in a scattering agar phantom and imaged with the system. The SNR was calculated from the resulting image according to $\mathrm{SNR} = \mu/\sigma$ where μ stands for mean signal intensity of the blood insertion and σ the standard deviation of the background signal.

Fig. 3.13 (a) depicts the SNR as a function of the number of averages (45 mJ/pulse) and (b) as a function of the laser energy (single pulse). The SNR increases linearly with the laser energy and until 130 averages as the square root of the number of averages. Above 130 averages there is no improvement of the SNR.

The measurements show the importance of an optimized light delivery because SNR scales linearly with the light energy whereas it only increases as the square root of the number of averages. The inability to further increase SNR by averaging above 130 averages show that beside stochastic electronic noise, which can be averaged out, there is an additional noise source of deterministic nature. An improved shielding of the transducer and cabling in further implementations may reduce this effect.

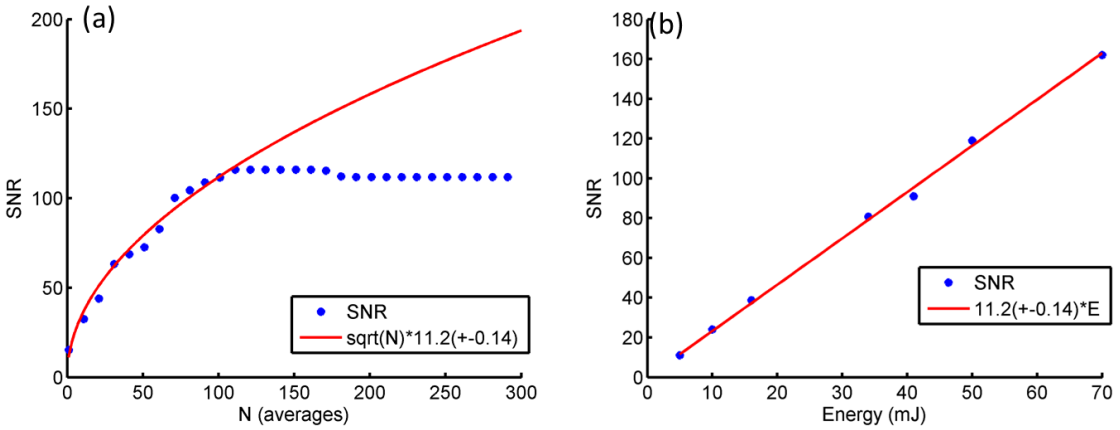

Fig. 3.13: SNR as a function of the number of averages (a) and the laser energy (b).

3.4.6 Spatial resolution

In the small animal scanner one has to distinguish between cross-sectional resolution (within the xy-plane) and slice thickness (in z-direction), herein also termed elevational resolution. The first is due to tomographic image formation and depends on the reconstruction algorithm, the latter due to the focusing properties of the transducer.

3.4.6.1 Cross-sectional resolution

To determine the cross-sectional resolution of the system experimentally, measurements of the system's point spread function (PSF) were made and compared to numerical simulations and the analytical formula presented in section 2.4.3.1. Four micrcospheres (Cospheric Inc., Santa Barbara, CA), each with a diameter of 100 µm and embedded in a light scattering agar cylinder, were imaged

in the system. The imaging wavelength was 740 nm. No signal averaging was performed. The experimental signals were deconvolved with the electrical impulse response (cf. section 4.2). For comparison, optoacoustic signals from absorbers with a diameter of 100 µm were simulated by summing up theoretical signals from spherical absorbers over the transducer surface according to Eq. (2.17). The speed of sound in water was c = 1506 ms^{-1}, corresponding to the one used for the experimental setup. Experimental and simulated signals were bandpass-filtered between 0.05 and 8 MHz. Reconstructions were done with the 2D IMMI method and inversion with the PLSQR algorithm (cf. section 4.4.2). The dimension of the PSF was estimated from the full width at half maximum (FWHM) of the Gaussian fit through the profiles. The resolution R was then obtained by deconvolving the finite size d of the object from the FWHM of the fit according to [96]

$$R = \sqrt{FWHM^2 - d^2} \tag{3.4}$$

Results

Fig. 3.14 (a) depicts the reconstruction of the four microspheres positioned in the imaging plane. The profile through the reconstruction of the central microsphere along the x-axis is shown in (b). The reconstruction of the simulated data is shown in (c) and the resolution of the system, as obtained from the experimental measurements, the simulation and theoretical formula, see Eqs. (2.39) and (2.42). This is given in (d) as a function of the radial position. The PSF of the system is spatially variant. It elongates in lateral direction (*i.e.* perpendicular to the acoustic axis of the transducer), when moved along radial lines away from the center of rotation of the transducer array, ranging from 150 µm in the center to about 550 µm at 1 cm distance. The dimension of the PSF in axial direction remains constant at about 150 µm. Theoretical formula, simulation and experimental measurements are in good agreement. Slight differences are due to the limited view problem and sparse angular sampling.

Discussion

It has to be noted, that using the 2D IMMI method it is theoretically possible to incorporate the spatial impulse response of the detector into the inversion procedure, like proposed by Rosenthal *et al.* [55]. This would correct for the lateral resolution loss due to the finite size of the detection element. This approach was tested, but it was found that, for the presented geometry, due to the sparse angular sampling and the limited view detection, the reconstruction problem is too ill-conditioned, and thus sensitive to data inconsistencies. On the other hand, for fine enough angular sampling (about 3 times per width of the detection element) and detection arcs larger than 180°, the method achieved homogenous cross-sectional resolution. The better approach is however a reduction of the width of the detection element as shown in Fig. 3.14 (d). At 300 µm width, the lateral resolution is 160 µm and thus about uniform within the 2 cm big area relevant for mouse imaging.

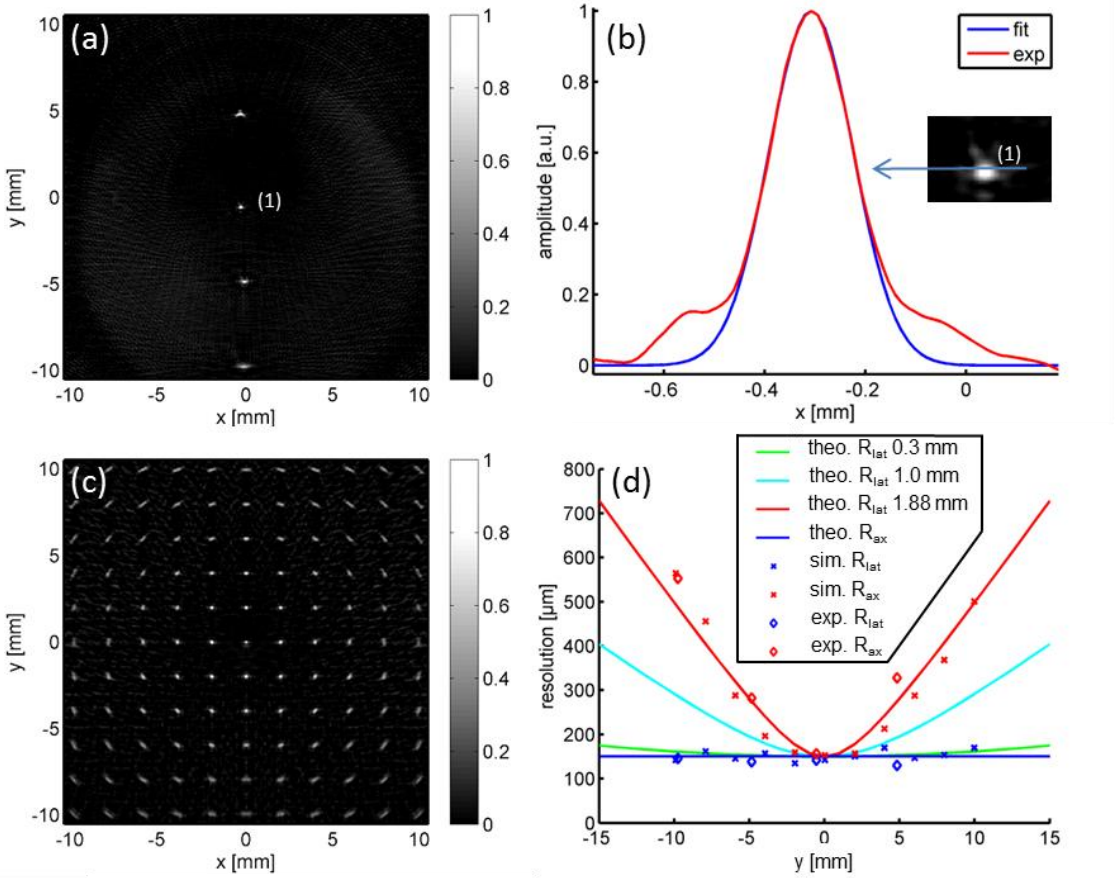

Fig. 3.14: (a) Point spread functions of four 100 µm in diameter big microspheres positioned in the imaging plane of the transducer. (b) Profile through the point spread function labeled (1) and the Gaussian fit. (c) Simulated point spread functions of 100 µm in diameter big spherical absorbers. (d) FWHM of the point spread functions according to experiment, simulation and theoretical formula (*W* = 0.3, 1 and 1.88 mm, respectively) presented in section 2.4.3.1.

3.4.6.2 Elevational resolution

The system uses focusing to reduce the system's sensitivity to a disc-shaped plane around the center of rotation of the transducer array. Since the focusing capacity depends on the frequency content of the optoacoustic signal, the ability to eliminate out-of-plane signals is also frequency dependent. To characterize the elevational resolution in the system the combined sensitivity field of the system for different frequencies (1, 2, 3, 5 and 7 MHz, respectively) was calculated using the ultrasound simulation package Field II [56, 94] as described in section 3.3.4. The FWHM of the combined sensitivity field in z-direction was taken as a measure of the slice thickness.

Results

Fig. 3.15 (a) depicts a slice through the combined sensitivity field of the system along the yz-plane for the different frequencies and (b) the transducer array for reference. The slice thickness of the system clearly varies with the frequency content of the signal. The higher the frequency, the better the focusing and elimination of out-of-plane signals. At 7 MHz the width of the combined sensitivity field is about 800 µm over a distance of approximately 8 mm. For lower frequencies, the width of the sensitivity field increases rapidly and is about 5 mm at 1 MHz.

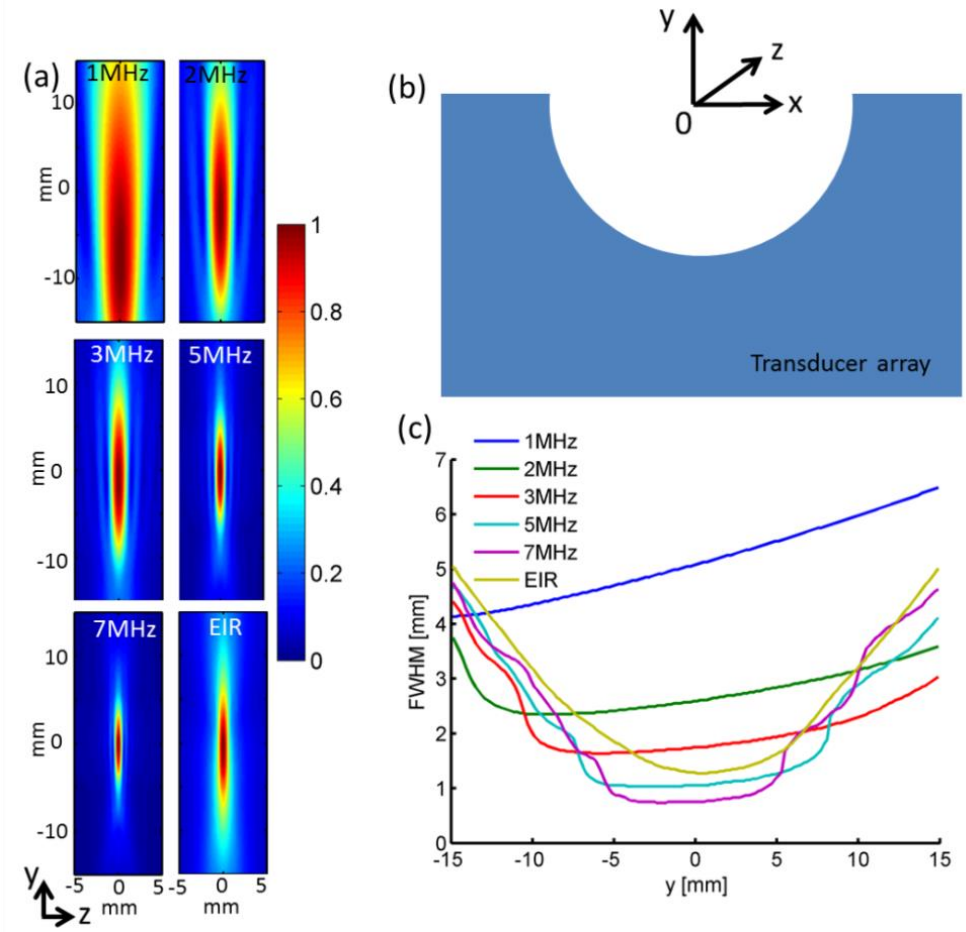

Fig. 3.15: (a) Section across the combined sensitivity field in the yz-plane through the center of the transducer array for different frequencies. The label EIR indicates the sensitivity field for all the frequencies allowed by the electrical impulse response of the detector. (b) A cartoon of the transducer array with reference. (c) FWHM of the combined sensitivity field for different frequencies and positions along the y-axis.

Discussion

The results described above indicate that small absorbers, located outside the imaging plane, have little influence on the cross-sectional reconstruction, because such emitted signals have shorter wavelengths, for which the focusing ability of the transducer is better. In contrast, a big absorber, located at the same position, affects the cross-sectional reconstruction due to the reduced focusing at longer wavelengths. The frequency dependency of the slice thickness is an inherent limitation of focusing-based image formation; the technique employed in this work to enable real-time imaging. For mesoscopic applications, with only slightly scattering samples (*e.g.* zebra fish, pupa), light sheet illumination can be used to excite optoacoustic signals only in the imaging plane and thus reduce out-of-plane signals. Yet, for deep tissue imaging, light sheet illumination is little effective due to strong light scattering resulting in excitation of a much thicker slice than the irradiated area on the surface. To correct for out-of-plane signals, it is beneficial to do a 3D reconstruction using data from different scanning positions. This will be part of chapter 5 which deals with advanced 3D reconstruction methods.

3.5 Summary and conclusion

This chapter described the development of a 2D real-time small animal imaging system that fulfills the previously unmet need of biomedical research for high frame-rate and practical *in vivo* multispectral whole body imaging capabilities. The novel concept incorporates optimized light energy delivery using cylindrical ring illumination confocal to the detection plane of a multi-element cylindrically focused transducer array and an innovative animal holder design for *in vivo* imaging. The animal holder is comprised of an acoustically and optically matched membrane, which allows placement of the animal in the center of the transducer array, while prohibiting direct contact with the surrounding matching medium utilized for optimally coupling acoustic response from the sample to the detector. The animal holder can be translated in elevation in order to collect a whole body data set. For spectrally resolved imaging, the system further enables multiple wavelength illumination in the near-infrared range.

The characterization of the system's performance showed good congruence with the simulations. The array has a central frequency of 4.7 MHz and a -6 dB reception bandwidth between 2.1 and 6.9 MHz. In that sense, its sensitivity is optimized for detecting structures with a size of 200 µm. The system's sensitivity is concentrated within a ring shaped area with a 1.6 cm diameter around the mechanical center of the transducer array. The in-plane resolution is dependent on the distance from the center of rotation and varies from 150 µm in the center to 550 µm at a distance of 1 cm. The minimally achievable slice thickness determined by the focusing ability of the transducer array at maximal frequency, is 800 µm.

It has to be noted that due to cost considerations, the array is comprised of 64 elements arranged on a 172° arc. Although the detection parameters were optimized within these constraints, this is not the optimal solution for mouse imaging. Because of sparse angular sampling and limited view detection, we face aliasing and blurring effects discussed in sections 2.4.6 and 2.4.7. Reconstruction-based approaches to improve on this are presented in sections 4.3 and 4.4. The best approach is to increase the detection aperture as much as possible (a 270° curvature is feasible with the animal holder concept presented herein), reduce the width of the elements (a width of 300 µm would be technically feasible and yield a lateral resolution of about 160 µm at 1 cm distance) and maximize the amount of detection elements in the array.

Mid 2013 we developed, based on the findings shown herein, an improved version of the small animal scanner with more elements (256), a larger detection arc (270°), a finer element width (0.7 mm) and toroid-focusing. Initial tests with the new system confirm the predictions made with respect to the improved imaging performance. In this work the system was not used and hence left outside further discussion.

4 Signal processing and 2D image reconstruction

4.1 Introduction

This chapter deals with methods required to convert the optoacoustic measurements into best images. Several steps are required for this purpose: First the measured optoacoustic signals have to be freed from the influence of the electrical impulse response. An approach how this can be achieved is presented in section 4.2. Then, especially for the presented system comprising only 64 detection elements, it is necessary to alleviate the aliasing artifacts due to the sparse angular sampling. A new method to achieve this, based on the computation of supplementary views, is presented in section 4.3. After that, 2D model-based image reconstruction in limited view detection scenarios is discussed. In contrast to full view detection scenarios, where IMMI inversions work without regularization [66], limited view reconstructions suffer from artifacts following a distinct pattern. Section 4.4 explains their physical underpinning and presents two regularization approaches to alleviate these artifacts for being able to do model-based reconstructions in limited view detection scenarios.

4.2 Correction for the electrical impulse response

Optoacoustic signals are broadband. Piezoelectric detection devices however have a relatively limited bandwidth and non-uniform frequency characteristics. The detection system acts as a bandpass filter and can distort the optoacoustic signal. Directly using the recorded raw pressure profiles might therefore lead to artifacts and loss of accuracy in the optoacoustic reconstructions [53]. The distortion of the optoacoustic signals is a linear process and is mathematically modeled by a temporal convolution with the electrical impulse response (EIR) of the system (cf. section 2.3.3). How the EIR can be determined experimentally was discussed in section 3.4.3. In this section, it is shown how it can be used to improve the reconstructions.

4.2.1 Method

To reverse the signal distortion due to the detection system, the detected signals have to be deconvolved with the EIR. Theoretically, this can be done in the Fourier domain by division with the electrical frequency response (EFR) which is the Fourier transform of the EIR. Using experimental data this might be problematic. Due to the limited detection bandwidth, noise in the signal can be increased significantly. To avoid the amplification of noise Wiener deconvolution is used herein. In the frequency domain Wiener deconvolution is defined as

$$P(f) = \left[\frac{1}{\mathrm{EFR}(f)} \cdot \frac{|\mathrm{EFR}(f)|^2}{|\mathrm{EFR}(f)|^2 + N}\right] P_d(f) \tag{4.1}$$

where $P(f)$ is the Fourier transform of the deconvolved optoacoustic signal, $P_d(f)$ the Fourier transform of the detected signal, $\mathrm{EFR}(f)$ the frequency response and N the noise floor of the detection system. The noise term in the denominator attenuates the scaling of noise in the data due to low system sensitivity [35]. Alternatively, for IMMI reconstruction it is possible to include the electrical impulse response into the forward model by convolving the individual columns of the matrix with the electrical impulse response like it is done in [66]. This has the advantage that no additional preprocessing of the signals is necessary when the forward matrix is calculated (except from signal filtering). Herein, only the Wiener deconvolution approach is employed. This approach has the advantage that it can be used for both backprojection reconstructions and IMMI inversions. In addition, convolving the forward model with the electrical impulse response reduces its sparseness, thus increases the matrix size and slows down the inversion, which is faster for sparser matrices. More information about IMMI inversions is given in section 4.4.

4.2.2 Performance tests

Test data

A 200 µm big polyethylene microsphere (Cospheric Inc., Santa Barbara, CA) embedded in a 1.9 cm diameter scattering agar cylinder ($\mu_s' = 10\ \mathrm{cm}^{-1}$) and a homogenous scattering and absorbing agar cylinder ($\mu_a = 0.6\ \mathrm{cm}^{-1}$, $\mu_s' = 10\ \mathrm{cm}^{-1}$) with the same dimensions were imaged with the 2D real-time system presented in chapter 3. Reconstructions were done with the backprojection algorithm (cf. section 2.4.2.1) with and without deconvolving the system's EIR from the measured optoacoustic signals.

Results

Fig. 4.1 shows the optoacoustic signal from the microsphere and the cylindrical phantom before and after deconvolution with the electrical impulse response measured as described in section 3.4.3. Before deconvolution the signal from the microsphere does not have the characteristic N shape. The signals from the cylinder show an additional peak. This creates a ring artifact at the surface of the cylinder (e) which might be misinterpreted as part of the object. The ring artifact disappears after deconvolution with the measured impulse response of the system. The streaks in the background are aliasing artifacts due to an insufficient angular sampling and limited view detection. A method to reduce aliasing artifacts is presented in section 4.3.

4.2.3 Conclusion

In order to avoid artifacts in the optoacoustic reconstructions the measured optoacoustic signals have to be corrected for the influence of the system's electrical impulse response. One possibility to achieve this is Wiener deconvolution. In all following paragraphs experimental signals are corrected for distortion due to the EIR.

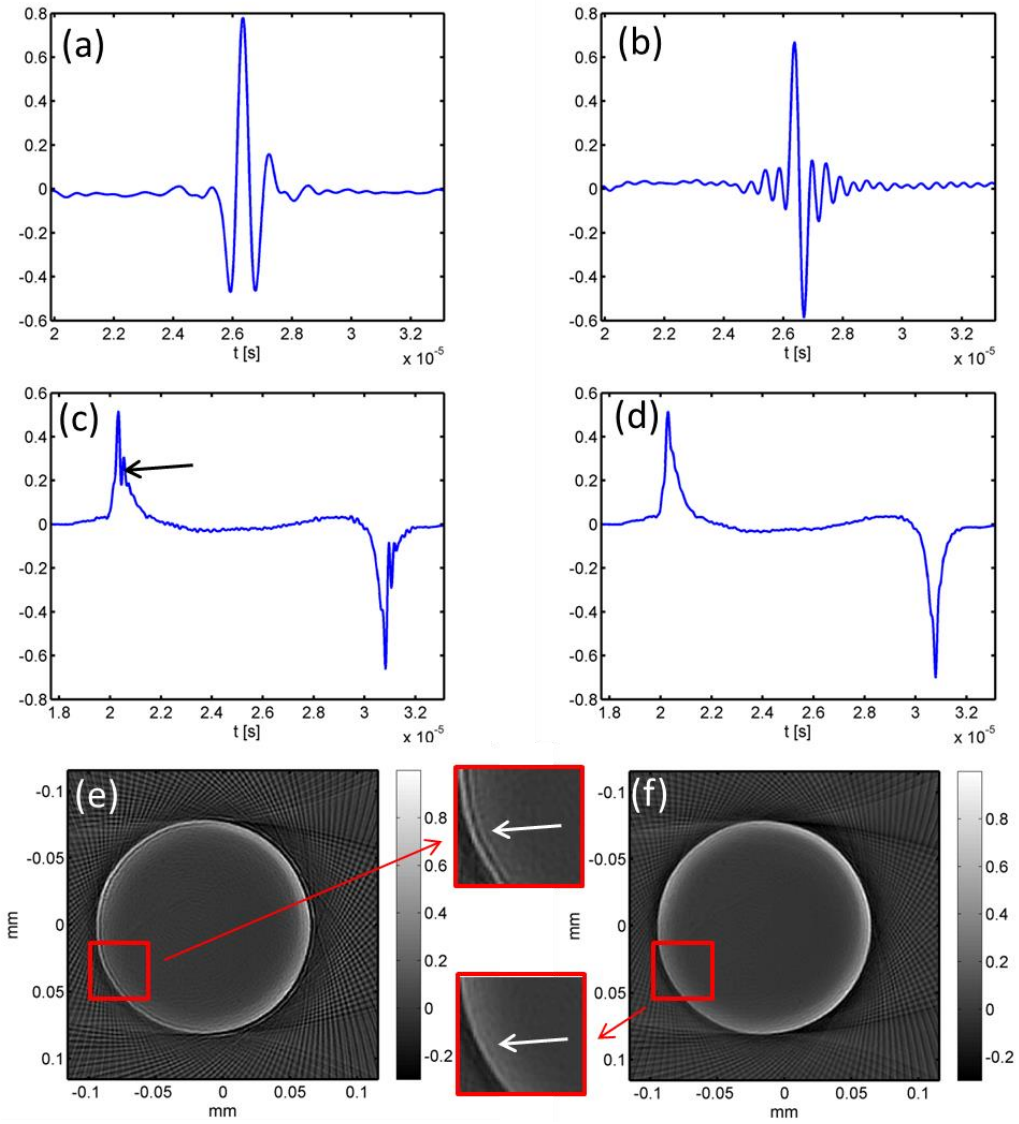

Fig. 4.1: Effects of the electrical impulse response (EIR). A recorded signal of a 200 µm big microsphere is shown in (a). Due to the EIR of the detection system, the signal does not show the typical N shape profile characteristic for spherical sources. (b) Signal after Wiener's deconvolution with the EIR. (c) Signal from a scattering and absorbing agar cylinder before correction showing an additional peak. (d) Signal after deconvolution not showing this peak. (e) Reconstruction of the cylinder without correction showing an erroneous ring surrounding the object. (f) Reconstruction with the corrected signals not showing this ring artifact.

4.3 Data interpolation to reduce aliasing artifacts

In optoacoustic tomography the acoustic field emitted from the object under investigation is measured in form of temporal signals along a detection surface or when using cylindrically focused transducers along a detection circle. In order to be able to reconstruct the object accurately, the acoustic field has to be sampled with at least twice the frequency of the detected optoacoustic signal. In many opto-acoustic imaging systems (*e.g.* the system presented in chapter 3) only an insufficient amount of angular views (tomographic projections) can be acquired. As a consequence the reconstructions show aliasing artifacts significantly reducing the image quality. It has been shown in [72] that in order to avoid these artifacts the

spatial sampling period has to smaller than half the size of the detection element, *i.e.* $r_0\Delta\varphi_0 < \delta/2$, where $\Delta\varphi_0$ is the angular sampling period, r_0 the radius of the detection circle and δ the size of the detection element. That is, depending on a size of the detection aperture a minimal amount of tomographic views N_{min} is needed to achieve aliasing artifact free reconstructions. Herein, in order to alleviate the aliasing artifacts, the use of artificial views is proposed, *i.e.* additional projections obtained by angular interpolation between measured projections. Next the method is introduced and tested on simulated and experimental data.

4.3.1 **Method**

The basic idea of the method is to supplement the measured projections by others obtained using linear interpolation in angle. The approach is heuristically motivated by a need of a minimal amount of tomographic views N_{min} to form an aliasing artifact free image and its successful use in X-ray computed tomography [97]. The method can be understood intuitively by considering the backprojection algorithm, although its use is not limited to the backprojection algorithm. When using the backprojection algorithm images are formed by backprojecting the optoacoustic signals measured at various tomographic detection positions onto spherical shells (or circles in 2D) and summing up the individual contributions, *i.e.*

$$H_r(\boldsymbol{r}) = \frac{\sum_{i=1}^{N} \Delta\Omega_i(\boldsymbol{r}, \boldsymbol{d_i}) \times b(\boldsymbol{d_i}, \bar{t} = |\boldsymbol{d_i} - \boldsymbol{r}|)}{\sum_{i=1}^{N} \Delta\Omega_i} \tag{4.2}$$

where $b(\boldsymbol{d_i}, \bar{t})$ is the backprojected quantity being computed from the measured pressure $p(\boldsymbol{d_i}, \bar{t})$, $\boldsymbol{d_i}$ the i^{th} detector position, $\Delta\Omega_i(\boldsymbol{r}, \boldsymbol{d_i})$ the solid angle element under which the detector is seen and $H_r(\boldsymbol{r})$ the reconstructed absorption distribution. If the detection arc is closed and detection positions are sufficiently densely spaced, the arcs originating from the individual backprojected signals will compensate each other due to the complementary information from different detection positions, yielding an image of the actual source distribution. If the angular sampling of the acoustic field is too sparse (*i.e.* $N < N_{min}$), this compensating effect is missing and partial streaks remain. Thus, by its very nature, the performance of the backprojection algorithm improves with the number of projections available and thus the idea to supplement the available data by artificial views. To obtain intermediate views we propose linear interpolation in angle between the measured views, *i.e.*

$$p(t, \varphi) = p(t, \varphi_i) + \frac{p(t, \varphi_{i+1}) - p(t, \varphi_i)}{\varphi_{i+1} - \varphi_i}(\varphi - \varphi_i) \tag{4.3}$$

where $p(t, \varphi)$ is the interpolated pressure signal for the viewing angle φ between the two real and neighboring detection positions φ_{i+1} and φ_i (*i.e.* $\varphi\epsilon[\varphi_i, \varphi_{i+1}]$). Higher order interpolation was also tested but without significant improvements.

4.3.2 Method evaluation on simulated and experimental data

Numerical simulations

Optoacoustic signals from a complex phantom were simulated using the k-wave optoacoustic simulation toolbox [98] for a 2D circular detection geometry with a radius of 4 cm and densely spaced point detectors. The simulation grid had a size of 802 x 802 x 5 voxels and each voxel a size of 100 x 100 x 100 µm³. A finite size detection element with a detection aperture of $\delta = 1$ mm was assumed by averaging the simulated point detector signals over the detection surface. Images were reconstructed with the 2D IMMI algorithm (cf. 2.4.2.2) using 720 (180 and 90) tomographic projections uniformly distributed on the 360° detection arc. Artificial projections were calculated by linear interpolation in angle to obtain a total of 720 projections. The results were compared to the reconstruction without aliasing (*i.e.* the one with 720 projections) by calculating the root-mean-square-deviation (RMSD).

Experimental data

The method was also tested experimentally on two phantoms using the optoacoustic small animal scanner developed herein. The first phantom consisted of several 200 µm diameter microspheres (Cospheric Inc., Santa Barbara, CA) embedded in a scattering agar phantom. A photograph of the microsphere distribution can be seen in Fig. 4.4 (a). A second phantom was created by printing a complex pattern onto a sheet of paper which was then inserted into a scattering agar phantom. A photograph of the phantom is shown in Fig. 4.4 (d) before it was completely filled with scattering agar. The 2D phantom contains a vessel similar structure and various round and ellipsoid shaped objects. Image reconstruction was done with the IMMI method on a 301 x 301 grid with a voxel size of 70 µm. For inversion the PLSQR algorithm (presented in section 4.4.2) was used.

To determine the number of artificial views required in the developed system to achieve optimal results, the signal to noise ratio (SNR) of the images was determined for different numbers of tomographic views (64, 96, 128, 192, 224, 256, 320, 384, 512).

Comparison of real and interpolated views

The sinogram (*i.e.* the set of one-dimensional signals placed next to each other in order of the viewing angle) of an incomplete data set is shown in Fig. 4.2 (a). Unavailable projections are displayed as blanks. The dataset after computation of additional views is shown in (b), the correct complete dataset in (c). A comparison between a real measured projection and the interpolated one is shown in (d), indicating that peaks in the interpolated signals are slightly underestimated.

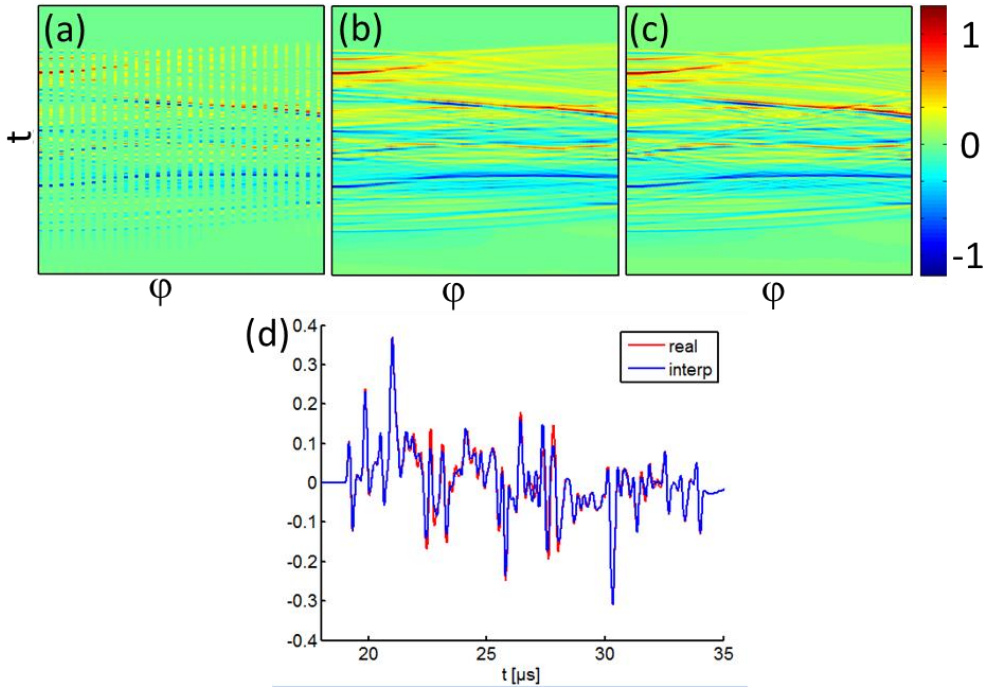

Fig. 4.2: (a) Sinogram of a dataset with insufficient angular views. Angles at which no data was sampled are set to zero. (b) Sinogram after linear interpolation in angle for the missing projections. (c) Sinogram of the complete dataset. (d) Comparison between real (red) and interpolated (blue) signals.

Reconstructions with real and interpolated views

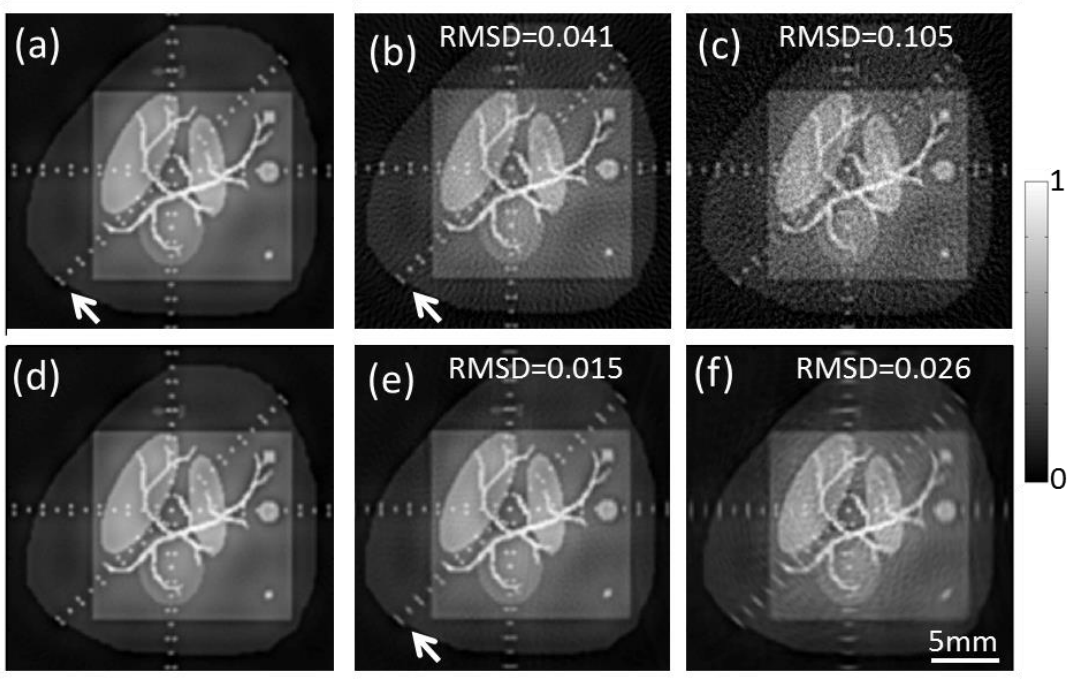

Fig. 4.3: The interpolation method tested on simulated data. (a) Full view (360°) reconstruction using detectors with an aperture size of 1 mm and 720 angular views sufficient to avoid aliasing. (b) Reconstruction with 180 (c) and 90 equidistant angular views. Streak artifacts are visible if an insufficient amount of views is used in the reconstruction. The second row shows the corresponding reconstruction using 720 projections supplemented by phantom views. The interpolation technique alleviates the aliasing artifacts but also reduces the lateral resolution as indicated by the white arrow.

Fig. 4.3 shows the optoacoustic reconstructions. In the first row we show the results using 720, 180 and 90 real projections. In the second row the reconstructions were the measured projections were supplemented with phantom views to obtain a total of 720 projections are shown. The reconstruction using 720 projections (a) shows an accurate image, the reconstructions with 180 (b) and 90 (c) projections are degraded by aliasing artifacts. Conversely, the reconstructed images using phantom views are smooth with no (e) or significantly reduced (b) aliasing artifacts. In contrast to a reconstruction with the complete dataset a slight loss in lateral resolution is visible in the periphery of the phantom as indicated by the white arrow, which worsens the sparser the angular sampling.

Optimal amount of artificial views in the developed system

The first column in Fig. 4.4 shows photographs of the phantoms utilized. The second column depicts the reconstruction with the available 64 tomographic views, the third column the reconstruction using 192 tomographic views including 128 phantom views. Aliasing artifacts are visible in (b) and (e), *i.e.* when no additional views are used. In case of the interpolated data the aliasing artifacts are significantly reduced. A zoom onto the yellow and green areas is shown in (h). As seen by the zoom onto the microspheres cluster delineated in red, there is a slight resolution improvement in the interpolated case. The SNR computed from the microsphere labeled with the green arrow in (b) and the lateral dimension of the microsphere labeled with the yellow arrow in (c) are shown in (g) as a function of the total number of projections used in the reconstruction. SNR increases until 192 projections and then starts saturating. From the microsphere in the periphery, we also see a slight lateral resolution loss of about 60 μm when doing the interpolation.

4.3.3 Discussion and Conclusion

Undersampling of the acoustic field leads to aliasing artifacts in the reconstruction. Whereas this can be avoided in scanning-based setups by a fine enough angular sampling, this poses a problem in setups with a fixed detection geometry like the one developed herein. To alleviate the aliasing artifacts the use of phantom views is proposed. The method consists of calculating one or more artificial views between each pair of real views in order to augment the original dataset and then proceed with the image reconstruction as usual. The method was tested on simulated and experimental data and it could be shown that it can significantly reduce aliasing artifacts. The amount of projections needed depends on the imaging system. It should be chosen to achieve a spatial sampling finer than half of the detector size but not much smaller since this has no positive effect on the reconstruction and only increases the amount of data to be processed. As a rule of thumb for a circular detection geometry the total amount of projections needed is $N_{min} \approx 3r_0\Delta\alpha/\delta$ where δ is the detector size, r_0 the radius of the detection circle and $\Delta\alpha$ the total detection aperture (in rad). In that sense 192 projections (real and artificial) equidistantly distributed on the 172° arc are a practical value for the small animal imaging system developed herein. Since computation time for the interpolation is negligible, the image formation time is approximately proportional the number of projections when using the backprojection algorithm and can therefore also be used for real-time image display. When using the IMMI method it has to be con-

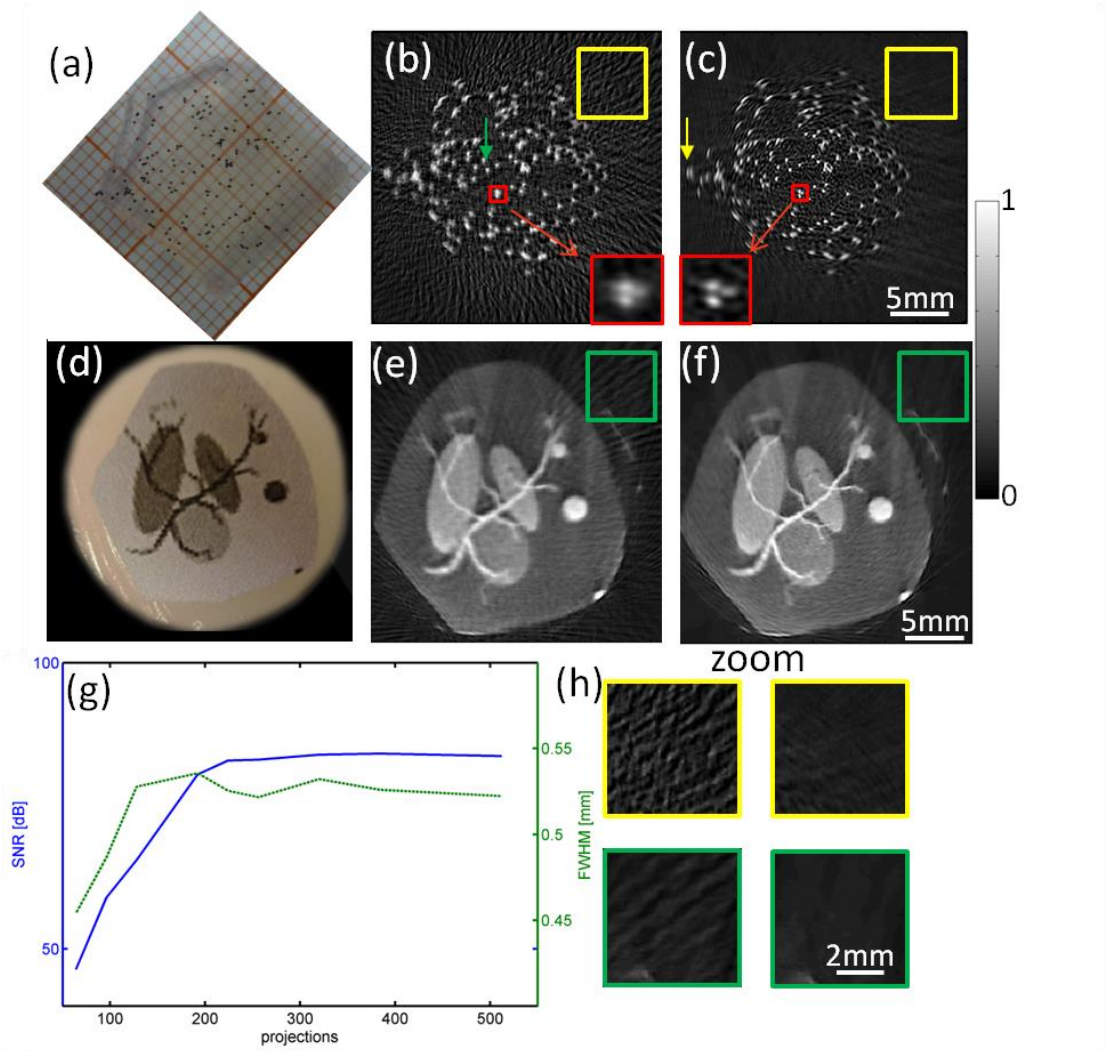

Fig. 4.4: The interpolation method tested on experimental data. The first column depicts a photograph of the phantom used. The second column shows the reconstruction without interpolation and the third column with intermediate views obtained by interpolation. The zoom onto the microsphere cluster delineated in red shows and resolution improvement for the reconstruction with interpolation. (g) displays the SNR and lateral dimension of the microsphere shown by the yellow arrow in (c) as a function of the number of projections (real + interpolated). (h) shows the zoom onto the yellow and green areas displaying a clear reduction of artifacts when using the interpolation technique.

sidered that the use of interpolated projections also increases the matrix size. A side effect of the interpolation method is a slight lateral blurring and lateral resolution loss, which becomes worse with sparser angular sampling. However compared to the image improvement by reducing the aliasing artifacts (RMSD 0.015 vs. RMSD 0.041), this this is an acceptable trade-off. The reason is that the interpolation method does not create new information but rather fills the gap in the image space due to a lack of spatial views by an estimate obtained from two adjacent tomographic views. Objects, whose spatial frequencies are not detected by the real measurements, remain invisible in the reconstruction using phantom views. In that sense the method can be considered as an adapted spatial blurring filter smoothing out streak artifacts due to aliasing. It has to be noted that there might be additional ways to reduce aliasing artifacts, for instance by simulating artificial projections based on an initial reconstruction using only the measured data set and then

recalculating in an iterative way an improved image including the simulated projections. Alternatively one could think of employing algebraic reconstruction techniques incorporating prior knowledge. Yet, none of these has been examined herein, because they are computationally more expensive and time consuming, whereas the focus of the presented method is on speed (*i.e.* achieving high temporal resolution) and ease of use.

4.4 Model-based optoacoustic inversions in partial view detection scenarios

A small animal imaging problem can be addressed as a 2D problem with light sheet illumination, to selectively generate optoacoustic signals in a narrow volume, and a collection of optoacoustic responses with detectors cylindrically-focused onto the same small volume and arranged on an arc surrounding the animal. Rosenthal *et al.* developed the 2D interpolated matrix model-based inversion algorithm (IMMI) presented in section 2.4.2.2 for image reconstruction in such a 2D scenario and they showed that for full view (360°) detection geometries this method has substantial advantages over the standard backprojection algorithms by not suppressing low frequency information and avoiding negative value artifacts [66].

Yet, in many imaging implementations full view detection cannot be achieved, due to mechanical and practical constraints such as limited access to the imaging plane or cost. Conversely, the lack of a complete (360°) tomographic dataset imposes inversion challenges and might compromise the accuracy of the reconstruction by rendering some parts of the object invisible. This is known as the limited view problem and was discussed in section 2.4.6. Hypothesizing that IMMI can also improve the reconstructions in limited view detection scenarios compared to back-projection algorithms (*i.e.* in the system developed herein), the IMMI method was studied in the context of partial view detection. It turned out that IMMI, which under ideal full view conditions, yields artifact free reconstructions [66], suffers from ill-conditioned forward matrices leading to error-prone reconstructions.

In this section it is shown that the reconstruction errors follow a distinct pattern. Based on the distinct properties of the reconstruction errors, two algorithms to minimize them in the IMMI framework are proposed and tested in simulations and experimentally using tissue mimicking phantoms. The study was published 2011 in Medical Physics under the title "*Model-based optoacoustic inversions with incomplete projection data"* [99].

4.4.1 Limited view artifacts

Limited view reconstructions pose a particular challenge in optoacoustic tomography. As discussed in section 2.4.2.2 the boundary of an object may be invisible in the reconstruction if the detection view is not sufficiently comprehensive. Specifically this happens when there is no normal line orthogonal to the boundaries intersecting the detection curve [71], because in such a situation the wavefront is not detected. IMMI, which yields artifact free reconstructions

under ideal full view conditions [66] suffers from an additional difficulty when implemented in limited view scenarios.

As the detection curve is reduced (blue line in Fig. 4.5 a), the inversion of the matrix relation in Eq. (2.34) becomes increasingly ill-conditioned and therefore more prone to errors. This effect is illustrated in Fig. 4.5 (b), where the condition number of the matrix is given for different arc lengths. In the specific scenario of limited view reconstruction, the errors are manifested in stripe artifacts, as shown in Fig. 4.5 (c) for a 170° detection arc. The artifacts are independent of the method used to solve Eq. (2.34), and are obtained for the LSQR algorithm as well as for the pseudo-inverse method. The stripes appear in the invisibility zone of the reconstructed image and do not fulfill the detection condition. The smaller the detection arc is, *i.e.* the more ill-conditioned the problem is, the stronger the stripes are. In addition, the stripes are more accentuated in deeper parts of the region not covered by ultrasound detectors. Thus regularization is necessary.

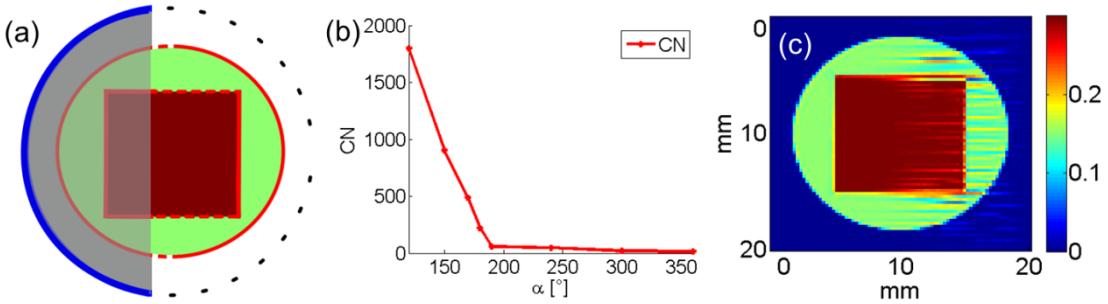

Fig. 4.5: (a) Reconstructable (solid red line) and "invisible" (dashed red line) boundaries of a round object with a square insertion partially lying in the "visibility region" (gray-shaded area) and the "invisibility domain" for a detector moving along the solid blue arc. Dashed boundaries blur away since they do not fulfill the detection criterion, *i.e.* they do not have a normal passing at least through one detector position. (b) The conditionnumber of the matrix M as a function of the detection arc. The higher the conditionnumber the more error-prone the inversion of M becomes. (c) IMMI reconstruction of the phantom. IMMI reconstructions show stripe artifacts in the invisibility domain. (Panels (a)-(c) published in [99], Copyright 2011, Am. Assoc. Phys. Med.)

The origin of the stripe artifacts is the same as the one of the blurring of interfaces not fulfilling the detection criterion. The stripes represent objects whose acoustic fields are generally undetected in the detector geometry. This effect is illustrated in Fig. 4.6 (a) and (b). Fig. 4.6 (a) shows a single stripe in the invisible zone and Fig. 4.6 (b) shows the energy of the corresponding acoustic field detected at different angles. The figure clearly shows that most of the acoustic energy is obtained at angles outside the detection arc. As a result of this effect, the available data is not sufficient to conclude whether the originating image had such stripes. Backprojection algorithms are based on additive formula in which contributions from different detectors are projected and summed up to form the image. As a result, the lack of data leads to an image without any characteristics that do not fulfill the detection condition. In contrast, IMMI is based on an optimization algorithm, in which the image is obtained by minimizing the mean square error (MSE) in Eq. (2.35). Since objects that do not fulfill the detection criterion have only minute effect on the MSE, any form of numerical or experimental inaccuracy may be interpreted by the algorithm to have been originated from such objects. Thus, in

contrast to backprojection algorithms, in which objects that do not fulfill the detection conditions are excluded from the reconstructed image or distorted, in IMMI such objects appear almost randomly and might dominate the image in the invisible zone.

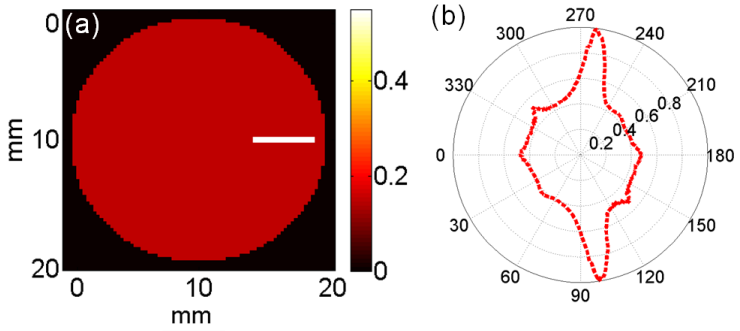

Fig. 4.6: (a) Phantom containing an insertion similar to the stripe artifacts in the "invisibility" domain. (b) The energy of its optoacoustic signal as a function of the detector position indicating a high directivity. As a result the optoacoustic signal of such structures cannot be detected in limited view detection scenarios with a detection arc smaller than 190° and consequently have a small effect on the mean square error in Eq. 6 which is minimized in order to obtain an image. Any form of numerical or experimental inaccuracies may therefore be misinterpreted by the optimization algorithm as originating from such objects. (Figure published in [99], Copyright 2011, Am. Assoc. Phys. Med.)

4.4.2 Regularization techniques

The reconstruction artifacts due to limited view geometry can be significantly reduced by regularizing the inversion in IMMI. The regularization is performed by exploiting the specific stripe shape of the artifacts. The stripes involve large variations in the direction perpendicular to their orientation; therefore, it would be beneficial to introduce a constraint that limits variations in this direction, *i.e.*

$$\min_{z} \left\| \mathbf{Dz} \right\|_2 \tag{4.4}$$

where $\mathbf{D} \in \Re^{(n-1)\times n}$ stands for a discrete approximation of the first derivative operator perpendicular to the ripple orientation. Without the loss of generality, it is assumed that we have a detection arc like the one shown in Fig. 4.5 (a). In this case, the stripe artifacts are horizontal, and the derivate operator writes as

$$\mathbf{D} = \begin{bmatrix} 1 & -1 & & \\ & 1 & -1 & \\ & & \ddots & \ddots \\ & & & 1 \quad -1 \end{bmatrix} \tag{4.5}$$

This side constraint penalizes strong variations in the pixel intensities along vertical lines (perpendicular to the stripe artifacts).

Two methods for performing the regularization were investigated. A direct method, which regularizes the pseudo-inverse of **M** by using truncated generalized singular

value decomposition (TGSVD) and an preconditioned iterative method (PLSQR) which searches the solution iteratively in a constrained subspace. The direct approach has the advantage of enabling a fast image reconstruction because for a given imaging geometry, the regularized pseudo-inverse can be computed in advance and be reused for consecutive reconstructions. The iterative method is appropriate for significantly larger matrices because in each iteration step only one column vector of the matrix is kept in the computer's working memory.

4.4.2.1 Truncated generalized singular value decomposition (TGSVD)

Truncated singular value decomposition (SVD) [100-103] is a common method for regularizing ill-conditioned inversion problems. The SVD of a matrix **M** is given by

$$\mathbf{M} = \mathbf{U}\Sigma\mathbf{V}^{\mathbf{T}} = \sum_{i=1}^{n} \mathbf{u}_i \sigma_i \mathbf{v}_i^T \tag{4.6}$$

where **U,V** are orthonormal matrices **($\mathbf{V^TV=U^TU=I_n}$)** with the column vectors $\mathbf{u}_i$ and $\mathbf{v}_i$ (i=1...n) and $\mathbf{\Sigma}$ is the diagonal matrix containing the singular values σ_i of **M** in descending order ($\sigma_1 > \sigma_2 \ldots > \sigma_n$). From Eq. (4.6) it follows that

$$\begin{aligned} \mathbf{M}\mathbf{v}_i &= \sigma_i \mathbf{u}_i \\ \left\| \mathbf{M}\mathbf{v}_i \right\|_2 &= \sigma_i \end{aligned} \tag{4.7}$$

Given that the matrix **M** connects the image vector **z** to the acoustic-signal vector **p**, the vectors $\mathbf{v}_i$ can be considered as eigen-images, whose corresponding normalized acoustic signals $\mathbf{u}_i$ can be considered as eigen-signals. The eigen-images are arranged such that the energy of their corresponding acoustic signal σ_i decreases with the index *i*. Using SVD, the solution to Eq. (2.35) can be written as a superposition of the eigen-images

$$\mathbf{z} = \sum_{i=1}^{n} \frac{\mathbf{u}_i^T \mathbf{p}}{\sigma_i} \mathbf{v}_i \tag{4.8}$$

where $\mathbf{u_i^T p}$ are the coefficients of the projection of **p** to the space spanned by $\{\mathbf{u}_i\}$. The effect that a certain eigen-signal has on the reconstruction is inversely proportional to its singular value σ_i. In ill-conditioned problems, $\sigma_i / \sigma_n >> 1$, therefore small variations or even noise in **p** values corresponding to high index eigen-signals can lead to perceived artifacts.

Regularization can be achieved by truncation of Eq. (4.8), *i.e.*

$$\mathbf{z}_k = \sum_{i=1}^{k} \frac{\mathbf{u}_i^T \mathbf{p}}{\sigma_i} \mathbf{v}_\mathbf{i} \quad \text{with } k < n \tag{4.9}$$

which can improve the stability of the inversion, since high index eigen-images, whose contribution to the solution in Eq. (4.8) is determined mostly by modeling errors and noise, are omitted in Eq. (4.9).

Ideally, the eigen-images that are cut off would contain only stripe artifacts. However, since the singular values usually decay gradually to zero, it is not possible to find an accurate cut-off value. For ensuring that stripe artifacts are not contained in the truncated solution it is possible instead to employ the generalized singular value decomposition (GSVD) [102]. In GSVD, the orthonormality of the eigen-images is discarded in order to generalize the decomposition to include the quality measure $\|\mathbf{Lz}\|_2$, where **L** stands for an generalized discrete derivate operator of order *p* ($\mathbf{L} \in \Re^{(n-p)\times n}, m \geq n \geq p$). The GSVD of the matrix pair **M** and **L** can be written as:

$$\mathbf{M} = U\begin{pmatrix} \mathbf{\Sigma} & \mathbf{0} \\ \mathbf{0} & \mathbf{I_p} \end{pmatrix}\mathbf{X}^{-1}, \qquad \mathbf{L} = \mathbf{V}(\mathbf{W},\mathbf{0})\mathbf{X}^{-1} \tag{4.10}$$

where $\mathbf{U} = [\mathbf{u_1}, \mathbf{u_2}, ..., \mathbf{u}_n] \in \Re^{m\times n}$ and $\mathbf{V} = [\mathbf{v_1}, \mathbf{v_2}, ..., \mathbf{v}_p] \in \Re^{(n-p)\times(n-p)}$ are orthonormal matrices and $\mathbf{X} = [\mathbf{x_1}, \mathbf{x_2}, ..., \mathbf{x_n}] \in \Re^{n\times n}$ is non-singular.

Further $\mathbf{\Sigma} = diag(\sigma_1, ..., \sigma_{n-p})$ and $\mathbf{W} = diag(\mu_1, ..., \mu_{n-p})$ such that $0 \leq \sigma_1 \leq ... \leq \sigma_{n-p} \leq 1$, $1 \geq \mu_1 \geq ... \geq \mu_{n-p} > 0$ and $\mu_i^2 + \sigma_i^2 = 1$. The σ_i are arranged in ascending order owing to historical reasons. The generalized singular values are defined as $\gamma_i = \sigma_i / \mu_i$. For practical solutions we considered herein only the first derivative (**L = D**, *p* = 1), which leads to the following set of equations:

$$\begin{aligned} &\mathbf{Mx}_i = \sigma_i \mathbf{u}_i \ (i = 1...n-1) \\ &\mathbf{Mx}_n = \mathbf{u}_n \\ &\|\mathbf{Mx}_i\|_2 = \sigma_i \ \ (i = 1...n-1) \\ &\|\mathbf{Mx}_n\|_2 = 1 \end{aligned} \tag{4.11}$$

and

$$\begin{aligned} &\mathbf{Dx}_i = \mu_i \mathbf{v}_i \ (i = 1...n-1) \\ &\mathbf{Dx}_n = 0 \\ &\|\mathbf{Dx}_i\|_2 = \mu_i \ \ (i = 1...n-1) \end{aligned} \tag{4.12}$$

.

It has to be noted that in GSVD, the vectors $\mathbf{x}_i$ play the role of eigen-images and that the eigen-images are ordered according to the energy of their corresponding normalized eigen-signals $\mathbf{u}_i$. In addition, the eigen-images are also organized according to the l_2 – norm of their derivatives $\|\mathbf{Dx}_i\|_2$.

For GSVD with *p* = 1, the solution to Eq. (2.35) can be written as a superposition of the eigen-images in the following compact form:

$$\mathbf{z} = \sum_{i=1}^{n-1} \frac{\mathbf{u}_i^T \mathbf{p}}{\sigma_i} \mathbf{x}_i + \left(\mathbf{u}_n^T \mathbf{p}\right) \mathbf{x}_n \tag{4.13}$$

The regularized solution is achieved by using the truncated generalized singular value decomposition (TGSVD):

$$\mathbf{z}_k = \sum_{i=n-k}^{n-1} \frac{\mathbf{u}_i^T \mathbf{p}}{\sigma_i} \mathbf{x}_i + \left(\mathbf{u}_n^T \mathbf{p}\right) \mathbf{x}_n \tag{4.14}$$

Because the cut-off eigen-images correspond to large μ_i values, the transition between low and high index eigen-values will be characterized by strong pixel variation on the axis on which the derivative operator **D** acts. Since it is assumed that the optoacoustic image does not contain such strong pixel variations, the quality of the reconstruction will not be sensitive to the choice of the regularization parameter *k.* TGSVD can be understood as a variation of TSVD in which the role of the l_2 norm of the solution $\|\mathbf{z}\|_2$ and eigen-images is replaced by the l_2 norm of the differentiated images $\|\mathbf{D}\mathbf{z}\|_2$. In TSVD, the contribution of eigen-images is truncated which would require high energy to marginally reduce the residual error, thus effectively, penalizing unnecessary high energy contributions. In contrast, in TGSVD it is the contribution of eigen-images in which a high energy for the differentiated images is required to marginally reduce the residual error which is truncated, thus penalizing unnecessary contributions with strong stripe-like variations.

Fig. 4.7 (a) shows the root mean square deviation (RMSD)

$$\mathrm{RMSD}(\mathbf{z}, \mathbf{z}_{ref}) = \frac{\left\|\mathbf{z} - \mathbf{z}_{ref}\right\|}{\left\|\mathbf{z}_{ref}\right\|} \tag{4.15}$$

between reconstruction **z** and known solution $\mathbf{z}_{\mathrm{ref}}$ for different phantoms in a 170° reconstruction as a function of the number of generalized singular values used in the reconstruction. We see that an optimal result is obtained for approximately the same number of singular values used in the reconstruction. This allows the determination the cut-off parameter based on a simulation study and use the same value for consecutive reconstructions.

4.4.2.2 Preconditioned LSQR (PLSQR)

The standard LSQR algorithm, described in section 2.4.2.2 minimizes the residual error Eq. (2.38) under the restriction that the solution lies in the Krylov subspace satisfying

$$K_k(\mathbf{M}^{\mathrm{T}}\mathbf{M}, \mathbf{M}\mathbf{p}) \approx span\{\mathbf{v}_1, ..., \mathbf{v}_k\}. \tag{4.16}$$

Hence, the solution after iteration *k* is similar to the solution of the TSVD method, *i.e.* early iterations are generally associated with high singular values of ***M*** and the late iterations with the low ones. In limited view scenarios in which ***M*** is ill-

conditioned the algorithm approaches the correct solution in early iterations but then diverges to a solution, which significantly deviates from the original image. Stopping the iterations before the artifacts appear can be a way to regularize the inversion. However, similar to the TSVD method, this penalizes high energy values $\|\mathbf{z}_k\|_2$ and therefore LSQR is not particularly adapted to deal with the stripe artifacts.

To improve the sensitivity of the regularization to the stripe artifacts the preconditioned LSQR algorithm (PLSQR) is employed [104, 105]. In contrast to the standard LSQR algorithm, in which stopping of iterations penalizes $\|\mathbf{z}_k\|_2$, PLSQR penalizes the more general functional $\|\mathbf{L}\mathbf{z}_k\|_2$ and therefore early iterations of the PLSQR algorithm are characterized by having low $\|\mathbf{L}\mathbf{z}_k\|_2$ values. By choosing **L = D** the stripe artifacts appear in later iterations than for the standard LSQR algorithm and consequently, there is a better separation between image relevant information and artifacts, which leads to a better reconstruction accuracy. The images in Fig. 4.7 (b) show for the LSQR and PLSQR method the contribution of the iteration after which the RMSD between reconstruction and original image has reached its minimum. Stopping the iterations obviously leads to a loss of image relevant low frequency information for the LSQR method, which is not the case for the PLSQR method.

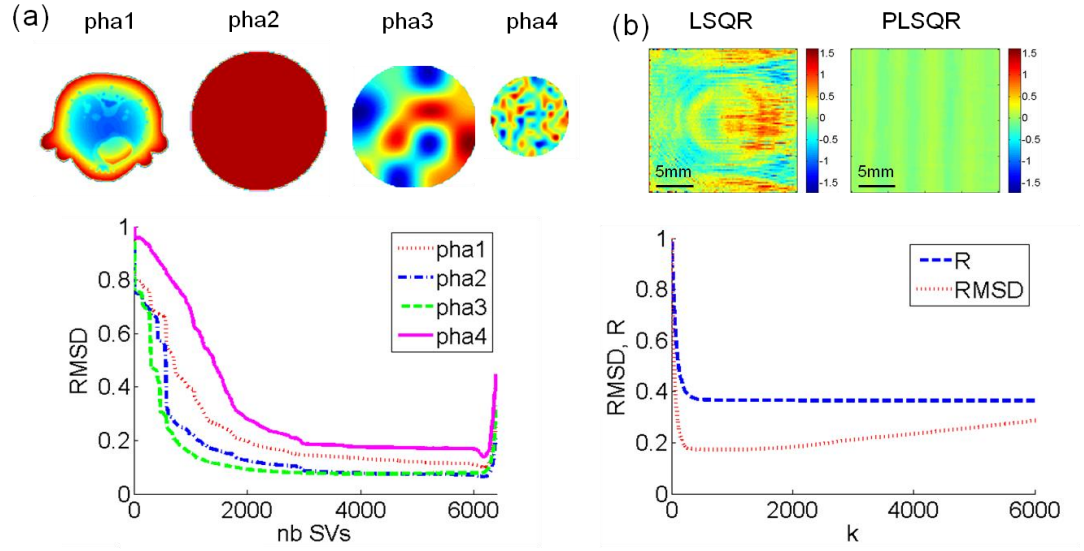

Fig. 4.7: (a) The RMSD between reconstruction and original image for the four phantoms shown as insets in a 170° limited view scenario for the TGSVD method. For all the phantoms the minimum RMSD is obtained approximately for the same number of singular values used in the reconstruction. Consequently, one can determine the number of SVs used in the reconstruction a priori in a simulation study based on an arbitrary phantom. (b) The RMSD between PLSQR reconstruction and solution and the corresponding residual error R for 170° reconstructions with noisy data (SNR = 8 dB) as a function of the iterations. Since the method is only slightly semi-convergent, the relative change of R can be used to devise a stopping criterion. The two inlays show the contribution of the iteration after the minimum of the RMSD has been reached, for the LSQR and the PLSQR algorithm. Stopping the iterations leads to a loss of image relevant low frequency information for the LSQR method, which is not the case for the PLSQR method. (Figure published in [99], Copyright 2011, Am. Assoc. Phys. Med.)

Fig. 4.7 (b) also shows the RMSD and the residual error R as a function of the number of iterations. Since the flat part of the residual error and the minimum of the RMSD correlate, it is possible to devise a stopping criterion based on the normalized relative change of the residual error

$$\left| \frac{R_k - R_{k-1}}{R_1} \right| \tag{4.17}$$

If it becomes smaller than a predefined threshold t_R, then the iterations are stopped. The implementation of PLSQR can be found in [104, 105].

4.4.3 Performance evaluation

Numerical simulations

A numerical study was performed to analyze the three reconstruction schemes considered herein, *i.e.* conventional IMMI and regularized IMMI using TGSVD, and PLSQR, under various limited view scenarios. In all the simulations presented in this section, the imaged object was a circular phantom with several insertions of variable size and shape. The bulk of the phantom had tissue-mimicking optical properties with a reduced scattering coefficient of μ_s' = 10 cm^{-1} and absorption coefficient of μ_a = 0.15 cm^{-1}. The insertion had the same scattering coefficient as the bulk, and absorption coefficient in values ranging from 0.2 to 0.4 cm^{-1}. The phantom was uniformly illuminated on its boundary, where the intensity on the boundary accepted the normalized value of 1. The light fluence within the phantom was calculated by a FEM solution to the light diffusion equation [73]. The originating optoacoustic image is shown in Fig. 4.8 (a), as well as the detection arc, over which the acoustic detectors are positioned. The three reconstruction algorithms were tested for the following detection arc spans: $\alpha = 360°$, 300°, 240°, 190°, 180°, 170°, 150° and 120°, respectively. In all the cases the angular increment between the transducer positions was held constant at 1°. The optoacoustic signal was simulated using the forward model given in Eq. (2.34). To create experimental conditions, the photoacoustic signal was corrupted with different levels of white noise: no noise, SNR = 28, 21, 8, 3 and 1.7 dB, respectively. The accuracy of the reconstructions was evaluated by the root mean square deviation (RMSD) between the reconstruction and the known solution given by Eq. (4.15).

For the PLSQR inversion iterations were terminated when the relative change of the normalized residual error fell below the threshold $t_R = 10^{-7}$. The number of generalized singular values used in the TGSVD reconstruction was determined by a simulation study based on phantom 4 seen in Fig. 4.7 (a).

Experimental test data

In addition to the numerical studies, the performance of the proposed algorithms was tested experimentally on tissue-mimicking phantoms. The phantoms were imaged in the optoacoustic tomography system described in Ref. [106] and briefly in section 3.2.1. The phantom employed in the experimental measurements was cylindrically shaped and had a diameter of 16 mm and a background reduced

scattering coefficient of μ_s' = 10 cm^{-1} and a background absorption of 0.5 cm^{-1}. A square absorbing insertion (5 mm edge length) was introduced in the center of the phantom. The insertion had scattering similar to the background while the optical absorption coefficient was set to 2.5 cm^{-1}. The acoustic signals were measured over 360° with an increment of 1°. Limited views were simulated by varying the number of projections (arc length). All reconstructions were performed on an 80 x 80 grid. The reconstructions were performed using the conventional Moore-Penrose pseudo-inverse IMMI and the PLSQR and TGSVD regularization techniques in which the regularization parameters were determined as in the simulation study. IMMI and the backprojection algorithm were also used for comparison.

The presented regularization approach was also tested on a more complex phantom imaged in the small animal scanner presented in chapter 3. The 64 measured projections were interpolated to a total set of 192. The reconstructed region of interest had a size of 21 x 21 mm^2 and was represented by 301 x 301 pixels. Each pixel had a size of 70 µm. The high number of pixels in the image prevented the use of TGSVD in reconstruction owing to memory limitations, and thus only PLSQR was tested.

Performance on simulated data

Fig. 4.8 (b)-(d) depict the RMSD between the reconstructed data and the simulated images when utilizing the Moore-Penrose pseudo-inverse, the TGSVD method and the PLSQR algorithm, respectively, as a function of the detection arc and the SNR assumed. For all three methods, the RMSD does not depend on the detection arc when it is wider than 190°. In that case, the model matrix is well conditioned, as seen in Fig. 4.5 (c), and regularization is not necessary. For narrower detection arcs, however, the forward problem becomes ill-conditioned and its inversion leads to a substantial increase in the RMSD of the IMMI reconstruction. Conversely, TGSVD and PLSQR reduce the RMSD, albeit not to the levels obtained for detection arcs wider than 190°.

Fig. 4.9 shows examples of reconstructed images. The reconstructions were obtained for an 80 x 80 grid, the same SNR of 8 dB and for three arc spans (240°, 170°, and 120°) presented on three columns from right to left. The first three rows present the not-regularized, PLSQR, and TGSVD IMMI reconstructions, respectively, whereas the fourth row presents the backprojection reconstruction. The figure shows that for the 240° wide arc, both regularized and Moore-Penrose pseudo-inverse based IMMI reconstructions achieve similar visual quality, close to that of the original image. In contrast, the backprojection reconstruction suffers from negative value artifacts that accentuate the boundary, and does not depict the light attenuation in the phantom [20]. In the 170° scenario, stripe artifacts appear in the Moore-Penrose pseudo-inverse based IMMI reconstruction. These artifacts are barely visible in the two regularized reconstructions, which both achieve visual quality close to the 240° case. Similarly, the backprojection reconstruction for the 170° and 240° cases is approximately the same. When the detection arc's span is further reduced to 120°, the stripe artifacts dominate the IMMI reconstruction. Although both regularization methods eliminate these artifacts, they do not achieve the same visual quality as the IMMI reconstructions in the 240° scenario. The

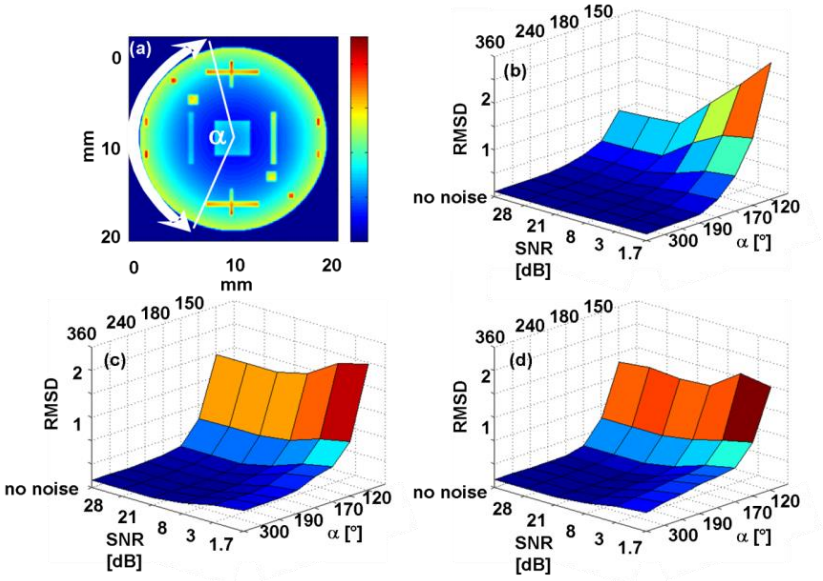

Fig. 4.8: (a) The phantom used in the numerical study representing the map of local laser energy deposition as well as the detection arc on which the virtual transducer is assumed to rotate around the sample. (b) RMSD between the reconstruction without regularization and the solution for different detection arcs and noise levels. (c)-(d) RMSD for the TGSVD method and the PLSQR algorithm. Both methods yield results of similar accuracy. The increase of the RMSD is due to the blurring of boundaries not fulfilling the detection criteria and not due to the stripe artifacts. (Figure published in [99], Copyright 2011, Am. Assoc. Phys. Med.)

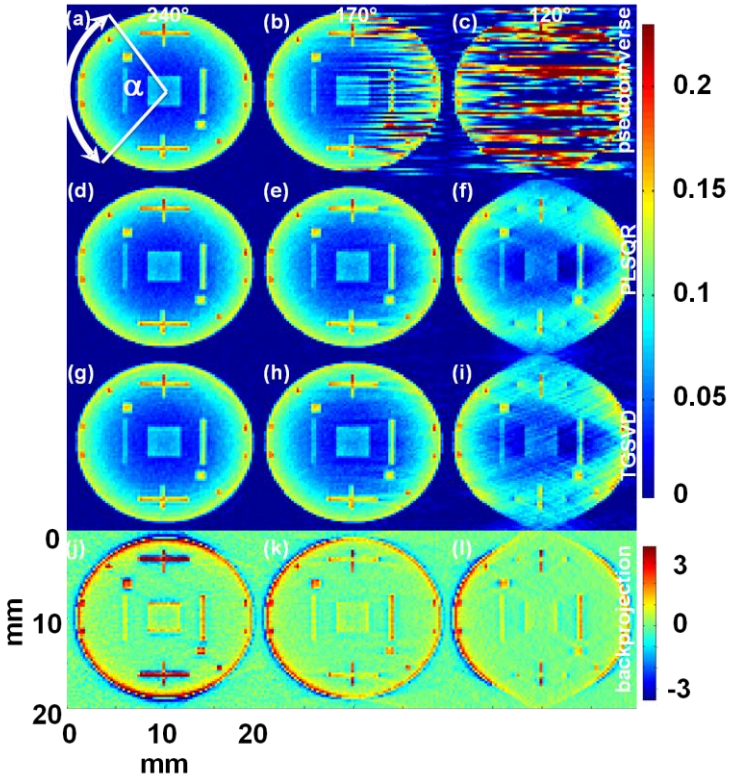

Fig. 4.9: (a)-(c) Reconstructions without regularization of the phantom shown in Fig. 4.8 (a) based on 240°, 170° and 120° detection arcs and 8 dB SNR. For detection arcs smaller than 190°, strong stripe artifacts appear which mask underlying object features. (d)-(f) PLSQR and (g)-(i) TGSVD reconstructions for the same conditions. Both techniques reduce the stripe artifacts, however the blurring of boundaries is still present for detection arcs smaller than 180°. (j)-(l) backprojection-based reconstructions. They are obviously not quantitative and suffer also from the blurring of boundaries. (Figure published in [99], Copyright 2011, Am. Assoc. Phys. Med.)

main effect visible in the 120° regularized reconstructions is blurring of the boundary at sections which do not fulfill the detection criterion. The same effect is visible in the backprojection reconstruction.

Performance on experimental data

Similarly to the simulated data, backprojection-based reconstructions accentuate the boundaries (Fig. 4.10 (j)-(l)) and exhibit negative value artifacts. In contrast, the model-based results, based on full view tomographic data (Fig. 4.10 (a), (d) and (g)) are all positive. In the limited view case without regularization (Fig. 4.10 (a) and (b)), the model-based reconstructions are corrupted by stripe artifacts which increase when the detection arcs becomes smaller. The presented regularization methods can greatly reduce these effects (Fig. 4.10 (e)-(f) for PLSQR and (h)-(i) for TGSVD). In congruence to the numerical study no differences between both methods are visible. Boundaries that do not fulfill the detection criterion, *i.e.* which do not have the normal passing through a detector position, cannot be recovered by either IMMI or the backprojection-based reconstructions.

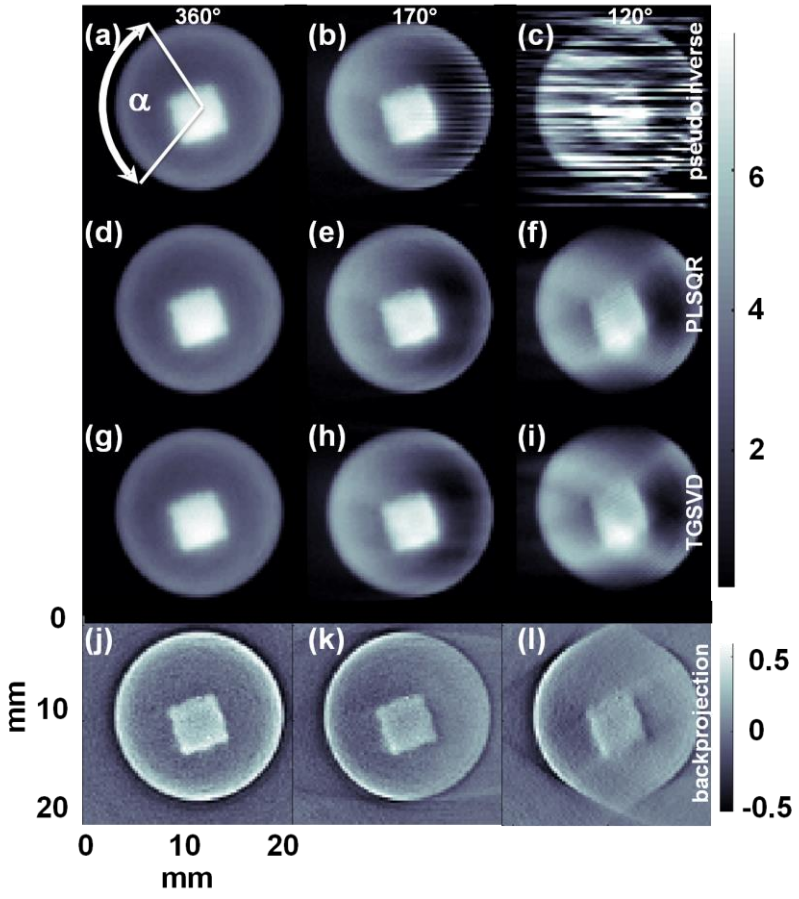

Fig. 4.10: Experimental reconstruction from a quadratic insertion (μ_a = 2.5 cm^{-1}) embedded in a homogenous scattering (μ_s' = 10 cm^{-1}) and slightly absorbing (μ_a = 0.5 cm^{-1}) cylindrical background. The columns correspond to the following detection arcs 360°, 170°, 120°, (a)-(c) the rows to not-regularized, (d)-(f) PLSQR, (g)-(i) TGSVD regularized IMMI reconstructions and (j)-(l) to back-projection reconstructions. IMMI reconstruction without regularization show strong stripe artifacts which mask underlying structures, regularization techniques allow correction. Both IMMI and backprojection reconstructions suffer from the blurring of boundaries not fulfilling the detection criteria. (Figure published in [99], Copyright 2011, Am. Assoc. Phys. Med.)

Compared to the simulated reconstructions, a subsidence of the image background is visible opposite to the detection arc (*e.g.* Fig. 4.10 (e) and (h)) which is due to experimental factors like transducers' frequency response and illumination inhomogeneities due to the varying illumination (cf. section 3.2.1) which have not been taken into account in the forward model. In the full view case this effect is not visible due to the redundancy of the data, *i.e.* the average of projections from opposite directions compensate these effects.

Fig. 4.11 (a) shows a photograph of phantom imaged in the small animal scanner. It was produced by printing a complex pattern onto a sheet of paper and embedding it into a scattering agar matrix. Fig. 4.11 (b) shows the reconstruction without regularization; Fig. 4.11 (c) the corresponding PLSQR reconstruction and (d) the backprojection reconstruction. Similar to the previous examples, PLSQR significantly reduced the stripe artifacts in the image, attaining higher image quality. Also, compared to the backprojection results, the low spatial frequencies are much better represented in the image. Since optoacoustic images are presented on a black to white colormap, dark areas in the paper phantom appear white in the reconstruction.

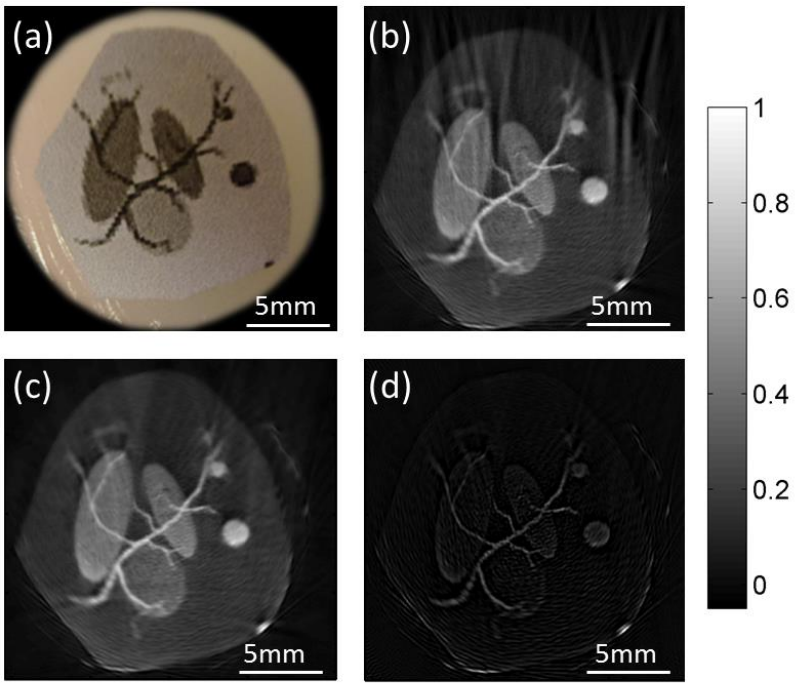

Fig. 4.11: (a) Photograph of the phantom imaged in the small animal scanner. (b) Model-based reconstruction without regularization showing artifacts. (c) Reconstruction with the PLSQR regularization. (b) backprojection reconstruction.

4.4.4 Discussion and Conclusion

The 2D optoacoustic reconstruction problem under limited view scenarios was studied using the model-based framework of IMMI. While in full view scenarios IMMI yields higher quality reconstructions than backprojection algorithms, in the limited view scenario it suffers from strong stripe artifacts that significantly degrade the reconstruction quality. These artifacts, which do not appear in backprojection

reconstructions, occur when the detection arc covers less than 190° of tomographic view. As a result, the optoacoustic data collected do not suffice for accurately determining the structure of the image object, leading to an ill-conditioned inversion problem.

In order to eliminate stripe artifacts and stabilize the inversion two regularization algorithms were employed: TGSVD and PLSQR. For both algorithms, the magnitude of the stripe artifacts reduces by introducing a side constraint that penalizes the image variation in the direction perpendicular to the orientation of the stripes. In TGSVD, generalized singular value decomposition was employed in which the singular values are arranged according to the side constraint value of the corresponding "singular" images. The regularization is performed by truncating the decomposition, eliminating the lowest generalized singular values, responsible for the stripe artifacts. In PLSQR, an iterative algorithm is used in which the early iterations lead to low values of $\|\mathbf{D}\mathbf{z}_k\|_2$ and thus the stripe artifacts appear only after a very high number of iterations.

Both methods have been tested in a simulation study for representative limited view scenarios and noise levels and subsequently validated on experimental data. The studies showed that, TGSVD and PLSQR are insensitive to the choice of the regularization parameter and therefore consistently lead to accurate reconstructions without the stripe artefacts. For detection arcs larger than 180° the results obtained are almost as accurate as for complete datasets. For narrower detection arcs, the methods presented are able to avoid the stripe artifacts; however the accuracy of the reconstructed images degrades due to blurring of parts in the image which do not fulfill the detection criterion. Regarding the reconstruction quality, TGSVD and PLSQR yielded comparable results. Yet, clear distinctions exist with regard to the computational efficiency. For the direct TGSVD method, the calculation of the pseudo-inverse does not require the measured optoacoustic data to be incorporated into the inversion process. Thus, especially for systems with fixed geometry, it is possible to pre-calculate the regularized pseudo-inverse, save it in the computer memory and use the same inverted matrix for all the reconstructions in this particular system. Reconstruction then becomes relatively fast because it only requires multiplication of a matrix with the vectors of the time-dependent optoacoustic measurements. On the other hand, the actual inversion of the forward model matrix might still demand a relatively long time and consume large amount of computer memory. For instance, in our reconstructions with fairly low resolution, it was necessary to invert large matrices of several GB, which would usually demand high performance computing resources and even then might normally take several hours to complete.

For PLSQR, the reconstruction process becomes memory efficient because, in each iteration only a single column is stored in the memory and thus large matrices can be easily dealt with. In addition, PLSQR is particularly suited for sparse matrices, which are typically constructed by the optoacoustic forward model. However, for each reconstruction, the minimization problem in Eq. (2.35) has to be solved again for every reconstructed slice.

The study has also revealed that regularized model-based reconstruction approaches have a clear advantage over the presented backprojection algorithm in terms of image quality when 2D limited tomographic view scenarios are considered.

4.5 Summary and Conclusion

This chapter was dedicated to signal processing and 2D image reconstruction in the developed system.

It was shown that the electrical impulse response of the presented system distorts the shape of the optoacoustic signals which creates artifacts in the reconstruction. Herein Wiener deconvolution was used to deconvolve the system's electrical impulse response from the measured optoacoustic signals to successfully correct the corresponding artifacts.

Also, a technique based on calculating phantom views was presented to alleviate aliasing artifacts due to a sparse angular sampling of the acoustic field. The method clearly improved the quality of the images reconstructed with the presented system but introduced a slight lateral resolution loss. An amount of 192 views (real and artificial) was found optimal for reconstructions in the presented system.

In addition, it was shown that 2D model-based reconstructions suffer from stripe artifacts in limited view scenarios. Their physical underpinning was explained and a direct and an iterative regularization approach were presented to avoid these artifacts in optoacoustic reconstructions involving limited views.

The presented signal and image reconstruction approaches are used in most of the applications shown in chapter 7. The next chapter presents an advanced reconstruction approach taking into account the spatial impulse response of the detector, which was conceived in this work to further improve the accuracy of 3D reconstructions in the system.

5 Advanced image reconstruction approaches

5.1 Introduction

Since a small animal imaging problem effectively resembles cylindrical measurement geometry, it was addressed by collecting optoacoustic responses using detectors cylindrically focused onto a common plane and arranged on an arc surrounding the animal for cross-sectional imaging. This approach has the advantage that large-area focused detectors can be densely placed around the imaged cross-section, leading to high in-plane resolution, good sensitivity and, as a result, 2D real-time imaging performance, by only a relatively small number of ultrasound detectors. Moreover, whole-body datasets can be collected as fast as within 20 seconds by scanning the mouse in z-direction, which is the direction perpendicular to the imaged plane. For cross-sectional reconstructions a two-dimensional reconstruction algorithm is employed assuming optical absorbers confined in the imaging plane. Yet, due to strong light scattering in biological tissue, focusing of light to the imaging plane is impeded, especially for deep tissue structures, and optoacoustic signals are also generated outside the imaging plane. Therefore, the system uses a focused detector array to reduce its sensitivity to out-of-plane signals. Yet, the focusing ability of the detectors is frequency dependent and thus the reduction of out-of-plane signals (cf. section 3.4.6.2). As a consequence, cross-sectional reconstructions might be affected by low-frequency out-of-plane signals, which compromise contrast and quantification. Moreover, 3D reconstructions suffer from a frequency and spatial dependent elevational resolution, defined as the resolution perpendicular to the imaging plane. To improve on this, complementary information collected outside the imaging plane has to be considered in the inversion procedure. Conventional 3D reconstruction approaches assuming point detectors are however not suited for this purpose since they do not consider the strong distortion of the photoacoustic signal due to the spatial impulse response of a focused detector (cf. section 2.3.4), back-project the signal into areas they do not originate from and thus yield results worse than the one achieved by stacking of the 2D cross-sectional reconstructions. This is shown in Fig. 5.1 depicting a slice parallel to the yz-plane through a 3D source distribution (a), the corresponding reconstruction obtained by stacking the individual 2D backprojection (BP) reconstructions (b) and by using the *3D BP* algorithm (c). Instead it is necessary to account for the shape and size of the detection element in the inversion procedure. First, this was done by Rosenthal *et al.* [55] for a 2D source distribution using the 2D IMMI method. They showed that for circular full-view detection geometry and 2D source distribution, it is possible to compensate the lateral blurring of the point-spread function due to the finite width of a detection element. Caballero *et al.* [107] showed that this is also possible in a linear scanning geometry using spherically focused transducers. Herein, this idea is translated to 3D and tested whether it improves the 3D imaging capabilities in the small animal imaging system. For that a 3D model-based reconstruction algorithm which was published 2012 by Déan-Ben and myself [108] is adapted to incorporate

the finite size of the transducer elements. This chapter is organized as follows. The theoretical basis of the 3D IMMI method is presented and the approach to incorporate the transducer shape into the model is discussed. Then it is explained how the translational symmetry of the reconstruction problem can be used to compress the matrix and thus reduce the memory requirements for the reconstruction problem. Following that the method is tested in numerical simulations with controlled data sets to evaluate its performance. The method is further tested on experimental data including phantoms and mice acquired with the system. The chapter will then conclude with a discussion of the performance achieved and the overall advantages and disadvantages of the method.

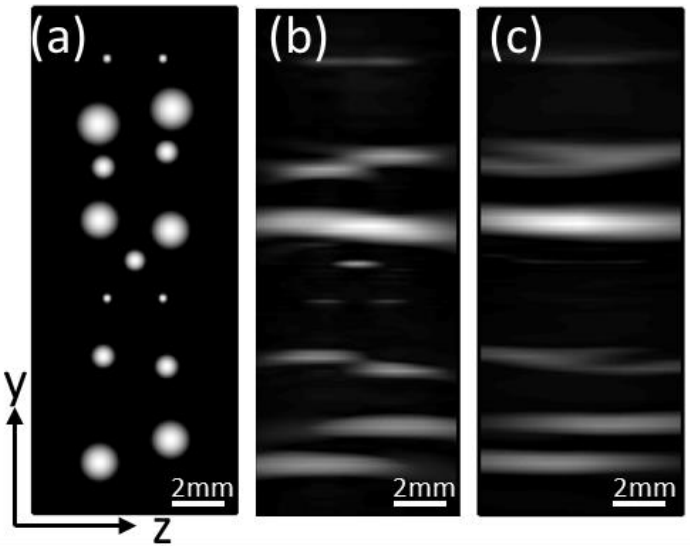

Fig. 5.1: (a) MIP view along x axis of the 3D source distribution reconstructed with (b) the *2D BP* reconstruction and (c) the *3D BP* reconstruction.

5.2 The 3D IMMI model

We described the 3D IMMI method in detail in [108]. For the sake of completeness, the theory is briefly reviewed herein.

The optoacoustic signal at position $\mathbf{r}$ and instant t is given by

$$p(\mathbf{r},t) = \frac{\Gamma}{4\pi c}\frac{\partial}{\partial t}\int_{S'(t)} \frac{H(\mathbf{r}')}{|\mathbf{r}-\mathbf{r}'|} dS'(t), \tag{5.1}$$

where $S'(t)$ is a time-dependent spherical surface for which $|\mathbf{r}-\mathbf{r}'| = ct$ and $H(\mathbf{r})$ the heating function corresponding to the absorbed electromagnetic energy (cf. section 2.2.3). In the 3D IMMI reconstruction procedure, this analytical forward model is discretised and inverted by algebraic means. For the discretization of the forward model the temporal derivative in Eq. (5.1) is approximated by

$$p(\mathbf{r},t) \approx \frac{I(\mathbf{r},t+\Delta t) - I(\mathbf{r},t-\Delta t)}{2\Delta t}, \tag{5.2}$$

with

$$I(\mathbf{r},t)=\int_{S'(t)}\frac{H(\mathbf{r}')}{|\mathbf{r}-\mathbf{r}'|}dS'(\mathbf{r},t). \tag{5.3}$$

The constant term in Eq. (5.1) is neglected for the sake of simplicity assuming arbitrary units. Considering a spherical coordinate system centered at $\mathbf{r}$, the surface element $dS'(\mathbf{r},t)$ can be expressed as

$$dS'(\mathbf{r},t)=|\mathbf{r}-\mathbf{r}'|^2\cos\phi\, d\phi d\theta \tag{5.4}$$

so that $I(\mathbf{r},t)$ is given by

$$I(\mathbf{r},t)=\iint_{\phi,\theta}H(r')\,|\mathbf{r}-\mathbf{r}'|\cos\phi\, d\phi\, d\theta \tag{5.5}$$

Thus, Eq. (5.5) can be discretized by considering a set of points in $S'(\mathbf{r},t)$ at positions $\mathbf{r}'_l$ equally spaced in ϕ and θ, so that

$$I(\mathbf{r},t)\approx\Delta\phi\,\Delta\theta\sum_l H(\mathbf{r}'_l)\,|\mathbf{r}-\mathbf{r}'_l|\cos\phi_l \tag{5.6}$$

For simplicity, the constant term $\Delta\phi\,\Delta\theta$ can be neglected when estimating the pressure in arbitrary units.

Considering that the optical absorbers, *i.e.*, the points where the optical absorption $H(\mathbf{r}')\neq 0$, are confined in a finite 3D region. Then, a discrete region of interest (ROI) can be defined consisting of a regular grid of points covering this region (solid circles in Fig. 5.2) located at positions $\mathbf{r}'_k$. The grid consists of n_{xy} *x* and *y* values separated a distance Δxy and n_z *z* values separated a distance Δz. The points corresponding to the discretized integral in Eq. (5.6) are depicted as hollow circles in Fig. 5.2. The optical absorption at these points $H(\mathbf{r}'_l)$ (for those points inside the grid) can be expressed as a function of the optical absorption at the eight neighbouring points of the grid by using trilinear interpolation, *i.e.*:

$$\begin{aligned}H(\mathbf{r}'_l)\approx{}&(1-\Delta x'_a)(1-\Delta y'_a)(1-\Delta z'_a)H_a+\Delta x'_a(1-\Delta y'_a)(1-\Delta z'_a)H_b\\&+(1-\Delta x'_a)\Delta y'_a(1-\Delta z'_a)H_c+(1-\Delta x'_a)(1-\Delta y'_a)\Delta z'_a\,H_e\\&+\Delta x'_a(1-\Delta y'_a)\Delta z'_a\,H_f+(1-\Delta x'_a)\Delta y'_a\,\Delta z'_a\,H_g\\&+\Delta x'_a\,\Delta y'_a(1-\Delta z'_a)H_a+\Delta x'_a\,\Delta y'_a\,\Delta z'_a\,H_h\end{aligned} \tag{5.7}$$

where $\Delta x'_a=(x'-x'_a)/\Delta xy$, $\Delta y'_a=(y'-y'_a)/\Delta xy$ and $\Delta z'_a=(z'-z'_a)/\Delta z$ and $H_k=H(x'_k,y'_k,z'_k)$. Then, by combining Eqs. (5.2), (5.6) and (5.7) the pressure in arbitrary units at a point $\mathbf{r}_i$ and at an instant t_j can be expressed as a linear combination of the optical absorption at the points of the grid, *i.e.*:

$$p(r_i, t_j) = \sum_{k=1}^{N} a_k^{ij} H(r'_k), \tag{5.8}$$

which corresponds to the discrete forward model that establishes the pressure as a function of the absorbed energy in the discrete ROI.

The theoretical pressure for a set of *P* transducer positions and *I* instants can be computed as a function of the optical absorption at the points of the grid with Eq. (5.8), so that a system of linear equations can be formulated, which is expressed in a matrix form as

$$\mathbf{p} = \mathbf{M}\mathbf{H} \tag{5.9}$$

being $\mathbf{M} \in \Re^{(P \cdot I) \times (n_{xy} \cdot n_{xy} \cdot n_z)}$ the model matrix, which depends solely on the geometry of the optoacoustic set-up and speed of sound in the medium, and $\mathbf{H}$ the optical absorption at the points of the grid arranged in vector form. The optoacoustic reconstruction consists of calculating the vector $\mathbf{H}$. This is done by minimizing the mean square difference between the theoretical pressure Eq. (5.9) and the measured pressure $\mathbf{p}_m$ at the same transducer positions and instants, *i.e.*:

$$\mathbf{H}_{sol} = \arg\min_{\mathbf{H}} \| \mathbf{p}_m - \mathbf{M}\mathbf{H} \|^2 \tag{5.10}$$

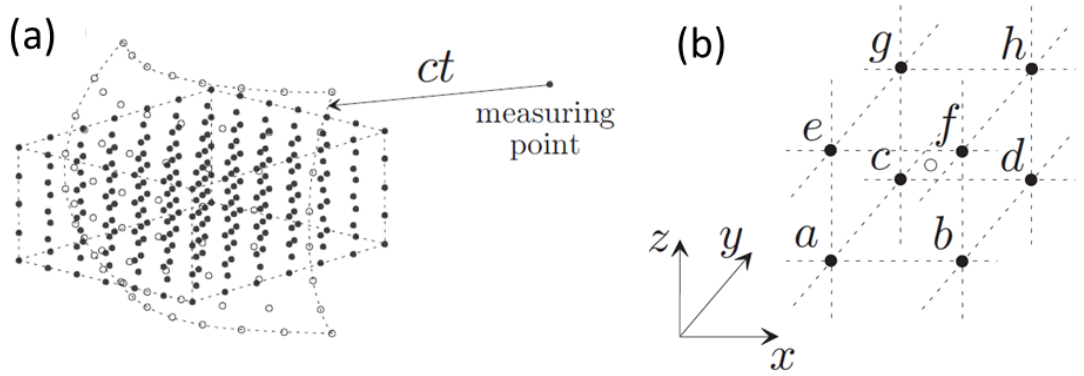

Fig. 5.2: 3D discretization of the optoacoustic forward model. (a) Grid points of the ROI (solid circles) along with the points used to discretize the integral (hollow circles). (b) Trilinear interpolation as a function of the eight neighbouring points. (Figure published in [109], Copyright 2012, IEEE).

5.3 Incorporating the transducer shape into the model

Detection of optoacoustic signals with detectors having a finite size leads to a spatial averaging and distortion of the measured signals because different points $\mathbf{r_d}$ of the transducer surface S detect the optoacoustic signal $p(\mathbf{r_d}, t)$ at different time points according to (cf. section 2.3.4)

$$p_d(t) = \int_S p(\mathbf{r_d}', t) dS(\mathbf{r_d}'). \tag{5.11}$$

In the model-based algorithm the time resolved optoacoustic signals $\mathbf{p_i}$ measured at the point $\mathbf{r_i}$ is expressed in form of a matrix relation

$$\mathbf{p_i} = \mathbf{M_i H} \tag{5.12}$$

where the $\mathbf{H}$ represents the optoacoustic source distribution and $\mathbf{M_i}$ the model matrix for a point detector at position $\mathbf{r_i}$. Combining the equations (5.11) and (5.12) the optoacoustic signal detected by a finite size detector $\mathbf{p}_\mathrm{d}$ can be discretized as

$$\mathbf{p}_\mathrm{d} = \mathbf{MH} = (\sum\nolimits_{\mathrm{i}\in\mathrm{S}} \mathbf{M_i})\mathbf{H} \tag{5.13}$$

where $\mathbf{M}$ represents the forward model for a finite size detector and i one point within the detection aperture S of the element. In that sense the forward model for a finite size detection element can be built by considering the detection surface as a set of discrete points and summing up the matrixes of the individual surface elements. In all what follows, a 3D model-based reconstruction with spatial impulse response will be termed *3D MB+SIR.*

5.4 Exploiting the matrix symmetry

The model matrix $\mathbf{M}$ has $P \cdot I \cdot n_{xy} \cdot n_{xy} \cdot n_z$ entries, where P stands for the number of tomographic views (projections) , I for the number of time instants at which the pressure signal is discretized and n_i $(i = xy, z)$ for the number of voxels in x-, y-, and z-direction. Although many of the matrix entries are zero and $\mathbf{M}$ sparse, becomes huge in 3D imaging scenarios [41]. To give a numerical example, the matrix for reconstructing a 22 x 22 x 8 mm³ big region with a rather modest voxel size of 200 x 200 x 200 µm³ and using 41 x 128 tomographic views (41 scanning positions in z-direction x 128 projections in the imaging plane) each comprising about 330 time instants, consists of about 1.7 million rows and around 0.5 million columns equivalent to approximately 590 Gbyte of data which has to be kept in the working memory of the PC. In order to compress the matrix size and reduce the memory requirements, a method to exploit the translational symmetry of the problem was developed in this work. Fig. 5.3 illustrates the principle. For simplicity the problem is illustrated in two dimensions with only three scanning positions in z-direction (S_1 to S_3). In Fig. 5.3 (a) we see the region of interest to be reconstructed delineated with solid lines. Fig. 5.3 (b) depicts the sub-matrix describing the optoacoustic wave propagation from the red voxels to the array located at position S_2. Each column of the sub-matrix represents the time-resolved signals from one voxel to the different sensor positions in the transducer array. Let's consider now scanning position S_3. Due to the symmetry of the problem the sub-matrix describing the wave propagation from the green voxels to the transducer array at position S_3 has to be the same as the matrix describing the wave propagation from the red voxels to position S_2. Thus it is possible to describe the wave propagation to S_3 by means of

the matrix calculated for S_2. In practical terms we calculate a forward model only for the central scanning position (here S_2) as depicted in (c), but for a region of interest double the size than the required one. This is necessary to represent all the distances. By rearranging the matrix elements like shown in (d) it is then possible to describe the wave propagation from each voxel to each transducer element, *i.e.* describe the whole model for a 3D reconstruction. The only condition is that the scanning positions are at a whole number multiples of Δz. Using iterative inversion methods (*e.g.* the LSQR algorithm) which require at each iteration step only a single column vector of the matrix and thus allow reordering the matrix elements according to the needs, it is possible to do the image reconstruction with a much smaller matrix size. The compression factor of the matrix achieved by this means is $P_s/2$, where P_s stands for the number of scanning positions. Coming back to the numerical example, this means that the matrix size is reduced by the factor of 20 and is only about 29.5 Gbyte big.

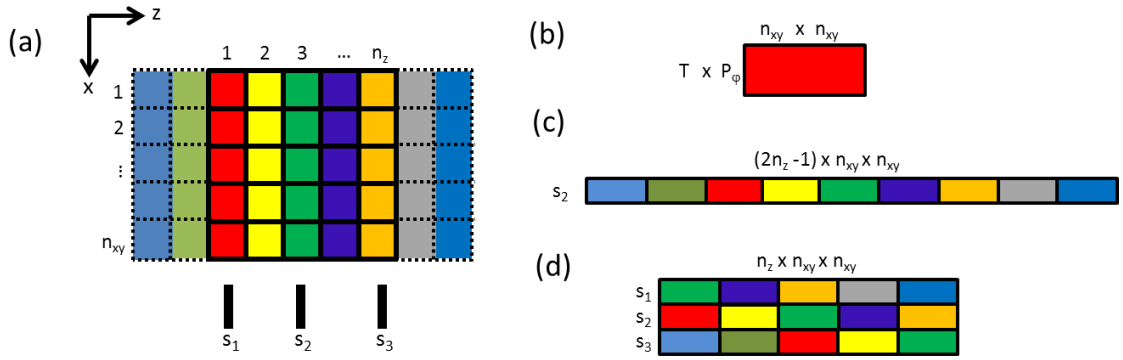

Fig. 5.3: Matrix compression for scanning in z-direction using the translational symmetry of the problem. (a) ROI to be reconstructed. For simplicity the problem is illustrated in 2D with only three scanning positions (S_1-S_3). (b) The sub-matrix describing the wave propagation from the red voxels in (a) to the array at scanning position 2. (c) The matrix calculated and stored in the computer memory. (d) The total matrix describing the wave propagation from each voxel to each sensor position. It is obtained by rearranging the elements of (c).

5.5 Numerical and experimental methods

5.5.1 Singular value analysis of the system matrix

In order to investigate how the focusing influences the numerical stability of the reconstruction problem a singular value analysis of the system matrix was performed. The singular value decomposition (cf. section 4.4.2) provides information about the capability of the system to reproduce features in the object space. A good imaging system should therefore be able to faithfully resolve as many eigen-images as possible. The energy of the acoustic signal from an eigen-image is proportional to the corresponding singular value, *i.e.* an eigen-image with a low singular value has little effect on the measured optoacoustic signal. The goal of the reconstruction is to recover the object, composed as a set of eigen-images, from the measured data. The singular values should therefore be as high as possible to guarantee that the corresponding eigen-images have significant effect on the optoacoustic signal and thus can be recovered, even in presence of noise. If the singular values are too low, the impact of the system noise leads to artifacts in the reconstruction. Therefore,

the more singular values are above this threshold, the more accurate and faithful the reconstructions with the imaging system.

To reduce memory requirements, and thus actually enable a singular value decomposition of the imaging operator, the analysis was reduced to two dimensions, which means scanning of a single detector in z-direction and reconstructing a 2D source distribution as illustrated in Fig. 5.3 (a). The forward model was calculated for a region of interest of 0.2 x 22 x 8 mm³ consisting of 1 x 111 x 41 voxels with a size of 200 x 200 x 200 µm³. Scanning in z-direction was simulated for several scanning apertures (4, 8, 16, 32, 64, 128 and 256 mm, respectively) with a constant step-size of 200 µm, both for a point detector and the focused detector of the small animal imaging system (height 15 mm, curvature 40 mm). The focused detector was simulated by discretizing its active surface by a set of 151 surface elements. The matrix of the point detectors was multiplied by 151 to achieve the same scaling. The singular value decomposition of the imaging operators were performed in Matlab *via* the built-in singular value decomposition function (svd, MATLAB version R2011b).

5.5.2 Implementation of the reconstruction algorithms

For *3D MB+SIR* image reconstruction a forward model was calculated on a 22 x 22 x 16 mm³ large Cartesian grid consisting of 181 x 181 x 21 voxels with a size of 122 x 122 x 400 µm³. For detection a 172° cylindrically focused transducer array was assumed comprising 128 elements confocal to the central slice of the region of interest. Each element of the array was shaped in elevation with a curvature radius of 40 mm and a chord length (height) of 15 mm in analogy to the elements employed in the small animal imaging scanner. In contrast, in azimuth direction (width) the elements were considered as point detectors to decrease computational burden. The shape of a single element is depicted in Fig. 5.6 (a). As explained in section 5.4, the calculated matrix is sufficient to model scanning in z-direction over 21 scanning positions within a 22 x 22 x 8 mm³ large volume and a step size of 400 µm by using symmetry relations. A voxel size of 400 µm in z-direction was chosen corresponding to half the maximal resolution that can be achieved by focusing (cf. section 3.4.6.2) to reduce memory requirements. The height of 8 mm corresponds to the width of the illumination ring. The spatial impulse response of the detection element was included into the model by summation of the matrices corresponding to individual surface elements of the transducer's active aperture according to Eq. (5.3) with a discretization period of 100 µm, *i.e.* each detector element consisted 151 point detectors. For the given parameter set, a finer discretization had no positive effect on the calculated model and only prolonged the computation time. For inversion the LSQR method (cf. section 4.4.2.2) was used, modified to exploit the translational symmetry of the matrix in each iteration step. All operations were implemented in Matlab and executed on a workstation with sixteen X5650 Intel Xeon cores, each with 2.67 GHz, and 144 Gb of RAM. For computation of the forward model the 16 processors run in parallel. For inversion only one core was used. The final size of the matrix, its computation time and the time for the inversion can be found in Table 1.

The results were compared to 2D backprojection (*2D BP*), 2D IMMI (*2D MB*), *3D MB* assuming point detectors and *3D MB+SIR* reconstructions using only data from one scanning position (*3D MB1SP+SIR)*. Volumetric images were obtained by stacking the individual cross-sectional slices. In the case of the *3D MB1SP+SIR* reconstructions, only the central slice from the reconstructed volume was used.

After reconstruction all results were linearly interpolated to a grid with uniform 50 x 50 x 50 µm³ voxel size.

Study	n_x, n_y ,n_z	voxel size [µm]	P_{array}	P_{scan}	T_{calc} [h]	matrix size [Gb]	1-iter [s]
3D MB+SIR	181 x 181 x 21	122 x 122 x 400	128	21	1.2	92.6	633
3D MB1SP+SIR	181 x 181 x 21	122 x 122 x 400	128	1	1.2	48	5

Table 1: Parameters for the matrices: n_x, n_y, n_z : number of voxels describing the region of interest; P_{array}: sensors in the array; P_{scan}: number of scanning positions in z-direction, T_{calc}: time it took to calculate one projection in the forward model, 1-iter: time it took to do one iteration.

5.5.3 Sliding volume technique

Big objects like whole mice cannot be reconstructed in a single inversion procedure, because the matrix describing the forward problem would be in the order of 900 Gbytes, even when using the translational symmetry, which is too large to be stored in the working memory of the computer. Therefore a sliding volume technique was devised. It is illustrated in Fig. 5.4 and consists of scanning a smaller volume of interest along the longitudional axis of the object (z-direction), reconstructing each volume with the *3D MB+SIR* method using data from adjacent scanning positions and then concatenating the central slices of the individual reconstructions. This is comparable to the *3D MB1SP+SIR* technique, except that data from several scanning positions is used for the inversion. The size of the volume of interest and scanning positions used in the reconstructions depends on the field of view of the transducers. If the field of view is constraint as it is the case for focused detectors, only the detectors which actually detect signals from the central slice of the volume of interest have to be considered in the inversion.

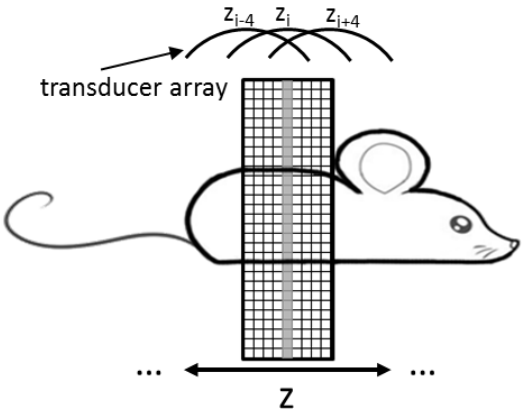

Fig. 5.4: Sliding volume technique for three scanning positions. The volume depicted by the grid and centered at z_i is reconstructed using data acquired with the array at scanning positions z_{i-4}, z_i and z_{i+4}. By scanning the volume through the sample and concatenating the central slices (here at z_i), a 3D reconstruction is obtained.

5.5.4 Simulation of theoretical signals

The reconstruction approaches were tested on a three dimensional truncated parabolic absorbers distribution,

$$H(x,y,z) = \begin{cases} 1 - \dfrac{\Delta x_s{}^2 + \Delta y_s{}^2 + \Delta z_s{}^2}{a^2}, & \Delta x_s{}^2 + \Delta y_s{}^2 + \Delta z_s{}^2 \leq a^2 \\ 0, & \Delta x_s{}^2 + \Delta y_s{}^2 + \Delta z_s{}^2 > a^2 \end{cases} \tag{5.14}$$

where a denotes the radius of one absorber, $\mathbf{r}_s$ its position and $\Delta x_s = x - x_s$, $\Delta y_s = y - y_s$ z$= z - z_s$. The optoacoustic signal of such a truncated parabolic absorber can be calculated analytically and is given by [110]

$$p(0,t) = \frac{\Gamma}{c}\left(c - \frac{cx_s^2}{a^2} - \frac{c^2}{x_s}t + \frac{3c^2x_s}{a^2}t - \frac{3c^3}{a^2}t^2 + \frac{c^4}{x_s a^2}t^3\right) \tag{5.15}$$

where for simplicity the transducer is supposed to be located at the origin of the coordinate system and the source at x_s. To consider the effect of the spatial impulse response (SIR), these analytical signals were averaged over the transducer surface according to Eq. (5.11) with a discrete spatial sampling period of 10 µm and a temporal sampling frequency of 200 MHz. The speed of sound was chosen to be 1506 ms^{-1} corresponding to the one used in the experimental imaging situations.

Moreover, signals were simulated for a complex 3D source distribution using the previously presented forward model, but on a different grid (ROI: 22 x 22 x 14 mm³, voxel size: 135 x 135 x 200 µm³). To avoid committing the inverse crime, the signals were further convolved with the electrical impulse response of the imaging system (cf. section 3.4.3). A cross-sectional and sagittal slice through the source distribution is depicted in Fig. 5.7 (d) and (e). Its extension in z-direction is 7.2 mm. Outside this area zero absorption was assumed.

5.5.5 Image quality assessment

Image quality was assessed by visual inspection. For that each reconstructed image was normalized to its maximum and displayed on the same colorbar. In case of the simulation study, the Pearson's correlation coefficient (Eq. (6.8)) between reconstruction result and solution was calculated as a metric of reconstruction accuracy.

5.5.6 Experimental data

The method was also tested on experimental data acquired with the small animal imaging system. Two phantoms and one mouse were imaged.

Phantom data

The phantoms were embedded in a 1.9 cm in diameter big agar cylinder with light scattering properties achieved by adding intralipid. The first phantom consisted of 5

black polyethylene microspheres with an approximate diameter of 200 μm (Cospheric BKPMS 180 - 210 μm) positioned along one line in the same slice as shown in Fig. 5.10. The second phantom was a loop made out of a blue 300 μm in diameter big thread. A photograph of the thread is shown in Fig. 5.11. The imaging wavelength was 750 nm and the step size for scanning in the elevational direction was 400 μm in both cases. For reconstruction, the same matrix as in the simulation study was employed. Since the system only allows measuring 64 projections per scanning position, the interpolation technique presented in section 4.3 was used to attain a set of 128. The iterations were terminated when the relative change in the residual error Eq. (4.17) was below 0.001.

Mouse data

One CD-1 nu/nu mouse (Charles River Laboratories, Sulzfeld, Germany) was imaged *in vivo* in supine position, *i.e.* lying on its back. The mouse was anesthetized with Isoflurane. A whole body dataset was acquired in 400 μm steps. For reconstructing the mouse, a sliding volume technique was used. The region of interest had a size of 22 x 22 x 8 mm^3 and was scanned in 400 μm steps in z-direction throughout the mouse. Each volume was reconstructed using data from 11 scanning positions symmetrically arranged around the central slice. Likewise the inversion procedure was terminated when the residual error was below 0.1%. The final 3D reconstruction was obtained by concatenating all the central slices of the individual reconstructions.

5.6 Results

5.6.1 Numerical stability of the imaging operator

Fig. 5.5 depicts the singular values in ascending order. For the same scanning aperture, the singular values of the point detectors are higher than for the focused detectors. This shows that the image reconstruction problem is more ill-conditioned for focused detectors and thus more affected by data inconsistencies. Also, less eigen-images can faithfully be recovered for a given noise level. When increasing the scanning aperture, singular values decay slower. This shows that by increasing the scanning aperture, the image reconstruction problem stabilizes and the object can be reproduced more accurately. Yet, the rate of improvement is considerably slower for focused detectors than for point detectors and actually becomes insignificant for scanning apertures beyond 16 mm. The reason is the limited field of view of the focused detector due to which, at a given distance, it does not detect signals from the object anymore. Overall, this study shows that by scanning a focused detection element, it is not possible to resolve all eigen-images and thus yield perfect 3D reconstructions, even by accurate modeling of the detectors. Some structures, in particularly the one perpendicular to the scanning direction, can simply not be resolved. This is in contrast to point detectors which, for a sufficiently long scanning aperture and sufficiently high SNR, can achieve this. On the other hand, focused detectors, due to their increased detection aperture, have the advantage of yielding

a higher SNR, which actually lowers the noise level of the system and the threshold below which the eigen-images become not useful.

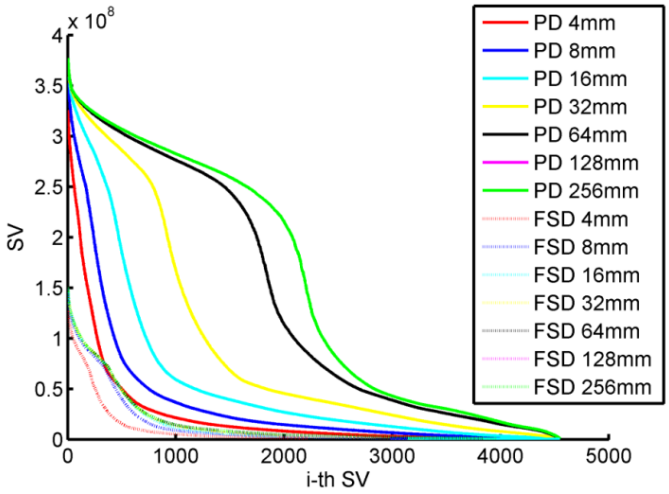

Fig. 5.5: Singular value analysis of the imaging operator for point and finite size detectors as a function of the scanning aperture.

5.6.2 Comparison between analytical and simulated signals

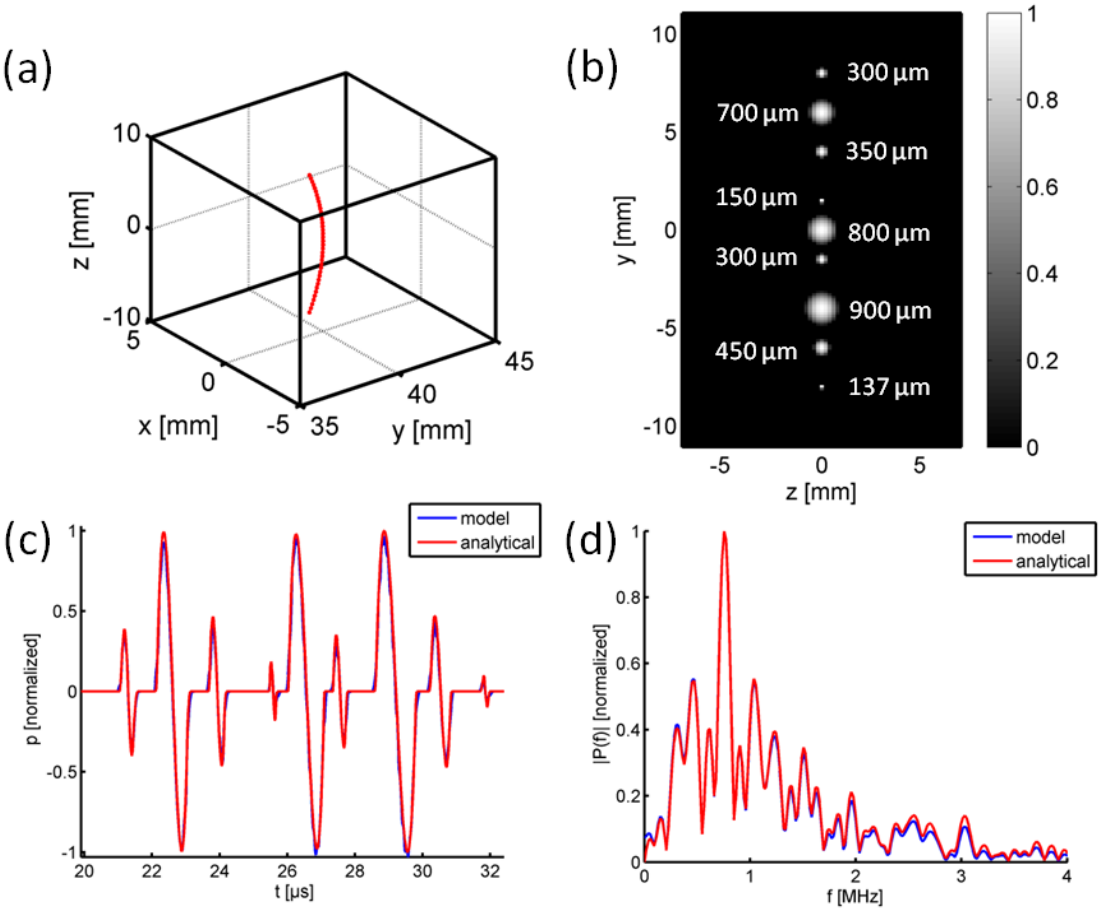

Fig. 5.6: Comparison between analytical signal and signal obtained from the model. (a) Shape of the transducer element and source distribution (b) for which the signal was calculated. The numbers next to the absorbers present their radius. (c) Comparison between analytical signal and signal from the model and the corresponding frequency spectra (d).

Fig. 5.6 compares the analytical signal and the signal from the model. The transducer for which the signals were calculated is shown in (a) and the source distribution in (b). The signals are shown in (c) and the corresponding frequency spectra in (d). The two signals show good agreement, both in the time and frequency domain, ensuring that the model is accurate. Minimal deviations at high frequencies are due to discretization errors produced by approximating the actual absorber distribution on a discrete grid. This can be improved by a finer discretization of the reconstruction grid.

5.6.3 Optimal choice of the region of interest

Fig. 5.7 depicts cross-sectional reconstructions obtained with the *3D MB1SP+SIR* method for the complex numerical phantom reconstructed on different regions of interest: (a) 22 x 22 x 1.2 mm³ (b) 22 x 22 x 7.6 mm³ and (c) 22 x 22 x 14 mm³. The originating source distribution is shown in (d) and (e). The correlation coefficient between reconstructed cross-sectional slice and solution for different heights of the region of interest is given in (f). It shows that in order to achieve the most accurate reconstruction it is necessary to select the height of the reconstructed region of interest according to the volume within which optoacoustic signals are generated. Herein, these are 7.2 mm. If the height of the region of interest is too small, low frequency out-of-plane signals are projected into the imaging plane leading to an over-estimation of low frequency components as shown in Fig. 5.7 (a). On the

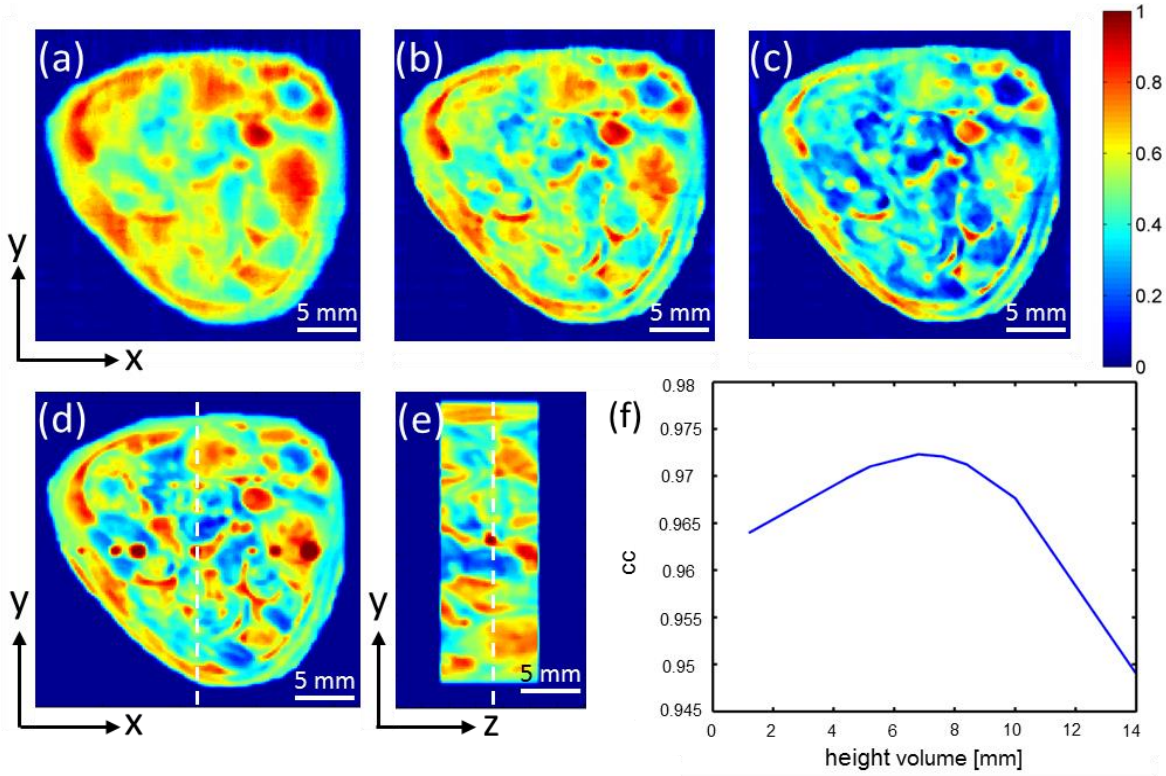

Fig. 5.7: Cross-sectional *3D MB1SP+SIR* reconstructions of simulated data for regions of interest with varying heights: (a) 1.2 mm, (b) 7.6 mm and (c) 14 mm height. A cross-sectional and sagittal slice through the originating 3D source distribution is shown in (d) and (e), respectively. The dashed lines indicate the location of the slices reconstructed. (f) shows the correlation coefficient between cross-sectional reconstruction and solution for different heights. Best accuracy is obtained when the region of interest corresponds to the area where the signal is generated from. Scalebar: 5 mm.

other hand, if the height of the region of interest is larger than the originating source distribution (*e.g.* Fig. 5.7 (c)), then the energy of the signal is distributed within a too big volume leading to an underestimation of low frequency components.

5.6.4 Algorithm performance with simulated data

Fig. 5.8 depicts sagittal slices through the *2D MB* (a), *2D BP* (b), *3D MB1SP+SIR* (c), *3D MB* (d) and *3D MB+SIR* (e) reconstruction of the truncated parabolic absorber distribution shown in (f). The focusing-based image formation techniques (a)-(c) display differently sized absorbers with different length. In addition, in the periphery, the absorbers show a banana shape. Both effects are due to frequency dependent focusing imperfections in combination with time of flight differences. The *3D MB* reconstruction with point detectors representing the visually most appealing result obtained after 2 iterations is shown in (d). Stopping the iterations that early was necessary because otherwise, due to the strong mismatch between model and experimental data, the model diverged to a solution merely representing artifacts, overall confirming that 3D reconstructions assuming point detectors are not suited in case of focused detection elements. On the other hand, the *3D MB+SIR* reconstructions resemble closely the originating source distribution. The absorbers do not show the banana shape and display more accurate intensity values. The actual source distribution could however not be resolved. The reason is the ill-conditionedness of the imaging operator due to which the inversion procedure becomes semi-convergent. This can be seen in Fig. 5.8 (e) depicting the residual error (R) and correlation coefficient (cc) as a function of the iteration step. First the method approaches the solution but then converges to an erroneous result by introducing errors. Reasons for the ill-conditionedness of the inversion are the limited detection arc of 172° (cf. section 4.4) and the finite detector size (cf. section 2.4.5).

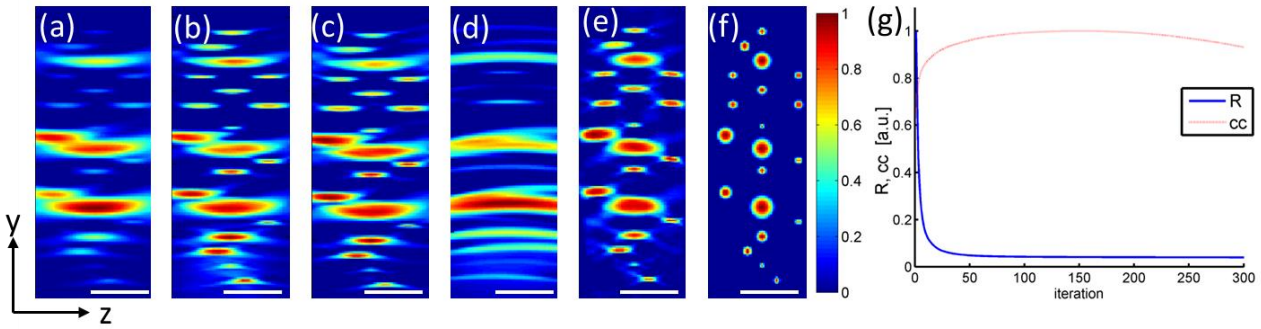

Fig. 5.8: Sagittal slices through the truncated parabolic absorber distribution reconstructed *with 2D MB* (a), *2D BP* (b), *3D MB1SP+SIR* (c*), 3D MB (d) 3D MB+SIR* (e) algorithm and solution (f). (g) Residual error (R) and correlation coefficient (cc) between solution and 3D MB+SIR reconstruction as a function of the iteration showing semi-convergence of the method. Scalebar: 4 mm.

Fig. 5.9 compares the reconstruction methods on the complex source distribution. The first row shows cross-sectional slices through the reconstructed volume and the second row transverse slices. The dashed lines in (e) and (j), respectively, indicate where the slices are taken from. Again, as seen from the images and the correlation coefficient, best results are achieved with the *3D MB+SIR* method. *2D MB*

reconstructions suffer from low frequency out-of-plane signals which reduce contrast and mask the high frequency components. *2B BP* reconstructions on the other hand accentuate small structures and boundaries but lack low frequency information. *3D MB+SIR* and *3D MB1SP+SIR* reconstructions do not show such problems. But only the *3D MB+SIR* algorithm manages to improves the image quality in z-direction, yet only to a limited extent, due to the semi-convergence of the method.

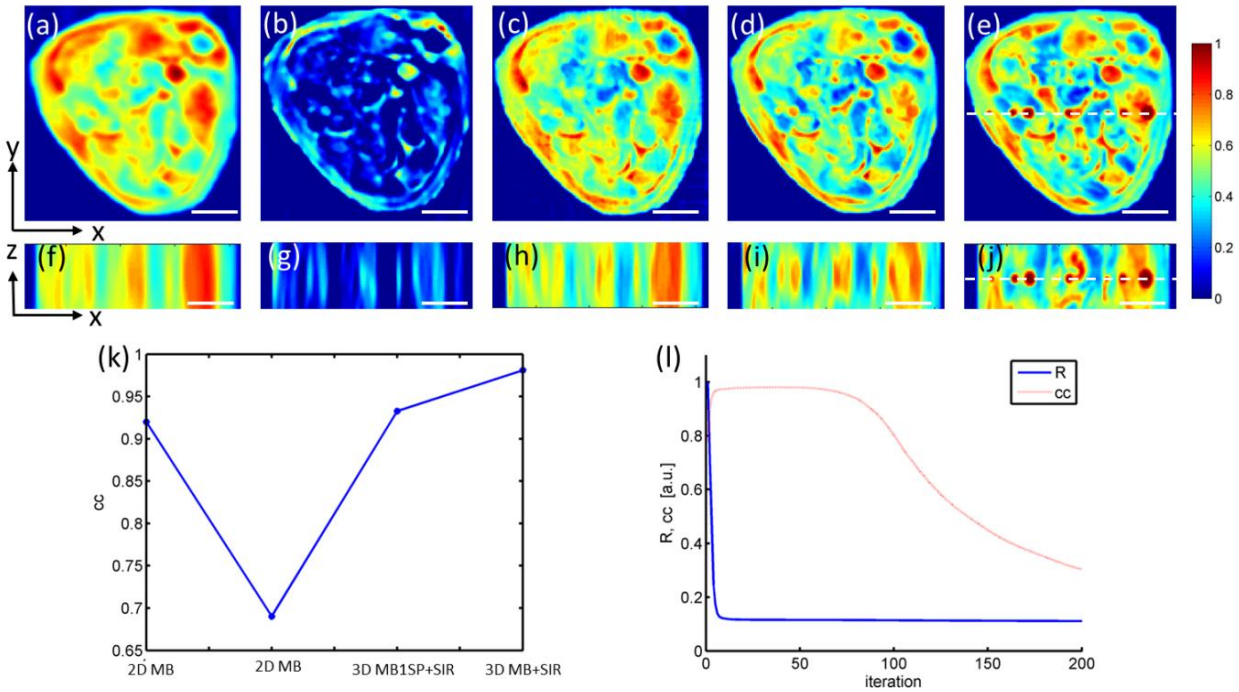

Fig. 5.9: Reconstructions of a complex phantom using the four algorithms. The first row depicts cross-sectional slices from the reconstructed volume, the second row slices along the xz-plane. From the left to the right we see *2D MB, 2D BP, 3D MB1SP+SIR* and *3D MB+SIR* reconstructions and the originating source distribution, respectively. (k) shows the correlation between reconstruction and solution as a function of the algorithm. (l) Residual error and correlation coefficient as a function of the iteration step. Scalebar: 5 mm

5.6.5 3D reconstructions using experimental data

Phantom data

Fig. 5.10 depicts the maximum intensitiy projection (MIP) of the volumetric reconstruction of the microsphere phantom along the x-direction using the *2D MB* (a), the *2D BP* (b), the *3D MB1SP+SIR* (c) and the *3D MB+SIR* algorithm (d). The profile through the third microsphere along z-direction is shown in (f). The length of the reconstructed microspheres as determined from their full-width-at-half-maximum (FWHM) in z-direction is given in (g). For the three stacking-based approaches, the microspheres are displayed with a length varying between 1.3 mm in the center of the region of interest and 3 mm in the periphery. In the periphery, they have a slight banana shape due to a longer time of flight in combination with a reduced focusing capacity. The microspheres in the *2D BP* reconstructions are about 200 - 400 µm shorter than for the *2D MB* and *3D MB1SP+SIR* algorithm. Best results are obtained for *3D MB+SIR* reconstructions. The length of the microspheres is

reduced to 900 ± 100 µm and is about uniform within the ROI. The *3D MB+SIR* reconstructions do also not show the banana shape.

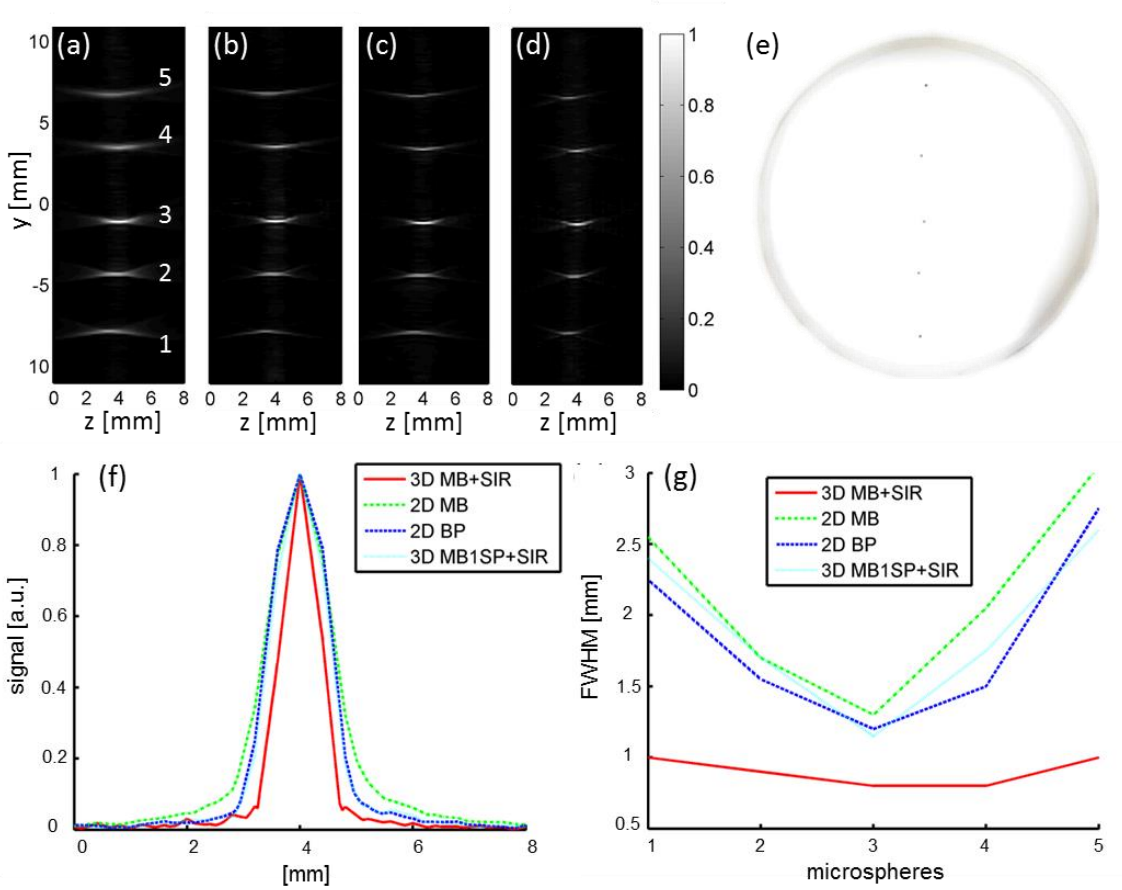

Fig. 5.10: Maximum intensity projection along the x-axis of the microsphere phantom reconstructed with (a) *2D MB*, (b) *2D BP*, (c) *3D MB1SP+SIR* and (d) the *3D MB+SIR* algorithm, respectively. (e) Photography of the microsphere phantom. (f) Profiles through microsphere 3 along the z-axis. (f) Length of the microspheres in z-direction as determined by their FWHM. Modeling the detector surface homogenizes resolution along the z-axis compared to stacking the cross-sectional reconstructions.

Fig. 5.11 shows in the first row a MIP view along the x-direction of the 3D reconstruction of the thread phantom obtained with the four approaches. The second row depicts a cross-sectional slice through the 3D volume as indicated by the yellow line. The profiles along the red line are shown in panel (i). A photo of the thread is shown in Fig 5.11 (j) for reference. The MIP view along the x-axis shows that *2D BP*, *2D MB* and *3D MB1SP+SIR* reconstructions are blurred in z-direction. Structures parallel to the y-axis are hardly visible. In contrast, when the spatial impulse response and data from several scanning positions is considered in the reconstruction, apparent improvement is achieved. The form of the thread is more accurately resolved and structures parallel to the y-axis are clearer visible. Out-of-plane signals are also reduced as seen from the cross-sectional images. The displayed thickness of the thread is in the order of 1 mm in z-direction and about 300 µm within the xy-plane. Thus it is displayed correctly in the xy-plane but not along the z-direction. The effect of the directivity of optoacoustic signals in combination with limited view detection is also perceived in this example, as the part of the thread oriented along the z-direction is reconstructed with higher

amplitude. The effect is however reduced compared to the other three approaches, for which elongated structures perpendicular to the scanning directions are hardly visible.

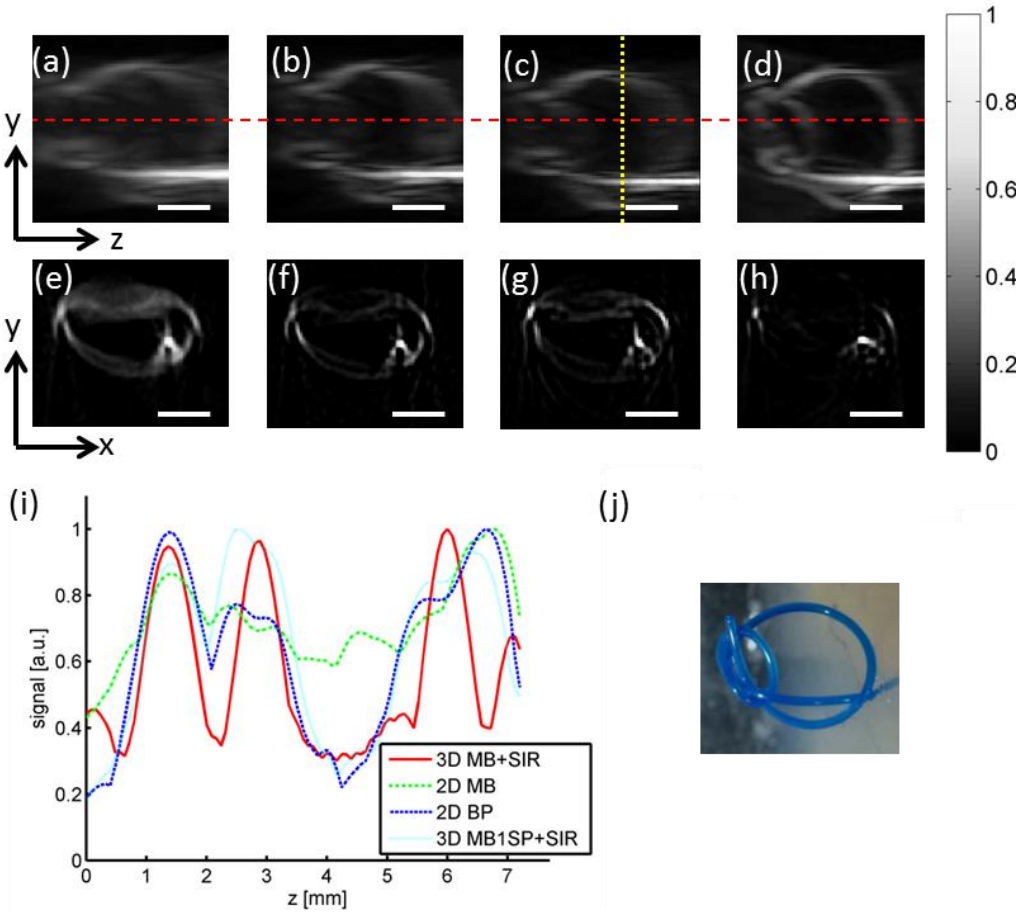

Fig. 5.11: Reconstruction of the thread phantom. The first row shows MIP views of the reconstructed volume using the (a) *2D MB,* (b) *2D BP,* (c) *3D MB1SP+SIR* and (d) *3D MB+SIR* algorithm, respectively. The second row depicts a cross-sectional slice through the reconstructed volumes as indicated by the yellow line. (i) shows a plot along the red line and (j) a photograph of the thread phantom. Scalebar: 2 mm.

In vivo mouse data

Finally, Fig. 5.12 depicts the whole body mouse reconstructions. The first four rows depict *2D MB, 2D BP, 3D MB1SP+SIR* and *3D MB+SIR* reconstructions, respectively. The fifth row a cross-sectional slice from the kidney region. The first column shows a MIP view of the whole 3D volume along the y-direction and the second column a single 300 µm thick transverse slice. The position where the cross-sectional and transverse slices were taken from are indicated by the red and yellow dashed line. Similar to the previous examples, the *3D MB+SIR* method yields significantly improved results. Elongated structures approximately perpendicular to the scanning direction, like the vertically oriented blood vessels seen in (e), are clearly resolved, which is not the case for the other three methods. As in the simulation study, small structure and boundaries are accentuated with the *2D BP* algorithm, whereas they are masked in the *2D MB* reconstructions by low frequency out-of-plane signals reducing contrast.

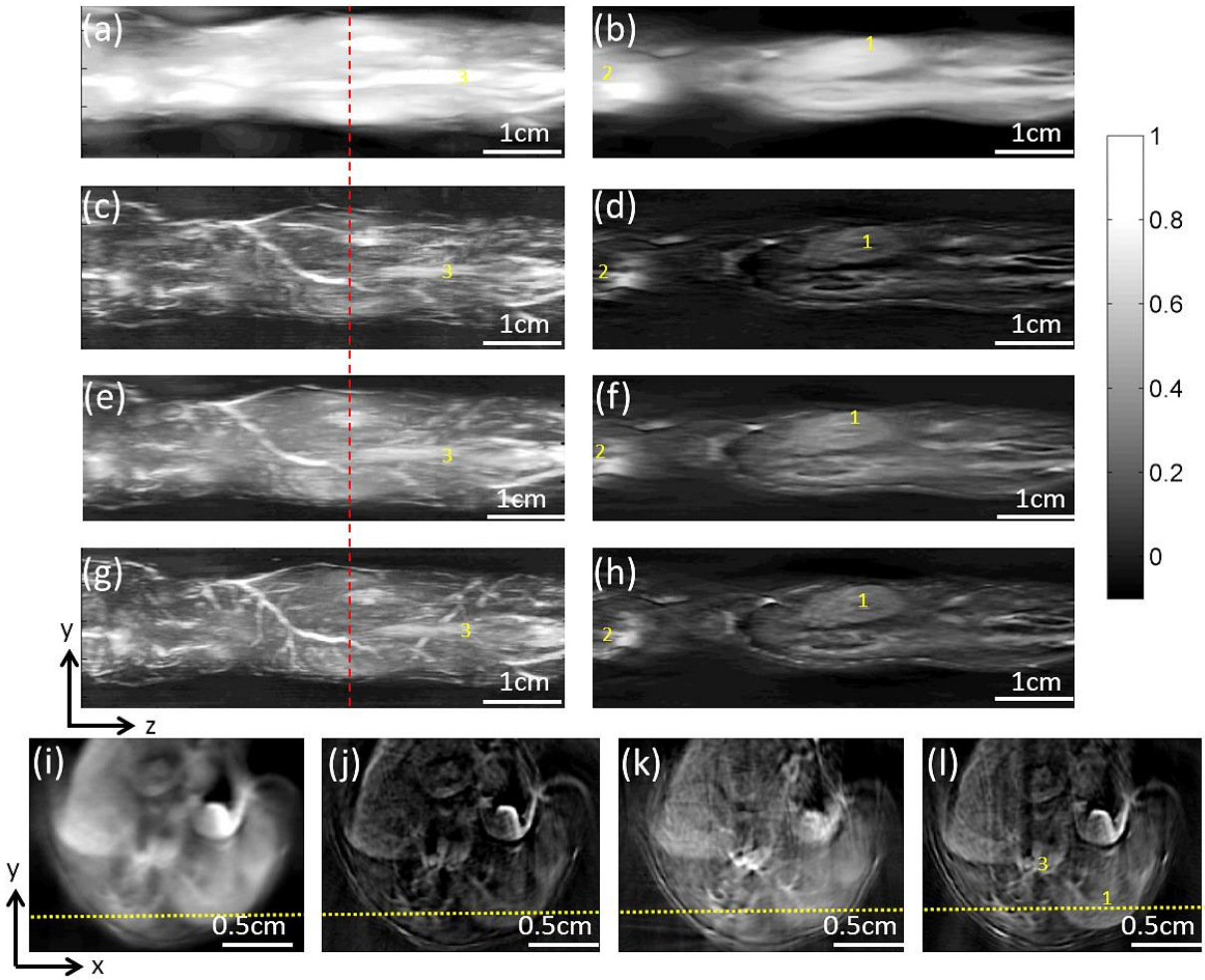

Fig. 5.12: Whole body mouse reconstructions. The first four rows show *2D MB*, *2D BP*, *3D MB1SP+SIR* and *3D MB+SIR* reconstructions, respectively. The fifth row shows cross-sectional slices from the area indicated by the red dashed line. The MIP view of the whole volume along the y-axis is shown in the first column, the MIP along a 300 µm thick transverse slice in the second column. 1: right kidney, 2: sagittal sinus, 3: vena cava.

5.7 Discussion and conclusion

Whereas scanning-based setups utilizing cylindrically focused transducers have many advantages such as enabling cross-sectional real-time imaging, good SNR and high in-plane resolution, accurate image reconstruction is a very challenging problem. This is because the spatial impulse response of the focused detector significantly distorts the measured optoacoustic signals. As a consequence, standard 3D reconstruction formula assuming point detectors are not suitable for image reconstruction.

To improve optoacoustic reconstructions in such a setting, the spatial impulse response has to be considered in the inversion process. Since this is not possible using analytical inversion formulations, such as the backprojection algorithms, a 3D model-based inversion scheme was adapted to account for the shape of the detection elements (*3D MB+SIR*). The spatial impulse response was included into the model by discretizing the active surface of the transducer by a set of point detectors. The method was tested in numerical simulations and validated on experimental data

from the small animal scanner and showed in both cases clear improvement of the reconstructions compared to the previously available and utilized *2D BP* and *2D MB* methods.

Best performance was achieved when tomographic views from several scanning positions were used in the inversion procedure. Structures perpendicular to the scanning direction, which were blurred in the 2D focusing-based approaches, were clearly resolved with the new method. Microspheres were displayed with a length of about 900 ± 100 µm in z-direction, independent of their positions and did not display the banana shape typically for the stacking approaches due to a combination of spatial dependent focusing and time of flight differences. But also 2D reconstructions, *i.e.* reconstructions which involve data from only one scanning position, became more accurate with the proposed approach. The advantage of *3D MB1SP+SIR* compared to the *2D MB* reconstructions is that the result is less affected by out-of-plane artifacts, which reduce contrast and mask small structures. This is because the method knows that the signal can come from a 3D volume and thus does not project all the low frequencies out of-plane signals, for which the focusing is weak, into the imaging plane. In contrast, the *2D MB* method is based on the assumption that it only receives in-plane acoustic signals, which is not completely valid in deep tissue due to the illumination of a bigger area and light scattering. Compared to backprojection reconstructions, the representation of low frequency information is improved, when the reconstructed volume corresponds to the illuminated area, *i.e.* the volume signals are generated from. A too big volume leads to an underestimation of low frequency information in the imaging plane, a too small volume to an overestimation. This is because the model distributes the energy within the whole region of interest according to sensitivity distribution of the system. Backprojection formulas underestimate the low frequencies because they do not consider the spatial impulse response and are only valid for 3D closed detection geometries. Also, they cannot deal with arbitrary detection geometries like the model-based inversion schemes. Since the system of equation is highly underdetermined for one scanning position, which becomes worse the more voxels are to be resolved, regularization is necessary. Herein, this was achieved by stopping the iterations, when the relative change in the residual error Eq. (4.17) become lower than 0.1%. What stacking of *3D MB1SP+SIR* reconstructions could not achieve, was resolving structures perpendicular to the scanning direction. This actually requires that data from several scanning position is used in the reconstruction. Such complementary information reduces the ill-conditionedness of the inversion problem and helps finding a more accurate solution. Nevertheless, due to the limited view detection in the small animal scanner and the finite detector size, the inversion procedure remained semi-convergent and iterations had to be stopped to avoid creation of artifacts. The heuristically determined stopping criteria for experimental data acquired with the small animal scanner was a relative change in the residual error lower than 0.1%. Additional simulations not shown herein indicated however that this issue improves for transducer arrays with more elements and a longer detection arcs, thus yielding even more accurate reconstructions.

Concerning practical image reconstruction this means that when only data from one scanning position is available, it is best to use the newly developed *3D MB1SP+SIR*

method for a region of interest corresponding to the illuminated area, *i.e.* the region where signals can originate from. When data from several scanning positions is available, the *3D MB+SIR* approach gives the best results. But in contrast to point-detectors, for which a sufficiently long scanning aperture can yield exact reconstructions, focused detectors cannot achieve this due to their constrained field of view. Thus there is also no benefit in enlarging the scanning aperture beyond the actual field of view of the transducer.

Yet, as all algebraic reconstruction problems, the method becomes very time and memory consuming as the resolution increases. The memory requirements for a 3D reconstruction are easily in the order of several hundreds of Gigabytes, although the matrix describing the imaging problem is sparse. The sparseness of a matrix with modeled detector shape is lower compared to the point detector analogue, thus more memory is required. This is because the finite detector size acts as a lowpass filter elongates the signal and thus reducing the number of zero elements. To reduce memory requirements and make model-based 3D reconstructions actually feasible, a method to exploit the translational symmetry of the reconstruction problem was devised and resulted in a size reduction of $P_s/2$ where P_s stands for the number of scanning positions included in the model. Moreover, non-isotropic voxels were used. Nevertheless, the memory requirements were still in the order of 100 Gbytes and a workstation computer with 144 Gbytes of RAM was necessary to do the reconstruction. Having established that considering the spatial impulse response in the inversion procedure actually improves the reconstructions in such a cylindrically scanning-based setup, future research has to focus on investigation of methods to further compress the matrix size in order to enable faster and higher resolution reconstructions. A promising approach to achieve this might be the decomposition of the forward model by wavelet packets as proposed and shown for the 2D case by Rosenthal et al. [111]. Beside reduction of the matrix size, this method has the advantage of enabling fast image reconstruction, especially in fixed array configurations. When the matrix is inverted, then the image reconstruction process is merely a multiplication of a matrix with a vector.

Moreover, approximating the detector surface by point detectors is computationally expensive. Acceleration in building the forward model was achieved by neglecting the azimuthal extension of the transducer. This was possible herein for two reasons: First, because in the presented system the width of the detection element has minor influence on the optoacoustic signal compared to its elevation extension. Second, because in order to correct the in-plane spreading of the point spread function (cf. section 3.4.6.1) by modeling the spatial impulse response, complementary views are required, either from overlapping detector positions, or from opposing views which both were not available in the small animal scanner. Nevertheless, it took three days to compute the forward model for the presented examples. Although this is quite long, this has little effect on practical imaging, because in the presented system, due to the fixed array configuration and controlled water temperature, the matrix has to be only calculated once and can be reused for other reconstructions. To speed up the modeling of the transducer surface, current work at IBMI focuses on approximating the active surface of the detection element by a set of lines instead of points. This reduces computation time, especially for broad flat detection elements.

On the other hand, the approximation by points presented herein leaves more flexibility for modeling curved or arbitrary shapes. To further speed up the computation time, the calculation of the forward model can be implemented on the Graphics Processing Unit (GPU) of the computer to achieve a higher order of parallelization.

6 Multispectral imaging

6.1 Introduction

The motivation of this research is the need for a tool to visualize different photo-absorbing molecules of biological importance, non-invasively, with high spatial resolution, deep inside living tissue, in particularly in mice. Because some highly concentrated and strongly absorbing intrinsic chromophores, such as hemoglobin or melanin, dominate single wavelength images, it can be challenging to identify specific substances, such as extrinsically administered contrast agents or genetically expressed proteins, within such a background, even if the selected wavelength corresponds to the absorption maximum of the agent of interest. This is illustrated in Fig. 6.1 (a) showing single wavelength images from the liver area of a euthanized mouse through which two plastic tubes were inserted and filled with the fluorochromes Indocyanine Green (ICG) and Cyanine7 (Cy7), respectively. It is not possible to identify the tubes within the tissue background signal solely based on their signal intensity in either of the images.

A typically approach to differentiate administered probes from intrinsic background absorbers is the subtraction of background measurements made before probe administration. Yet, this requires the exact same animal positioning which is difficult to realize, especially in longitudinal imaging studies where measurements are required on time-points several hours or even days apart [4].

To overcome this limitation, multi-wavelength illumination in combination with multi-spectral unmixing has been proposed by Razansky *et al.* in [6]. It allows the spectral signatures of the absorbers to be taken into account as an additional source of information and thus enables their specific detection. Fig. 6.1 (b) depicts the spectral profiles obtained from the two locations (1 and 2) where the tubes are located and from a blood vessel (3) clearly indicating different spectral characteristics based on which it is possible to differentiate between absorbers and resolve them individually as shown in (c) and (d).

This chapter deals with the problem of multispectral imaging in deep tissue. Starting with the formulation of the multispectral unmixing problem and the particular challenges in deep tissue, namely spectral coloring due to wavelength dependent light attenuation, two multispectral unmixing algorithms for detection of molecular agents are presented and tested in simulation and on experimental data. The first is a spectral fitting approach which attempts to detect molecular agents by fitting the multispectral dataset in a least squares sense to a set of spectral components assumed to represent the absorbing entities [4]. The second method proposed by Glatz *et al.* and myself in 2011 [112], is a blind unmixing approach, which, in contrast to the spectral fitting approach, does not require a priori knowledge about absorbing spectra. It detects the agent by statistical means as spectral outliers that exhibit a significantly different spectrum than the surrounding background. The rational for employing a blind unmixing approach for spectral decomposition is that for *in vivo* tissue measurements, reliable spectral information for all potential

contributions to the signal is generally not available, due to spectral coloring and reconstruction inaccuracies and unexpected background absorbers. Also, the spectra might change depending on the biochemical environment or the concentration [112]. The spectrum of hemoglobin (cf. section 2.2.1) for instance depends on its oxygenation level and the spectrum of Indocyanine Green (ICG), a frequently used fluorescent dye, on its concentration [113].

In the second part of this chapter, methods for light attenuation correction are discussed. As photon fluence is strongly attenuated in tissue as a function of depth and wavelength due to scattering and absorption, absorbers at different depths will be excited differently. Thus an absorber embedded deep within tissue may appear weaker than one close to the tissues surface so that the overall comparability of signals from different depths is severely limited. A method is proposed based on a ratio normalization using images acquired at several different wavelengths. Moreover, it will be shown in simulation and experiments that this approach can partially compensate for this effect.

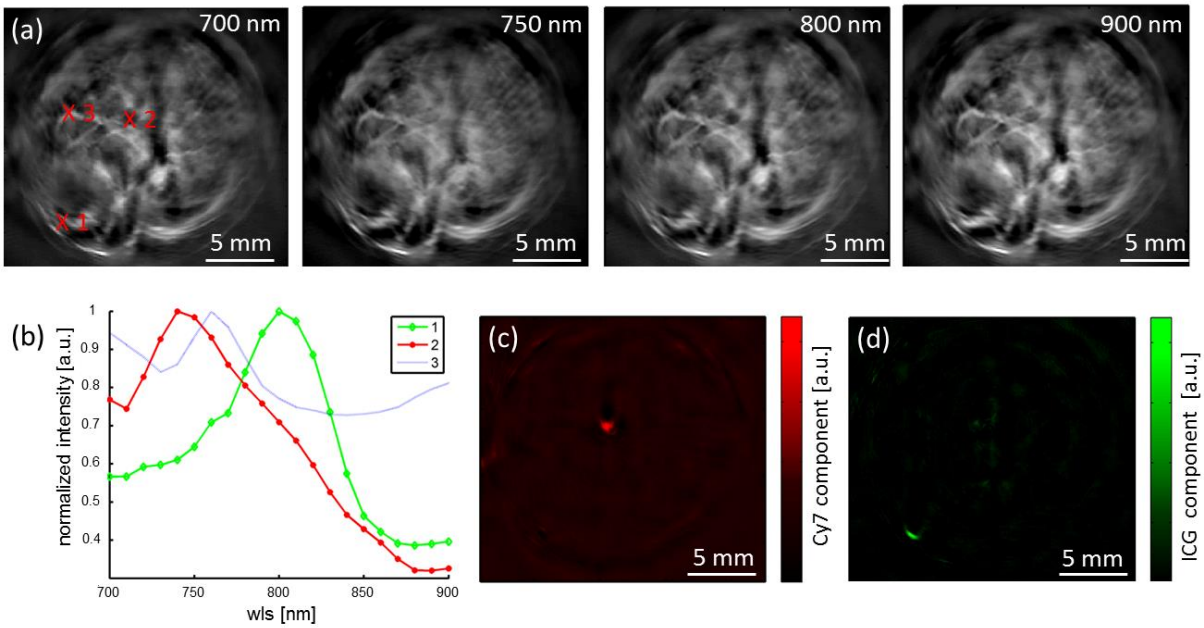

Fig. 6.1: (a) Single wavelength images at 700, 750, 800 and 900 nm, respectively, from the liver area of a euthanized mouse. Two plastic tubes were inserted into the mouse and filled with the fluochromes Cy7 and ICG, respectively. The tubes are masked by the background signal from the tissue. (b) Spectral profile obtained from the locations labeled 1, 2, 3 indicating the ability to differentiate between different absorbers. Unmixed Cy7 component and unmixed ICG component.

6.2 Multispectral unmixing for specific absorber detection

6.2.1 The multispectral unmixing problem

Optoacoustic images are proportional to the absorbed electromagnetic energy $H(\boldsymbol{r}, \lambda_i)$, thus the product of light fluence $\phi(\boldsymbol{r}, \lambda_i)$ and the combined contribution of

all absorbing moieties localized within the resolution limited elementary volume at $\boldsymbol{r}$, *i.e.*

$$H(\boldsymbol{r},\lambda_i) = \phi(\boldsymbol{r},\lambda_i)\sum_{j=1}^{l}\mu_{a,j}(\boldsymbol{r},\lambda_i) = \phi(\boldsymbol{r},\lambda_i)\sum_{j=1}^{l}\varepsilon_j(\lambda_i)c_j(\boldsymbol{r}) \tag{6.1}$$

where $\mu_{a,j}(\boldsymbol{r},\lambda_i) = \varepsilon_j(\lambda_i)\, c_j(\boldsymbol{r})$ is the absorption coefficient of the j-th absorber, $\varepsilon_j(\lambda_i)$ its molar extinction coefficient at the wavelength λ_i and $c_j(\boldsymbol{r})$ its concentration (cf. section 2.2.3.2).

The goal of multispectral imaging and unmixing is the specific and spatially resolved detection of photo-absorbers (*e.g.* molecular probes) in deep tissue based on their distinct spectral signature. From Equation (6.1) we see that this is a very challenging task. On the one hand, because not only the probe contributes to the spectrum measured from a single image pixel, but also numerous other tissue constituents, such as oxygenated and deoxygenated hemoglobin (most dominant), but also others like melanin, water, lipids and unknown metabolites [4]. This is because the resolution is too low to resolve the different spectral entities (*i.e.* absorbing molecules) individually. On the other hand, we see that the reconstructed intensity value is proportional to the light fluence. As photon fluence is strongly attenuated in tissue as a function of depth due to scattering and absorption, additional difficulties arise in form of a signal drop with depth and since the fluence attenuation in tissue is wavelength dependent in tissue to a potential distortion of the spectral response. This is known as spectral coloring and has as consequence that the measured spectral profile in deep tissue deviates from the original spectral signature. The actual distortion depends hereby on the absorbers present in the illumination path [114]. Moreover, experimental factors, which are difficult to account for in the image reconstruction, such as out-of-plane signals (cf. section 3.4.6.2), acoustic heterogeneities, noise or limited-view detection, may result in reconstruction artifacts without physical meaning (*e.g.* negative values) which further complicate the spectral unmixing problem. Finally there might be motion, especially when imaging living objects, due to breathing, heartbeat, pulse or involuntarily muscle activity. Motion is problematic, because, for MSOT to work robustly, it is important that the set of multi-wavelength images is acquired from the same tissue slice or volume, *i.e.* having the tissue at the same position, orientation and at the same morphological and physiological state throughout the wavelength scanning process.

6.2.2 **Spectral fitting**

Assuming that it is possible to correct for the light fluence $\phi(\boldsymbol{r},\lambda_i)$ in Eq. (6.1), then it is possible to set up a system of linear equations, which takes the form

$$\boldsymbol{M} = \boldsymbol{AC}\,. \tag{6.2}$$

where $\boldsymbol{M} \in \Re^{m\times n}$ is the measurement matrix with n being the number of data points (*i.e.* pixels in each image) and m the number of single wavelength images acquired. $\boldsymbol{A} \in \Re^{m\times l}$ is the mixing matrix in which the columns contain the spectral

signatures of the l distinct sources (*i.e.* optoacoustic absorbers). It determines how the sources contribute wavelength-wise to the measured data. $C \in \Re^{l \times n}$ is the unknown matrix containing the concentration of each distinct absorber in the mixed pixel [4]. Knowing the absorption spectra of the expected sources, *i.e.* the matrix $\boldsymbol{A}$, Eq. (6.2) can be solved for the unknown concentrations c_i in each pixel in the sense of least square minimization for instance by the Moore-Penrose pseudoinverse $\boldsymbol{A}^+$ (cf. Eq. (2.36)) [4, 112]

$$\boldsymbol{C} = \boldsymbol{A}^{\dagger}\boldsymbol{M}. \tag{6.3}$$

For experimental data, *i.e.* in presence of measurement errors, Taruttis [37] proposed to add a non-negativity constraint to the inversion of Eq. (6.2) for instance by using the *lsqnonneq* algorithm (MATLABR2011b, The MathWorks Inc., Natick, MA, 2011). The reason is that conventional least square inversion allows every possible combination of absorption spectra, thus also those which yield unphysical negative concentrations. Using a non-negativity constraint can avoid this.

6.2.3 Blind unmixing

Blind unmixing techniques are widely used in various fields including among others astronomy [115], pattern recognition [116] and fluorescent imaging [117]. They do not require any exact a priori information about the spectra of the target or background absorbers. Instead the multispectral data set is analyzed in a statistical sense to find similarities and differences in the spectral behavior of the data [118]. The probe is then identified as the spectral component that shows a different spectral behavior than the background. Herein, a combination of principal component analysis (PCA) [119] and independent component analysis (ICA) [120] is used for blind target detection.

6.2.3.1 Principal component analysis (PCA)

Principal Component Analysis (PCA) [119] is a blind unmixing technique based on the assumption that the measured data (*i.e.* the single wavelength images) is statistically correlated, whereas the source components (*i.e.* the absorbing entities) are mutually uncorrelated. For unmixing the correlated measurement data is transformed into a new coordinate system spanned by uncorrelated orthogonal basis vectors which are called principal components. The projections onto the basis vectors are the uncorrelated source components. In this basis the source components are ordered according to the largest variance and hence energy, *i.e.* the first principal component presents the data with the largest variance, the second one the largest remaining variance, and so on [112, 121]. Since all measurements are perturbed by noise, which should have less variance or energy than the actual data, PCA yields a sorting of the data according to their information content, *i.e.* the first components with a lot of variance represents the most relevant information, whereas the components of higher order mostly represent noise [122]. Consequently, PCA can be used for dimension reduction by omitting the principal components of higher order.

The transformation matrix $\boldsymbol{P_{PCA}}$ that projects the measured data $\boldsymbol{M}$ onto the new orthogonal basis constituting the principal components can be obtained from the eigenvalue decomposition of the covariance matrix of $\boldsymbol{M}$ and yields

$$\boldsymbol{C_{PCA} = P_{PCA} M = U^T M} \tag{6.4}$$

where $\mathbf{U}$ is the orthonormal eigenvector matrix of the covariance matrix of $\boldsymbol{M}$ and $\boldsymbol{C_{PCA}}$ the matrix of the calculated principal components. The eigenvalues of the covariance matrix are an indicator of the data variance for this component, *i.e.* can be used to distinguish relevant components from noisy ones. The eigenvectors can be considered as the estimated spectral absorption profile of the unmixed components [112, 118].

6.2.3.2 Independent component analysis (ICA)

This technique is based on the assumption that the source components of the mixed multispectral dataset are statistically independent. In analogy to PCA, the measurement data is expressed in a new basis following the stronger criterion of statistical independence [112]. In order to identify these source components, the algorithm seeks a transformation

$$\boldsymbol{C_{ICA} = P_{ICA} M} \tag{6.5}$$

of the dependent multispectral dataset $\boldsymbol{M}$ into a set of independent variables, where $\boldsymbol{P_{ICA}}$ stands for the transformation matrix and $\boldsymbol{C_{ICA}}$ for the independent components. This is accomplished by minimizing their Gaussianity because according to the central limit theorem, statistical independent variables are less Gaussian than their mixed counterparts [112]. Herein, the FastICA algorithm [123] is used to do the independent component analysis. It finds the independent components by iteratively maximizing the kurtosis (fourth order statistical moment) as a measure for the non-Gaussianity. The spectra of the independent components can be obtained from $\boldsymbol{P_{ICA}^T}$**.** By not relying on orthogonality of the basis vectors, ICA generally achieves better separation of the different spectral components than PCA which tries to represent the data in an orthogonal space [121]. However, in contrast to the PCA algorithm, the ICA algorithm does not provide the eigen-values and therefore no measure of the component's significance. It rather retrieves a set of randomly-ordered components, one for each available dataset [121]. Therefore, especially for big datasets comprising much more wavelengths than actually expected absorbers, ICA needs some preprocessing in order to eliminate components of low relevance. Otherwise the dataset will contain many components only representing noise which makes interpretation of the data challenging [112].

6.2.3.3 Combined PCA-ICA

The idea to overcome this problem is a presorting of the data with the PCA algorithm according to their relevance. By omitting all the noise terms (*i.e.* the high order components) a reduced number of measurements can be given to the ICA algorithm, which reduces the complexity while preserving almost all the information. The number of PCA components kept generally is chosen according to the expected number of sources constituting the mixture, *i.e.* 3 in case of normal tissue without melanin and one extrinsic contrast agent. The actual spectral unmixing is then done with the ICA algorithm based on the reduced subset of PCA data. This improves the performance of the ICA algorithm since noisy data is omitted

and simplifies the identification of the relevant spectral sources due to the reduced amount of output data. The unmixing according to the PCA-ICA scheme is then

$$\boldsymbol{C_{PCA/ICA} = P_{ICA} P'_{PCA} M} \tag{6.6}$$

where P'_{PCA} is the transformation matrix of the reduced subset [112]. Contrary to pure PCA or ICA, the spectra obtained from the PCA-ICA approach are not the absorption spectra of the actual source components but rather the spectra of the independent components in the principal component space. The reason is that the reduced principal components are used as input data for the ICA algorithm and not the measured data. To obtain the actual absorption spectra the unmixed component matrix can be inverted and multiplied with the original measurement matrix according to

$$\boldsymbol{S = M C^{\dagger}_{PCA/ICA}} \tag{6.7}$$

where † denotes the Moore-Penrose pseudo-inverse and S the matrix with the absorption spectra [112].

6.2.3.4 Automatic component identification

To automatically identify the probe component within the unordered components obtained from the ICA algorithm, the Pearson's correlation coefficient between the unmixed and the theoretical spectrum of the probe were calculated as proposed by Glatz [124]. It is defined as

$$r = \frac{\frac{1}{n}\sum_{i=1}^{n}(x_i - \bar{x})(y_i - \bar{y})}{\sqrt{\sum_{i=1}^{n}(x_i - \bar{x})^2} \cdot \sqrt{\sum_{i=1}^{n}(y_i - \bar{y})^2}} \tag{6.8}$$

where x_i denotes the *i*-th value of the unmixed spectra, y_i the values of the theoretical spectra and $\bar{x}, \bar{y}$ the corresponding mean values. The Pearson's correlation coefficient yields values between -1 and 1 and it is maximal for positive correlation, zero for no correlation and minimal for negative correlation. Since the spectra resulting from the ICA algorithm might be inverted, the maximum of the absolute value $|r|$ was used to automatically identify the component.

6.2.4 Motion artifact reduction by averaging

For MSOT to work robustly, the tissue sample to be imaged has to be in exact the same position, orientation and physiological state during the multi-wavelengths acquisition process. Since MSOT is a high-resolution modality, even moderate motion of the subject during acquisition of the multi-wavelengths dataset may compromise the accuracy of the unmixing result. Yet when imaging live subjects, there is always motion due to respiration, heartbeat or involuntary muscular activities. To compensate for these movements, several techniques can be applied. Ideally, one uses a high power laser with a high repetition rate and fast wavelength tuning, so that a multispectral dataset can be acquired within a time interval during which movements are insignificant. Beginning 2013 such a laser source has become available and using this technology we could develop the first handheld multi-spectral-optoacoustic imaging device for clinical applications [125]. During this thesis

this technology was however not available yet. Alternatively one could use external triggering to acquire data at the same instance during a breathing or heartbeat cycle. This is a standard technique in imaging modalities like CT or MRI. Yet, it requires the use of additional devices such as heart-monitors and intubation, which make the imaging process tedious [37, 126]. Alternatively image registration methods [127] might be used, which detect movement in between single laser pulses and compensate for them by reversing the deformation. Due to the non-linear nature of the deformation and the wavelength dependency of the image features sophisticated registration methods are required. Investigations of such methods are beyond the scope of this work. Therefore, for multispectral imaging of living subjects, signal averaging is applied, although not necessary from a signal to noise ratio point of view, to average out the movement. The drawback of this approach is a slight loss of resolution and an increased imaging time.

6.2.5 Tests with simulated and experimental data

The ability of the presented unmixing algorithms to detect specific absorber based on their spectral signature is tested in numerical simulation, on phantoms and *ex vivo* mouse data.

Numerical simulations

A 2 cm diameter cylindrical phantom was simulated. The background absorption of the phantom was assumed to be 70% oxygenated blood with an absorption coefficient of $\mu_a = 0.3\ \mathrm{cm}^{-1}$ at a wavelength of $\lambda = 800\ \mathrm{nm}$ and a constant reduced scattering coefficient of $\mu_s' = 10\ \mathrm{cm}^{-1}$. These values were chosen to mimic average mouse tissue properties in the near infrared [9]. In addition we assumed 16 insertions, always four of them containing the fluorescent dyes Cy7 (Molecular Probes®) and Indocyanine green (ICG, Pulsion) as well as oxy-hemoglobin (Hb) and deoxy-hemoglobin (HbO_2) on top of the background absorption.

A schematic representation of the phantom is shown Fig. 6.2 (a) and the spectral profiles of the different absorbers in (b). The concentration of the absorbers within the insertion was varied to yield absorption coefficients between 0.2 and 1 cm^{-1} at the peak absorption for the fluorescent dyes and the isobestic point for Hb and HbO_2 respectively.

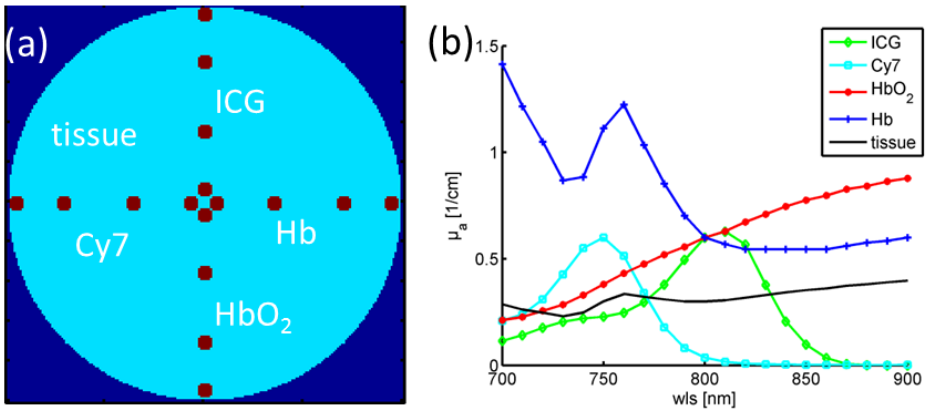

Fig. 6.2: (a) The phantom employed in the simulation study. Background absorption was assumed to be 70% oxygenated blood. The 16 insertions were filled with ICG, Cy7, Hb and HbO_2, respectively. (b) Absorption spectra of ICG, Cy7, Hb, HbO_2 and the tissue background absorption as utilized in the simulation study.

Light fluence in the phantom was simulated for 21 equally spaced wavelengths ranging from 700 to 900 nm using a FEM based package for modeling Near-Infrared light transport in tissue [73]. Light fluence at the boundary of the object was assumed constant for the illumination, *i.e.* $\phi(\boldsymbol{r}, \lambda) = 1\ (\mathrm{a.u.})$. The absorbed light energy (*i.e.* the initial optoacoustic pressure) was obtained by multiplying the absorption coefficients with the simulated light fluence distribution according to equation (2.13).

The set of 21 images corresponding to the different wavelength was unmixed using spectral fitting and blind unmixing based on the PCA-ICA method. For ICA the four most relevant components were kept as identified by PCA.

Experimental data

Experimental measurements were done with the developed small animal scanner. 21 images were acquired with equally spaced wavelengths ranging from 700 to 900 nm. Signals were deconvolved with the electrical impulse response and filtered between 0.05 and 7 MHz in case of the first phantom and from 0.2 to 7 MHz in case of the second phantom. For inversion, the PLSQR algorithm was used. The single wavelength images were normalized by the laser tuning curve to compensate for energy variations between different wavelengths.

In a first experiment an agar phantom was imaged. Black India ink and intralipid were added to the agar solution to yield a background absorption with a constant absorption coefficient $\mu_a = 0.2\ \mathrm{cm}^{-1}$ and a reduced scattering coefficient $\mu_s' = 10\ \mathrm{cm}^{-1}$. Two insertions with Cy7 and two insertions with gold nanorods (GN) were included at different depths within the phantom. The peak absorption of these contrast agents was approximately $\mu_a = 1\ \mathrm{cm}^{-1}$ as measured with a spectrometer. White straws, enclosing the insertions, were used to avoid diffusion of the contrast agents. In addition to the contrast agents, india ink and intralipid was also included in all four insertions with absorption equal to the background. The unmixing was done with the spectral fitting method using the non-negativity constraint and the absorption spectra of ink, GN and Cy7 (Fig. 6.3 (a)) and by blind unmixing.

In a second experiment, in order to showcase detection of contrast agents in deep tissue, two plastic tubes with an inner diameter of 300 µm were inserted at different depths along the longitudinal axis of a five weeks old euthanized CD1 mouse. Hair was removed with a hair removing lotion. The tubes were filled with ICG. Since ICG binds to plasma proteins, which slightly changes the absorption spectrum compared to their solution in water [128], the ICG was dissolved in 35mg/ml albumin, in order to work with an absorption spectrum more similar to *in vivo* conditions. Four concentration were tested (c = 1.25, 2.5, 5 and 10 µM, respectively) with a peak absorption of μ_a = 0.5, 1, 2 and 4 cm^{-1}, respectively, at a wavelength of 800 nm. The spectral profiles measured with the spectrometer are depicted in Fig. 6.3. In one experiment, the ICG solution in the inner tube was replaced with a 4 µM Cy7 solution having a peak absorption of $\mu_a = 2.3\ \mathrm{cm}^{-1}$. The multispectral datasets were acquired from the liver area. Signals were averaged 50 times. The laser per pulse energy was 70 mJ at a wavelength of 850 nm. For unmixing spectral fitting and PCA-ICA based blind unmixing was used. Furthermore, the signal to noise ratio of

the unmixed results were determined according to $\mathrm{SNR} = \mu/\sigma$, where μ stands for mean unmixed signal intensity in the area of the absorber and σ the standard deviation of the background signals.

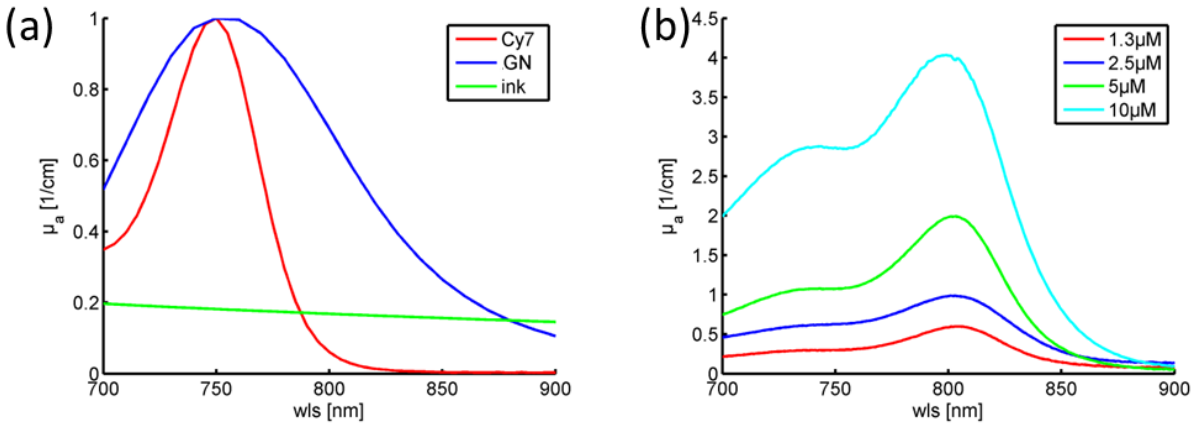

Fig. 6.3: Absorption spectra of absorbers used in (a) the phantom experiment and (b) the mouse experiment.

6.2.6 Results – spectral unmixing without light fluence correction

Spectral coloring in a typical small animal experiment

Fig. 6.4 illustrates the effect of spectral coloring due to wavelength dependent light fluence attenuation. Fig. 6.4 (a) and (b) shows the simulated initial pressure at 750 and 800 nm, respectively. The spectral profiles from the different insertions are depicted in (c)-(f). They are normalized to their maximum to highlight the spectral coloring. From the outside to the inside the tubes are labeled with increasing numbers. Fig. 6.4 (g) shows the spectral profile obtained from the two tubes inserted into the mouse and filled with ICG and (h) the same profiles normalized to their maximum. We see that the amplitude of the initial optoacoustic pressure and its spectral behavior change with depth. This is due to the wavelength dependent light attenuation in tissue. When propagating through tissue, light is scattered and absorbed by objects in the propagation path. Thus an absorber embedded deep within tissue sees less light energy and with a different spectral characteristic than one close to the animal's surface and consequently also displays a different spectral behavior in the image. Nevertheless we also see that, even 1 cm inside the tissue, the characteristic signature of the dye insertions, *i.e.* the characteristic peak at around 750 nm and 800 nm for Cy7 and ICG respectively, is conserved. On the other hand, the spectra of Hb and HbO_2 lose their characteristic features. This is because their absorption spectra is much closer to the overall background absorption being 70% oxygenated blood and thus more affected by the spectral coloring because when propagating through tissue the light fluence is dominantly attenuated in the spectral bands characteristic for Hb and HbO_2. Overall, the example clearly illustrates the challenge of accurate unmixing due to light fluence attenuation and the extent of the spectral coloring phenomenon in deep tissue MSOT imaging.

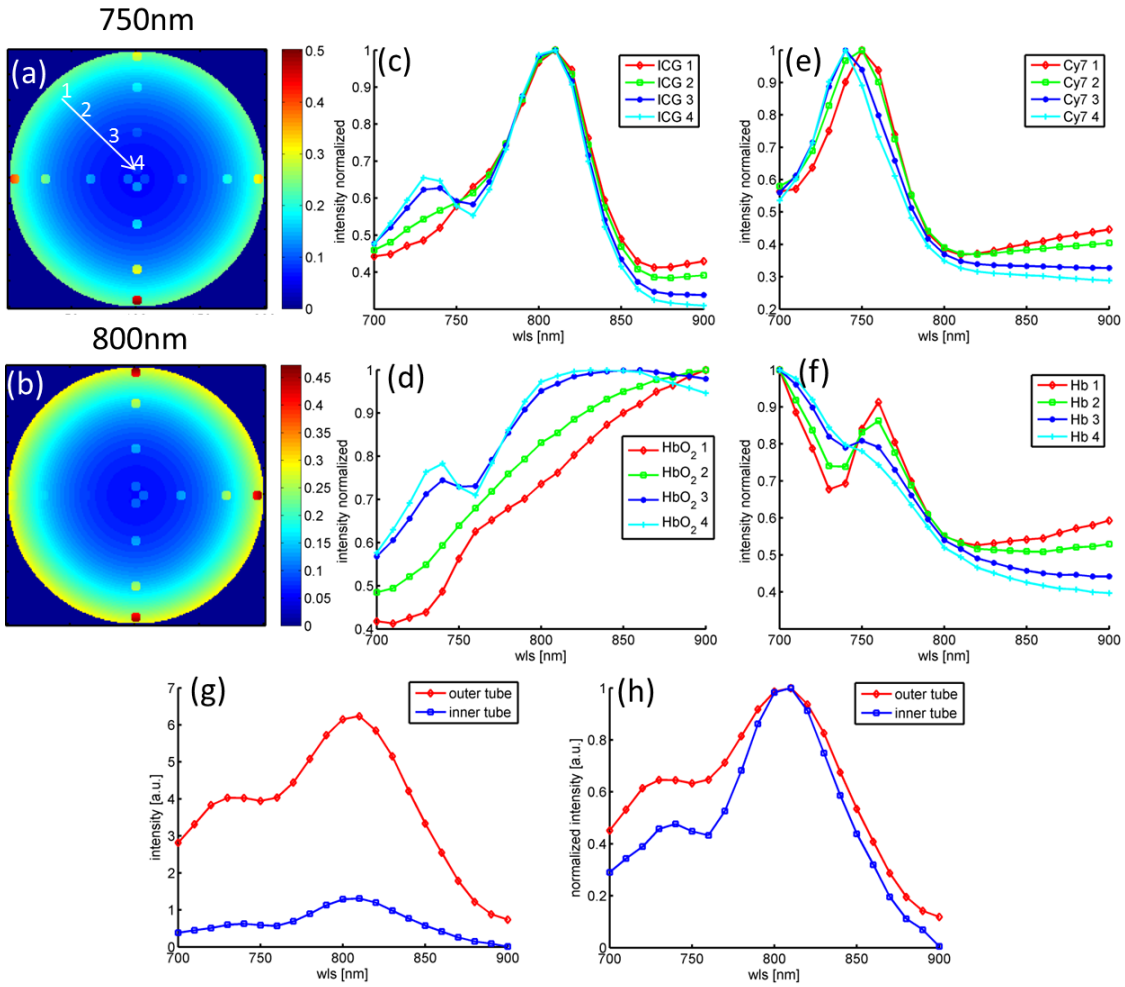

Fig. 6.4 Effect of light fluence attenuation. (a) Single wavelength image at 750 nm and (b) at 800 nm. Normalized spectral dependency of the initial pressure generated in (c) the ICG, (d) the Cy7 (e) the HbO_2 and (f) the Hb insertion of the simulated phantom. (g) Spectral profile of the two tubes within the mouse and (h) normalized to their maximum. Light fluence attenuation leads to a signal decrease and a distortion of the spectral signature.

Unmixing results - numerical simulation

The results of the simulation study are shown in Fig. 6.5. The unmixing results obtained by spectral fitting are shown in the first column, the results of PCA-ICA unmixing in the second and the unmixed signal intensity as a function of the absorption coefficient of the probe in the insertion (which is generally proportional to the probe concentration) in the third column. The first row shows the results for the Cy7 component and the second row for the unmixed ICG component. In the shown images the probe had a peak absorption of 0.6 cm^{-1}. For all five absorber concentrations tested both spectral fitting and blind unmixing could resolve the probes based on their spectral signature. The amplitudes are however reduced for greater depths due to the increased attenuation of light. Also, there is slight cross-talk visible, which is less for PCA-ICA unmixing than for spectral fitting. This is due to spectral coloring. The unmixed signal intensity scales linearly with the probe's peak absorption for the tested concentrations yet due to light attenuation with reduced slopes for deeper insertions.

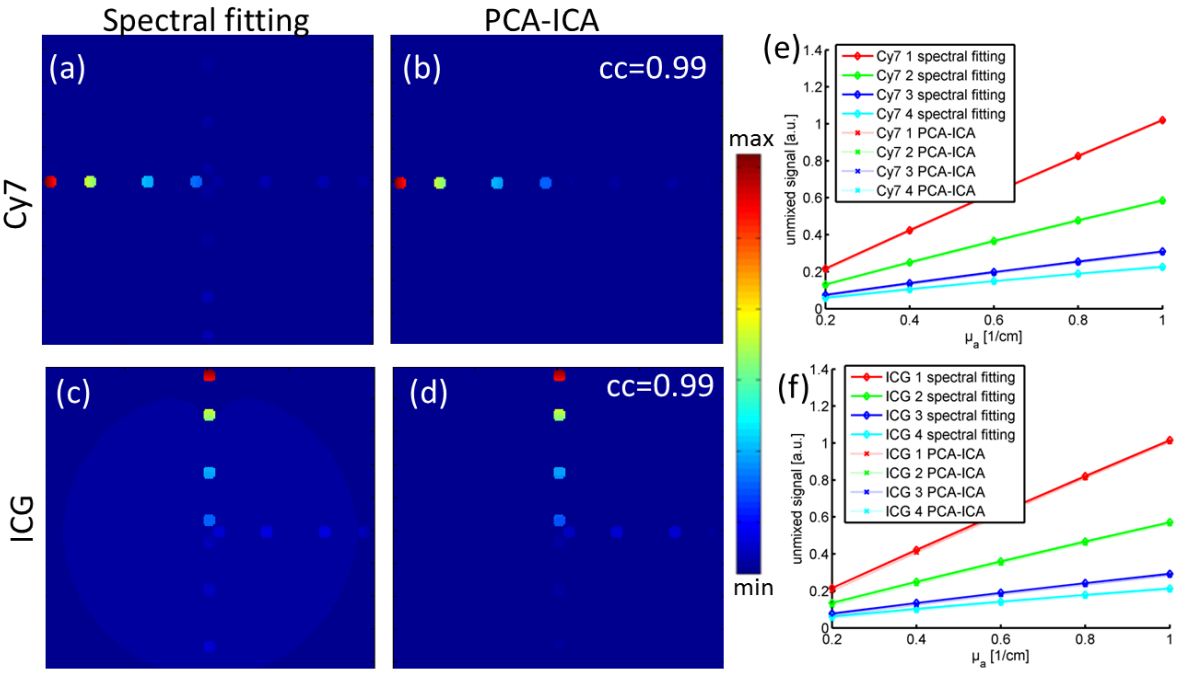

Fig. 6.5: Unmixing results of the simulation study. The first column depicts the results obtained by spectral fitting, the second column by blind unmixing, the third column the intensity of the unmixed signal as a function of the absorption coefficient of the dye. The first row depicts the unmixed Cy7 component, the second row the unmixed ICG component.

Unmixing results - experimental phantom

Fig. 6.6 displays the results of the phantom experiment. Single wavelength images at 750 nm (approximately the absorption peak of Cy7) and at 780 nm (almost the absorption peak of GN) are shown in the first column. The small black arcs are due to acoustic reflections due to impedance mismatches between agar and straw. The unmixing results obtained by spectral fitting are shown in the second column and the results of blind unmixing in the third. The inner insertions are weaker than the outer ones due to light attenuation. Again, the result of spectral fitting shows slightly more cross-talk than the one for blind unmixing.

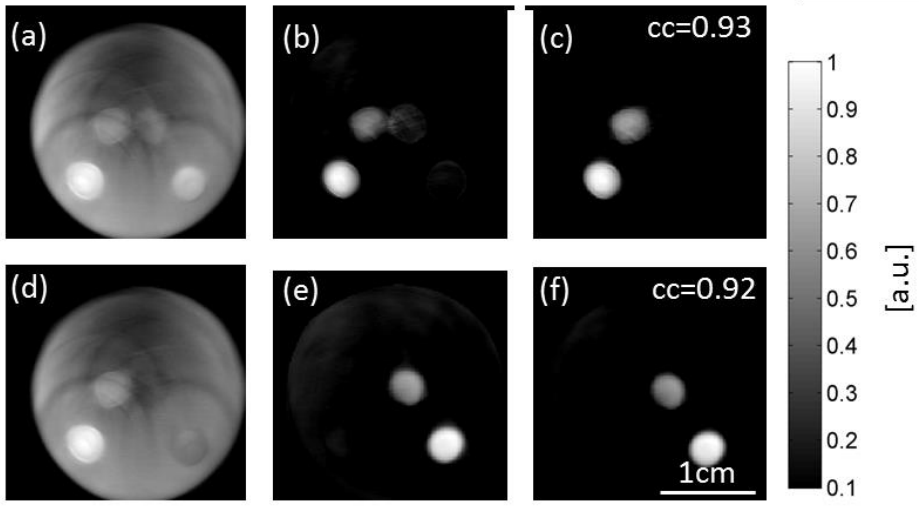

Fig. 6.6: Unmixing results of the phantom study. The first column depicts single wavelength images at (a) 750 nm and (d) 780 nm. The second column, *i.e.* (b) and (e), depicts the results obtained by spectral fitting and in the third column, *i.e.* (c) and (f), the results obtained by blind unmixing are presented: (a)-(c) for unmixed Cy7 as well as (d)-(f) for GN.

Unmixing results - *Ex vivo* mouse

Fig. 6.7 depicts the results of the *ex vivo* mouse imaging. A single wavelength reconstruction acquired at 800 nm is presented in Fig. 6.7 (a) showing several anatomical structures, notably liver blood vessels. Both tubes are filled with 5 µM ICG. Although imaged at the peak absorption wavelength of ICG, the tubes cannot be recognized in a single wavelength image due to the strong inherent background absorbers masking the tubes. Fig. 6.7 (b) and (e) depicts the ICG component after spectral fitting for a ICG concentration of 2.5 and 10 µM. Fig. 6.7 (b) and (e) the blind unmixing results for the same concentrations. The tubes are now clearly recognizable. One is located in the center, the other in the periphery of the body of the mouse. Although having the same concentration, the inner tube is displayed with a lower intensity than the outer tube. This is due to light attenuation. Fig. 6.7 (d) depicts the SNR of the two tubes resolved as a function of concentration and the unmixing algorithm. Again we see the linear dependency between unmixed signal strength and peak absorption also with varying slopes for different depths. Overall blind unmixing yields a higher SNR then the spectral fitting methods. Fig. 6.1 depicts the results from the situation where the outer tube was filled with ICG and the inner tube with Cy7 showing that it is possible to simultaneously resolve several chromophores.

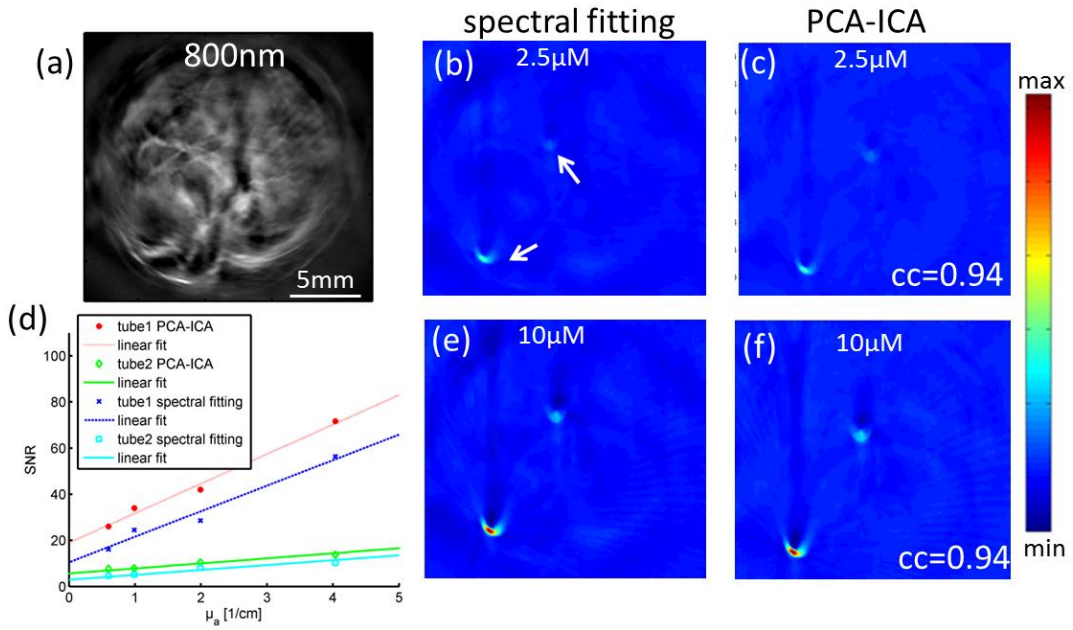

Fig. 6.7: Multispectral unmixing in deep tissue. Panel (a) shows a single wavelength image (λ = 800 nm) from a mouse's liver region in which we inserted two tubes filled with ICG (5 µM). Panels (b) and (e) depict the unmixing results obtained by spectral fitting for two different ICG concentrations clearly showing the two tubes invisible in the single wavelength images. Panel (c) and (f) show the results of blind unmixing. Panel (d) shows the SNR of the unmixed signal of the outer and inner tube for both methods as a function of different peak absorptions.

6.2.7 Discussion

In this section the subject of multispectral imaging for molecular probe detection was presented. It was shown that accurate unmixing is a challenging task because of the wavelength dependent attenuation of the light fluence in tissue, due to which

the measured spectral signature and amplitude of the absorber signal is distorted. Also not all absorbers contributing to the MSOT signal might be known.

Therefore, in addition to spectral fitting where the multispectral dataset is fitted in a least squares sense to a set of spectral components assumed to represent the absorbing moieties, a blind unmixing scheme was presented which, in contrast to spectral fitting, does not require exact a priori knowledge about the signature of the all the absorbing entities but detects different spectral components based on statistical means.

Both methods were tested on simulated and experimental data, without a priori correction of the light fluence. It was found that both methods could specifically resolve molecular probes (here ICG and Cy7) over general tissue background absorption, even in deep tissue where the spectral signatures are affected by spectral coloring. The signal to noise ratio achieved blind unmixing was higher than for spectral fitting and visible cross-talk less suggesting that blind unmixing has better detection capabilities in deep tissue where the distortion of the spectral signatures is increased.

Yet, in both cases the intensities of the unmixed components did not represent the exact absorption values. Because of light fluence attenuation, they were reduced with depth. For a specific position the signal intensity scaled linearly with the peak absorption value of the absorber. Hence even when light fluence attenuation effects are not corrected, it is possible to detect the location of a specific absorber by means of MSOT but it is impossible to quantitatively compare signals from different depths. On the other hand localized comparison of different probe concentrations seems possible. In that sense MSOT has the potential to examine the temporal pharmacokinetic behavior of molecular probes in tissue (*e.g.* its dwell time at a specific location), in particular when the probes is rather localized as it was in the examples shown. In such a situation the overall light fluence distribution is hardly affected by a change of probe concentration and thus maintained over time.

However, if a large amount of probe significantly changes its spatial distribution over time, *e.g.* at the beginning it is distributed throughout the tissue, but after a while it is localized within a small area, or if tissue oxygenation significantly changes, then the overall light fluence distribution will also change and with it the measured spectral signature from the probes, overall compromising the unmixing accuracy and thus comparability of the results. This can be seen from the spectral coloring examples presented. The measured spectra of Hb and HbO_2 are significantly more corrupted in deep tissue by spectral coloring than the one of ICG and Cy7. Thus unmixing becomes more error-prone with depth and yields more biased results. The reason is that an absorber distorts the spectra of the incident light fluence in exactly the spectral bands characteristics for its spectral signature. Thus the more absorbers with a specific absorption profile are present in tissue; the more the measured spectra of the downstream absorbers are corrupted in their signature bands. In this sense it is beneficial for molecular probe detection, if the probe is localized and has a spectral signature significantly differing from the one of the background absorbers.

Although blind unmixing achieved higher detection sensitivity than spectral fitting, it might be beneficial in some situations to use spectral fitting. The reason is that

spectral fitting is deterministic in contrast to the blind unmixing approaches which incorporate uncertainty in their performance. When doing spectral fitting, the data is projected onto a fixed set of axis defined by the input absorption spectra. Blind unmixing on the other hand is data driven and searches a set of independent axis which serves, when the data is projected onto, to highlight different patterns in the data. Thus, if the structure of the data changes (*i.e.* if there are non-stationary absorbers or if new absorbers manifest) then the choice of axis might also change [121]. To assure the same choice of axis and thus make unmixing results from different time points comparable, the complete dataset should be unmixed at the same time.

Concerning detection sensitivity, it was possible to resolve 2.5 µM of ICG about 1 cm deep inside tissue with a signal to noise ratio of 5 with spectral fitting and 7 with blind unmixing. According to the Rose criterion, this is sufficient to distinguish image features at 100% certainty [122, 129]. Yet this value has to be treated with caution and must not be considered as a universally valid sensitivity limit. Actually, the probe detection capability depends on a multitude of parameters, which have not all been examined in this work. Important factors are also the location, microenvironment, shape and orientation of the absorbing structure. If the absorber is located behind an air filled cavity, the optoacoustic signal from the probe might not be able to propagate to the transducer because of impedance mismatches, thus remains invisible. Utilizing limited view detection this might also happen due to the directivity of optoacoustic signals. Additional important factors for molecular probe detection by multispectral means are the probes spectral characteristics with respect to the background absorption, its efficiency to generate an optoacoustic signals but also the wavelengths selection and the unmixing algorithm employed.

6.3 Approaches for light attenuation correction

As seen from the previous section light fluence attenuation is a big challenge in deep tissue multispectral optoacoustic imaging. As photon fluence is strongly attenuated in tissue as a function of depth and wavelength due to scattering and absorption, absorbers at different depths will be excited differently. Thus, an absorber embedded deep within tissue may appear weaker than one close to the tissues surface so that the overall comparability of signals from different depths is severely limited. Also their reconstructed spectral signature will change depth. As a consequence spectral unmixing becomes challenging and blind unmixing approaches may be required to support unmixing in such a situation (cf. section 6.2.3).

6.3.1 Existing correction attempts

Several attempts have been proposed in the literature to correct for this inhomogeneous excitation artifacts. Approaches range from corrections by dividing the optoacoustic image by an analytical Bessel function as an estimate for the light fluence [36], over simulated light fluence distributions [130] and empirical correction attempts [131] to sparse decompositions [132] and non-linear model-based inversion schemes [133]. All the methods have their advantages and drawbacks.

The normalization by a Bessel function is a practical approach for cylindrically shaped homogenous phantoms with uniform background scattering and absorption and homogenous surface illumination. Under these conditions the light fluence is given by a modified Bessel function of the first kind (see section 2.2.3.3), which can be used to normalize the optoacoustic reconstruction to correct for the light attenuation. However for mice, which have spatially dependent optical properties and no cylindrically shape, this approach is only a crude approximation.

Normalization with a simulated light fluence can be applied to different shapes but also requires a priori knowledge of the underlying optical properties and the illumination distribution on the tissue boundaries. Yet, both are generally unknown or only partially known in experimental imaging scenarios therefore not followed herein [134].

Empirical correction attempts are based on reference measurements using the same tissue type than the one overlaying the region of interest to obtain an estimate of the light transmission. Beside their impracticability, the method has the additional drawback of being highly dependent upon the tissue structure, composition and physiology [58].

Sparse decomposition is data driven approach which does not require any a priori knowledge about the optical properties. It separates light fluence from the optical absorption based on the assumption that slowly varying information in the image corresponds to the light fluence and fast varying information to optical absorption and uses methods of sparse signal representation to isolate optical absorption from light fluence. This makes it more robust in experimental situations than the approaches based on a numerical estimation of the light fluence [132]. The method was tested on experimental phantoms and mice imaged in the small animal scanner. Whereas the method worked on simple agar phantoms, it could not correct for the light attenuation in mice. In addition, due to the long computation time of approximately 3 hours per 2D image, the method becomes impractical in many experimental situations.

6.3.2 Ratio normalization

Herein a different method is proposed based on a ratio normalization using images acquired at several different wavelengths. Jetzfellner and myself published this approach in its basis form 2011 in [134]. The method uses two images at different wavelengths for which the probe spectrum changes considerably but the background absorption remains approximately constant. The two images are then subtracted and divided by the one for which the probe absorption is low according to

$$I = \frac{\phi(\boldsymbol{r},\lambda_1)\mu_a(\boldsymbol{r},\lambda_1) - \phi(\boldsymbol{r},\lambda_2)\mu_a(\boldsymbol{r},\lambda_2)}{\phi(\boldsymbol{r},\lambda_2)\mu_a(\boldsymbol{r},\lambda_2)} \approx \frac{\mu_a(\boldsymbol{r},\lambda_1) - \mu_a(\boldsymbol{r},\lambda_2)}{\mu_a(\boldsymbol{r},\lambda_2)} \tag{6.9}$$

to obtain an image I of relative absorption change normalized by the background absorption on a per pixel basis. In Eq. (6.9), $\phi(\boldsymbol{r},\lambda_i)$ stands for the light fluence and $\mu_a(\boldsymbol{r},\lambda_i)$ for the absorption coefficient. Under the assumption that the light fluence

is wavelength independent, this normalization eliminates the light fluence. The resulting image represents a measure for the probe concentration which is proportional to the absorption change normalized to the total background absorption. Yet subtraction is not a very sensitive unmixing method. Hence, in order to work efficiently, this approach requires probes with a steep spectral absorption profile in a narrowband wavelength range (< 40 nm) for which the background absorption is approximately constant.

To increase the sensitivity of the approach, the method can be extended to several wavelengths in combination with spectral unmixing. The result of the spectral unmixing being proportional to $\phi(\boldsymbol{r})c_p(\boldsymbol{r})$, where $\phi(\boldsymbol{r})$ represents the effect of the light fluence and $c_p(\boldsymbol{r})$ the probe concentration, is then divided by an estimate of the light fluence $\phi_{est}(\boldsymbol{r})$

$$I = \frac{\phi(\boldsymbol{r})c_p(\boldsymbol{r})}{\phi_{est}(\boldsymbol{r})} \approx c_p(\boldsymbol{r}) \tag{6.10}$$

to yield an image independent of changes in signal strength due to the light fluence. To estimate the light fluence it is convenient to use a single wavelength image close to 797 nm being the isobestic point of hemoglobin which is the dominant background absorber in the near infrared wavelength range. Since the molar extinction coefficients of oxygenated and deoxygenated hemoglobin are the same at this wavelength, the optoacoustic image $c_{blood}(\boldsymbol{r})\phi(\boldsymbol{r}, 797\ \mathrm{nm})$ is proportional to the blood concentration and in contrast to other wavelengths not dependent on its oxygenation status. Moreover, when the blood is homogenously distributed in tissue, *i.e.* $c_{blood}(\boldsymbol{r}) = const$, then the optoacoustic image is proportional to the light fluence, thus can be directly used for correcting the influence of light attenuation. Yet, blood is generally not homogenously distributed in tissue. There might be areas (*e.g.* blood vessels) where the blood concentration is higher than elsewhere. In such a case the image can be low pass filtered to remove such areas with sharp variations in the background absorption.

6.3.3 Tests using simulated and experimental data

The presented normalization approach has been tested in simulation and experimentally on an agar phantom and an *ex vivo* mouse. The phantoms used in the study have been described in detail in section 6.2.5. The results of the blind unmixing study have been used for testing the normalization approach. The light fluence estimate was computed from the 800 nm single wavelength image, reconstructed with the PLSQR algorithm for a frequency band of 50 kHz to 6 MHz. For removing blood vessels in the normalization image a median filter was used with a kernel of 40 x 40 pixels (*medfilt2.m* MATLABR2011b, The MathWorks Inc., Natick, MA, 2011). In case of the experimental data, a constant value defined as 1.001 times the minimum of the normalization image was added to the denominator to compensate for unphysical negative values present in experimental situation and avoid division by zero.

6.3.4 **Results**

Simulation study

The results of the simulation study are shown in Fig. 6.8. The single wavelength image at 800 nm is shown in panel (a) for the absorbers with a peak absorption value of 0.6 cm^{-1}. The estimate of the light fluence obtained by lowpass-filtering the 800 nm reconstruction is shown in panel (d). Panel (b) and (c) depict the unmixed Cy7 component without and with light fluence correction and (d) the profiles along the insertions. The corresponding images for the ICG insertions are shown in (f)-(h). The ratio between the retrieved concentration within an insertion and the outer insertion is shown as a function of the peak absorption value in (i) and (j). The method could recover, depending on the concentration, 89 ± 5% and 92 ± 3% of the correct ICG and Cy7 value respectively. The correcting effect is less at higher absorber concentrations because they increase the spectral variations in the light fluence patter and thus impede the estimation thereof.

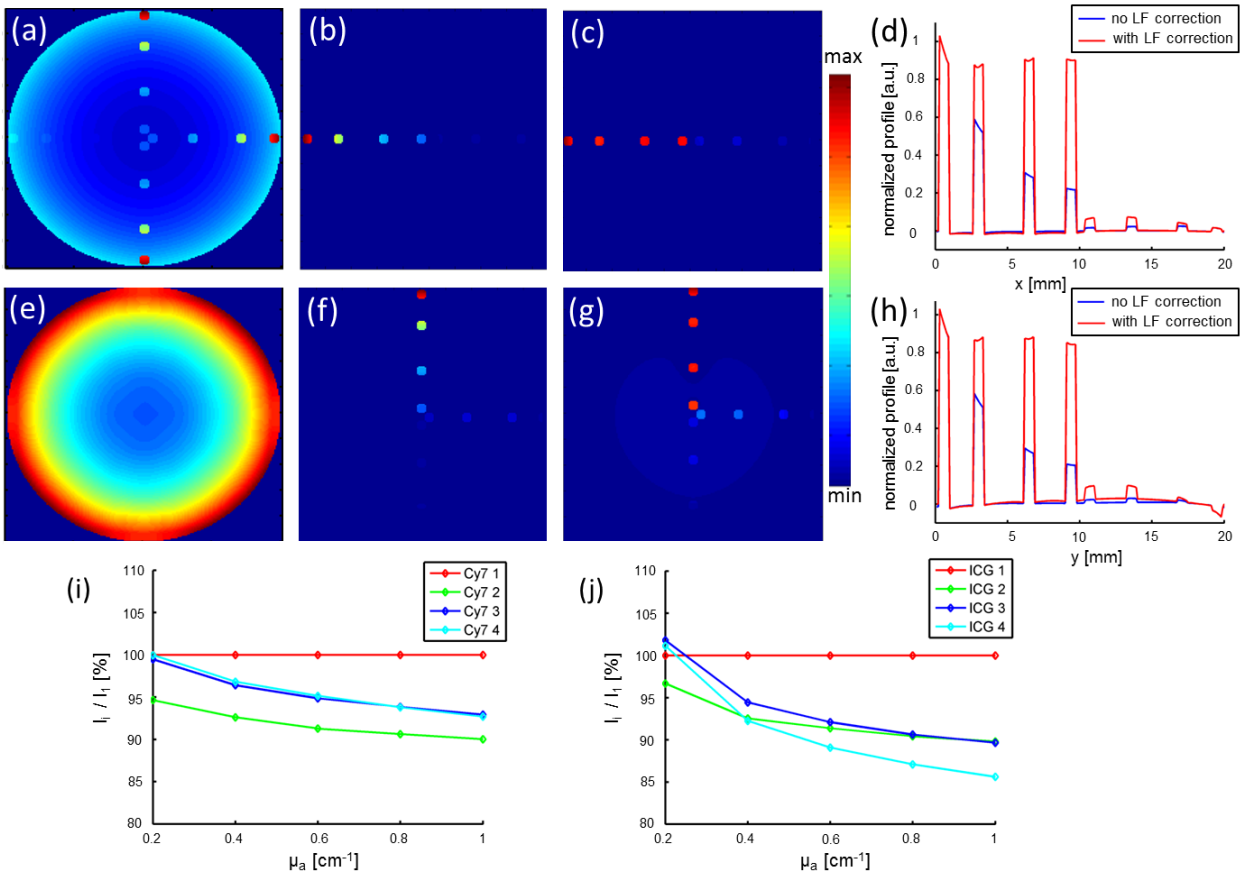

Fig. 6.8: Results of the simulation study with wavelength dependent background absorption. (a) Single wavelength image at 800 nm. (b) Unmixed Cy7 component without and (c) with light fluence correction. (d) Profile through the retrieved components. (e) Estimated light fluence used for correcting the unmixing results. (f) Unmixed ICG component, (g) corrected for light attenuation and (h) the corresponding profile. (i) and (j) depicts the ratio between the recovered concentration in the different insertions and the outer one as a function of the peak absorption value.

Phantom data

Fig. 6.9 displays the results of the phantom experiment. Panel (a) shows a single wavelength image 750 nm. Panel (b) and (c) depicts the unmixing results without compensation of the light attenuation. The inner insertions are weaker than the outer due to light attenuation. Panel (d) shows the estimate of the light fluence used for correcting the unmixing results. It was obtained by lowpass-filtering the 800 nm reconstruction with a 40 x 40 median filter. A binary mask obtained by segmenting the image before smoothing was used to eliminate values outside the support of the object due to the smoothing. Panels (e) and (f) show the unmixing result after division by the estimated light fluence. The profiles through the insertions along the dashed lines are shown in (g) and (g). Before correction the strength of the inner Cy7 insertion was about 64% (65% for GN) of the outer one, after correction 103% (98% for GN). The presented normalization approach obviously corrects for the amplitude reduction due to light attenuation but also increases the noise level in the image as seen in panel (f).

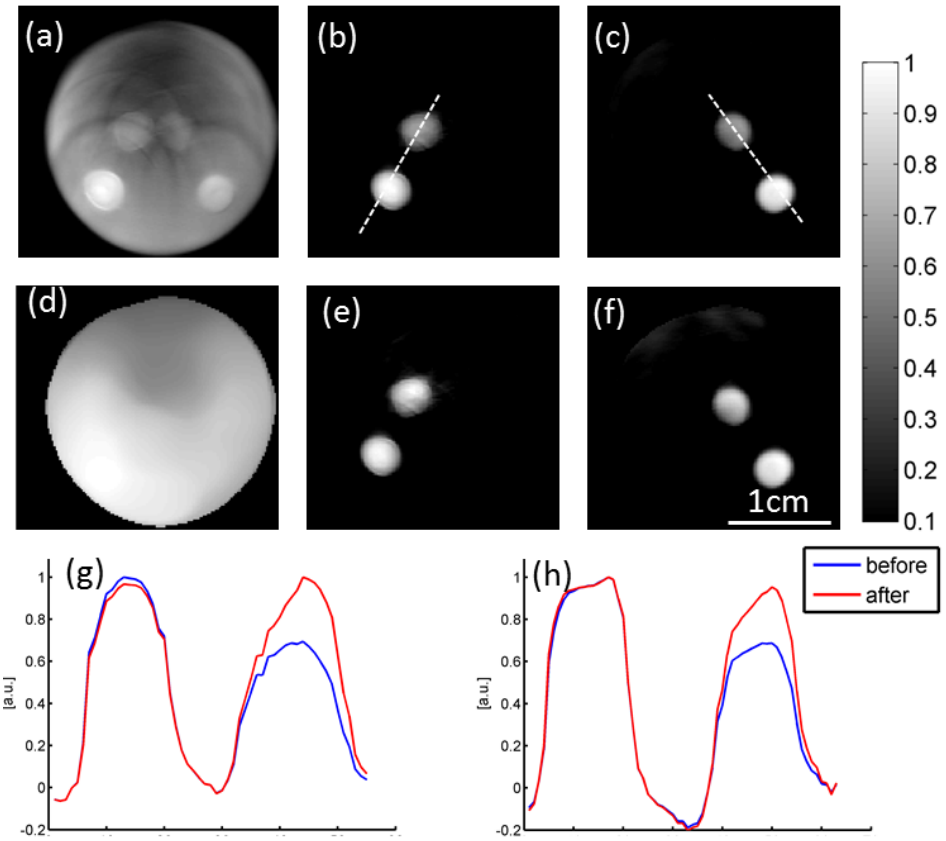

Fig. 6.9: Results of the phantom study. (a) Single wavelength image at 750 nm showing the phantom with the two insertions. (b) Unmixed Cy7 and (c) unmixed GN signal. (d) Estimated light fluence used for correcting the unmixing results. (e) Light attenuation corrected Cy7 component and (f) GN component. (g)-(h) Profiles through the unmixed components along the dashed line before and after division by the estimated light fluence.

Ex-vivo mouse

Fig. 6.10 depicts the results of the deep tissue imaging experiment. The first row shows the unmixed component before (a) and after (b) light fluence correction for an ICG concentration of 2.5 µM. The profile along the dashed line is shown in (c). The corresponding images for a 10 µM concentration are shown in the second row.

(g) and (h) show the estimated light fluence for these two concentrations. The ratio between the retrieved MSOT signals of the two tubes without and with light fluence correction as a function of the concentration is shown in (g). Before normalization the relative amplitude of the inner tube was 21 ± 6% of the outer tube, after normalization 83 ± 8% depending on the concentration. The normalization obviously corrects the effect of light attenuation but as seen from the images also increases the noise level.

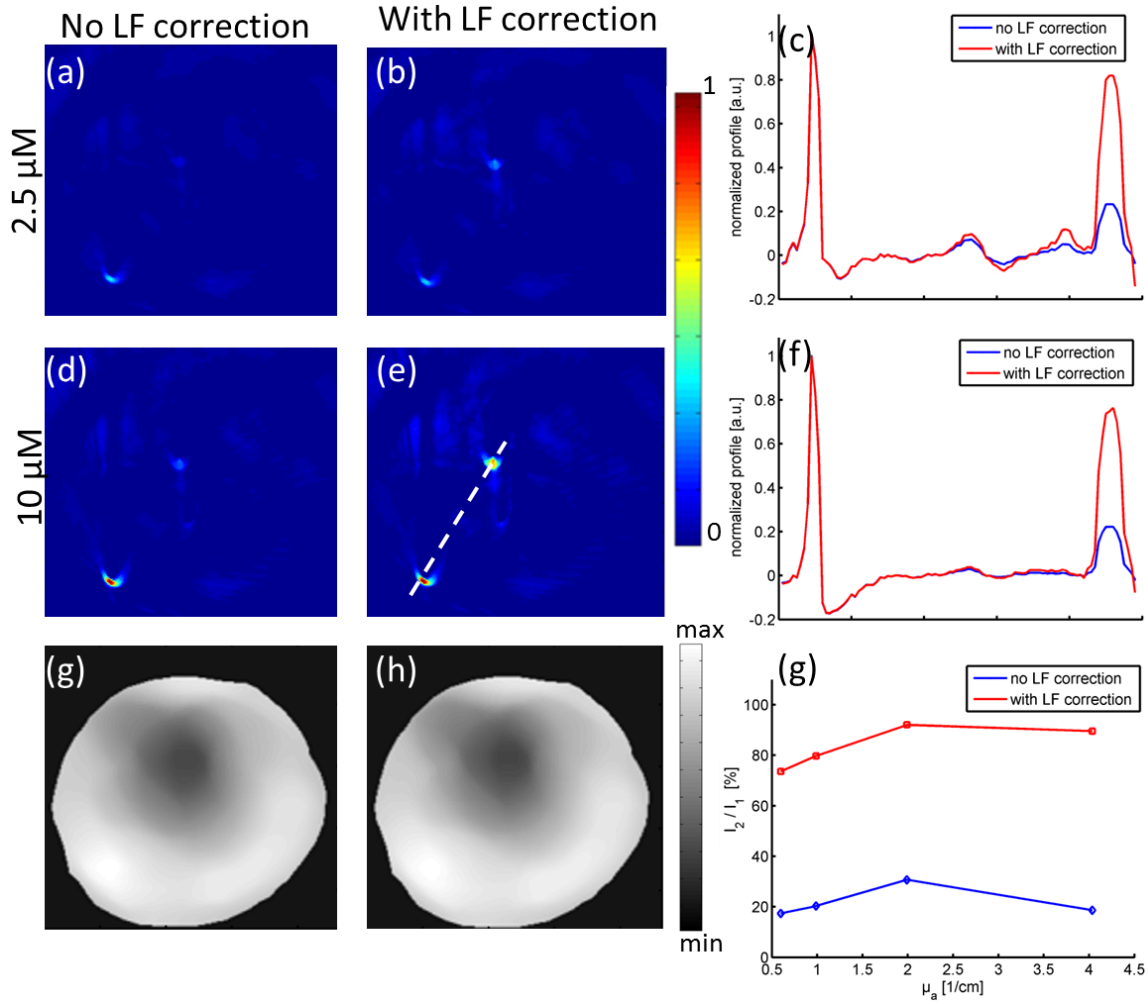

Fig. 6.10: Results of the study in real tissue. (a) Single wavelength image at 800 nm from the liver region of mouse post-mortem with two plastic tubes inserted containing ICG. (b) Estimated light fluence. (c) Profiles through the unmixed results before and after light attenuation correction. (d) Unmixed ICG component and (e) light attenuation corrected ICG component.

6.3.5 Discussion

Optoacoustic signals are proportional to the absorbed electromagnetic energy. Due to light attenuation in tissue an absorber deep inside tissue appears weaker than the same absorber close to the tissue surface. Thus, comparison of signals obtained from absorbers at different depths is inherently difficult.

To account for light attenuation effects, a simple but efficient normalization approach has been proposed in which the unmixed optoacoustic images are divided by an estimate of the light fluence heterogeneity obtained from a low pass filtered

single wavelength image acquired close to the isobestic point of hemoglobin. The approach was tested in simulation, on experimental phantoms and *ex vivo* mouse data and revealed higher reconstruction accuracy than reconstructions without light fluence correction by displaying similar absorbers located at different depth with comparable amplitudes. In this manner, the normalization approach presents a potent alternative to correction methods that employ complex calculations for fluence estimations inside tissues typically based on estimates of unknown tissue scattering properties.

The method has nevertheless some inherent limitations. Being a normalization method it may increase the noise in the resulting images. In addition, it is based on the assumption of small spectral variations of the light fluence, thus only corrects the wavelength independent effects of the light attenuation. For that reason, the method could correct the attenuation effects with a higher accuracy for the ink phantom (which has an almost flat background absorption spectrum) than in the simulation study or the mouse experiment. Also, presence of a significant amount of probe in big areas may change the light fluence pattern and thus hamper the estimation of the light fluence distribution.

To overcome this limitation, light attenuation correction should ideally be done on a per-wavelength basis before the unmixing. However, errors in the estimation of the light fluence would potentially scale up in the unmixing and thus significantly compromise the quantification accuracy. In fact, an accurate estimation of the light fluence is a difficult task which does not only require precise knowledge of the optical absorption and scattering coefficients but also accurate reconstruction of the low frequency information representative for the light fluence. The system developed herein uses cylindrically focused ultrasound transducers for 2D image reconstruction. Yet, acoustic focusing is frequency dependent and the system detects more out-of-plane signals in the low frequency range than in the high frequency range. This in combination with the limited view detection leads to errors in the reconstruction of the light fluence and thus makes light fluence corrections in single wavelength images very challenging. The method proposed herein is a ratiometric approach based on a division of two images. In this way this approach yields a relative measure and directly eliminates artifacts due to experimental inaccuracies such as out-of-plane signals but also spatial differences due to varying detector sensitivity [134].

It has also to be noted that with the current experimental system, for some areas of the mouse's body (*e.g.* lung area, intestines), reconstructed single wavelength images might show unphysical negative value artifacts in the upper part of the image (*i.e.* distant to the transducer) which are due to acoustic heterogeneities within the mouse in combination with experimental limitations of the current setup such as out-of-plane signals and limited view detection. In such a situation the method presented herein is compromised and applicable only after adding a constant term to the normalization image to avoid division by zero. Due to these experimental limitations the correcting effect achieved in *ex vivo* mouse experiment was also reduced compared to the simulation study. Yet, it is expected that this issue of negative values is improved in systems with more detection elements, an increased detection arc (about 270°) and potentially light sheet illumination to

reduce out of plane signals, so that the method becomes applicable on whole cross-sections everywhere in the mouse.

Overall, the presented approach is a direct, fast and straightforward method to compensate for the wavelength independent part of light fluence attenuation which despite of its simplified character generates a satisfying correction of the light fluence attenuation.

6.4 Summary and conclusions

In this chapter the subject of specific absorbers detection by multispectral means was discussed. The challenges were explained and two unmixing approaches presented: the first is based on fitting known absorption spectra to the set of multi-wavelength images, the latter is a blind unmixing approach involving principal and independent component analysis and does not require any a priori knowledge about the spectra of the absorbers present in tissue. In deep tissue blind unmixing yields higher detection sensitivity than spectral fitting which is due to the depth dependent distortion of the spectral profiles following wavelength dependent light attenuation.

We have also seen that due to light attenuation in tissue, the same absorber at different depths is reconstructed with different amplitudes, thus complicating comparison of signals from different depths. A simple ratiometric approach was presented, based on the normalization of the unmixed components with the lowpass filtered single wavelength image acquired at 797 nm corresponding to the isobestic point of blood in order to compensate the depth dependent amplitude reduction. The approach could correct for the wavelength independent part the light attenuation yielding an improved amplitude ratio.

7 Applications

7.1 Introduction

Various *in vivo* small animal studies, employing the small animal scanner and algorithms developed herein, have been performed to validate and characterize the imaging performance resolving anatomical, functional and molecular contrast by means of MSOT. As mentioned in the introductory chapter, it is of high scientific and economic interest to develop an imaging methodology capable of achieving this. The next chapter presents a few applications and is structured as follows: section 7.2 shows morphological imaging based on hemoglobin contrast. Section 7.3 showcases imaging of perfusion after injection of Indocyanine Green (ICG). Section 7.4 showcases molecular imaging capabilities by detecting agents that target phosphatidylserine on apoptotic cells within tumor tissue. Finally, section 7.5 showcases the ability to study pharmacokinetics by tracking the temporal evolution of normal and liposomal ICG in the blood stream.

7.2 Anatomical imaging based on hemoglobin-based contrast

The purpose of this section is to validate the feasibility to do whole body imaging of mice resolving intrinsic hemoglobin-based contrast. Some of the work described herein was published in Nature Protocols in 2011, under the title "*Volumetric real-time multispectral optoacoustic tomography of biomarkers"* [92].

Method

For imaging the mice were anesthetized using Isoflurane and positioned in supine position in the animal holder. The mice were translated through the imaging plane in order to obtain different cross-sectional images along their body. After imaging, the mice were euthanized, frozen and cryosliced for anatomical validation of the optoacoustic images. In addition one mouse was imaged at the liver area with a frame rate of 10 Hz in order to track movements due the breathing motions. The imaging wavelength was 750 nm in all the cases. All procedures involving animals and their care were conducted in full agreement with the institutional guidelines, complying with national and international laws and regulations.

Results

Fig. 7.1 shows a stack of representative cross-sectional optoacoustic reconstructions of a mouse imaged in supine position. The reconstruction was done with the 2D IMMI method. Fig. 7.1 (b)-(d) show slices through the mouse's abdomen, liver area and head as well as photographs of the corresponding cryoslices. There is accurate congruence between features in the non-invasive optoacoustic images and the anatomical photographs of the cryosliced mouse. The abdominal image for instance, clearly reveals the kidneys, the spleen, the spine and major vessels like the vena cava. In the upper abdomen image we see the liver with its internal vasculature, in

the head slice the brain with surrounding vessels. Differences observed in the images and the cryoslices can be explained by slight organ movements between the optoacoustic and cryoslice imaging, the different vertical resolutions of the two methods and differences in the exact location that the images and the cryosliced images were acquired from.

Fig. 7.2 shows a whole body scan of a second mouse. Images were reconstructed with the *3D MB+SIR* algorithm. Cross-sectional slices are shown in (a). Maximum intensity projections in y-direction of 0.3 mm thick coronal slices from different depths are shown in (b)-(c). The location of the slices is indicated in the cross-sectional reconstructions depicted in (a). Organs like kidney and liver and major vasculature like vena cava, portal vein or the sagittal sinus are clearly visible in the coronal slices. MIPs of the whole mouse from two different orthogonal views are shown in (e) and (f).

Real-time imaging is showcased by monitoring the respiratory motions of a mouse at a 10 Hz frame rate. Fig. 7.3 (a)-(c) depicts three consecutive frames from the time-series acquired. Arrows indicate structures which undergo strong movements. Fig. 7.3 (d)-(f) shows the superposition of the first frame (blue) and the consecutive frames (red) in order to highlight the movement. There is obvious movement between consecutive frames. Individual images are however not affected by the movement, since all the data necessary for a reconstruction is acquired at a single laser pulse, thus free of blurring due to motion.

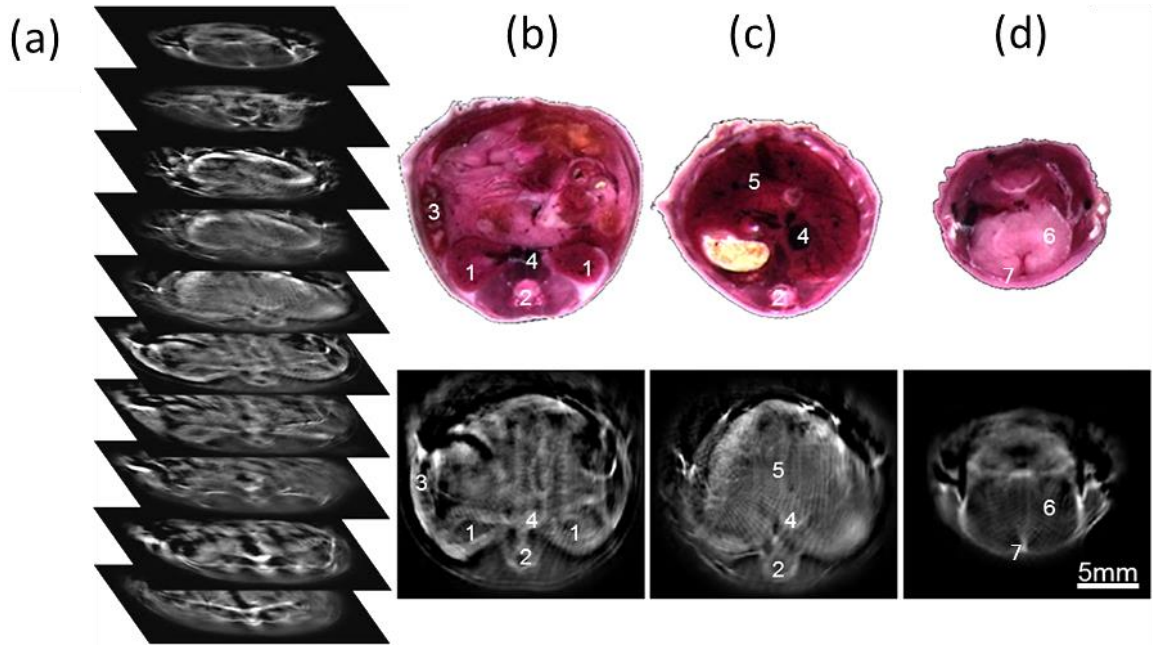

Fig. 7.1: Single wavelength optoacoustic images of mouse anatomy. (a) Stack of crossectional optoacoustic images throughout the whole body of a nude atymic CD1 mouse, as well as individual reconstructions done at the abdominal (b), thoracic (c) and head (d) levels. Photographs of the corresponding *ex vivo* cryoslices are also shown. 1: kidneys, 2: spine, 3: spleen, 4: vena cava, 5: liver, 6: brain, 7: sagittal sinus. (Panels (a) and (c) published in [92], Copyright 2011, Nature publishing group).

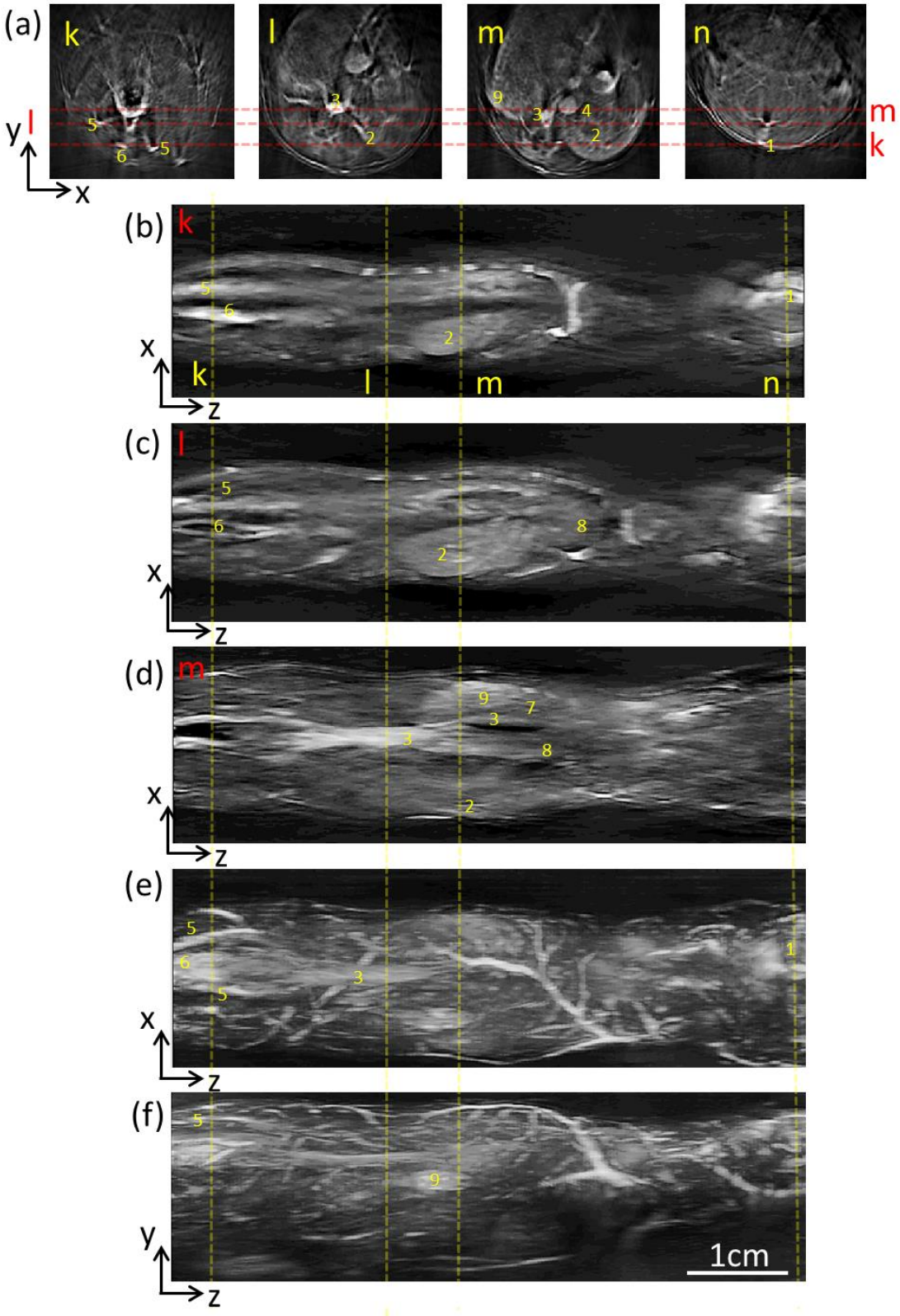

Fig. 7.2: *In vivo* whole body scan of a mouse at 800 nm. (a) Cross-sectional slices at different heights indicating where the longitudinal slices have been taken from. (b) MIP in y-direction over a 1 mm thick volume at position k, (c) position l and (d) position m. (e) shows the MIP of the 3D reconstruction along the y-axis and (f) along the x-axis. 1: sagittal sinus; 2: right kidney; 3: vena cava; 4: portal vein; 5: ischiatic vein; 6: middle vein; 7: vasculature below rips; 8: liver.

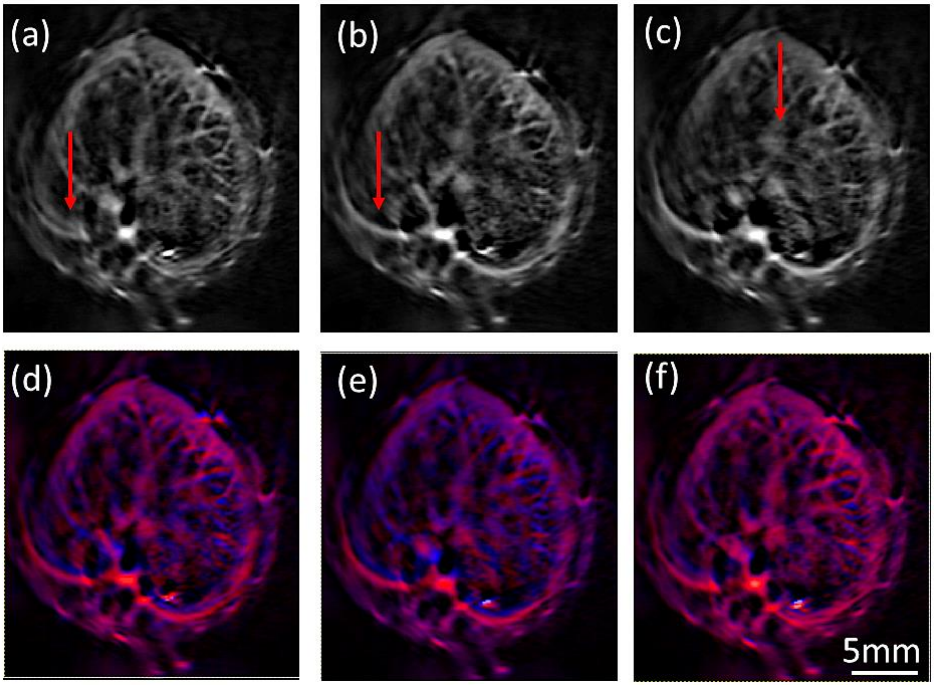

Fig. 7.3: Consecutive frames of a video acquired at the liver region showing the respiratory movements of a 5 weeks old CD1 mouse imaged at a 10 Hz frame rate (a)-(c). Arrows indicate structures which move due to the respiratory movement. Overlay between the frame of the first time-point (blue) and the consecutive frames (red) accentuating the movement of the structures (d)-(f).

Discussion

The unique design of the system enables convenient whole body imaging of living mice. This is showcased by the stack of cross-sectional images throughout the whole body of a living mouse. All major organs, such as kidneys, spleen, liver and brain, can be visualized non-invasively based on PA imaging. Since MSOT is sensitive to hemoglobin contrast, the vasculature is also clearly visible. One can further recognize that the image quality is superior in the lower part of the image. This is due to the limited view problem as discussed in section 2.4.6. In order to image other clinically relevant structures such as heart, intestine or carotid arteries in more detail, the mouse can be positioned in prone position. Such images where shown by Taruttis *et al.* in [135-137], using the system developed herein for cardiac imaging applications. In future implementations with more detection elements and an almost closed detection arc the image quality in the upper half will improve significantly making the currently required prone/supine position change obsolete. Since the system is optimized to acquire a dataset for a cross-sectional reconstruction in parallel without the need of data averaging, it is possible to translate the animal at constant speed during continuous data acquisition for a fast whole body scan. If the animal is translated at 4 mms^{-1}, then a single wavelength whole body scan can be done within 20 s. This is considerably faster than the 8 minutes of scanning time achieved in other optoacoustic small animal scanner (cf. section 3.2.2). Eventually, a stack of cross-sectional 2D images can be fed in a volumetric visualisation toolbox for direct 3D or maximum intensity pseudo 3D representation. However, coronal or sagittal slices have a lower resolution than cross-sectional ones, because the resolution in z-direction depends on the focusing capacities of the

transducer. Since the complete dataset for a cross-sectional reconstruction is acquired in parallel, the individual cross-sectional images are free of motion artefacts. This is clearly shown by imaging the liver during a breathing motion of the mouse. Each individual image is sharp without blurring, although motions occur as seen by comparing consecutive frames. This performance characteristic is unique to the optoacoustic imaging system developed herein and imaging systems that are able to achieve such real-time image formation, are not yet described elsewhere.

7.3 Imaging of perfusion

The goal of this study is to achieve functional imaging by tracking dynamic changes. Here, we monitor kidney perfusion after intravenous injection of Indocyanine Green (ICG). In addition, it is shown for the first time *in vivo* that multispectral unmixing can be used to detect extrinsic absorbers such as ICG based on their spectral signature. This study was published 2010 in Optics Letters under the title "*Video rate optoacoustic tomography of mouse kidney perfusion"* [77] and it was to my knowledge the first time that dynamic processes have been monitored deep inside tissue by means of optoacoustic imaging and that multispectral unmixing was applied to resolve contrast agents in living mice.

Method

For imaging, a female, 8 weeks old CD1 mouse was anesthetized with a mixture of ketamine and xylazine and hair was removed with a hair removing lotion. The animal was then placed in the supine position in the imaging chamber and 300 nmol of Indocyanine Green (ICG) solution was injected systemically. Indocyanine green is a fluorescence dye widely used in clinical applications, such as ophthalmic angiography, for determining cardiac output, hepatic function, and liver blood flow. Upon intravenous injection, ICG rapidly binds to plasma proteins and is thereby confined to the vascular space [138]. This and its absorption maximum at 805 nm near the isobestic point of oxyhemoglobin and deoxyhemoglobin makes it particularly suited for angiographic applications [113]. Following single-pulse measurements of kidney perfusion at constant position and at a wavelength of 800 nm, a multispectral dataset of the kidney was acquired at 9 wavelengths (750, 770, 790, 810, 830, 850, 870, 890 and 910 nm, respectively). In contrast to the video-rate perfusion imaging that was performed at 10 Hz without averaging, here 50 averages were acquired per wavelength in order to average out the movements of the mouse. Per-wavelength energy variations were corrected by powermeter readings done before imaging. For unmixing the spectral fitting method presented in section 6.2.2 was employed using three spectra (ICG, oxygenized and deoxygenized hemoglobin) shown in Fig. 7.6 (b). Fluence variations inside the tissue have not been corrected. After imaging, the animal was euthanized, cryosliced and photographed for confirmation of the non-invasive optoacoustic images.

Results

Fig. 7.4 depicts results from the real-time imaging studies and corresponding confirmatory *ex vivo* imaging. Fig. 7.4 (a) shows a stack of subsequent single wavelength (800 nm) optoacoustic slices obtained *in vivo* from the pelvis and the

kidney region. Fig. 7.4 (b) shows the slice which was imaged during the injection of ICG while the photograph of a cryoslice through the mouse kidneys at a similar height is presented in Fig. 7.4 (c). There is accurate congruence between features in the non-invasive optoacoustic imaging and the anatomical photograph of the cryosliced mouse. Beside the kidneys, the spine, surrounding muscle and vasculature are also clearly identified on the optoacoustic image. Differences observed in the images can be explained by slight organ movements between *in vivo* and *ex vivo* imaging and differences in the exact height that the *in vivo* images and the cryosliced images were acquired from.

Fig. 7.5 shows a time series of images acquired in real time after ICG injection as single wavelength images (a) and as an overlay of the contrast enhancement observed (color) superimposed on the image before injection of ICG (b). Frames at different time points were selected to show the dynamics of ICG kidney perfusion. About 16 seconds after injection of ICG there is the first appearance of ICG in the imaging plane, showing as a localized activity in the center of the image. In the subsequent slices, a gradual spread of the dye into the kidneys can be observed while an increasing number of vascular structures enhance their contrast due to presence of ICG. 540% contrast increase was measured in the vessel in (a) highlighted by the arrow.

Finally, Fig. 7.6 (a) shows a multi-spectral optoacoustic (MSOT) image, which detects the ICG presence based on its unique spectral signature instead of resolving it as an absorption difference over a background image. ICG has a characteristic absorption spectrum [113] in the 750-900 nm spectral window that differs significantly from the spectra of blood [6] and overall background tissue (Fig. 7.6 (b)) and it was resolved herein with per-pixel multispectral decomposition [4].

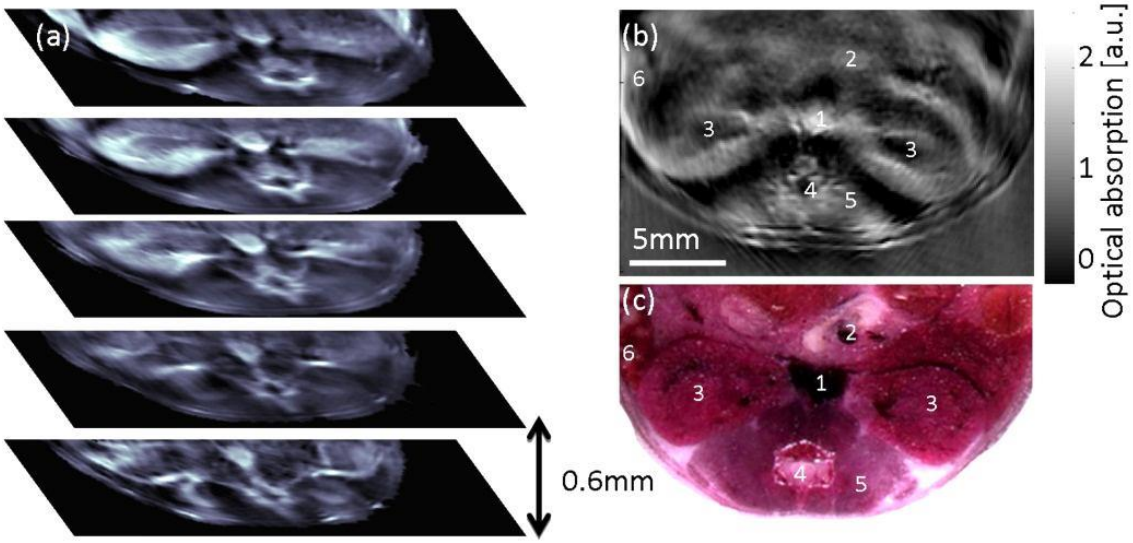

Fig. 7.4: (a) A stack of representative slices of a 3D dataset of the pelvis and kidney region of a female 8 weeks old CD1 mouse. (b) Cross-sectional optoacoustic image before injection of the slice in which the kinetics of ICG was monitored. (c) Photograph of a cross-sectional cryoslice at a height corresponding to that shown in (b): 1. vena cava, 2. portal vein, 3. kidneys, 4. spinal cord, 5. backbone muscles and 6. spleen. (Figure published in [77], Copyright 2010, Optical Society of America).

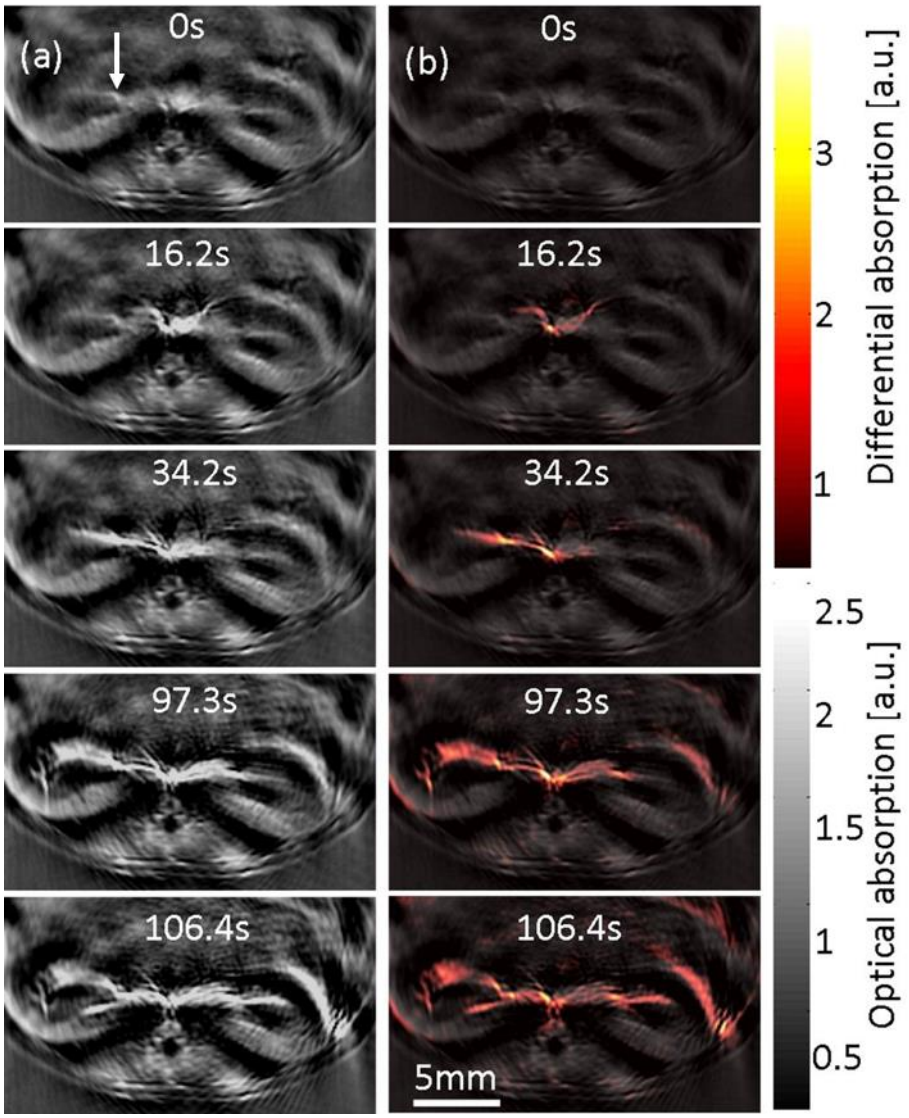

Fig. 7.5: (a) Crossectional optoacoustic images at different timepoints of the kidneys of a female CD1 mouse illuminated at 800 nm after having injected 0.33 µmol of ICG. (b) Superposition of the difference image and single wavelength image before injection. (Figure published in [77], Copyright 2010, Optical Society of America).

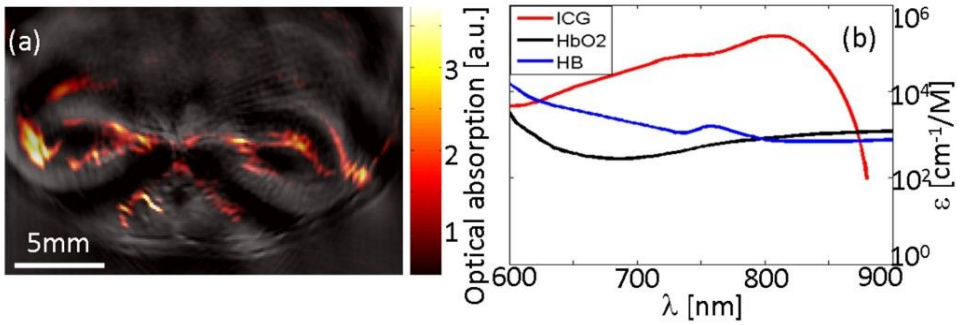

Fig. 7.6: (a) Superposition of a single wavelength image (890 nm) and the unmixed component corresponding to the ICG signal. (b) Molecular extinction coefficient of ICG [113], oxygenized and deoxygenized hemoglobin. (Figure published in [77], Copyright 2010, Optical Society of America).

Discussion

Functional imaging performance was demonstrated by resolving mouse kidney anatomy and perfusion using ICG, an exogenously introduced blood-pool agent. Images produced were congruent with corresponding photographs of the mouse anatomy, based on cryoslices obtained from the same animal imaged with MSOT. Spectral unmixing further demonstrated the ability of the system to visualize externally administered contrast based on its unique spectral signature without using background measurements made prior to the probe administration. Kidneys play a crucial role in physiology, they filter the blood to remove waste from the blood stream and excrete them, and maintain homeostasis (electrolyte concentrations, control of blood volume and regularization of blood pressure) [139]. Also, a number of diseases are related to altered renal perfusion, such as essential hypertension [140] or acute renal failure [141] and therefore many efforts have been made to visualize the renal morphology and perfusion. Existing techniques reach from invasive contrast-specific flow measurements in computed tomography (CT) [142-144], magnetic resonance imaging [145] and ultrasound [146], to non-invasive techniques like arterial spin-labeling techniques [147]. Optoacoustic tomography, providing in real-time both anatomical and functional information about the perfusion, can therefore become a promising alternative for these existing methods.

7.4 Molecular imaging

A versatile pool of optical reporter agents and imaging methods for enhancement and probing of anatomical features and molecular pathways in tumor tissue is available [3, 148]. The optical contrast is provided by fluorochromes [19] and other organic dyes, quantum dots [33] and several forms of nanoparticles [31, 149] with a large selection of accumulation, targeting and activation mechanisms [150, 151]. However, their *in vivo* visualization is challenging, due to intensive light scattering in tissues. As a consequence, established methods such as fluorescence molecular tomography generally attain low spatial resolution and suffer from low imaging speed [152, 153]. Moreover, questions related to the exact probe localization (*e.g.* necrotic foci within the tumors versus surface of the tumor blood vessels) cannot be answered using those methods. MSOT on the other hand, yields high resolution even in deep tissue. The goal herein is to showcase that MSOT can be used to detect such molecular contrast agents in tumors. This is done exemplarily for novel optical probe comprising a synthetic zinc(II)-dipicolylamine complex conjugated to a near-IR carbocyanine fluorophore (subsequently called PSS-794). It has recently been shown that this probe can selectively target anionic membrane-bound phosphatidylserine (PS), exposed by dead and dying cells within xenograft tumors in rat and mouse models [154]. Usually restricted to the inner leaflet of the plasma membrane, phosphatidylserine is selectively exposed as an early event during cell apoptosis, which is a crucial mechanism of cell number control in various physiological and pathological events [155]. Herein it is shown that PSS-794 can be detected in tumors *in vivo* with high resolution using MSOT. This study was published 2012 in EJNMMI research with the title *"High resolution tumor targeting in living mice by means of multispectral optoacoustic tomography"* [156].

Materials and methods

For imaging, four female, 8 weeks old athymic CD-1 nude mice, containing 4T1 tumor allografts were used. The tumors were obtained by injecting 0.8 x 10^5 4T1 cells subcutaneously into the mouse's neck where they were allowed to grow for 7 days, reaching a diameter of 0.4 to 0.5 cm. The PSS-794 imaging probe was prepared as previously reported [157]. The first two tumor-carrying mice were injected intravenously *via* the tail vein 24 hours prior to imaging with 6 $mgkg^{-1}$ (100 nmol) and 3 $mgkg^{-1}$ (50 nmol) of the probe, respectively. A third mouse was injected 3 hours prior imaging with probe amount of 3 $mgkg^{-1}$ (50 nmol). For control, a fourth mouse was injected with 3 $mgkg^{-1}$ (50 nmol) of Indocyanine Green (ICG), a non-targeted dye having spectral characteristics similar to PSS-794 in the near-infrared [77]. The mice were anesthetized with a mixture of ketamine and xylazine and placed in the supine position in the animal holder. Cross-sectional multispectral optoacoustic image datasets were acquired through the tumor at 6 different wavelengths in the NIR-window (700, 740, 760, 780, 800 and 900 nm, respectively).

Reconstruction of single-wavelength optoacoustic images was done with interpolated matrix model inversion (IMMI) method [66]. Prior to inversion, the raw optoacoustic signals were bandpass-filtered between 50 and 7 MHz and deconvolved with the combined electrical impulse response of the ultrasonic detectors and the acquisition system. For inversion of the forward matrix, the iterative PLSQR algorithm has been used. To selectively detect the biodistribution of the probe over intrinsic tissue absorption background, blind multispectral unmixing (cf. section 6.2.3) was applied.

For validation purposes, one mouse was also imaged *ex vivo* with a 360° free-space FMT-XCT system, which combines fluorescence molecular tomography (FMT) with small animal X-ray CT (XCT) into a hybrid imaging device [158]. The system was capable of simultaneous three-dimensional visualization of small animal anatomy and biodistribution of fluorescent probes *in vivo*. For volumetric FMT reconstructtions, 12 angular projections distributed over full 360° range were acquired close to the excitation and emission wavelengths of PSS-794. Following the FMT-XCT measurement, the euthanized mice were cooled to -80°C. For further verification of the *in vivo* MSOT and FMT images, cross-sectional colour photographs (RGB) and fluorescence images were also obtained using a cryotome, supplemented by a home-built multispectral epi-fluorescence system [159]. The system consisted of a white light source and a sensitive CCD camera with motorized filter wheels for selection of the excitation and emission wavelengths.

After cryolicing, selective tissue samples in the tumor area were used for histological validation for highly specific detection of apoptosis using commercially available annexin V antibody (Abcam PLC, Cambridge, United Kingdom).

Results

Fig. 7.7 depicts the molar extinction coefficient of the targeted PSS-794 probe in 35 $mgml^{-1}$ albumin, acquired using a fiber optic spectrophotometer (model USB 2000, Ocean Optics Inc., Dunedin, FL), as well as the spectra of oxygenized and deoxygenized haemoglobin. The spectrum of PSS-794 has a characteristic shape with an absorption maximum at 810 nm close to the isobestic point of blood. It thus

differs significantly from the major background tissue absorbers, making it well suited for multispectral optoacoustic detection with high sensitivity.

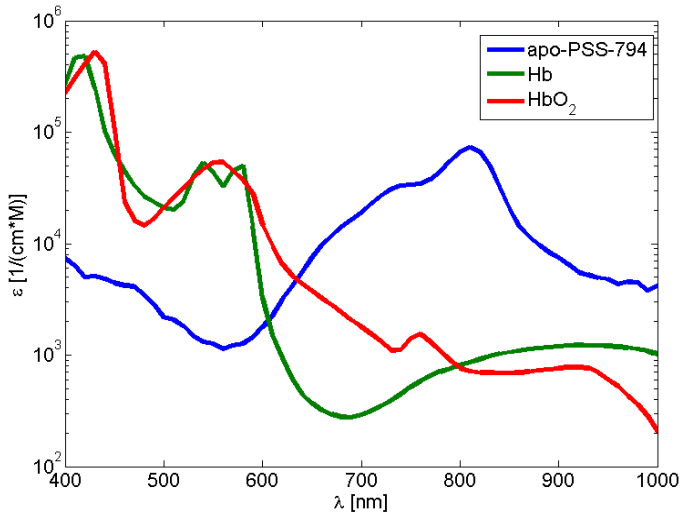

Fig. 7.7: Molar extinction coefficient of PSS-794 in 35 mgml^{-1} albumin along with extinction spectra of oxygenized and deoxygenized hemoglobin. (Figure published in [156], Copyright 2012, Springer).

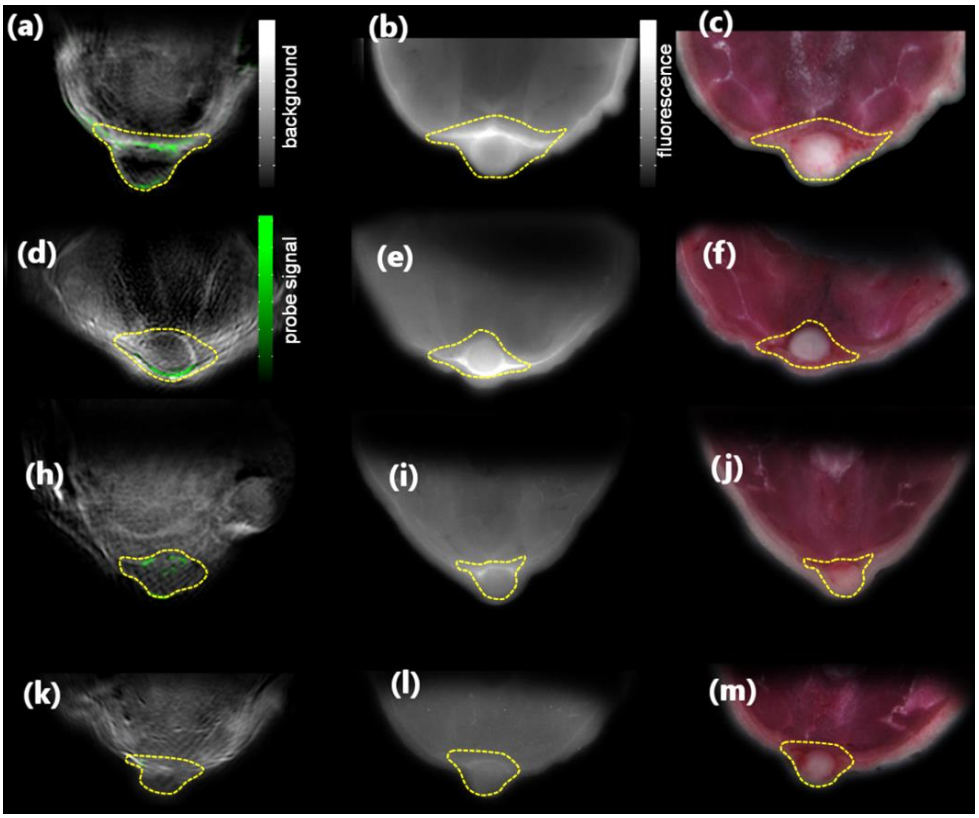

Fig. 7.8: Imaging of targeted marker (PSS-794) in 4T1 tumor-bearing mice. In the first column the MSOT images are shown. (a) and (d) show superposition of a single-wavelength (anatomical) optoacoustic image (in gray scale) and the unmixed component corresponding to the PSS-794 signal in colour for the two mice imaged 24 hours after injection. (h) shows the unmixed PSS-794 signal for the mouse imaged 3 hours post injection, and (k) the ICG signal also imaged 3h post injection. The second column shows the corresponding epi-fluorescence images of cryoslices through the tumor. Color photograph of cryoslices are shown in the third column. The tumor margins are delineated in yellow. (Figure published in [156], Copyright 2012, Springer).

Fig. 7.8 (a), and (d) show the spectrally unmixed MSOT signals from the two mice imaged *in vivo* 24 hours after injections. The single wavelength optoacoustic images acquired at 900 nm are shown in grey scale while the spectrally unmixed MSOT signals are superimposed in colour. Fig. 7.8 (h) shows the result from the mouse imaged 3 hours after injection and Fig. 7.8 (k) the result for the mouse injected with ICG. The PSS-794 signal is visible in all the three cases, whereas signal from ICG is not detectable. Apparently, analysis of the high-resolution MSOT images clearly shows that the PSS-794 probe mainly accumulates in the blood vessels surrounding the tumours while no infiltration of the probe into the tumour mass occurs.

On the other hand, reconstruction of the subsequent *ex vivo* FMT measurement, shown in Fig. 7.9 (c), generally confirms the fact that the probe accumulated around the tumour areas. Yet, due to the lower resolution of the method, it is difficult to determine whether the fluorescence signal is originating only from the vasculature or from within the tumour parenchyma. The exact origin of the fluorescence signal is also not recognizable from the poorly resolved transillumination fluorescence image (Fig. 7.9 (d)). The results of the validation cryo-slicing and epi-fluorescence studies, made on euthanized mice, are shown in Fig. 7.8 (b), (e), (i), (l). The colour pictures of the cryo-sliced mouse in Fig. 7.8 (c), (f), (j) and (g) show the actual location of the tumor mass, which can also be readily delineated on the single-wavelength optoacoutic images. In summary, both the *in vivo* MSOT and the *ex vivo* epi-fluorescence images clearly reveal that the fluorescence signal of the PSS-794 probe is localized in the blood vessels surrounding the tumour. Observation of the Annexin V-positive areas in the histological image in Fig. 7.9 (e) suggests that only a relatively small number of apoptotic cells exist in the tumor.

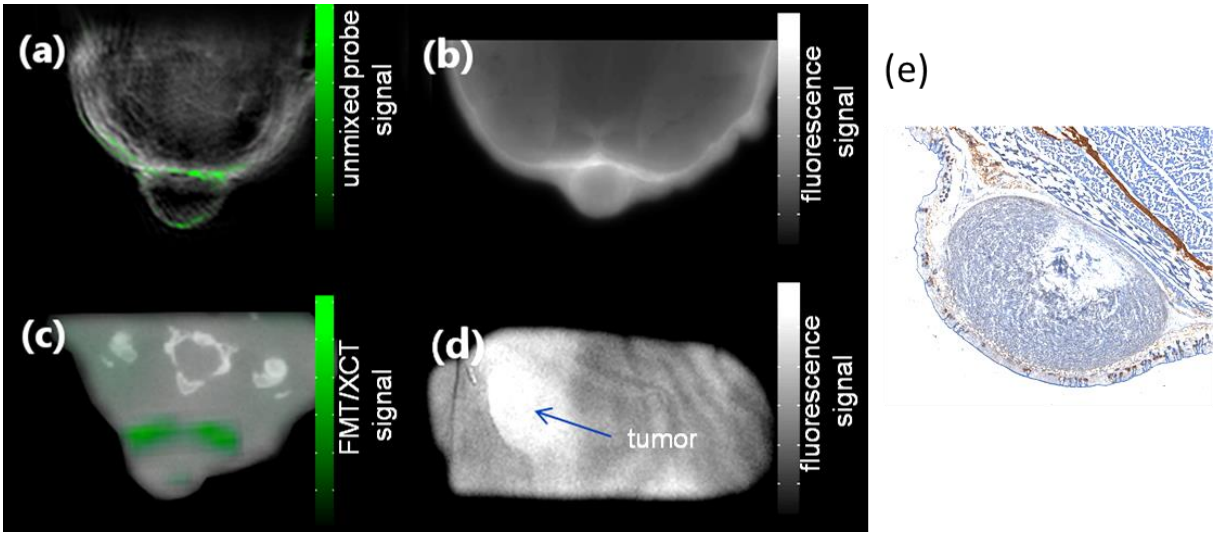

Fig. 7.9: Comparison between optical imaging and MSOT. (a) shows the MSOT image and (b) the corresponding epi-fluoresence image. An FMT-XCT reconstruction is shown in (c) and a planar transillumination image in (d). (e) Representative histological slice of the tumor mass. (Figure published in [156], Copyright 2012, Springer).

Discussion

Previous studies have shown that the fluorescent PS-targeting probe, PSS-794, can be used to image apoptotic/necrotic tissues often found inside tumors by optical methods [160].

Here, it is demonstrated for the first time that PSS-794 does not infiltrate into the tumor mass of 4T1 tumor allografts. Lack of depth resolution during planar fluorescence imaging may lead to the conclusion that PSS-794 is concentrated in the tumor mass, whereas it is actually located in the periphery around the tumor. Even the use of three-dimensional optical tomography (FMT) has not attained the sufficient spatial resolution that would enable the determination of the precise location of the probe. In contrast, the much higher resolution of the MSOT revealed accumulation of the PSS-794 in the blood vessels surrounding the tumor area and clearly showed no infiltration into the tumor mass. This lack of extravasation has been also confirmed by the post-mortem epi-fluorescence images. This suggests that the imaging time-point (1 week post tumor cell inoculation), the vasculature of the model is not leaky. The lack of extravasation can be explained by the fact that both ICG and PSS794 are known to associate with serum proteins, and it is hard for the large protein/dye complex to extravasate from the neovasculature, especially if there is a high interstitial pressure in the tumor [161]. The unspecific ICG dye is not detected in the imaging area at all, which suggests that the observed PSS-794 signal is the results of targeting a certain biomarker, most likely the phosphatidyl-serine(PS) exposed on vessel walls of the neovasculature [162, 163]. There is evidence that 20 to 40% of the blood vessel surfaces in all tumors and metastases that are larger than 1 mm expose PS, even though these endothelial cells are vital and not apoptotic [164]. Moreover, it normally takes 6 to 24 h to exert the enhanced permeability and retention (EPR) effect [165]. Thus the strong PSS-794 signal at the tumor-border by 3 h (Fig. 7.8 h) cannot be explained either by the EPR effect. This is because, if the tumor vasculature were to be leaky, both PSS-794 and ICG should have been observed within the tumor parenchyma. In any case, the current study showcases the power of MSOT to uncover new high resolution information about the precise location of imaging probes within sites of disease.

In conclusion, MSOT was used to accurately detect the targeted PSS-794 probe *in vivo* over strong background absorption of blood with spatial resolution up to 150 µm, attaining unprecedented image quality for deep-tissue imaging of optical contrast. The enhanced resolution of the MSOT clearly showed that the probe mainly localizes in the vessels surrounding the tumor, suggesting that the probe gains its tumor selectivity by targeting the PS that is exposed on the surface of the tumor blood vessels. The MSOT results further correlated well with cryoslices and epi-fluorescence images of *ex vivo* specimens. Overall, this study demonstrates the high potential of MSOT to broadly impact the fields of tumor diagnostics and preclinical drug development.

7.5 Determining pharmacokinetic properties by MSOT imaging

Pharmacokinetics (PK) involves the study of drug absorption, distribution and elimination and is an important part of drug development, because PK parameters - such as the clearance rate of an administered agent from the blood pool - determine drug exposure and thus efficacy [166]. Moreover, regulatory agencies require PK analysis to be part of any new drug application. Typically, pharmacokinetic para-meters are determined by bleeding the animal at specific time points in order to measure the concentration of the agent. In order to be able to draw a meaningful curve containing multiple time points, this has to be done for several animals and thus requires a lot of time, money and is prone to inter mouse variations. Possessing a method to determine pharmacokinetic properties of a probe non-invasively and *in vivo* is therefore highly beneficial. It can reduce the amount of animals needed and associated costs and accelerates drug development. The goal of the research, presented in this section, is to use the real-time imaging ability of the MSOT system developed herein to determine the clearance rate of externally administered agents in living animals non-invasively. In this experiment liposomally encapsulated Indocyanine green (ICG) and non-encapsulated ICG was used. ICG is a clinically approved fluorescent dye. It is cleared from the bloodstream by the liver followed by biliary excretion and has a half-time in the blood stream between 150 and 180 s [167]. Compared to free ICG, liposomally encapsulated ICG displays a slight red-shift and increased stability, both with regard to shelf-life and *in vivo* stability [168]. Furthermore, the formulation contains a PEGylated lipid that leads extended circulation times compared to non-PEGylated formulations. PEGylation of particles leads to decreased uptake by the reticulo-endothelial system (RES), the main clearance mechanism for liposomes [169].

Methods

ICG-containing liposomes were provided by iThera Medical, GmbH (Neuherberg, Germany). Briefly, 100 µmol of neutral lipids dissolved in chloroform were dried by rotary evaporation followed by 1 hour desiccation. The lipids were then hydrated with 5 mL HEPES buffered saline (150 mM NaCl, 7.5 mM HEPES; pH = 7.4) containing 2 µmol ICG. After bath sonication the liposomes were extruded 11 times through a 200 nm membrane followed by a second extrusion through a 100 nm membrane (11 times). Lastly, the liposomes were purified from en-capsulated ICG by gel filtration (Sephadex CL-4B); the encapsulation percentage was 99%, leading to a final ICG concentration of 0.4 mM.

For imaging, two female BALB/c nude mice were anesthetized with Isoflurane and a tail vein catheter was placed before the animal was positioned in prone position in the imaging chamber. A well-perfused abdominal region of the mouse was then continuously imaged immediately before and for 30 minutes after injection of 50 nmol of ICG or liposomal ICG. Multiple wavelengths (710, 735, 760, 800, 850 and 900 nm, respectively) were used, allowing for spectral unmixing and 50 averages were taken at each wavelength to account of animal movement. After imaging the mice were euthanized and the ICG content in plasma was determined by fluores-cence spectroscopy [168].

Optoacoustic images were reconstructed with the IMMI method. For separation of the spectral components, spectral fitting was performed. The input spectra were the spectrum of ICG, oxygenized and deoxygenized hemoglobin.

To analyze the pharmacokinetics of the injected probes in plasma, the unmixed MSOT signal corresponding to the ICG component was monitored in a large vessel as indicated in Fig. 7.10 by the red circle. Furthermore, the experimental data was fitted to an exponential function to determine the half-life of the probes in the plasma.

Results

Fig. 7.10 depicts the unmixed ICG components superimposed onto the 900 nm single wavelength images. The transparency map of the overlay scales linearly with the intensity of the unmixed signal. Images are shown for free and liposomal ICG at three different time-points: before injection (left panels), directly after injection (middle panels) and 30 minutes after injections (right panels). In contrast to liposomal ICG, free ICG cannot be detected in the t = 30 min image. Fig. 7.11 depicts the measured concentration versus time curves for the two components and their numerical fit. Unmixed ICG values were converted to ICG-concentrations by extrapolating from ICG concentration in the blood pool measured post-mortem 30 min after injection by fluorescence spectroscopy. From the fit the half-life of free ICG in the blood pool was calculated to be 3 min and the half-life of liposomal ICG to be 106 min.

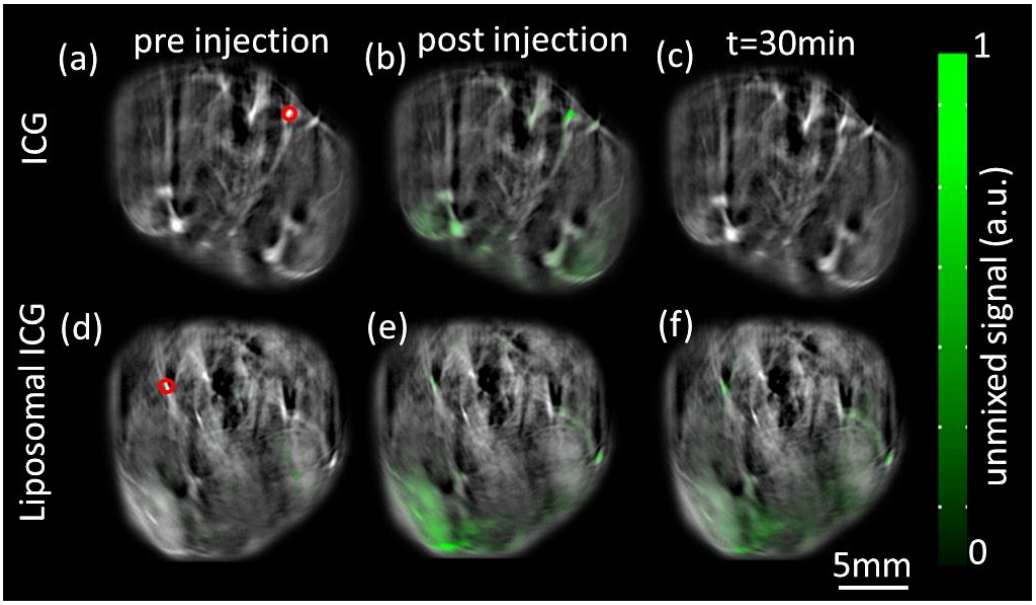

Fig. 7.10: Visualization of clearance of non-encapsulated and liposomal ICG from the bloodstream. Images show the unmixed ICG signal superimposed onto the single wavelength image acquired at 900 nm. Images are shown for three time points: pre-injection (left panels), immediately after injection (middle panels) and 30 minutes post injection (right panels). The red circles indicate the region of interest the signals were acquired from.

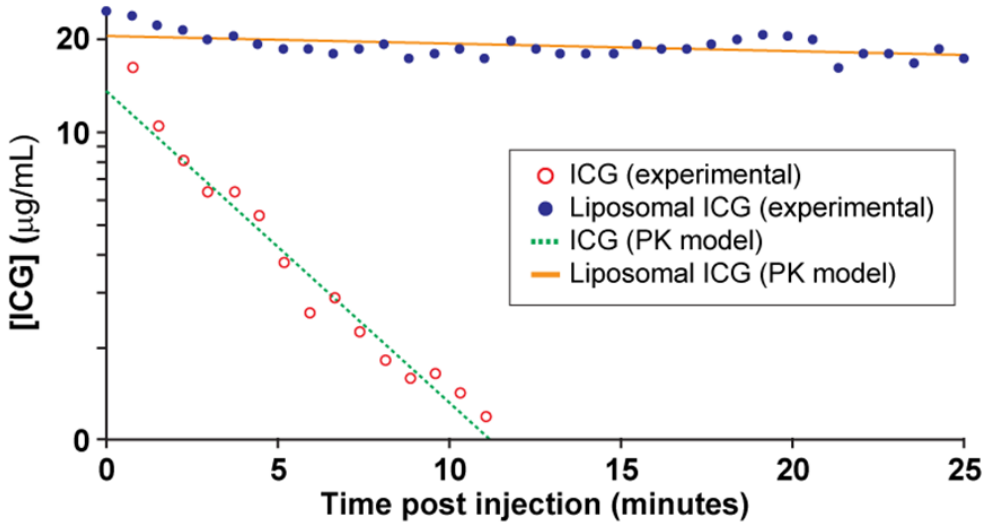

Fig. 7.11: Measurement and pharmacokinetic modeling of the ICG plasma-concentration vs. time curves. The vessels within which the ICG concentration is tracked are indicated in Fig. 7.10 by the red circles. Unmixed optoacoustic values were converted to ICG-concentrations by determining ICG plasma levels at t = 30 min by fluorescence spectroscopy and extrapolation.

Discussion

This study showed the ability of MSOT to non-invasively examine the clearance of free and liposomal ICG from the blood pool. The half-life of ICG was determined to be about 3 minutes which is in good agreement with the values from literature [167]. Liposomally encapsulated ICG was retained much longer in the plasma yielding a half-life of 106 minutes. The circulation time of liposomes can be tuned by changing the degree of PEGylation. The polymer shield influences surface charge, hydrophilicity, steric effects and plasma protein binding of the liposomal formulation, all leading to decreased uptake by macrophages that constitute the RES [170]. Although a multispectral dataset was used herein to determine the clearance rate of the probes from the blood stream, an alternative approach is to use single wavelength images, acquired at the absorption peak of the probe and subsequent monitoring of the optoacoustic signal strength within the area of interest. Compared to the multispectral approach, the single wavelength approach can yield a much higher temporal resolution with up to ten data points per second. The multispectral approach on the contrary has the advantage that it resolves the probe over the background, *i.e.* in addition to the information about the probe's pharmacokinetics; it can also provide information about its biodistribution. Temporal resolution of multispectral data acquisition can be improved by minimizing the number of wavelengths imaged or by faster tuning lasers. In conclusion, this study showed the possibility to determine the pharmacokinetics of administered drugs quickly and non-invasively by means of MSOT without the need of bleeding or sacrificing the animal, thus reducing the number of animals needed and saving time. Overall, this study shows that MSOT can help accelerating the screening of new drug-candidates.

7.6 Conclusion

MSOT is unique with its combination of resolution, penetration depth and molecular sensitivity. No other imaging modality offers this performance. Although the distinct properties of MSOT were theoretically known [4], MSOT has not been used for imaging mice before. Utilizing the properties of the small animal scanner developed herein, several examples of the use of MSOT for resolving anatomical, dynamic and molecular information in living mice are established. This has tremendous potential for small animal imaging.

Specifically, a whole-body scan of a mouse based on intrinsic contrast was presented and it was shown that clinically relevant targets such as kidney, liver, spleen, heart and brain, as well as the major vasculature, are accessible with the system.

Moreover, it could be showcased that it is possible to monitor dynamic processes such as breathing motions and perfusion after injection of ICG with unprecedented temporal and spatial resolution. It was also the first time that systemic administered ICG was resolved over background absorbers by means of MSOT.

Molecular imaging performance was showcased by detecting phosphatidylserine targeting contrast agent in tumor xenografts. MSOT yielded a superior image quality and resolution than established fluorescence imaging techniques such as epi-fluorescence imaging and hybrid FMT/XCT. Also, it was the first study showcasing that targeting fluorescent agents can be detected by means of MSOT *in vivo*.

Finally, benefiting from the high temporal and spatial resolution of the system it could be shown that pharmacokinetic properties such as the clearance rate of contrast agents (here liposomal and normal ICG) from the blood pool can be determined.

The results shown here can be transferred to many different imaging settings and scenarios in cancer research and drug development in general. Lately, this has been shown on several occasions in more biological oriented studies by colleagues using the developments presented herein.

Selected examples are:

- Imaging of the mouse heart cycle [135] and monitoring cardiovascular dynamics by means of circulating gold nanorods [136] done by Taruttis *et al.*
- Imaging tumour heterogeneities by means of MSOT done by Herzog *et al.* [171]
- Brain and Glioblastoma tumor characterization by Burton *et al.* [172]
- Imaging of vaccinia virus-mediated melanin production by Stritzker *et al.* [173]
- Use of gold nanoprisms as optoacoustic signal amplifiers for *in vivo* bioimaging by Bao *et al.* [174].

8 Towards 3D real-time imaging

8.1 Introduction

In the previous chapters it was shown that 2D optoacoustic imaging using a 1D cylindrically focused detector array is limited by a frequency dependent suppression of out-of-plane signals. As further shown, this can be improved by scanning the array over several positions and modeling the spatial impulse response of the transducer. Nevertheless the elevational resolution remains lower than the inplane resolution. Moreover, the presented model-based inversion schemes are computationally very demanding, so that large scale imaging studies become impractical.

With the goal to overcome these limitations a second system has been conceived. Using a 2D transducer array, *i.e.* elements arranged on a surface rather than a 1D arc and thus not relying on acoustic focusing for suppression of out-of-plane signals, it attains a higher elevational resolution than the previously presented 2D imaging system. Moreover, the system can image small 3D volumes in real-time. This approach has several potential advantages: First, dynamic processes, such as the biodistribution of molecular probes, can be monitored in the entire volume of interest. Second, motion artifacts that degrade the image quality when imaging living specimen can be avoided. Third, three dimensional information in real-time could enable image guided interventions like needle biopsies and localized drug deposition [175]. Finally, 3D real-time performance can greatly decrease the time required for experiments and increase throughput.

A proof-of-principle study, using a sparse distribution of only 15 transducers, showcased the feasibility of three-dimensional, real-time imaging. However, only simple and isolated objects such as rods or point-sources were imaged, albeit with poor resolution and inappropriate for biological samples as only 15 detectors were used [176]. Thus there still was a need to establish the ability for real-time 3D imaging in tissue. Efficient implementation of such an imaging system is however challenging as it requires simultaneous collection of time-resolved optoacoustic signals from a large number of points (projections) around the imaged object as well as sufficiently fast data collection and processing capabilities. The system described here, utilizes simultaneous acquisition of signals from 256 points distributed over a spherical surface surrounding the sample. Thereby, volumetric reconstructions can be obtained at 10 frames per second, limited by the pulse repetition rate of the laser. The system was published 2012 in Optics Express with the title ”*Three-dimensional optoacoustic tomography at video rate*” [177] and was used to demonstrate the previously undocumented ability to do 3D real-time imaging of tissue. In the following paragraphs the system is described and its ability to image complex static structures and dynamic processes in real-time and in 3D is showcased. At the end, suggestions for improvements for future implementations are discussed.

8.2 Materials and methods

8.2.1 Imaging system

A layout of the imaging system is depicted in Fig. 8.1 (a) from two orthogonal views. A photograph of the implementation is shown in (b). It is based on a custom-made 256 element transducer array (Imasonic SaS, Voray, France) covering a solid angle of 240° in azimuth and 75° in elevation around the imaged object. By having a larger detection aperture than the 2D imaging system it can detect more complementary tomographic views. In between the two hemispheres there is a 1.9 cm gap for illumination purposes. Illumination is therefore normal to the surface of the sample and not effected by different mouse diameters, in contrast to the 2D real-time imaging system with slightly oblique illumination. The individual elements are manufactured using piezocomposite technology with a central frequency of approximately 3.3 MHz and bandwidth (FWHM) of 4.3 MHz. The electrical impulse response of the system was determined as described in section 3.4.3 and is shown in Fig. 8.1 (b). The individual elements, having dimensions of 4 x 4 mm^2, are arranged in space in 8 rows as depicted in Fig. 8.1 (d). The number of elements per row is [28, 32, 34, 34, 34, 34, 32, 28], respectively. The inter-element spacing in azimuth direction is 1.5 and 2.5 mm in elevations. Sections along the xy-, xz- and yz-plane of the simulated sensitivity field of a single transducer are shown in the first column of Fig. 8.1 (e) while sections through the combined sensitivity field, *i.e.* summation of the sensitivity fields of all the elements, are displayed in the second column of Fig. 8.1 (e). In this way, an effective imaging region of about 12 x 9 x 7 mm^3, defined by the region within -6 dB of the combined sensitivity field, can be covered using a single laser pulse. The sensitivity of the system was determined to be 7 μVPa^{-1} ± 5% over a 1 to 7 MHz bandwidth. Excitation light originates from a tuneable (680-900 nm) optical parametric oscillator laser (Phocus, Opotek Inc., Carlsbad, CA), delivering less than 10 ns pulses with repetition frequency of 10 Hz (cf. section 3.3.1). The beam is guided into a custom-made silica fused-end fiber bundle (CeramOptics GmbH, Bonn, Germany) consisting of 630 fibers partitioned into 10 arms. The individual arms are attached at the illumination gap to create a ring-shaped illumination pattern of approximately 9 mm width upon the surface of the imaged object. The optoacoustic signals are digitized at a sampling frequency of 40 megasamples per second by two synchronized custom-made multi-channel analog to digital converter, each with 128 channels and a 12-bit resolution over a 16 mV range (Falkenstein Mikrosysteme, Taufkirchen, Germany). The laser's Q-switch provides the trigger for the acquisition. The sample is placed in the holder presented in section 3.3.3, comprising of a transparent and water impermeable membrane that averts direct contact of the imaging object with water. A linear stage (LTM 80F 300, OWIS GmbH, Staufen, Germany) allows translation of the sample holder in the axial *z*-direction for acquisition of three-dimensional data sets from different regions of the sample.

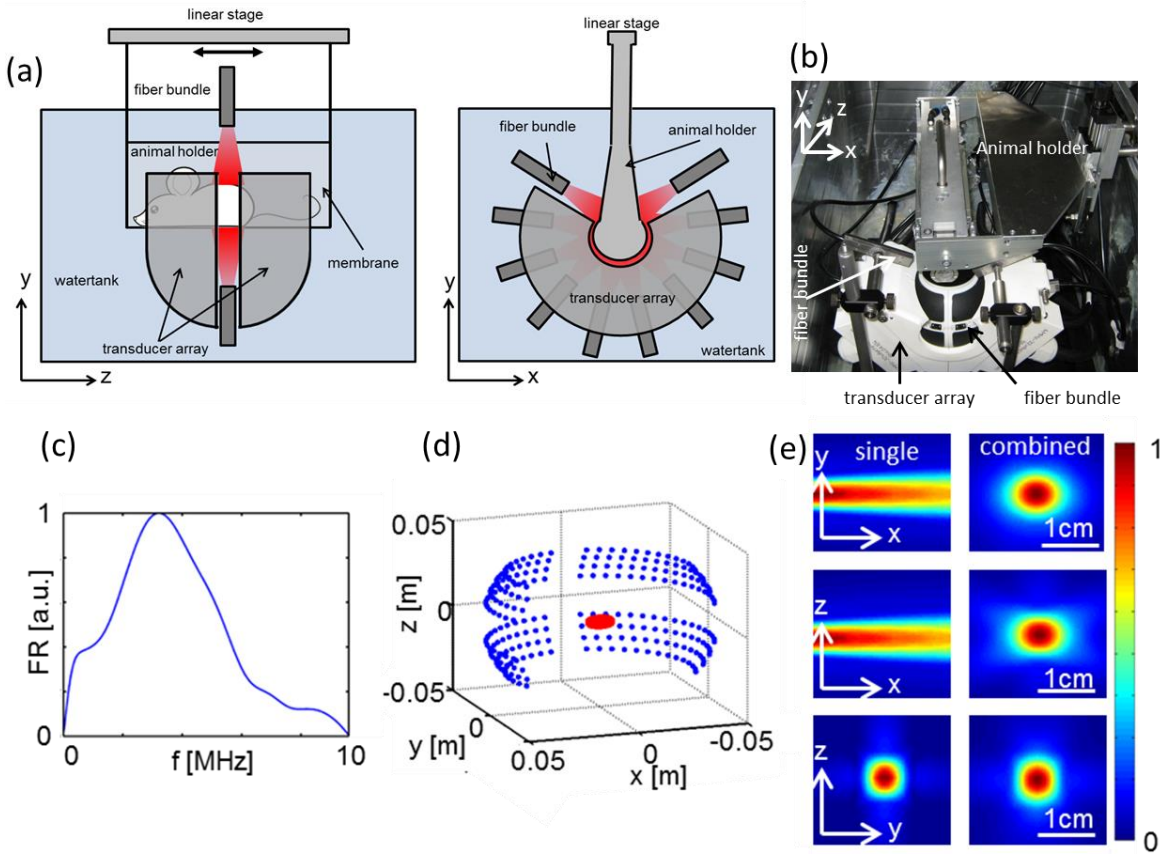

Fig. 8.1: The imaging system. (a) A schematic representation of the major components seen from two different directions. (b) Photograph of the system. (c) Frequency response of the transducer. (d) Arrangement in space of the individual transducer elements. (d) Sections through the sensitivity field of a single transducer element (first column) and the combined sensitivity field of the system (second column). The sections are centered at (0,0,0). The single transducer element is located at (-5,0,0) cm. The -6 dB combined sensitivity field region is depicted in red in (d). (Panels (a), (c), (d) and (e) published in [177], Copyright 2012, Optical Society of America).

8.2.2 Signal processing and image reconstruction

In a first step, the signals are deconvolved with the electrical impulse response (cf. section 4.2) and then bandpassfiltered with a Chebychev filter with cut-off frequencies of 0. 1 and 7 MHz to remove low and high frequency noise. The filtered signals are subsequently used for image reconstruction with a modified back-projection algorithm in which the signals are weighted with the sensitivity field of the particular transducer element so that the absorbed laser energy $H(r_j')$ at a point r_j' is given by

$$H(r_j') = \sum_i S_i(r_j') \left[p(r_{i,} t_{ij}) - t_{ij} \frac{\partial p(r_{i,} t_{ij})}{\partial t} \right] \tag{8.1}$$

where $S_i(r_j')$ is the sensitivity of the i-th element for a signal generated at r_j' and $p(r_{i,} t_{ij})$ is the pressure measured at the position r_i of the i-th element at instant $t_{ij} = |r_j' - r_i| c^{-1}$. This kind of weighting avoids that signals are backprojected into areas, where the sensitivity of the elements is low, *i.e.* where they are not detected from. The sensitivity field of a single transducer element (Fig. 8.1 (d) first column)

was computed numerically as previously described in section 3.4.4 using the open-source software Field II [56, 94]. As we have shown in [108], 3D model-based reconstructions yield slightly better results than the backprojection approach, yet due to the increased computational burden were not considered herein for real-time imaging.

8.2.3 System characterization

Basic imaging performance was tested with two different phantoms using illumination at 760 nm. All images were acquired without averaging, *i.e.* using single laser pulses. The first phantom consisted of a light scattering cylinder with a diameter of 1.9 cm containing a 100 µm in diameter black absorbing microsphere (Cospheric LLC Santa Barbara, CA). The microsphere was moved in the imaging plane to three different positions, namely (0,0,0), (-5,0,0) and (-10,0,0) mm, in order to characterize the resolution of the system in different directions. For each position, the corresponding point-spread-function was calculated with the backprojection algorithm within a volume of 22 x 22 x 3 mm^3 consisting of 600 x 600 x 75 voxels and compared with the analytical formula (cf. 2.4.3.1). The second phantom was used in order to showcase the real-time performance of the system. It consisted of a transparent tube with an inner diameter of 300 µm embedded in a scattering agar cylinder. The tube was perfused with diluted ink yielding an absorption coefficient of 5 cm^{-1}. The ROI was 21 x 21 x 10 mm^3 while the reconstruction was done using 201 x 201 x 100 voxels.

8.2.4 Mouse imaging

To test performance in the presence of realistic heterogeneous tissues, an excised mouse heart embedded into a scattering agar cylinder was imaged. Likewise, the reconstruction was done with the sensitivity-weighted backprojection algorithm. The ROI contained a volume of 15 x 15 x 10 mm^3 and consisted of 151 x 151 x 100 voxels.

Whole body imaging performance was showcased with a 10 days old CD1 mouse. The mouse was euthanized according to approved institutional regulations regarding animal experiments while the hair was removed with a depilatory lotion. It was placed in the animal holder in supine position and scanned with 200 µm steps along its longitudinal axis over a total distance of 4 cm. The imaging wavelength was 760 nm. For each scanning position, a volume of 16 x 16 x 8 mm^3 was reconstructed using 161 x 161 x 81 voxels. The individual volumes were then merged into a larger volume by averaging the intersecting parts. In that way it was possible to cover the whole length of the mouse.

Finally, several *in vivo* experiments were performed in order to assess the real-time operation. In the first experiment, the heartbeat of a 10 day old mouse was visualized. For this, a CD1 mouse was anesthetized, shaved and placed in prone position into the animal holder. The water temperature was stabilized at 32°C. Ultrasound gel was used to improve acoustic coupling. Signals were acquired at the heart level with a frame rate of 10 Hz. The laser wavelength was set to 850 nm. In

the second experiment, perfusion of contrast agent through the brain of an adult atymic CD1 mouse was monitored. The mouse was injected with 130 nmol of Indocyaninegreen (ICG) through its tail vein while imaging was done at 800 nm wavelength (near the absorption peak of ICG) with a frame rate of 10 Hz.

8.3 Results

8.3.1 System characterization

Fig. 8.2 (a)-(f) depicts cross-sectional images of the microparticle with the first and second row representing cross-sections within the xy-plane and yz-plane, respectively. The positions of the microsphere are (0,0,0) mm (see first column), (-5,0,0) mm (cf. second column) and (-10,0,0) mm (cf. third column). Clearly, the resolution is anisotropic and is also not constant along some of the axis. The radial and transverse resolutions are subsequently estimated as the full width at half maximum (FWHM) along the radial and transverse directions in analogy to the resolution estimation in section 3.4.6. The radial resolution of approximately 200 µm is only bandwidth limited, thus spatially invariant and in good agreement with the theoretically predicted value (cf. chapter 2.4.3.1). The transverse resolution however varies significantly between 200 µm in the center of the array, degrading to approximately 850 µm at a distance of 10 mm from the center, as shown in Fig. 8.2. The reconstructed microsphere at the center of the transducer array is slightly elongated towards the z-direction. The reason for this is the reduced elevational aperture (75°) of the system, which provides relatively limited view in this direction. A larger elevational angle and more transducer elements would improve the resolution. The 3D real-time imaging capability has been showcased by monitoring ink flow through a plastic tube. Consecutive frames are shown in Fig. 8.3. A video (Movie 1) of the ink flowing through the tubing imaged at 10 frames/s is available in the online version of reference [177].

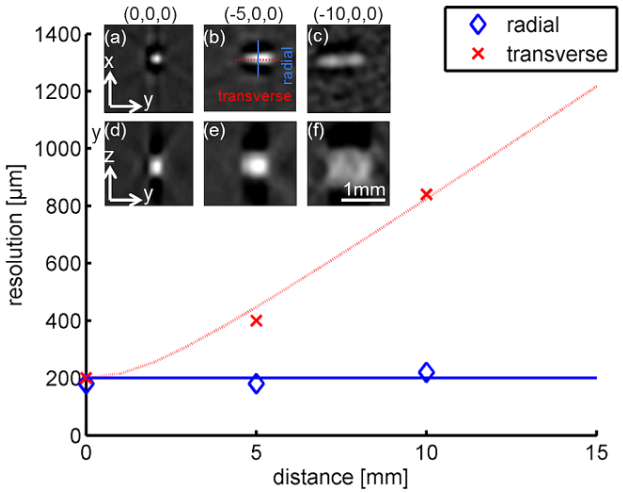

Fig. 8.2: Radial and transversal resolution of the system as a function of the position. The insets show reconstructed images of a 100 µm microsphere located at the coordinates (0,0,0) mm (first column), (-5,0,0) mm (second column), and (-10,0,0) mm (third column). The first row depicts the cross-sections through the microsphere along the xy-plane. The second row the cross-sections along the yz-plane. (Figure published in [177], Copyright 2012, Optical Society of America).

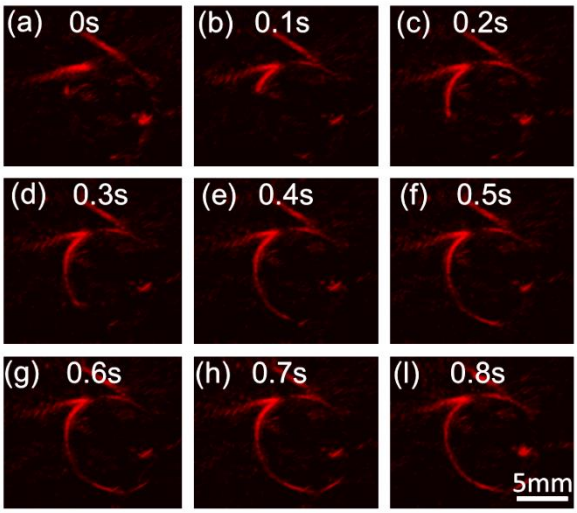

Fig. 8.3: Visualization of ink flowing through a plastic tube. Each frame, displayed by maximum intensity projection (MIP) of the 3D volume, depicts one time instant.

8.3.2 Mouse data

Fig. 8.4 depicts the maximum intensity projection (MIP) images of the excised mouse heart along two representative directions along with a cross-sectional slice and a photograph of the excised mouse heart. Single shot images acquired within 100 ms are shown (no averaging). A rotational movie (Movie 2) showing the MIP from different viewing angles is also available in the online version of reference [177]. High resolution anatomy of the heart can be clearly identified in the images, including the two ventricles separated by the septum, the aortic arch as well as some other coronary vessels.

Fig. 8.5 (a) depicts the MIP of optoacoustic images of the sacrificed 10 day old mouse, with the corresponding photograph shown in Fig. 8.5 (b). A rotational video (Movie 3) showing the reconstruction from different angles is further available in reference [177]. Since optoacoustic imaging is dominantly sensitive to hemoglobin-based contrast, mainly the vasculature of the animal is visible. High resolution details (sagittal sinus, the frontal cerebral arteries or the longitudinal fissure of cerebrum) are also visible when zooming into the mouse brain (Fig. 8.5, panels (c)-(f)).

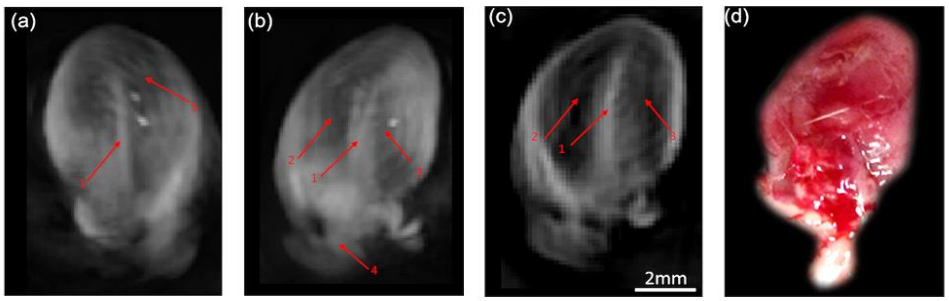

Fig. 8.4: Single shot imaging of an excised mouse heart. The maximum intensity projection (MIP) of the heart along two directions is shown in (a) and (b). (c) depicts a cross-sectional slice through the heart. (d) shows a photograph of the mouse heart. A movie file (Movie2) showing the volume rotating is available in the online version of the journal. 1: Septum; 2: right ventricle; 3: left ventricle; 4: aorta; 5: coronary vessels. (Figure published in [177], Copyright 2012, Optical Society of America).

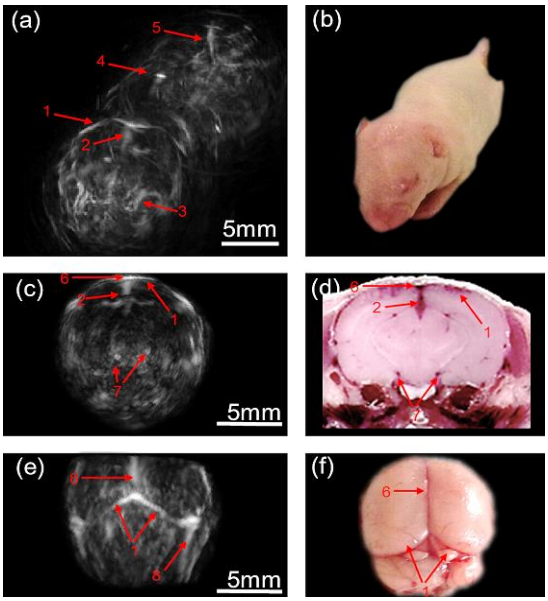

Fig. 8.5: Volumetric reconstruction of a babymouse. (a) MIP of the mouse vasculature. (b) Photograph of the babymouse to indicate the orientation of the volumentric reconstruction. (c) MIP of a 1 cm thick region through the mouse brain, (d) a corresponding cryoslice, (e) the MIP from the top and (f) a photograph of an excised mouse brain. 1: Transverse sinus; 2: longitudional fissure of cerebrum; 3: left supraorbital vein; 4: thoratic aorta; 5: right iliac artery; 6: sagittal sinus; 7: frontal cerebral arteries; 8: superior cerebral vein. (Figure published in [177], Copyright 2012, Optical Society of America).

Fig. 8.6 shows cross-sectional reconstructions of the 10 days old mouse imaged at the heart region during a diastolic (a) and systolic (b) phase of the heart cycle as well as a photograph of a cryoslice through a mouse's heart area for comparison. A video (Movie 4) is available in reference [177]. The video is displayed in slow motion at 5 frames/s, even though the images have been acquired at 10 frames/s. One can recognize the heart, including the septum (1), the two ventricles (2 and 3) and the lung (4). Both in the images and the video, one can clearly see the change of the size of the heart due to the pumping movement. An increase of the signal intensity in the left ventricle during the diastolic phase is also visible due to the filling of the ventricle with oxygen enriched blood coming from the lungs. In the movie file it is also possible to distinguish between the heart and breathing motions. The breathing motions are less frequent and have larger magnitude as compared to the heart movements. Naturally, the reconstructions from the heart area have generally poor quality and low resolution, presumably due to propagation artifacts introduced by lungs which contain acoustically-mismatched air cavities.

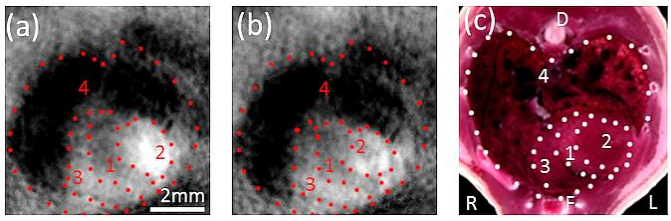

Fig. 8.6: Cross-sectional reconstructions of a babymouse at the heart region during (a) a diastolic and (b) a systolic phase. 1: Septum; 2: left ventricle; 3: right ventricle; 4: lung. (c) depicts a cryoslice through the heart area of a mouse for comparison. (Figure published in [177], Copyright 2012, Optical Society of America).

Finally, Fig. 8.7 depicts perfusion of ICG through the brain of an adult mouse. Panels (a)-(c) correspond to MIP images along the z-axis at three different time points while (d)-(f) are MIPs along the y-direction captured at the same time points. One can clearly recognize an enhancement in the vasculature contrast following injection of the ICG. Panel (g) depicts the average optoacoustic signal strength in the vein indicated by the white arrow. Although the data is affected by laser energy fluctuations, a clear tendency is visible. During the first 10 seconds the signal is constant while a sudden increase of the signal strength occurs right afterward due to the ICG injection, followed by a plateau in the optoacoustic signal strength.

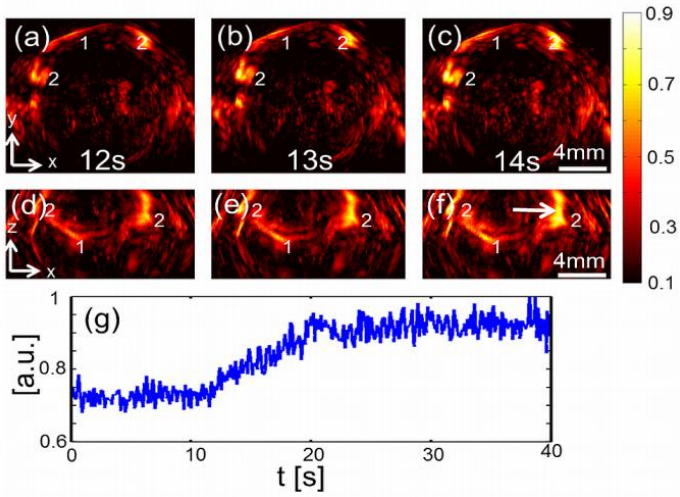

Fig. 8.7: 3D imaging of brain perfusion after injection of ICG. (a)-(c) MIP of the reconstructed volume along the z-direction at three different time points. (d) - (f) corresponding MIP along the y-axis. (g) signal intensity as a function of time in the vessel indicated by the arrow in (f). 1: Transverse sinus; 2: superior cerebellar vein. (Figure published in [177], Copyright 2012, Optical Society of America).

8.4 Discussion and conclusion

It was described how the optoacoustic phenomenon can be leveraged for generating a complete volumetric tomographic dataset using a single laser pulse. This characteristic is unique to the system described in this chapter and this possibility does not exist in other imaging modalities, as it is usually necessary to perform sequential excitation of the object from multiple source locations in order to acquire tomographic data required for efficient volumetric image reconstructions. This is also the approach taken in previously described, dedicated 3D small animal photoacoustic imaging systems (cf. section 3.2.2). In these systems, the ultrasound array containing 64 transducers is rotated around the imaging object to acquire several thousand tomographic views that are used for 3D reconstruction. Although high isotropic resolutions can be achieved using this methodology, the temporal resolution is poor, rendering such systems less useful for dynamic studies.

In contrast, with the optoacoustic tomography system that is described here, it is shown to be possible to attain three-dimensional optoacoustic volumetric reconstructions of approximately 12 x 9 x 8 mm^3, with a single laser pulse (under

20 ns), using simultaneous acquisition of optoacoustic responses from 256 locations (projections around the object). This limits the temporal resolution to the laser repetition rate, which is 10 frames/second in the current set-up, but could be modulated for future implementations. Compared to scanning-based setups, which require several pulses to form a volumetric image, the 3D reconstructions herein are not affected by animal motion. By relying on tomographic reconstruction for image formation instead of focusing, the elevational resolution is improved compared to the previously developed 2D system. Moreover, by having a larger detection aperture, the system can acquire more complementary views and is less sensitive to the limited view problem (cf. section 2.4.6). It was established that a sequence of three-dimensional images at a frame rate of 10 Hz can be retrieved with the system, which allows tracing dynamic events such as perfusion of contrast agents, breathing and heartbeat. Having shown for the first time the ability to track non-invasively dynamic processes in 3D in deep tissue is an important technological and scientific advance, which promises wide-ranging applications in biological research, drug development and clinical practice.

However, it has to be noted that the presented implementation suffers from some limitations with respect to whole body imaging of mice. Most importantly, the system images volumes with the dimensions of 12 x 9 x 8 mm^3, this is a relatively small effective imaging volume compared to the whole body of an adult mouse. Obviously, if volumes larger than 12 x 9 x 8 mm^3 need to be imaged, it is necessary to scan the imaging volume through the sample, optimally in all three spatial dimensions (x, y and z) to have maximal sample coverage, and merge the reconstructed volumes. Feasibility of this approach has been shown in Fig. 8.5, but comes at the price of decreased temporal resolution. Also, the resolution is anisotropic and strongly degrading away from the center of the transducer array. Both effects are due to a combination of sparse transducer distribution, limited view detection, the rather big size of the elements, which constrain their field of view and distort the measured signal, and the big width of the illumination gap preventing detection of signals from the surface (cf. sections 2.4.5, 2.4.6 and 2.4.7). Rotation of the transducer around the z-axis (or the x- and y-axis) to reduce the sparseness of the angular sampling would improve the image quality within the effective imaging volume but is inappropriate for imaging whole mouse cross-sections due to the strong degradation of the lateral resolution outside the center.

To improve the imaging quality and make the system suitable for whole body mouse imaging, it is important to capture the ultrasound waves from as many positions as possible and to maximize the angles of acceptance for each point of the illuminated volume. Thus the transducer elements have to be sufficiently small, so that each one sees the whole cross-section of the mouse, and densely distributed over a possibly closed detection surface (cf. section 2.4.2). With the data acquisition and processing technology utilized in this study, we can currently collect and process up to 512 tomographic projections in parallel, with potential for future improvements. Hence by using more detection elements, there is a way to improve the presented image quality. Nevertheless, previously described dedicated 3D small animal imaging systems use several thousand tomographic views to reconstruct a whole mouse [60]. Thus from a technical and economic point of view, this amount of data is too

much to be acquired with a single transducer array in parallel. High quality 3D imaging of big volumes such as mice require scanning (rotating) of the detection device around the sample and are therefore currently not feasible in real-time. 3D real-time imaging will rather find its application as a diagnostic tool for localized probing of small tissue volumes, for example in handheld mode. Based on the experience acquired from this initial prototype, current research at the institute for biological and medical imaging (IBMI) focuses on the development of such devices, for pre-clinical and clinical applications.

9 Conclusion and future outlook

This chapter summarizes the accomplishments of the presented work and gives an outlook on future developments.

9.1 Conclusion

At the beginning of this thesis in the year 2009, multispectral optoacoustic tomography (MSOT) was in its infancy. Although the advantages of the technology (rich optical contrast, high ultrasound resolution, save use and potential real-time operation) were theoretically known and initial proof-of-principle experiments resolving fluorescent dyes in excised mouse legs or fluorescent proteins in mesoscopic zebra-fish became available, there was no experience with *in vivo* multispectral optoacoustic imaging of mice nor adequate small animal imaging systems and questions about the general feasibility, the optimal approach and the benefit of MSOT as a small animal imaging modality were open.

An important goal of this work was the development of a novel concept for an optoacoustic small animal imaging system for practical multi-spectral whole-body *in vivo* imaging of mice, easily accessible for the research community. Therefore different instrumentation and detection geometry related effects were analyzed at the beginning of this thesis, with respect to their influence on the image reconstruction accuracy. It was shown that the optoacoustic signal strength scales with the deposited light energy, therefore light delivery is an important issue. Also shown was, that optoacoustic signals are broadband with its frequency content depending on the size of the optoacoustic source. The detection device should therefore provide a detection bandwidth adapted to the frequency content of the signals from the structures to be resolved. Moreover, it was shown that a finite size detector acts as a low-pass filter and blurs the reconstruction. Therefore, from a resolution standpoint, detectors should be as small as possible. However, this contrasts SNR requirements, due to which detector elements should be big. Lastly, it was shown that sparse spatial sampling creates aliasing artifacts and limited view detection leads to potentially “invisible” objects.

Based on the findings a 1D multi-element piezocomposite transducer array, with elements cylindrically focused onto a common plane and arranged on an arc around the imaged object, in combination with confocal illumination, was considered the best suited approach for detection of the optoacoustic responses in a small animal imaging experiment. It has the advantage of providing high in-plane resolution, good sensitivity and 2D real-time performance utilizing only a relatively small number of ultrasound detectors.

A prototype small animal imaging system was implemented based on this concept including an innovative animal positioning approach that shields the animal from the surrounding coupling medium and thus allowing *in vivo* whole body scans without the need to reposition the animal. Overall, the system provides cross-sectional

imaging at the laser-repetition rate and whole body imaging by translating the animal along its longitudinal axis. Imaging and component performance was analyzed on phantoms and mice. The cross-sectional resolution was determined to be between 150 and 550 µm depending on the position. The ability to do whole body imaging was demonstrated by scanning a whole mouse and resolving the anatomical hemoglobin contrast. Imaging of dynamic processes was exemplarily shown by tracking breathing motions and monitoring contrast enhancement in the kidneys due to perfusion of systemically administered Indocyanine green, a clinically approved near-infrared fluorochrome, frequently tagged to a specific compounds to make them detectable by fluorescent means. Molecular imaging performance was exemplarily showcased by resolving the Indocyanine green in the kidneys over the intrinsic background absorbers based on the probes spectral signature by multispectral means and by detecting optical reporter agents (here a phosphatidylserine targeting fluorescent dye) within mouse xenograft tumors. Overall, these proof-of-concept studies showcased for the first time the ability of MSOT to resolve in parallel anatomical, functional and molecular information, non-invasively in living mice. Having established that it is possible with the system to access all areas of the mouse body, resolve dynamic processes and detect molecular agents, it follows that the system can be applied to study different biological scenarios and molecular probes, in particular pharmacokinetics and biodistribution of such agents and thus can become a powerful tool for biological research. In the meantime the system was used by coworkers on various other occasions for instance for imaging the cardiovascular system including heart cycle and heart infarction [135-137, 178], pharmacokinetics and biodistributions of various contrast agents (*e.g.* gold nanorods, fluorescent dyes) [174, 178], tumor heterogeneities [171] and glioblastoma brain tumors [172]. Today, follow-ups of the initial system are commercially available by iThera Medical GmbH[6], thus validating the existing need within the biomedical research community for imaging equipment that is capable of answering such biological questions.

In addition to the 2D real-time system, a 3D real-time system was built in this work. It was showcased of being capable of imaging small tissue volumes in 3D at the laser repetition rate. It was the first system that could image complex structures (*e.g.* an excised mouse heart), brain perfusion (contrast enhancement due to circulating ICG) and a heart cycle in real-time and 3D. Compared to the 2D approach relying on focusing to suppress out-of-plane signals, the 3D approach has the advantage of achieving higher elevational resolution and, since it depends on computed recons-tructions, quasi-independent of the frequency of the optoacoustic signal. Yet, for real-time imaging of bigger volumes, *e.g.* adult mouse cross-sections, the system has to be optimized by a denser spatial sampling (*i.e.* more detection elements), a size reduction of the detection elements to reduce the effect of the spatial impulse response and a smaller illumination gap.

Beside system development, a big emphasis of this work was put on algorithm development for improving reconstruction and multispectral unmixing accuracy. In that context, it was shown that it is important to compensate for the electrical

[6] The author declares no financial interest in this company.

impulse response of the detection system to avoid reconstruction artifacts due to signal distortion. Moreover, an interpolation technique was presented to alleviate aliasing artifacts due to the sparse angular sampling in a fixed array configuration. In addition, 2D model-based image reconstruction was analyzed in limited view detection scenarios and it was found that for detection arcs shorter than 180° the inversion becomes severely ill-conditioned leading to stripe artifacts. To compensate for these artifacts and make 2D model-based image reconstruction actually possible in the limited view small animal imaging system, two regularization schemes have been presented. It was also shown that standard 3D reconstruction approaches which assume point detectors (*e.g.* the 3D backprojection algorithm) are inadequate for 3D reconstructions in a scanning-based setup employing cylindrically focused detectors due to the signal distortion by the finite detector size. Stacking of cross-sectional slices yield better results in such a situation but images are still affected by the frequency dependent focusing properties of the detector. To improve on the 3D reconstruction capability of the system, a 3D model-based reconstruction approach was adapted to incorporate the specific shape of the detector into the model. It was shown that by this means, 3D image reconstruction becomes more accurate in particular by better resolving structures oriented perpendicular to the scanning direction. But also 2D reconstructions, *i.e.* cross-sectional image reconstructions using only data from one scanning position, become more exact with this newly developed approach, compared to the initially available backprojection and 2D IMMI methods. By matching the volume of interest in the model to the actual volume where signals are generated from, one can reduce the erroneous projection of out-of-plane signals into the imaging plane.

Finally, the aspect of multispectral unmixing was analyzed, which refers to the detection of molecular probes over background absorbers based on their spectral signature. It was shown that it is possible to detect molecular probes by these means even deep inside the mouse. Quantitative unmixing, *i.e.* the exact determination of the molecular probe concentration is however severely complicated by wavelength dependent light attenuation in tissue causing spectral coloring and signal reduction with penetration depth. So that it becomes difficult to compare signals from different depths. Since this strongly depends on the actual absorber distribution and the oxygenation saturation level of the tissue, it is challenging to compensate for this effect in a quantitative manner. In addition, there are practical instrumentation related limitations such as limited view detection and frequency dependent out-of-plane signals which cause additional inaccuracies. As an initial step, blind unmixing by independent component analysis was considered for probe detection in such a scenario with an undefined corruption of the spectral signature and for localized probes it showed higher detection sensitivity compared to spectral fitting approaches. Moreover, it was shown that normalization of the unmixing results by an estimate of the light fluence heterogeneity obtained from a low pass filtered single wavelength image acquired close to the isobestic point of hemoglobin can partially compensate the signal reduction with depth due to light fluence attenuation. Unmixing errors due to spectral coloring are however not corrected thereby. More advanced approaches to compensate for these artifacts including accurate light fluence modeling are currently under investigation.

In conclusion, this work presents system and algorithm development for multi-spectral optoacoustic tomography of small animals. It was established on selected examples that MSOT can actually resolve in high resolution, anatomical, dynamic and molecular information in mice overall showcasing the tremendous potential of the technology.

9.2 Outlook

Imaging performance achieved in this work was limited by the use of only 64 elements arranged on a short (172°) detection arc. It will significantly improve by upgrading the presented system with a transducer array comprising more elements arranged on a longer detection arc (at least 270°). Having more complementary information available, the optoacoustic inversion problem will become more stable and artifacts less overall benefiting molecular probe detection and quantification thereof. It has however to be noted, that for a 2D imaging system utilizing a 1D cylindrically focused array like the one developed herein, due to the mapping of a 3D source distribution to a 2D signal distribution and consequent reconstruction of 2D slices, there will be always some quantification inaccuracies due to out-of-plane signals despite all the improvements achieved by modeling the transducer surface. When targeting accurate volumetric reconstructions, closed detection surfaces with possibly small detection elements are required.

Concerning algorithm for molecular target detection there are various other multispectral unmixing algorithms with different strength and weaknesses available from the literature [118], which, due to the presented limitations of the utilized once, could yield better molecular agent detection performance. Promising initial results[7] have been achieved by statistical background modeling using adaptive matched filter approaches [179]. Future research should focus on a performance comparison of different algorithms to identify the most suited one.

Also, the problem of an exact light fluence correction is still unsolved, especially in *in vivo* imaging situations with unknown optical properties. Benefiting from improved image quality, the presented correction attempts are however expected to perform better and more robustly. Due to the strong ill-conditioning and non-linearity of the optical problem, accurate inversion will remain an important challenge in the future.

Nevertheless, because to its unique performance characteristics and the ability to resolve optical absorption contrast with high resolution deep inside tissue, MSOT increasingly attracts biomedical professional with the goal to use it as a tool for biomedical oriented applications and various studies are currently under investigation.

Moreover, the presented developments and methods can be translated to clinical setting. Dima *et al.* used the presented transducer array with adapted illumination

[7] Personal communication from Stratis Tzoumas at the Institute for Biological and Medical Imaging (IBMI)

scheme for non-invasive imaging of human carotids [80]. This proof of principal study showed that it is possible to reach this clinical relevant structure and thus may give the possibility to use optoacoustic imaging as a diagnostic tool for early arthrosclerosis detection. Moreover, the system is currently used for imaging arthritic inflammation in the finger joints. Following up our initial experiences with 3D real-time imaging, Déan-Ben *et al.* developed a cup shaped system for real-time imaging of small 3D volumes in hand-held mode. Benefiting from novel fast per pulse tuning laser technology becoming available, we have also recently published the first real-time multispectral optoacoustic handheld scanner [125] and demonstrated tracking of oxygenation changes in tissue in real-time. Using this system we are currently evaluating the ability to use MSOT in analogy to clinical ultrasound imaging as a diagnostic tool to examine tissue viability.

Furthermore, various research groups all over the world have presented other compelling optoacoustic imaging implementations ranging from optoacoustic microscopy with resolution between 15 and 45 µm depending penetration depth (1 to 3 mm) [27, 58, 59], to optoacoustic endoscopy and intravascular catheters, and to mammo-graphy systems [83-85]. If the current pace of technological innovations and method development is kept, it is expected that in the next 5-10 years MSOT will become an important tool in biomedical imaging and clinical decision making.

Acknowledgements

I would like to thank Prof. Vasilis Ntziachristos and Prof. Daniel Razansky for giving me the opportunity of pioneering with them the interesting and promising field of multispectral optoacoustic tomography. Working with such renowned and visionary scientists was a very inspirational experience for me. Special thanks for their advice, feedback and support in writing my scientific publications and for giving me the possibility to present my research at international conferences.

I would like to thank Dr. Xosé-Luis Déan-Ben for stimulating discussions and successful scientific cooperations which lead to the publications *"Three-dimensional optoacoustic tomography at video rate"* and *"Accurate model-based reconstruction algorithm for three-dimensional optoacoustic tomography"* and proof-reading of parts of this thesis. Further-more I want to acknowledge Dr. Amir Rosenthal for his advice in various situations and support on the paper *"Model-based optoacoustic inversions with incomplete projection data"* and thank Dr. Wouter Driessen for his precious support doing the pharmacokinetic study and for proof reading of this thesis. Thanks also to Dr. Eva Herzog for her biological and animal handling support in the studies about video-rate kidney perfusion and high resolution targeting of tumors as well as Angelique Ale for providing the FMT data therefore.

Thanks also to my office colleagues for providing a good working atmosphere, fruitful discussions and a free exchange of ideas which helped to mutually deepen our under-standing of optoacoustic imaging. Among them, special thanks to Miguel Angel Araque Caballero for sharing simulation code and the successful collaboration on the publication *"Optoacoustic determination of spatio-temporal responses of ultrasound sensors"* and to Alexander Dima for providing the 2D IMMI code and "tech-support". Thanks also to Thomas Jetzfellner for the experimental data used in the study about model-based optoacoustic inversions with incomplete projection data and to Erwin Bay for his collaborations in projects outside the context of this thesis.

Moreover, I also want to thank Dr. Jerome Gateau for scientific advice on various occasions and Dr. Nikos Deliolanis and Jürgen Glatz for their collaboration in the study on the topic "Blind unmxing". Also, I want to acknowledge the contribution of Josef Konradl and Till Gradinger in designing the imaging chamber of the 2D real-time small animal imaging system and thank them, together with Marcin Kacprowicz and Stefan Morscher, for continuously improving the initial prototype and making it available for other students. Thanks to Pouyan Mohajerani for providing the light fluence simulation code.

Furthermore, I want to thank Adrian Taruttis, Stefan Kellenberger, Jing Claßen, Dr. Neal Burton, Stratis Tzoumas, Rui Ma, Daniel Queiros, Murad Omar, Andreas Oancea for their help and collaboration on various small side projects and the technical personal Sarah Glasl, Florian Jürgelait, Uwe Klemm for precious support in animal handling and cryoslicing.

Also thanks to the administrative personal Silvia Weinzierl, Susanne Stern, Zsuszanna Öszi, Dr. Andreas Murr, Dr. Veronica Erben and Dr. Christiane Ogorek for their help in administrative matters.

To the rest of my IBMI coworkers I like to say thanks for the friendly work atmosphere they provided.

Finally, a lot of personal thanks to my fiancée Dr. Pauline Desclaux, my parents and brother for their precious support in difficult situation and patience when working long hours and on the weekend.

Publication list

Publications in peer-reviewed journals

1. **A. Buehler**, E. Herzog, D. Razansky, V. Ntziachristos, "Video rate optoacoustic tomo-graphy of mouse kidney perfusion", *Opt. Lett.* **35**, 2475-2477 (2010).
2. T. Jetzfellner, A. Rosenthal, **A. Buehler**, A. Dima, K.-H. Englmeier, V. Ntzia-christos, D. Razansky, "Optoacoustic tomography with varying illumination and non-uniform detection patterns", *JOSA A* **27**, 2488-2495 (2010).
3. T. Jetzfellner, A. Rosenthal, **A. Buehler**, K.-H. Englmeier, D. Razansky, V. Ntzia-christos, "Multispectral optoacoustic tomography by means of normalized spectral ratio", *Opt. Lett.* **36**, 4176-4178 (2011).
4. D. Razansky, **A. Buehler**, V. Ntziachristos, "Volumetric real-time multispectral opto-acoustic tomography of biomarkers", *Nat. Protoc.* **6**, 1121-1129 (2011)[8].
5. J. Glatz, N. C. Deliolanis, **A. Buehler**, D. Razansky, V. Ntziachristos, "Blind source unmixing in multi-spectral optoacoustic tomography", *Opt. Express* **19**, 3175 -3184 (2011).
6. **A. Buehler**, A. Rosenthal, T. Jetzfellner, A. Dima, D. Razansky, V. Ntziachristos, "Model-based optoacoustic inversions with incomplete projection data", *Med. Phys.* **38**, 1694-1704 (2011).
7. **A. Buehler**, E. Herzog, A. Ale, B. D. Smith, V. Ntziachristos, D. Razansky, "High resolution tumor targeting in living mice by means of multispectral optoacoustic tomography", *EJNMMI Research* **2**, 14 (2012).
8. **A. Buehler**, X. L. Dean-Ben, J. Claussen, V. Ntziachristos, D. Razansky, "Three-dimensional optoacoustic tomography at video rate", *Opt. Express* **20**, 22712 -22719 (2012).
9. X. L. Dean-Ben, **A. Buehler**, V. Ntziachristos, D. Razansky, "Accurate model-based reconstruction algorithm for three-dimensional optoacoustic tomo-graphy", *IEEE TMI* **31**,10 (2012).
10. **A. Buehler**, M. Kacprowicz, A. Taruttis, V. Ntziachristos, "Real-time handheld multi-spectral optoacoustic imaging", *Opt. Lett.* **38**, 8 (2013).
11. M. Á. A. Caballero, A Rosenthal, **A. Buehler,** D. Razansky, V. Ntziachristos, "Optoacoustic determination of spatio-temporal responses of ultrasound sensors", in *IEEE Transactions on Ultrasonics Ferroelectrics and Frequency Control,* **60**, 6 (2013).
12. D. Queiros, X. L. Deán-Ben, **A. Buehler**, D. Razansky, A. Rosenthal, V. Ntzia-christos, „Modeling the shape of cylindrically focused transducers in three-dimensional optoacoustic tomography", *Journal of Biomedical Optics* **18**, 7 (2013).
13. **A. Buehler**, X. L. Deán-Ben, D. Razansky, A. Rosenthal, V. Ntziachristos, „Volumetric Optoacoustic Imaging With Multi-Bandwidth Deconvolution", *IEEE TMI* **33**, 4 (2013).

[8] Equal contribution of the first two authors in the *Nature Protocols* publication

14. L. Vionnet, J. Gâteau, M. Schwarz, **A. Buehler**, V. Ermolayev, V. Ntziachristos „24MHz Scanner for Optoacoustic Imaging of Skin and Burn”, *IEEE TMI* **33**, 2 (2013).
15. M. Schwarz, **A. Buehler**, V. Ntziachristos „ Isotropic high resolution optoacoustic imaging with linear detector arrays in bi-directional scanning”, *Journal of Biophotonics* (2014).

International conference contributions and proceedings

1. **A. Buehler**, D. Razansky, N. Deliolanis, V. Ntziachristos, "Fast acquisition multispectral photoacoustic imaging system for small animal imaging", Poster presented at *442. WE-Heraeus-Seminar: Molecular Imaging*, Bad Honnef, Germany, Oct. 5-8, 2009.
2. **A. Buehler**, E. Herzog, D. Razansky, V. Ntziachristos, "Visualization of mouse kidney perfusion with multispectral optoacoustic tomography (MSOT) at video rate"; Published in Proceedings *Photons Plus Ultrasound: Imaging and Sensing 2011*, SPIE, vol. 7899, 2011; Oral presentation given at the conference in San Francisco (CA), USA, Jan. 22-27, 2011.
3. S. Morscher, J. Glatz, N. C. Deliolanis, **A. Buehler**, D. Razansky, V. Ntziachristos "Blind spectral unmixing to identify molecular signatures of absorbers in multispectral optoacoustic tomography", published in Proceedings *Photons Plus Ultrasound: Imaging and Sensing 2011*, SPIE, vol. 7899, 2011.
4. T. Jetzfellner, A. Rosenthal, **A. Buehler**, A. Dima, K. H. Englmeier, V. Ntziachristos, D. Razansky, "Tomographic optoacoustic inversion in dynamic illumination scenarios"; Poster abstract published in Proceedings *Photons Plus Ultrasound: Imaging and Sensing 2011*, SPIE, vol. 7899, 2011.
5. **A. Buehler**, D. Razansky, V. Ntziachristos, "Multispectral optoacoustic tomography of structure and biomarkers in mice"; Oral presentation given at *European Conferences on Biomedical Optics*, Munich, Germany, May 22-26, 2011.
6. S. Morscher, J. Glatz, N. C. Deliolanis, **A. Buehler**, A. Sarantopoulos, D. Razansky, V. Ntziachristos, "Spectral unmixing using component analysis in multispectral optoacoustic tomography"; Poster presented at *European Conference on Biomedical Optics*, Munich, Germany, May 22-26, 2011.
7. **A. Buehler**, E. Herzog, B. D. Smith, D. Razansky, V. Ntziachristos, "High resolution imaging of molecular probes in living mice by means of multispectral optoacoustic tomography (MSOT)"; Poster at *2011 World Molecular Imaging Congress,* San Diego (CA), USA, Sept. 7-10, 2011.
8. **A. Buehler**, D. Razansky, V. Ntziachristos, "Whole body imaging of structure and molecular bio-markers with real-time multispectral optoacoustic tomography"; Presented at *2011 World Molecular Imaging Congress,* San Diego (CA), USA, Sept. 7-10, 2011.
9. **A. Buehler**, S. Morscher, D. Razansky, V. Ntziachristos, "High resolution imaging of mouse anatomy and molecular probes in mice by means of multispectral

optoacoustic tomography (MSOT)"; Published in Proceedings *Photons Plus Ultrasound: Imaging and Sensing 2012*, SPIE, vol. 8223, 2012.

10. **A. Buehler**, E. Herzog, A. Ale, B. D. Smith, V. Ntziachristos, D. Razansky, "High resolution imaging of phosphatidylserine-exposing cells within live tumor allograft by means of multispectral optoacoustic tomography (MSOT)"; Poster presented at *2012 World Molecular Imaging Congress,* Dublin, Ireland, Sept. 5-8, 2012.
11. **A. Buehler**, X. L. Deán-Ben, J. Shi, V. Ntziachristos, D. Razansky, "Real-time three dimensional optoacoustic imaging of perfusion", Poster presented at *2012 World Molecular Imaging Congress,* Dublin, Ireland, Sept. 5-8, 2012.
12. X. L. Deán-Ben, **A. Buehler**, V. Ntziachristos, D. Razansky, "Three-dimensional single-shot optoacoustic visualization of excised mouse organs with model-based reconstruction"; Published in Proceedings *Photons Plus Ultrasound: Imaging and Sensing 2013*, vol. 8581, 2013.
13. D. Queiros, X. L. Deán-Ben, **A. Buehler**, D. Razansky, A. Rosenthal, V. Ntziachristos „Incorporating geometric detector properties into three-dimensional optoacoustic tomography"; Poster at *European Conferences on Biomedical Optics*, Munich, Germany, May 12-26, 2013.
14. **A. Buehler**, M. Kacprowicz, A. Taruttis, V. Ntziachristos, „real-time handheld multispectral optoacoustic imaging", Oral presentation given at *European Conferences on Biomedical Optics*, Munich, Germany, May 12-26, 2013.

Bibliography

1. P. Zansonico, *Small Animal Imaging*. 1st ed., F. Kiessling & B. J. Pichler (Eds.), Springer-Verlag, Berlin Heidelberg, 2011.
2. V. Ntziachristo et al., *Looking and listening to light: the evolution of whole-body photonic imaging.* Nature Biotechnology, 2005. **23**(3): p. 313-320.
3. R. Weissleder and M. J. Pittet, *Imaging in the era of molecular oncology.* Nature, 2008. **452**(7187): p. 580-589.
4. V. Ntziachristos and D. Razansky, *Molecular imaging by means of multispectral opto-acoustic tomography (MSOT).* Chemical Reviews, 2010. **110**(5): p. 2783-2794.
5. D. Razansky, C. Vinegoni and V. Ntziachristos, *Imaging of mesoscopic-scale organisms using selective-plane optoacoustic tomography.* Physics in Medicine and Biology, 2009. **54**(9): p. 2769-2777.
6. D. Razansky, C. Vinegoni and V. Ntziachristos, *Multispectral photoacoustic imaging of fluorochromes in small animals.* Optics Letters, 2007. **32**: p. 2891-2893.
7. D. Razansky et al., *Multispectral opto-acoustic tomography of deep-seated fluorescent proteins in vivo.* Nature Photonics, 2009. **3**(7): p. 412-417.
8. J. Gamelin et al., *A real-time photoacoustic tomography system for small animals.* Optics Express, 2009. **17**(13): p. 10489-10498.
9. A. Soubret and V. Ntziachristos, in: *Textbook of in vivo Imaging in Vertebrates.* 1st ed., V. Ntziachristos, A. Leroy-Willig and B. Tavitian (Eds.), John Wiley & Sons, Chichester, West Sussex, England, 2007, p. 388.
10. B. T. Cox et al., *k-space propagation models for acoustically heterogeneous media: Application to biomedical photoacoustics.* Journal of the Acoustical Society of America, 2007. **121**(6): p. 3453-3464.
11. T. F. Massoud and S. S. Gambhir, *Molecular imaging in living subjects: seeing fundamental biological processes in a new light.* Genes & Development, 2003. **17**(5): p. 545-580.
12. R. Weissleder, *Scaling down imaging: Molecular mapping of cancer in mice.* Nature Reviews Cancer, 2002. **2**(1): p. 11-18.
13. S. Ogawa et al., *Brain magnetic resonance imaging with contrast dependent on blood oxygenation.* Proceedings of the National Academy of Sciences of the United States of America, 1990. **87**(24): p. 9868-9872.
14. L. V. Wang and H.-I. Wu, *Biomedical Optics: Principles and Imaging*, L. V. Wang & H.-I. Wu (Eds.), Wiley-Interscience, 2007.
15. V. Ntziachristos, *Going deeper than microscopy: the optical imaging frontier in biology.* Nature Methods, 2010. **7**(8): p. 603-614.
16. R. H. Webb, *Theoretical basis of confocal microscopy.* Confocal Microscopy, 1999. **307**: p. 3-20.
17. W. Denk, J. H. Strickler and W. W. Webb, *Two-photon laser scanning fluorescence microscopy.* Science, 1990. **248**(4951): p. 73-76.
18. J. S. Reynolds et al., *Imaging of spontaneous canine mammary tumors using fluorescent contrast agents.* Photochemistry and Photobiology, 1999. **70**(1): p. 87-94.
19. V. Ntziachristos et al., *Fluorescence molecular tomography resolves protease activity in vivo.* Nature medicine, 2002. **8**(7): p. 757-760.
20. R. B. Schulz et al., *Hybrid System for Simultaneous Fluorescence and X-Ray Computed Tomography.* IEEE Transactions on Medical Imaging, 2010. **29**(2): p. 465-473.
21. A. Ale et al., *Imaging performance of a hybrid x-ray computed tomography-fluorescence molecular tomography system using priors.* Medical Physics. **37**(5): p. 1976-1986.

22. R. A. Kruger et al., *Thermoacoustic molecular imaging of small animals.* Mol. Imaging, 2003. **2**(2): p. 113-123.
23. X. D. Wang et al., *Noninvasive laser-induced photoacoustic tomography for structural and functional in vivo imaging of the brain.* Nature Biotechnology, 2003. **21**(7): p. 803-806.
24. X. D. Wang et al., *Photoacoustic tomography of biological tissues with high cross-section resolution: Reconstruction and experiment.* Medical Physics, 2002. **29**(12): p. 2799-2805.
25. L. V. Wang, *Photoacoustic Imaging and Spectroscopy,* L. V. Wang (Ed.), CRC Press, Boca Raton, Florida, USA, 2009.
26. M. H. Xu and L. H. V. Wang, *Photoacoustic imaging in biomedicine.* Review of Scientific Instruments, 2006. **77**(4): p. 041101.
27. H. F. Zhang et al., *In vivo volumetric imaging of subcutaneous microvasculature by photoacoustic microscopy.* Optics Express, 2006. **14**(20): p. 9317-9323.
28. R. I. Siphanto et al., *Serial noninvasive photoacoustic imaging of neovascularization in tumor angiogenesis.* Optics Express, 2005. **13**(1): p. 89-95.
29. G. Ku et al., *Imaging of tumor angiogenesis in rat brains in vivo by photoacoustic tomography.* Applied Optics, 2005. **44**(5): p. 770-775.
30. M. Pramanik et al., *Design and evaluation of a novel breast cancer detection system combining both thermoacoustic (TA) and photoacoustic (PA) tomography.* Medical Physics, 2008. **35**(6): p. 2218-2223.
31. A. De La Zerda et al., *Carbon nanotubes as photoacoustic molecular imaging agents in living mice.* Nature Nanotechnology, 2008. **3**(9): p. 557-562.
32. M. Eghtedari et al., *High sensitivity of in vivo detection of gold nanorods using a laser optoacoustic imaging system.* Nano Letters, 2007. **7**(7): p. 1914-1918.
33. X. H. Gao et al., *In vivo molecular and cellular imaging with quantum dots.* Current Opinion in Biotechnology, 2005. **16**(1): p. 63-72.
34. A. G. Bell, *The production of sound by radiant energy.* Science, 1881. **2**(49): p. 242-253.
35. C. H. Li and L. H. V. Wang, *Photoacoustic tomography and sensing in biomedicine.* Physics in Medicine and Biology, 2009. **54**(19): p. R59-R97.
36. D. Razansky and V. Ntziachristos, *Hybrid photoacoustic fluorescence molecular tomography using finite-element-based inversion.* Medical Physics, 2007. **34**(11): p. 4293-4301.
37. A. Taruttis, *Multispectral optoacoustic tomography for imaging of disease biomarkers*, PhD thesis, Technical University of Munich, 2012. http://nbn-resolving.de/urn/resolver.pl?urn:nbn:de:bvb:91-diss-20120712-1084377-0-8
38. B. A. J. Angelsen, in: *Ultrasound Imaging*, B. A. J. Angelsen. (Ed.), Vol. 1., Emantec AS, Trondheim, 2000, p.697.
39. X. L. Deán-Ben, D. Razansky and V. Ntziachristos, *The effects of acoustic attenuation in optoacoustic signals.* Physics in Medicine and Biology, 2011. **56**(18): p. 6129-6148.
40. D. Razansky, *Multi-Spectral Optoacoustic Tomography – Volumetric Color Hearing in Real Time.* IEEE Journal of Selected Topics in Quantum Electronics, 2012. **18**(3): p. 1235-1243.
41. M. À. A. Caballero, *Optoacoustic Imaging with Full-Knowledge of Sensor Properties*, PhD thesis, Technical University of Munich, 2012 (in review).
42. C. G. A. Hoelen and F. F. M. de Mul, *A new theoretical approach to photoacoustic signal generation.* Journal of the Acoustical Society of America, 1999. **106**(2): p. 695-706.
43. D. Razansky, J. Baeten and V. Ntziachristos, *Sensitivity of molecular target detection by multispectral optoacoustic tomography (MSOT).* Medical Physics, 2009. **36**(3): p. 939-945.
44. R. Paschotta, *Encyclopedia of Laser Physics and Technology*, Vol. 1, Wiley-VCH Verlag GmbH Co., Weinheim, 2001.

45. D. Razansky, *Multi-Spectral Optoacoustic Tomography – Volumetric Color Hearing in Real Time.* IEEE Journal of Selected Topics in Quantum Electronics, 2012. **18**(3): p. 1235-1243.
46. D. Razansky, *Multi-Spectral Optoacoustic Tomography – Volumetric Color Hearing in Real Time.* IEEE Journal of Selected Topics in Quantum Electronics, 2012. **18**(3): p. 1235-1243.
47. T. L. Szabo, *Diagnostic ultrasound imaging*, J. Bronzino (Ed.), academic press series in biomedical engineering, Vol. 1, Elsevier, Burlington, 2004.
48. K. K. Shung and M. Zipparo, *Ultrasonic transducers and arrays.* IEEE Engineering in Medicine and Biology Magazine, 1996. **15**(6): p. 20-30.
49. R. Nuster et al., *Full field detection in photoacoustic tomography.* Optics Express, 2010. **18**(6): p. 6288-6299.
50. A. Rosenthal, D. Razansky and V. Ntziachristos, *High-sensitivity compact ultrasonic detector based on a pi-phase-shifted fiber Bragg grating.* Optics Letters, 2011. **36**(10): p. 1833-1835.
51. E. Z. Zhang et al., *In vivo high-resolution 3D photoacoustic imaging of superficial vascular anatomy.* Physics in Medicine and Biology, 2009. **54**(4): p. 1035-1046.
52. V. Kozhushko et al., *Focused array transducer for two-dimensional optoacoustic tomography.* Journal of the Acoustical Society of America, 2004. **116**(3): p. 1498-1506.
53. A. Rosenthal, V. Ntziachristos and D. Razansky, *Optoacoustic Methods for Frequency Calibration of Ultrasonic Sensors.* IEEE Transactions on Ultrasonics Ferroelectrics and Frequency Control, 2011. **58**(2): p. 316-326.
54 T.D. Khokhlova, et al., *Optoacoustic imaging of absorbing objects in a turbid medium: ultimate sensitivity and application to breast cancer diagnostics.* Applied Optics, 2007. **46**(2): p. 262-272.
55. A. Rosenthal, V. Ntziachristos and D. Razansky, *Model-based optoacoustic inversion with arbitrary-shape detectors.* Medical Physics, 2011. **38**(7): p. 4285-4295.
56. J. A. Jensen and N. B. Svendsen, *Calculation of pressure fields from arbitrarily shaped, apodized and excited ultrasound transducers.* IEEE Transactions on Ultrasonics Ferroelectrics and Frequency Control, 1992. **39**(2): p. 262-267.
57. R. Ma et al., *Multispectral optoacoustic tomography (MSOT) scanner for whole-body small animal imaging.* Optics Express, 2009. **17**(24): p. 21414-21426.
58. P. Beard, *Biomedical photoacoustic imaging.* Interface Focus, 2011. **1**(4): p. 602-631.
59. K. Maslov, G. Stoica and L. H. V. Wang, *In vivo dark-field reflection-mode photoacoustic microscopy.* Optics Letters, 2005. **30**(6): p. 625-627.
60. H. P. Brecht et al., *Whole-body three-dimensional optoacoustic tomography system for small animals.* Journal of Biomedical Optics, 2009. **14**(6): p. 064007.
61. J. Laufer et al., *In vivo photoacoustic imaging of mouse embryos.* Journal of Biomedical Optics, 2012. **17**(6): p. 06220.
62. K. P. Kostli et al., *Temporal backward projection of optoacoustic pressure transients using Fourier transform methods.* Physics in Medicine and Biology, 2001. **46**(7): p. 1863-1872.
63. M. H. Xu and L. H. V. Wang, *Universal back-projection algorithm for photoacoustic computed tomography.* Physical Review E, 2005. **71**(1): p. 016706.
64. H. B. Jiang, Z. Yuan and X.J. Gu, *Spatially varying optical and acoustic property reconstruction using finite-element-based photoacoustic tomography.* Journal of the Optical Society of America: a-Optics Image Science and Vision, 2006. **23**(4): p. 878-888.
65. G. Paltauf et al., *Iterative reconstruction algorithm for optoacoustic imaging.* Journal of the Acoustical Society of America, 2002. **112**(4): p. 1536-1544.
66. A. Rosenthal, D. Razansky and V. Ntziachristos, *Fast semi-analytical model-based acoustic inversion for quantitative optoacoustic tomography.* IEEE Transactions on Medical Imaging, 2010. **28**(12): p. 1997-2006
67. G. H. Golub and C. F. Van Loan, *Matrix Computations*, 3rd Ed., John Hopkins, 1996.

68. C. C. Paige and M. A. Saunders, *LSQR: an algorithm for sparse linear equations and sparse least squares*, ACM Trans. Math. Softw., 1982. **8**: p. 43-71.
69. M. Xu and L. V. Wang, *Analytic explanation of spatial resolution related to bandwidth and detector aperture size in thermoacoustic or photoacoustic reconstruction.* Physical Review E, 2003. **67**(5): p. 056605.
70. T. D. Khokhlova, I. M. Pelivanov and A. A. Karabutov, *Optoacoustic tomography utilizing focused transducers: The resolution study.* Applied Physics Letters, 2008. **92**(2): p. 024105.
71. Y. Xu et al., *Reconstructions in limited-view thermoacoustic tomography.* Medical Physics, 2004. **31**(4): p. 724-733.
72. M. Xu, *Photoacoustic computed tomography in biological tissues: algorithms and breast imaging*, PhD thesis, Texas A&M University, 2004.
73. H. Dehghani et al., *Near infrared optical tomography using NIRFAST: Algorithm for numerical model and image reconstruction.* Communications in Numerical Methods in Engineering, 2009. **25**(6): p. 711-732.
74. L. V. Wang, *Prospects of photoacoustic tomography.* Medical Physics, 2008. **35**(12): p. 5758-5767.
75. S. A. Ermilov et al., *Laser optoacoustic imaging system for detection of breast cancer.* Journal of Biomedical Optics, 2009. **14**(2): p. 024007.
76. B. Z. Yin et al., *Fast photoacoustic imaging system based on 320-element linear transducer array.* Physics in Medicine and Biology, 2004. **49**(7): p. 1339-1346.
77. A. Buehler et al., *Video rate optoacoustic tomography of mouse kidney perfusion.* Optics Letters, 2010. **35**(14): p. 2475-2477.
78. K. Maslov et al., *Optical-resolution photoacoustic microscopy for in vivo imaging of single capillaries.* Optics Letters, 2008. **33**(9): p. 929-931.
79. A. Dima and V. Ntziachristos, *Optoacoustic imaging for clinical applications: devices and methods.* Expert Opinion on Medical Diagnostics, 2011. **5**(3): p. 263-272.
80. A. Dima and V. Ntziachristos, *Non-invasive carotid imaging using optoacoustic tomography.* Optics Express, 2012. **20**(22): p. 25044-25057.
81. C. Kim et al., *Deeply penetrating in vivo photoacoustic imaging using a clinical ultrasound array system.* Biomedical Optics Express, 2010. **1**(1): p. 278-284.
82. J. J. Niederhauser et al., *Combined ultrasound and optoacoustic system for real-time high-contrast vascular imaging in vivo.* IEEE Transactions on Medical Imaging, 2005. **24**(4): p. 436-440.
83. R. A. Kruger et al., *Photoacoustic angiography of the breast.* Medical Physics, 2010. **37**(11): p. 6096-6100.
84. D. Piras et al., *Photoacoustic Imaging of the Breast Using the Twente Photoacoustic Mammoscope: Present Status and Future Perspectives.* IEEE Journal of Selected Topics in Quantum Electronics, 2010. **16**(4): p. 730-739.
85. F. Ye, S. Yang and D. Xing, *Three-dimensional photoacoustic imaging system in line confocal mode for breast cancer detection.* Applied Physics Letters, 2010. **97**(21): p. 213702.
86. A. B. Karpiouk, B. Wang and S. Y. Emelianov, *Development of a catheter for combined intravascular ultrasound and photoacoustic imaging.* Review of Scientific Instruments, 2010. **81**(1): p. 014901.
87. B. Wang et al., *Intravascular Photoacoustic Imaging.* IEEE Journal of Selected Topics in Quantum Electronics, 2010. **16**(3): p. 588-599.
88. J.-M. Yang et al., *Photoacoustic endoscopy.* Optics Letters, 2009. **34**(10): p. 1591-1593.
89. T. Jetzfellner et al., *Interpolated model-matrix optoacoustic tomography of the mouse brain.* Applied Physics Letters, 2011. **98**(16): p. 163701.
90. T. Jetzfellner et al., *Optoacoustic tomography with varying illumination and non-uniform detection patterns.* Journal of the Optical Society of America: a-Optics Image Science and Vision, 2010. **27**(11): p. 2488-2495.

91. C. Li et al., *Real-time photoacoustic tomography of cortical hemodynamics in small animals.* Journal of Biomedical Optics Letters, 2010. **15**(1): p. 010509.
92. D. Razansky, A. Buehler and V. Ntziachristos, *Volumetric real-time multispectral optoacoustic tomography of biomarkers.* Nature Protocols, 2011. **6**(8): p. 1121-1129.
93. K. Zell et al., *Acoustical properties of selected tissue phantom materials for ultrasound imaging.* Physics in Medicine and Biology, 2007. **52**(20): p. N475-N484.
94. J. A. Jensen, *Field: A Program for Simulating Ultrasound Systems.* Medical and Biological Engineering and Computing, 1996. **34**(1): p. 351-353.
95. M. A. Anastasio et al., *Half-time image reconstruction in thermoacoustic tomography.* IEEE Transactions on Medical Imaging, 2005. **24**(2): p. 199-210.
96. S. Manohar et al., *The Twente Photoacoustic Mammoscope: system overview and performance.* Physics in Medicine and Biology, 2005. **50**(11): p. 2543-2557.
97. G. H. Weiss, A. J. Talbert and R. A. Brooks, *The use of phantom views to reduce CT streaks due to insufficient angular sampling.* Physics in Medicine and Biology, 1982. **27**(9): p. 1151-1162.
98. B. E. Treeby and B. T. Cox, *k-Wave: MATLAB toolbox for the simulation and reconstruction of photoacoustic wave fields.* Journal of Biomedical Optics, 2010. **15**(2): p. 021314.
99. A. Buehler et al., *Model-based optoacoustic inversions with incomplete projection data.* Medical Physics, 2011. **38**(3): p. 1694-1704.
100. P. C. Hansen, *Truncated SVD solutions to discrete ill-posed problems with ill-determined numerical rank.* SIAM J. Sci. Stat. Comput, 1990. **11**: p. 503-518.
101. P. C. Hansen, *Regularization tools: a Matlab package for analysis and solution of discrete ill-posed problems.* Numerical Algorithms, 1994. **6**: p. 1-35.
102. P. C. Hansen, *Regularization, GSVD and truncated GSVD.* BIT, 1989. **29**: p. 491-504.
103. S. Morigi, L. Reichel and F. Sgallari, *A truncated projected SVD method for linear discrete ill-posed problems.* Numerical Algorithms, 2006. **43**(3): p. 197-213.
104. P.C. Hansen, *Rank-deficient and discrete ill-posed problems. Numerical aspects of linear inversion,* SIAM, Philadelphia, 1997.
105. P. C. Hansen, *Regularization tools version 4.0 for Matlab 7.3.* Numerical Algorithms, 2007. **46**(2): p. 189-194.
106. R. Ma et al., *Multispectral optoacoustic tomography (MSOT) scanner for whole-body small animal imaging.* Optics Express, 2009. **17**(24): p. 21414-21426.
107. M. À. A. Caballero et al., *Model-based optoacoustic imaging using focused detector scanning.* Optics Letters, 2012. **37**(19): p. 4080-4082.
108. X. L. Deán-Ben et al., *Accurate model-based reconstruction algorithm for three-dimensional optoacoustic tomography.* IEEE Transactions on Medical Imaging, 2012. **31**(10): p. 1922-1928.
109. X. L. Deán-Ben et al., *Accurate model-based reconstruction algorithm for three-dimensional optoacoustic tomography.* IEEE Transactions on Medical Imaging, 2012. **31**(10): p. 1922-1928.
110. D. Queirós et al., *Modeling the shape of cylindrically focused transducers in three-dimensional optoacoustic tomography.* Journal of Biomedical Optics **18**, 7 (2013).
111. A. Rosenthal et al., *Efficient Framework for Model-Based Tomographic Image Reconstruction Using Wavelet Packets.* IEEE Transactions on Medical Imaging, 2012. **31**(7): p. 1346-1357.
112. J. Glatz et al., *Blind source unmixing in multi-spectral optoacoustic tomography.* Optics Express, 2011. **19**(4): p. 3175-3184.
113. M. L. J. Landsman et al., *Light-Absorbing Properties, Stability, and Spectral Stabilization of Indocyanine Green.* Journal of Applied Physiology, 1976. **40**(4): p. 575-583.
114. B. Cox et al., *Quantitative spectroscopic photoacoustic imaging: a review.* Journal of Biomedical Optics, 2012. **17**(6): p. 061202.
115. M. Funaro, E. Oja and H. Valpola, *Independent component analysis for artefact separation in astrophysical images.* Neural Networks, 2003. **16**(3-4): p. 469-478.

116. B. A. Draper et al., *Recognizing faces with PCA and ICA.* Computer Vision and Image Understanding, 2003. **91**(1-2): p. 115-137.
117. E. M. C. Hillman and A. Moore, *All-optical anatomical co-registration for molecular imaging of small animals using dynamic contrast.* Nature Photonics, 2007. **1**(9): p. 526-530.
118. N. Keshava, *A Survey of Spectral unmixing algorithms.* Lincoln Laboratory Journal, 2003. **14**(1): p. 55-78.
119. I. T. Jolliffe, *Principal Component Analysis,* 2nd Ed., Vol. 2., 2002: Springer.
120. A. Hyvärinen and E. Oja, *Independent Component Analysis:Algorithms and Applications.* Neural Networks, 2000. **13**(4-5): p. 411-430.
121. G. D. Clifford, *Course materials for HST.582J / 6.555J /16.456J, Biomedical Signal and Image Processing, Spring 2007.* MIT OpenCourseWare (http://ocw.mit.edu), Massachusetts Insittute of Technlogy, 2007.
122. S. Morscher, *Component Based Unmixing in Multi-Spectral Optoacoustic Tomography*, Master thesis, Technical university of Munich, 2011.
123. E. Bingham and A. Hyvarinen, *A fast fixed-point algorithm for independent component analysis of complex valued signals.* International Journal of Neural Systems, 2000. **10**(1): p. 1-8.
124. J. Glatz, *Unmixing fluorescent proteins in multispectral optoacoustic tomography*, Master thesis, Technical university of Munich, 2010.
125. A. Buehler et al., *Real-time handheld multispectral optoacoustic imaging.* Optics Letters, 2013. **38**(9): p. 1404-1406.
126. D. J. Pole et al., *Cardic and respiratory gating for a small animal spect-CT system*, in: *2010 IEEE Nuclear Science Symposium Conference Record,* 2010, p. 2177-2180.
127. J. Salvi et al., *A review of recent range image registration methods with accuracy evaluation.* Image and Vision Computing, 2007. **25**(5): p. 578-596.
128. M. L. Landsman et al., *Light-absorbing properties, stability, and spectral stabilization of indocyanine green.* Journal of Applied Physiology, 1976. **40**(4): p. 575-83.
129. D. Stokes, *Principles and Practice of Variable Pressure: Environmental Scanning Electron Microscopy*, Vol. 1, John Wiley & Sons, Cornwall, 2008.
130. T. Jetzfellner et al., *Performance of iterative optoacoustic tomography with experimental data.* Applied Physics Letters, 2009. **95**(1): p. 013703.
131. X. D. Wang et al., *Noninvasive imaging of hemoglobin concentration and oxygenation in the rat brain using high-resolution photoacoustic tomography.* Journal of Biomedical Optics, 2006. **11**(2): p. 024015.
132. A. Rosenthal, D. Razansky and V. Ntziachristos, *Quantitative optoacoustic signal extraction using sparse signal representation.* IEEE Trans. Med. Imaging, 2009. **28**(12): p. 1997-2006.
133. B. T. Cox, S. R. Arridge and P. C. Beard, *Estimating chromophore distributions from multiwavelength photoacoustic images.* Journal of the Optical Society of America: a-Optics Image Science and Vision, 2009. **26**(2): p. 443-455.
134. T. Jetzfellner et al., *Multispectral optoacoustic tomography by means of normalized spectral ratio.* Optics Letters, 2011. **36**(21): p. 4176-4178.
135. A. Taruttis et al., *Motion clustering for deblurring multispectral optoacoustic tomography images of the mouse heart.* Journal of Biomedical Optics, 2012. **17**(1): p. 016009.
136. A. Taruttis et al., *Real-time imaging of cardiovascular dynamics and circulating gold nanorods with multispectral optoacoustic tomography.* Optics Express, 2010. **18**(19): p. 19592-19602.
137. A. Taruttis et al., *Multispectral optoacoustic tomography of myocardial infarction.* Photoacoustics, 2012. **1**(1): p. 3-8.

138. I. J. Fox et al., *A new dye for continuous recording of dilution curves in whole blood independent of variations in blood oxygen saturation.* Circulation, 1956. **14**(5): p. 937-938.
139. A. C. Guyton and J. E. Hall, *Textbook of Medical Physiology*. Vol. 10, Saunders, Pennsylvania, 2000.
140. S. E. Bradley, *Physiology of Essential Hypertension.* American Journal of Medicine, 1948. **4**(3): p. 398-415.
141. H. H. Rasmussen and L. S. Ibels, *Acute-Renal-Failure - Multivariate-Analysis of Causes and Risk-Factors.* American Journal of Medicine, 1982. **73**(2): p. 211-218.
142. P. Dawson, *Functional imaging in CT.* European Journal of Radiology, 2006. **60**(3): p. 331-340.
143. M. D. Bentley et al., *Measurement of Renal Perfusion and Blood-Flow with Fast Computed-Tomography.* Circulation Research, 1994. **74**(5): p. 945-951.
144. X. Liu et al., *Renal Perfusion and Hemodynamics: Accurate in Vivo Determination at CT with a 10-Fold Decrease in Radiation Dose and HYPR Noise Reduction.* Radiology, 2009. **253**(1): p. 98-105.
145. L. Ludemann et al., *Absolute Quantification of Regional Renal Blood Flow in Swine by Dynamic Contrast-Enhanced Magnetic Resonance Imaging Using a Blood Pool Contrast Agent.* Investigative Radiology, 2009. **44**(3): p. 125-134.
146. K. Kalantarinia et al., *Real-time measurement of renal blood flow in healthy subjects using contrast-enhanced ultrasound.* American Journal of Physiology-Renal Physiology, 2009. **297**(4): p. F1129-F1134.
147. D. S. Williams et al., *Perfusion Imaging of the Rat-Kidney with MR.* Radiology, 1994. **190**(3): p. 813-818.
148. F. Kiessling, D. Razansky and F. Alves, *Anatomical and microstructural imaging of angiogenesis.* European Journal of Nuclear Medicine and Molecular Imaging, 2010. **37**: p. S4-S19.
149. X.-H.Peng et al., *Targeted magnetic iron oxide nanoparticles for tumor imaging and therapy.* International Journal of Nanomedicine, 2008. **3**(3): p. 311-321.
150. V. Ntziachristos et al., *Concurrent MRI and diffuse optical tomography of breast after indocyanine green enhancement.* Proceedings of the National Academy of Sciences of the United States of America, 2000. **97**(6): p. 2767-2772.
151. G. Valentini et al., *In vivo measurement of vascular modulation in experimental tumors using a fluorescent contrast agent.* Photochemistry and Photobiology, 2008. **84**(5): p. 1249-1256.
152. V. Ntziachristos et al., *Visualization of antitumor treatment by means of fluorescence molecular tomography with an annexin V-Cy5.5 conjugate.* Proceedings of the National Academy of Sciences of the United States of America, 2004. **101**(33): p. 12294-12299.
153. D. E. Sosnovik et al., *Fluorescence tomography and magnetic resonance imaging of myocardial macrophage infiltration in infarcted myocardium in vivo.* Circulation, 2007. **115**(11): p. 1384-1391.
154. B. A. Smith et al., *Optical Imaging of Mammary and Prostate Tumors in Living Animals using a Synthetic Near Infrared Zinc(II)-Dipicolylamine Probe for Anionic Cell Surfaces.* Journal of the American Chemical Society. **132**(1): p. 67-69.
155. G. Evan and T. Littlewood, *A matter of life and cell death.* Science, 1998. **281**(5381): p. 1317-1322.
156. A. Buehler et al., *High resolution tumor targeting in living mice by means of multi-spectral optoacoustic tomography.* EJNMMI Research, 2012. **2**: p. 14.
157. W. M. Leevy et al., *Optical imaging of bacterial infection in living mice using a fluorescent near-infrared molecular probe.* Journal of the American Chemical Society, 2006. **128**(51): p. 16476-16477.
158. R. B. Schulz et al., *Hybrid System for Simultaneous Fluorescence and X-ray Computed Tomography.* IEEE Trans. Med. Imaging, 2009. **29**(2): p. 465-473.

159. A. Sarantopoulos, G. Themelis and V. Ntziachristos, *Imaging the Bio-Distribution of Fluorescent Probes Using Multispectral Epi-Illumination Cryoslicing Imaging.* Molecular Imaging and Biology, 2010. **13**(5): p. 874-885.
160. B. A. Smith et al., *Optical Imaging of Mammary and Prostate Tumors in Living Animals using a Synthetic Near Infrared Zinc(II)-Dipicolylamine Probe for Anionic Cell Surfaces.* Journal of the American Chemical Society. **132**(1): p. 67-69.
161. M. Y. Berezin et al., *Rational Approach To Select Small Peptide Molecular Probes Labeled with Fluorescent Cyanine Dyes for in Vivo Optical Imaging.* Biochemistry, 2011. **50**(13): p. 2691-2700.
162. H. Kenis and C. Reutelingsperger, *Targeting Phosphatidylserine in Anti-Cancer Therapy.* Current Pharmaceutical Design, 2009. **15**(23): p. 2719-2723.
163. P. E. Thorpe, *Targeting anionic phospholipids on tumor blood vessels and tumor cells.* Thrombosis Research. **125**: p. S134-S137.
164. S. Ran, A. Downes and P. E. Thorpe, *Increased exposure of anionic phospholipids on the surface of tumor blood vessels.* Cancer Research, 2002. **62**(21): p. 6132-6140.
165. H. Maeda, *The enhanced permeability and retention (EPR) effect in tumor vasculature: The key role of tumor-selective macromolecular drug targeting*, in: *Advances in Enzyme Regulation*, G. Weber (Ed.), Vol. 41, 1st Ed, Elsevier Science Ltd, 2001, p. 189-207.
166. J. H. JLin and A. Y. H. Lu, *Role of pharmacokinetics and metabolism in drug discovery and development.* Pharmacological Reviews, 1997. **49**(4): p. 403-449.
167. G. R. Cherrick et al., *Indocyanine Green - Observations on Its Physical Properties, Plasma Decay, and Hepatic Extraction.* Journal of Clinical Investigation, 1960. **39**(4): p. 592-600.
168. S. T. Proulx et al., *Quantitative Imaging of Lymphatic Function with Liposomal Indocyanine Green.* Cancer Research, 2010. **70**(18): p. 7053-7062.
169. M. C. Woodle et al., *Versatility in lipid compositions showing prolonged circulation with sterically stabilized liposomes.* Biochimica et Biophysica Acta, 1992. **1105**(2): p. 193-200.
170. D. Papahadjopoulos et al., *Sterically stabilized liposomes improvements in pharmacokinetics ans antitumor therapeutic efficacy.* Proceedings of the National Academy of Sciences of the United States of America, 1991. **88**(24): p. 11460-11464.
171. J. Stritzker et al., *Vaccinia virus-mediated melanin production allows MR and optoacoustic deep tissue imaging and laser-induced thermotherapy of cancer.* Proceedings of the National Academy of Sciences of the United States of America, 2013. **110**(9): p. 3316-20.
172. E. Herzog et al., *Optical imaging of Cancer Heterogeneity with multispectral optoacoustic tomography.* Radiology, 2012. **263**(2): p. 461-468.
173. N. C. Burto et al., *Multispectral Optoacoustic Tomography (MSOT) Brain Imaging and Characterization of Glioblastoma.* NeuroImage, 2012. **65**: p. 522-528.
174. C. Bao et al., *Gold nanoprisms as optoacoustic signal nanoamplifiers for in vivo bioimaging of gastrointestinal cancers.* Small, 2013. **9**(1): p. 68-74.
175. L. Xiang et al., *4-d photoacoustic tomography.* Scientific Reports, 2013. **3**: p. 1113.
176. P. Ephrat et al., *Four-dimensional photoacoustic imaging of moving targets.* Optics Express, 2008. **16**(26): p. 21570-21581.
177. A. Buehler et al., *Three-dimensional optoacoustic tomography at video rate.* Optics Express, 2012. **20**(20): p. 22712-22719.
178. A. Taruttis, *Fast multispectral optoacoustic tomography (MSOT) for dynamic imaging of pharmacokinetics and biodistribution in multiple organs.* PLoS ONE, 2012. **7**(1): p. 30491.
179. F. C. Robey et al., *A CFAR adaptive matched filter detector.* IEEE Transactions on Aerospace and Electronic Systems, 1992. **28**(1): p. 208-216.